MICROCOPY RESOLUTION TEST CHART

BUREAU OF STANDARDS-1963-A

MASTER COPY   -   FOR REPRODUCTION PURPOSES

②

DTIC FILE COPY

REPORT DOCUMENTATION PAGE

DTIC
ELECTE
R 1 3 1988
D

AD-A192 514

1a. REPORT SECURITY CLASSIFICATION	1b. RESTRICTIVE MARKINGS
Unclassified	

3. DISTRIBUTION/AVAILABILITY OF REPORT
Approved for public release; distribution unlimited.

5. MONITORING ORGANIZATION REPORT NUMBER(S)
ARO 22279.25-PH

6a. NAME OF PERFORMING ORGANIZATION	6b. OFFICE SYMBOL (If applicable)	7a. NAME OF MONITORING ORGANIZATION
Oklahoma State University		U. S. Army Research Office

6c. ADDRESS (City, State, and ZIP Code)	7b. ADDRESS (City, State, and ZIP Code)
Stillwater, Oklahoma 74078	P. O. Box 12211 Research Triangle Park, NC 27709-2211

8a. NAME OF FUNDING/SPONSORING ORGANIZATION	8b. OFFICE SYMBOL (If applicable)	9. PROCUREMENT INSTRUMENT IDENTIFICATION NUMBER
U. S. Army Research Office		DAAG29-85-K-0056

8c. ADDRESS (City, State, and ZIP Code)	10. SOURCE OF FUNDING NUMBERS			
P. O. Box 12211 Research Triangle Park, NC 27709-2211	PROGRAM ELEMENT NO.	PROJECT NO.	TASK NO.	WORK UNIT ACCESSION NO.

11. TITLE (Include Security Classification)
Laser Spectroscopy Investigations of Materials for Solid State Laser Systems

12. PERSONAL AUTHOR(S)
Richard C. Powell

13a. TYPE OF REPORT	13b. TIME COVERED	14. DATE OF REPORT (Year, Month, Day)	15. PAGE COUNT
Final	FROM 1/16/85 TO 1/15/88	Februrary 1988	

16. SUPPLEMENTARY NOTATION
The view, opinions and/or findings contained in this report are those of the author(s) and should not be construed as an official Department of the Army position, policy, or decision, unless so designated by other documentation

17.	COSATI CODES		18. SUBJECT TERMS (Continue on reverse if necessary and identify by block number)
FIELD	GROUP	SUB-GROUP	Laser Spectroscopy, Laser Systems, Solid State Laser Systems, Optical Devices, Fiber Crystals, Laser Crystals

19. ABSTRACT (Continue on reverse if necessary and identify by block number)

Some of the results of major importance from this work are: (1) The development of a method for producing laser-induced grating optical devices in glasses; (2) The elucidation of the effects of Mg on inhibiting the photorefractive response of lithium niobate; (3) The demonstration of tunable single pass gain from a closed shell ion in

Abstract continued on reverse side

20. DISTRIBUTION/AVAILABILITY OF ABSTRACT	21. ABSTRACT SECURITY CLASSIFICATION
☐ UNCLASSIFIED/UNLIMITED ☐ SAME AS RPT. ☐ DTIC USERS	Unclassified

22a. NAME OF RESPONSIBLE INDIVIDUAL	22b. TELEPHONE (Include Area Code)	22c. OFFICE SYMBOL

DD FORM 1473, 84 MAR   83 APR edition may be used until exhausted.   All other editions are obsolete.

ABSTRACT CONTINUED:

cont'd the visible spectral region; (4) A demonstration of the decrease
in fluorescence quenching in fiber crystals; (5) A demonstration
of the effects of thermal annealing on the infrared absorption
and visible emission in Ti-sapphire laser crystals; and (6) A
measurement of the pump band to metastable state relaxation rate
in alexandrite laser crystals.

LASER SPECTROSCOPY INVESTIGATIONS OF MATERIALS

FOR SOLID STATE LASER SYSTEMS

Richard C. Powell, Ph.D.
Principal Investigator

Department of Physics
OKLAHOMA STATE UNIVERSITY
Stillwater, Oklahoma 74078

FINAL REPORT

ABSTRACT

This report summarizes the research done in the Department of Physics of Oklahoma State University supported by the U.S. Army Research Office under contract number DAAG29-85-K-0056 from January 15, 1985 through January 14, 1988. The research involves the use of laser spectroscopy techniques such as four-wave mixing, high power picosecond pulse pumping, and time-resolved site-selection spectroscopy to characterize dynamical optical processes such as energy migration, multiphoton absorption, radiationless relaxation, and the photorefractive effect in materials with potential applications in optical technology. The materials investigated include existing laser crystals such as alexandrite, titanium doped sapphire, Nd-YAG, and neodymium pentaphosphate as well as several potential rare earth and transition metal laser crystals. In addition, photorefractive processes were studied in lithium niobate and bismuth silicate crystals and in rare earth doped glasses. Some of the results of major importance from this work are: (1) The development of a method for producing laser-induced grating optical devices in glasses; (2) The elucidation of the effects of Mg on inhibiting the photorefractive response of lithium niobate; (3) The demonstration of tunable single pass gain from a closed shell ion in the visible spectral region; (4) A demonstration of the decrease in fluorescence quenching in fiber crystals; (5) A demonstration of the effects of thermal annealing on the infrared absorption and visible emission in Ti-sapphire laser crystals; and (6) A measurement of the pump band to metastable state relaxation rate in alexandrite laser crystals.

2

CONTENTS

IV. CHARACTERISTICS OF PHOTOREFRACTIVE CRYSTALS

IV.1 Lithium Niobate

A. Analysis of Holographic Grating Scattering Patterns in $LiNbO_3$
B. Laser-Induced Grating Characteristics in Doped Lithium Niobate Crystals
C. Anisotropic Self-Diffraction in Mg-Doped $LiNbO_3$

IV.2 Bismuth Silicate

A. Temperature Dependence of the Dynamic Response of the Photorefractive Signal in $Bi_{12}SiO_{20}$

V. EFFECTS OF DISORDER AND NONLINEAR OPTICAL PROPERTIES OF RARE EARTH DOPED GLASSES

V.1 Homogeneous Linewidths

A. Comparison of the Spectral and Temeprature Dependences of the Homogeneous Linewidths in Eu^{3+}-Doped Fluoride and Oxide Glasses

V.2 Holographic Gratings

A. Laser-Induced Refractive Index Gratings in Eu-Doped Glasses
B. Relationship Between Laser-Induced Gratings and Vibrational Properties of Eu-Doped Glasses

4

I. INTRODUCTION

Optical technology based on solid state lasers is now playing a vital role in military systems. However, the current state-of-the-art of solid state laser development is materials limited. There are a limited number of solid state laser systems that are field operational at this time and they have a limited range of operational parameters. Nonlinear optical materials required for laser systems have a similar limited availability. The research and development requirement for characterizing new materials for these applications has been identified as a high priority area for the Army in a recent report by the National Research Council entitled "Achieving Leadership in Materials Technology for the Army of the Future". The goal of the research described in this report was to enhance the understanding of fundamental physical processes involved in solid state laser systems so this information can be used to develop the ability to predict optimum materials for specific application requirements.

This research utilized a variety of different laser spectroscopy experimental techniques to characterize the properties of laser and photorefractive materials. These techniques include four-wave mixing (FWM), time-resolved site-selection spectroscopy (TRSS), and picosecond pulse multiphoton absorption. The project was divided into four thrust areas according the type of materials being investigated: rare earth doped laser crystals; transition metal doped laser crystals; photorefractive crystals; and optical glasses. The major interest in the laser crystals focused on the physical processes affecting the pumping dynamics: energy migration; radiationless relaxation; and multiphoton exci-

5

tation. The major interest in the photorefractive crystals involved identifying the mechanism causing the photorefractive response and determining the effects of defects on the response characteristics. The major interest in the glass studies was developing a technique for generating laser-induced gratings in glasses. The important results obtained during the three years of this contract are briefly outlined in this section and presented in detail in the remainder of the report.

I.1   Summary of Research Accomplishments

The first thrust area of this research contract involves rare earth doped laser materials. High power pumping of Nd^{3+} ions in garnet host crystals was shown to involve sequential two-photon excitation processes through real intermediate states. Four-wave mixing results on NdP_5O_{14} laser crystals were shown to be affected by excited state resonances. In addition, energy transfer among rare earth ions was investigated in several different laser host crystals. These results are important in furthering our understanding of the spectral dynamics of rare earth doped laser crystals.

The second thrust area focuses on transition metal laser materials. An extensive spectroscopic investigation of alexandrite laser crystals was completed, involving characterizing the effects of both Cr^{3+} ion-ion interaction and electron-phonon interaction. The most important results are the determination of the pump band to metastable state radiationless relaxation rate and the properties of spectral and spatial energy diffusion. The optical properties of Ti-sapphire laser crystals were also

studied with specific attention on the absorption band in the infrared and the emission band in the blue spectral region. Thermal annealing was shown to significantly change these bands. Several unconventional potential laser crystals were investigated. The thermal quenching of the fluorescence of Mn_2SiO_4 crystals was found to be greatly improved by laser-heated pedestal growth of fibers of the material. The results show the importance of this type of crystal growth technique and the laser potential for this type of material. The properties of Cr^{3+} and Rh^{2+} in sodium-beta"-alumina were studied but the poor material quality prevented obtaining laser emission. Tunable single pass gain was obtained from Ti^{4+} in lithium germanium oxide crystals under picosecond pulse excitation. However, for longer pulse excitation quenching or damage occurred before lasing threshold was reached.

One of the most important results in studying photorefractive crystals was developing a technique for computer fitting small angle scattering patterns from laser-induced holographic gratings. This provides the ability for determining independent values for grating thickness and modulation depth as well as checking for the presence of multiple Fourier components. This technique was applied to Mg-doped lithium niobate along with analyzing the scattering dynamics, two beam coupling, and anisotropic self-diffraction. The results provide a better understanding of the effects of Mg in minimizing the photorefractive response of these crystals. Initial work was begun on similar studies of bismuth silicate crystals.

The final thrust area focuses on Eu^{3+}-doped glasses. Fluorescence line narrowing techniques were used to determine the thermal and spectral properties of the homogeneous linewidth in both oxide and fluoride glasses and the results were shown to be consistent with a theory based on line broadening by fractons. The most important result of this contract from the perspective of optical technology applications is the development of a method for producing laser-induced holographic gratings in these glasses. This is associated with generating a significant amount of local vibrational energy through radiationless relaxation processes in the Eu^{3+} ions. These gratings can be used for optical devices such as demultiplexers and holographic storage.

I.2 Publications and Personnel

The work performed during the three years of this contract resulted in 25 publications, one doctoral thesis, four masters theses, and numerous unpublished presentations and colloquia. These are listed in Table I.

The personnel making major contributions to this research include the principal investigator, Richard C. Powell, and several visiting scientists and graduate students. The visiting scientists were:

Prof. Brahim Elouadi, Mohammed V University, Morocco;

Prof. Liu Xingren, Changchun Institute of Physics, China;

Prof. Luis Arizmendi, Universidad Autonoma de Madrid, Spain;

Prof. H.C. Chow, Southern Illinois University;

Dr. Frederic M. Durville, Universite Lyon I, France;

Dr. Andrzej Suchocki, Polish Academy of Sciences, Poland.

8

The first three were supported by their institutions while the latter three were financed by this contract. Dr. J.K. Tyminski worked as a post-doctoral research associate on this project and is now a staff scientist at Spectra Technology. The graduate students support by this contract include G.J. Quarles, G.D. Gilliland, E.G. Behrens, and M.L. Kliewer. All four received their masters degrees from this work. G.J. Quarles also received his doctoral degree and is now working in the solid state laser group at the Naval Research Laboratory in Washington, D.C. The other three students are continuing their graduate studies for the doctoral degree here at Oklahoma State University.

It is a pleasure to acknowledge the collaboration with a number of colleagues. Important contributions to this research were made by:

Dr. G.M. Loiacono, Philips Laboratories;

Prof. R.S. Feigelson, Stanford University;

Dr. J.B. Bates, Oak Ridge National Laboratory;

Dr. M.R. Kokta, Union Carbide Corp.;

Dr. J.L. Caslavsky, Army Materials and Mechanics Research
Center;

Dr. J.C. Walling, Allied Corp.

In addition, numerous colleagues at Oklahoma State University provided support in specific aspects of this research. In the area of crystal growth and characterization, Profs. J.J. Martin, W.A. Sibley, and L.E. Halliburton of the Physics Department, Profs. S.L. Holt and E.M. Holt of the Chemistry Department, and Prof. Z. AlShaieb of the Geology Department were especially helpful. Prof. G.S. Dixon of the Physics Department collab-

orated on the theoretical interpretation of the spectral effects of disorder in glasses.

TABLE I

PUBLICATIONS, THESES, AND PRESENTATIONS

PUBLICATIONS

G.J. Quarles, G.E. Venikouas, and R.C. Powell, "Sequential Two-Photon Excitation Processes of Nd^{3+} Ions in Solids", Phys. Rev. B $\underline{31}$, 6935 (1985).

R.C. Powell, L. Xi, X. Gang, G.J. Quarles, and J.C. Walling, Spec⁺roscopic Properties of Alexanddrite Crystals", Phys. Rev. J $\underline{32}$, 2788 (1985).

R.C. Powell, J.L. Caslavsky, Z. Al-Shaieb, and J.M. Bowen, "Growth, Characterization and Optical Spectroscopy of Al_2O_3:Ti^{3+}", J. Appl. Phys. $\underline{58}$, 2331 (1985).

R.C. Powell, "Laser Spectroscopy of Alexandrite Crystals: Four-Wave Mixing, Two-Photon Absorption, and Time-Resolved Site-Selection Spectroscopy", J. Physique $\underline{46}$, C7-403 (1985).

H.C. Chow, M.J. Kliewer, J.K. Tyminski, and R.C. Powell, "Analysis of Holographic Grating Scattering Patterns in $LiNbO_3$ Crystals", J. Opt. Soc. Am. B $\underline{3}$, 668 (1986).

L. Xingren, X. Gang, and R.C. Powell, "Fluorescence and Energy Transfer Characteristics of Rare Earth Ions in $BaYF_5$ Crystals", J. Solid State Chem. $\underline{62}$, 83 (1986); also published in Acta Physica Sinica $\underline{36}$, 108 (1987).

R.C. Powell, J.K. Tyminski, A.M. Ghazzawi, and C.M. Lawson, "Dynamics of Population Gratings in NdP_5O_{14} Crystals", IEEE J. Quant. Electron. $\underline{QE-22}$, 1355 (1986).

R.C. Powell, B. Elouadi, L. Xi, G.M. Loiacono, and R.S. Feigelson, "Optical Spectroscopy of Mn_2SiO_4 Crystals", J. Chem. Phys. $\underline{84}$, 657 (1986).

R.C. Powell, "Problems Associated with Active Ion Distributions in Solid State Laser Materials", Proc. Mat. Res. Soc., Vol. 60, Defect Properties and Processing of High-Technology Nonmetallic Materials, ed. Y. Chen, W.D. Kingery, and R.J. Stokes (MRS, Pittsburgh, 1986) p. 395.

G.M. Loiacono, M.F. Shone, G. Mizell, R.C. Powell, G.J. Quarles, and B. Elouadi, "Tunable Single Pass Gain in Titanium-Activated Lithium Germanium Oxide", Appl. Phys. Lett. $\underline{48}$, 622 (1986).

R.C. Powell, G.E. Venikouas, L. Xi, J.K. Tyminski, and M.R. Kokta, "Thermal Effects on the Optical Spectra of Al_2O_3:Ti^{3+}, J. Chem. Phys. $\underline{84}$, 662 (1986).

D.K. Sardar, G.J. Quarles, R.C. Powell, and M.R. Kokta, "Spectroscopic Properties of $La_3Lu_2Ga_3O_{12}:Nd^{3+}$ Crystals", Advances in Laser Science-I, ed. W.C. Stwalley and M. Lapp (AIP, NY, 1986) p. 214.

F.M. Durville, E.G. Behrens, and R.C. Powell, "Laser-Induced Refractive Index Gratings in Eu-Doped Glasses", Phys. Rev. B 34, 4213 (1986).

E.G. Behrens, F.M. Durville, and R.C. Powell, "Observation of Erasable Holographic Gratings at Room Temperature in Eu^{3+}-Doped Glasses", Opt. Letters 11, 653 (1986).

R.C. Powell, "Laser Spectroscopy Measurements on Tunable Solid State laser Materials", Proc. of the Tunable Solid State Laser Conference-II, eds. A.B. Budgor, L. Esterowitz, and L.G. DeShazer (Springer-Verlag, Berlin, 1986), p. 5.

F.M. Durville, E.G. Behrens and R.C. Powell, "Relationship Between Laser-Induced Gratings and Vibrational Properties of Eu-Doped Glasses", Phys. Rev. B 35, 4109 (1987).

F.M. Durville, G.S. Dixon, and R.C. Powell, "Comparison of the Spectral and Temperature Dependences of the Homogeneous Linewidths in Eu^{3+}-Doped Fluoride and Oxide Glasses", J. Luminescence 36, 221 (1978).

R.C. Powell, G.E. Venikouas, L. Xi, and J.B. Bates, "Optical Spectroscopy of Cr^{3+} and Rh^{2+} in Sodium Beta"-Alumina", J. Luminescence 37, 1 (1987).

A.B. Suchocki, G.D. Gilliland, R.C. Powell, J.M. Bowen, and J.C. Walling, "Spectroscopic Properties of Alexandrite Crystals II", J. Luminescence 37, 29 (1987).

A.B. Suchocki, G.D. Gilliland, and R.C. Powell, "Four-Wave Mixing Measurements of Energy Migration and Radiationless Relaxation Processes in Alexandrite Crystals", Phys. Rev. B 35, 5830 (1987).

L. Arizmendi, M.J. Kliewer, and R.C. Powell, "Laser-Induced Grating Characteristics in Doped Lithium Niobate Crystals", J. Appl. Phys. 61, 1682 (1987).

L. Arizmendi and R.C. Powell, "Anisotropic Selfdiffraction in Mg-Doped $LiNbO_3$", J. Appl. Phys. 61, 2128 (1987).

L. Arizmendi and R.C. Powell, "Temperature Dependence of the Dynamic Response of the Photorefractive Signal in $Bi_{12}SiO_{20}$", J. Appl. Phys. 62, 896 (1987).

B. Elouadi, R.C. Powell, and S.L. Holt, "Investigation of Energy Transfer Processes in Nb-Compensated $CaMoO_4$ Crystals", J. Solid State Chem. 69, 369 (1987).

J.M. Allen, A. Suchocki, R.C. Powell, and G. Loiacono, "Spectroscopic Properties and Four-Wave Mixing in $Li_6Ge_8O_{12}:Mn^{4+}$", Phys. Rev. B $\underline{36}$, 6729 (1987).

INVITED PRESENTATIONS

R.C. Powell, "Laser-Induced Grating Studies of Exciton and Charge Transport Properties of Inorganic Crystals", Am. Chem. Soc. Symposium on Transport Phenomena in Solids, Miami, May 1985.

R.C. Powell, "Laser Spectroscopy of Alexandrite Crystals: Four-Wave Mixing, Two-Photon Absorption, and Time-Resolved Site-Selection", Int. Conf. on Dynamical Processes of Excited State in Solids, Lyon, July 1985.

R.C. Powell, "Four-Wave Mixing and Multiphoton Absorption Processes of Ions in Solids", Physics Department Colloquium, University of Lyon, France, July 1985.

R.C. Powell, "Laser Spectroscopy", Physics Department Colloquium, University of Oklahoma, Norman, Sept. 1985.

R.C. Powell, "Problems Associated with Active Ion Distributions in Solid State Laser Materials", Materials Research Society Meeting, Boston, Dec. 1985.

R.C. Powell, "Laser Spectroscopy of Solids", Research Colloquium, Lawrence Livermore National Laboratory, Jan. 1986.

R.C. Powell, "Laser Spectroscopy of Solids", Physics Department Colloquium, Oklahoma State University, March 1986.

R.C. Powell, "Laser Spectroscopy Measurements on Tunable Solid State Laser Materials", Tunable Solid State Laser Conference, Zigzag, OR, June 1986.

R.C. Powell, "Laser-Induced Grating Spectroscopy of Ions in Solids", Physics Department Colloquium, University of New Mexico, Albuquerque, Nov. 1986.

R.C. Powell, "Laser-Induced Grating Spectroscopy of Ions in Solids", Materials Research Colloquium, Sandia National Laboratory, Albuquerque, Nov. 1986.

R.C. Powell, "Laser Applications", Sigma Xi Lecture, University of Oklahoma Medical Center, Oklahoma City, Dec. 1986.

R.C. Powell and W.A. Sibley, "Optically Active Applications of Ions in Glass", International Conference on Fluoride Glass, Monterey, Jan. 1987.

R.C. Powell, "Laser-Induced Grating Spectroscopy", Physics Department Colloquium, Montana State University, Bozeman, Feb. 1987.

R.C. Powell, "Four-Wave Mixing Spectroscopy of Ions in Solids",
Am. Phys. Soc. Meeting, New York, March 1987. BAPS 32, 465
(1987).

R.C. Powell, "Four-Wave Mixing Spectroscopy of Ions in Solids",
Research Seminar, Bell Labs, Murray Hill, NJ, April 1987.

R.C. Powell, "Four-Wave Mixing Spectroscopy of Ions in Solids",
Physics Colloquium, University of Connecticut, Storrs, May
1987.

R.C. Powell, F.M. Durville, A. Suchocki, G.D. Gilliland, G.J.
Quarles, and G. Boulon, "Laser-Induced Grating Spectroscopy
of Ions in Solids", Lasers MP-2 Conf., Lyon, July 1987.

R.C. Powell, F.M. Durville, E. Behrens, and G.S. Dixon, "Laser
Spectroscopy of Rare Earth-Doped Glasses", Int. Conf. on
Luminescence, Beijing, China, August 1987.

R.C. Powell, "Laser-Induced Grating Spectroscopy of Ions in
Solids", Int. Laser Science Conf., Atlantic City, November
1987.

CONTRIBUTED PRESENTATIONS

G.S. Dixon, X. Gang, and R.C. Powell, "Fluorescence Line
Narrowing of the $^5D_0-^7F_0$ Transition in Eu^{3+}-Doped Glasses",
Am. Phys. Soc. Meeting, Baltimore, March 1985. BAPS 30, 370
(1985).

R.C. Powell, X. Gang, L. Xi, and J.C. Walling, "Laser
Spectroscopy of Alexandrite Crystals", Am. Phys. Soc.
Meeting, Baltimore, March 1985. BAPS 30, 571
(1985).

J.K. Tyminski, R.C. Powell, H.C. Chow, and M.L. Kliewer,
"Analysis of Scattering Patterns and Decay Dynamics of
Photorefractive Gratings in $LiNbO_3$ Crystals", NBS Conference
on Basic Properties of Optical Materials, Gaithersburg, May
1985.

G.S. Dixon, R.C. Powell, and X. Gang, "Fractons and the
Homogeneous Linewidth of the $^5D_0-^7F_0$ Transition in Eu^{3+}-
Doped Glasses", Int. Conf. on Dynamical Processes of Excited
States of Ions and Molecules in Solids, Lyon, July 1985.

G.J. Quarles and R.C. Powell, "Spectral Dynamics of Eu^{3+}-Doped
Glasses Under High Power Picosecond-Pulse Excitation", Opt.
Soc. Am. Meeting, Washington, Oct. 1985.

G.J. Quarles and R.C. Powell, "High Power, Picosecond-Pulse
Excitation of Ions in Solids", Oklahoma Academy of Sciences
Meeting, Shawnee, Nov. 1985.

M.L. Kliewer and R.C. Powell, "The Photorefractive Effect of
$LiNbO_3$", Oklahoma Academy of Sciences Meeting, Shawnee,
Nov. 1985.

D.K. Sardar, G.J. Quarles, R.C. Powell, and M.R. Kokta, "Spectro-
scopic Properties of $La_3Lu_2Ga_3O_{12}:Nd^{3+}$ Crystals". Int. Laser
Science Conf., Dallas, November 1985. BAPS 30, 1845 (1985).

G.S. Dixon and R.C. Powell, "Role of Electron-Fracton Interac-
tions in Energy Transfer in Glasses", Am. Phys. Soc.
Meeting, Las Vegas, March 1986. BAPS 31, 277 (1986).

G.J. Quarles and R.C. Powell, "Picosecond Spectroscopy Studies of
Two-Photon Processes in Eu^{3+} Ions in Glasses", Am. Phys.
Soc. Meeting, Las Vegas, March 1986. BAPS 31, 658 (1986).

G.D. Gilliland, A.B. Suchocki, and R.C. Powell, "Nondegenerate
Four-Wave Mixing Efficiency in Alexandrite Crystals",
Am. Phys. Soc. Meeting, Las Vegas, March 1986. BAPS 31, 658
(1986).

R.C. Powell, E.G. Behrens, and F.M. Durville, "Erasable Holo-
graphic Gratings in Eu-Doped Glasses", Opt. Soc. Am.
Meeting, Seattle, October 1986.

F.M. Durville, R.C. Powell, and G. Boulon, "Four-Wave Mixing in
Cr-Doped Garnet Crystals", Lasers MP-2 Conf., Lyon, July
1987.

R.C. Powell, A. Suchocki, G.D. Gilliland, and G.J. Quarles,
"Four-Wave Mixing in Cr^{3+}-Doped Laser Crystals: Ruby,
Emerald, Alexandrite, and Garnets", Int. Conf. Dynamical
Processes in Excited States in Solids, Sukuba, Japan, July
1987.

G.J. Quarles, A. Suchocki, R.C. Powell, and S. Lai, "Spectroscopy
and Four-Wave Mixing in Emerald", Opt. Soc. Am. Meeting,
Rochester, October 1987.

G.D. Gilliland, R.C. Powell, and L. Esterowitz, "Spectroscopic
and Lasing Properties of $Ba_3YbF_8:Ho^{3+}$", Tunable Laser Conf.,
Williamsburg, October 1987.

M.J. Kleiwer and R.C. Powell, "Spectral Effects of Stimulated
Emission Under High Power, Picosecond Pulse Excitation",
Tunable Laser Conf., Williamsburg, October 1987.

THESES

"Laser Induced Gratings in Eu^{3+}-Glasses", E.G. Behrens, M.S.

    Thesis, Oklahoma State University, Dec. 1986.

"Spectroscopic Properties of Alexandrite Crystals", G.D.

    Gilliland, M.S. Thesis, Oklahoma State University, May 1986.

"The Photorefractive Effect in $LiNbO_3$", M.L. Kliewer, M.S.

    Thesis, Oklahoma State University, May 1986.

"Spectroscopic Studies of $Y_3Al_5O_{12}:Nd^{3+}$ Under High-Power,

    Picosecond-Pulse Excitation", G.J. Quarles, M.S. Thesis,

    Oklahoma State University, May 1985.

"Laser Spectroscopic Studies of Europium-Doped Glasses and

    Emerald", G.J. Quarles, Ph.D. Thesis, Oklahoma State

    University, Dec. 1987.

II.   SPECTRAL DYNAMICS OF RARE EARTH LASER CRYSTALS

The following four manuscripts present details of the results obtained on several rare earth doped laser crystals. The first three involve Nd^{3+} as the active ion and the first two of these are direct extensions of the results reported in our 1985 final report on Army Contract DAAG29-82-K-0041. The FWM results on NdP_5O_{14} provide further information concerning the exciton dynamics in this crystal and demonstrate how excited state resonances affect FWM signal characteristics. The picosecond pulse excitation results on Nd-YAG provide information concerning the type of two-photon absorption processes occurring with this type of pumping. Spectroscopic studies of host sensitized energy transfer in Nd-doped molybdates are described in the third manuscript. This may be a technique to enhance pumping efficiencies in Nd-doped laser materials. Initial spectroscopic studies were also begun on Nd-doped garnet crystals and the results will be described in detail during the next contract period. In the final manuscript, the spectroscopic properties of rare earth ions in $BaYF_5$ crystals are described. The decreased thermal quenching in this type of fluoride host makes this crystal attractive as a laser host material. The investigation of rare earth doped fluoride crystals will continue during the next contract period.

Dynamics of Population Gratings in NdP_5O_{14} Crystals

RICHARD C. POWELL, JACEK K. TYMINSKI, ALI M. GHAZZAWI,
AND CHRISTOPHER M. LAWSON

Abstract—Four-wave mixing signals from transient population gratings established in NdP_5O_{14} crystals were analyzed to obtain information on the pumping dynamics and exciton migration characteristics in this material. As the laser pump wavelength is scanned through an Nd^{3+} absorption band, the exciton diffusion coefficient is found to vary in a manner consistent with site selection within the inhomogeneously broadened profile. Deviations from simple signal decay patterns are observed whenever the laser is tuned to excited state resonances. In addition, recent theoretical developments are applied to the grating decay data to determine the degree of coherence in the exciton motion.

I. Introduction

IN a recent series of papers, we have reported on the characteristics of exciton migration in NdP_5O_{14} crystals using degenerate four-wave mixing techniques to establish and probe Nd^{3+} population gratings [1]–[3]. Beam depletion due to the strong absorption in this stoichiometric rare earth material made it necessary to pump in the vibronic wings of the absorption transitions. We report here the results of extending this work by using nondegenerate four-wave mixing and ultrathin samples so that the pump laser could be scanned through the absorption band. The wavelength dependence of the four-wave mixing signal shows the presence of strong spatial diffusion with weak spectral diffusion of energy in this material, and also reveals additional grating effects which occur at the positions of excited state resonances in the excitation spectrum. The characteristics of the exciton dynamics in this material are determined by analyzing the data with the corrected model of Kenkre [4]. This shows the degree of coherence in the exciton migration under different experimental conditions.

Fig. 1 shows the experimental setup used in this work. A Spectra Physics stabilized ring dye laser with Rhodamine-6G pumped by an argon laser was used as the excitation source, while the probe beam was provided by an He–Ne laser. Transient four-wave mixing signals were recorded by chopping the writing beams off and using an EGG–PAR boxcar integrator and signal averager combi-
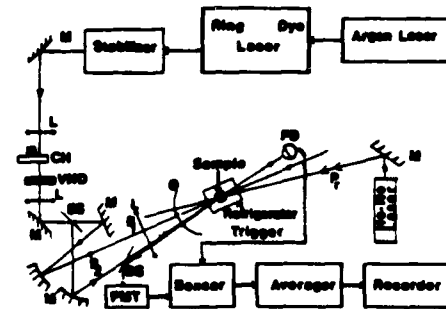
Fig. 1. Schematic diagram of experimental apparatus mounted on a vibration isolated table. M = mirror, L = lens, CH = chopper, VND = variable neutral density filter, BS = beam splitter, PMT = photomultiplier tube, PD = photodiode.

nation to analyze the decay patterns. For low-temperature measurements, the samples were mounted in a cryogenic refrigerator. Details of the crystal growth and properties of NdP_5O_{14} have been described previously [5], [6].

II. Excitation Wavelength Dependence

In order to investigate the four-wave mixing characteristics in an excitation region of high absorption, samples of NdP_5O_{14} were cleaved to dimensions of about 5 mm square and less than 1 mm thick. The sample was aligned so that the grating was formed along the a axis of the crystal. The write beams from the dye laser were scanned point by point through the Nd^{3+} absorption band near 580 nm, and at each point measurements were made of the fluorescence lifetime of the 890 nm emission as well as the grating decay rate as a function of crossing angle of the write beams. The simplest relationship between the grating decay rate W_g and the diffusion coefficient D of the excitons destroying the grating through migration can be written as [7]

$$D = (W_g - 2W_f)\lambda^{-2}/[32\pi^2 \sin^2 (\theta/2)] \qquad (1)$$

where W_f is the fluorescence decay rate, λ is the wavelength of the laser write beams in the crystal, and θ is the write beam crossing angle in the crystal.

Fig. 2 shows the results of this investigation. The solid line shows the room temperature absorption spectrum in this wavelength region. The structure is due to the overlapping of the Stark components of the $^2G_{7/2}$ and $^4G_{5/2}$ multiplets. The fluorescence lifetime was found to be approximately independent of temperature and excitation wavelength in this region of excitation with an average
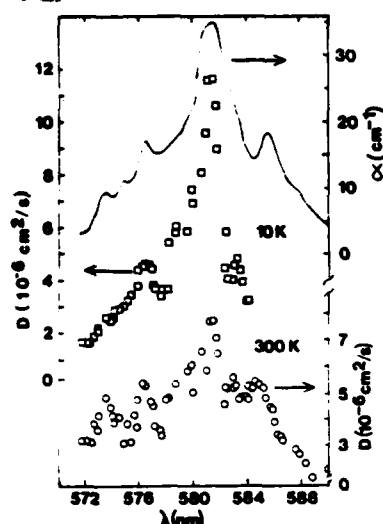
Fig. 2. Spectral dependence of exciton diffusion coefficient. The solid line represents the room temperature absorption band in the region of excitation. The circles and squares represent the values of the diffusion coefficient at room temperature and 10 K. respectively. determined from four-wave mixing signals.

Fig. 3. Room temperature absorption spectrum in the near UV spectral region of a NdP_5O_{14} crystal 0.125 cm thick. (See text for explanation of notation at top of figure.)

value of 116 μs. The values of the exciton diffusion coefficient found at each excitation wavelength using (1) with the measured values of W_g and W_f at $\theta = 9.5°$ are also shown in Fig. 2. At room temperature. the magnitude of D varies between about 2×10^{-6} and 8×10^{-6} cm^2 · s^{-1} which is consistent with the value reported earlier for direct excitation into an absorption band above the metastable state [1]. The structure observed in D as a function of excitation wavelength follows the structure observed in the absorption spectrum. This can be attributed to the fact that each spectral transition is inhomogeneously broadened due to strains in the lattice. and the narrow line laser selectively excites a subset of ions located in sites whose transition wavelength is in resonance with the laser wavelength. Since the diffusion coefficient is sensitive to the separation between ions in equivalent sites. the higher density of ions in a specific type of site with a transition wavelength at line center allows for a greater value of D. This evidence for site selection and spatial energy migration without strong spectral diffusion is consistent with results reported previously for different types of excitation [1]–[3].

At 11 K, the spectral structure in D becomes even more pronounced as seen in Fig. 2. This is due to the decrease in the homogeneous broadening of the transitions by phonons which results in a greater amount of site selectivity. An interesting observation is that at excitation wavelengths of 584 nm and greater. no steady-state four-wave mixing signal could be established. Instead. the signal initially increased in intensity and then decreased to zero in a matter of several seconds whenever the laser beams were aligned in this spectral region. The signal could be reestablished only by scanning the laser to a different region of the crystal or decreasing the laser wavelength.
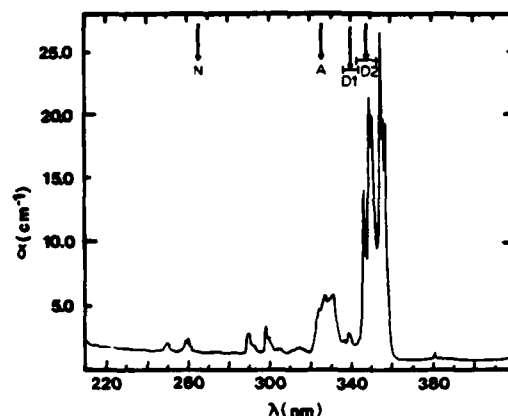
The unconventional signal behavior described above was not observed for the shorter wavelength Stokes vibronic excitation used in previous investigations [3]. However. for excitation with the 514.5 nm line of an argon laser, other unconventional signal behavior was reported [1]. For this wavelength. the laser pumps an absorption band made up of overlapping components of the $^2G_{9/2}$ and $^4G_{7/2}$ levels and the observed four-wave mixing signal profiles were double exponential decays. The longer decay rate varied with the write beam crossing angle in a way consistent with probe beam scattering from a population grating formed in the $^4F_{3/2}$ metastable state. The origin of the shorter component of the signal decay was not identified. The measured decay time of this component was 45 μs. independent of write beam crossing angle.

In order to identify the origin of the unconventional signal patterns for four-wave mixing which occur for excitation in specific spectral regions. we considered the effects of excited state absorption. Fig. 3 shows the absorption spectrum of NdP_5O_{14} in the near UV spectral region at room temperature. If excited state absorption occurs from the $^4F_{3/2}$ metastable state, the termination of the transitions will be in the spectral regions designated at the top of this figure. Region $D2$ represents the range of dye laser excitation used in this study, while $D1$ represents the range of dye laser excitation used previously [3]. The position designated A represents the termination of an excited state absorption transition using argon laser excitation. The important observation in this figure is that the region $D1$ lies between two strong absorption bands, whereas A is near the peak of one of the absorption bands and the high-energy part of $D2$ covers a region which is in an area of low absorption. while the low-energy part of $D2$ covers a region which is in an area of high absorption. These differences are even greater at low temperatures where the absorption bands are sharper.

Comparing these observations to the results described above indicates that normal four-wave mixing signals as-
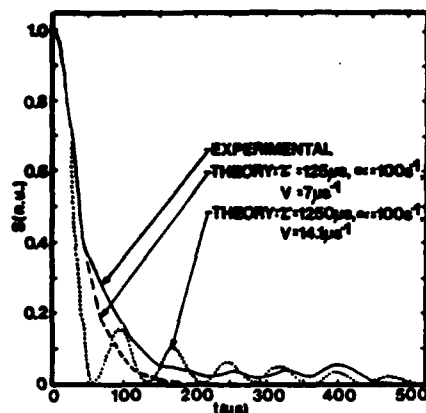
Fig. 4. Oscillatory four-wave mixing signal decay pattern. The solid line represents the experimental data obtained on NdP$_5$O$_{14}$ at 10 K with resonant excitation in the high-energy wing of the $^2G_{7/2}$ absorption band. The broken line represents the prediction of (7) with $\tau = 125$ μs, $\alpha = 10^2$ s^{-1}, and $V = 7.0 \times 10^6$ s^{-1}. The dotted line represents the prediction of (7) with $\tau = 1250$ μs, $\alpha = 10^2$ s^{-1}, and $V = 1.41 \times 10^7$ s^{-1}.

In [3], it was shown that under special conditions, oscillatory signal decay patterns were observed. These types of oscillations can be caused by several different types of physical effects, the most prominent of which involves local heating [7]. In [3], the effects of local heating are considered in detail and are shown to be unable to predict the observed characteristics of the oscillations in the FWM signal observed for this case. The only effect consistent with conditions of the experiment is the presence of coherence in the motion of the excitons. The expression of Wong and Kenkre used to describe exciton migration under these conditions [9] has been reformulated into a simpler expression. The time dependence of the normalized four-wave mixing signal is given by [4]

$$S(t) = e^{-2t/\tau}[J_0(bt)e^{-\alpha t}$$

$$+ \alpha \int_0^t due^{-\alpha(t-u)}J_0(b\{t^2 - u^2\}^{1/2})]^2 \qquad (7)$$

where $b = 4\pi Va/\Lambda_e$. Fig. 4 shows typical experimental data exhibiting an oscillatory decay pattern. As discussed in [3], the theoretical expression predicts that the oscillations will always decrease in intensity and have a constant period, whereas the intensity and period of the oscillations in the observed data increase with time. Typical theory curves are shown in Fig. 4 to demonstrate the types of oscillatory patterns predicted by (7). The early decay portion of the curve can only be fit for values of b of about 1.4×10^4 s^{-1} and the measured decay time of 125 μs, whereas the latter portion of the pattern is better fit by [7] using $b = 4.2 \times 10^4$ s^{-1} and $\tau = 1250$ μs. The fittings are less sensitive to the value of α and can only provide a value for an upper limit of about 10^4 s^{-1}. Using (3)–(6) leads to the parameters describing the exciton migration listed in Table I. In comparison to the results associated with the exponential decay pattern described above, these low-temperature results indicate a significant increase in

the degree of coherence of the motion. Although (7) has a different form from the equation used in [3], the qualitative aspects of the results are the same. The need to assume time-dependent changes in V and τ is still not fully understood, but may be associated with effects not included in the theoretical treatment such as local heating, spectral diffusion, and quenching of excitons.

IV. SUMMARY AND CONCLUSIONS

The results discussed above indicate that the exciton migration in NdP$_5$O$_{14}$ can be described as a diffusive motion with a mean free path greater than several lattice spacings. It is important to emphasize that the term coherence used to describe this type of motion refers to the distance traveled between scattering events [10]. In this context, nearest neighbor hopping migration is "incoherent" motion, while migration involving longer mean free paths is "partially coherent" motion. This is different from the term coherence used to describe a coherent state of the system prepared by resonantly pumping the metastable state with a laser. The theory of Kenkre [4], [9] is developed specifically to describe the four-wave mixing signal for the case of exciton migration occurring after some process such as radiationless relaxation has destroyed any initial conditions of coherence in the system. This is consistent with the conditions of our experiment. Under different initial conditions, the signal decay patterns will have very different shapes [11], [12]. The results for NdP$_5$O$_{14}$ indicate that even for the unfavorable excitation condition of a Stokes vibronic transition at room temperature, the coherence length for the motion is about 26 lattice sites. This increases to over 2000 lattice sites at low temperatures for excitation directly into one side of an absorption band lying above the metastable state. The fact that the values of the diffusion coefficient reported here are similar to those reported previously is not surprising since the corrected expression for K from [4] is equivalent to the initial expression used from [9] in the limit $\alpha\tau \gg 1$ which is the case for NdP$_5$O$_{14}$.

The observation of oscillations in the decay pattern is consistent with the presence of a high degree of coherence in the exciton migration. The origin of the simultaneous threefold increase in the ion–ion interaction rate and the order of magnitude increase in the fluorescence decay time within the time of the experiment needed to describe the observed signal decay pattern is difficult to determine. The time-dependent increase in V occurs on a time scale consistent with thermal diffusion in this material [3], and thus may be related to a local heating effect. Since the laser excites a level significantly above the metastable state, radiationless relaxation will generate phonons simultaneously with the creation of excitons. Another possibility is the presence of spectral energy migration. Although this is known to be a weak effect in NdP$_5$O$_{14}$ [6], some evidence of spectral migration has been observed in the temperature and power dependences of four-wave mixing in this material [3]. Since the excitation producing the oscillatory signal decay patterns is on the high-energy wing

of an absorption band, spectral migration would predominantly move the energy to ions with transitions nearer the center of the inhomogeneously broadened band. As shown in Fig. 2, the exciton diffusion coefficient increases significantly between the edge and center of the absorption band. The fact that the fluorescence lifetime increases with time while the exciton diffusion coefficient increases indicates that the lifetime change is not associated with enhanced migration to exciton trapping sites where fluorescence quenching occurs [13]. The results imply that quenching interactions decrease as the resonant ion–ion interactions increase, which again may be due to spectral migration or decreased local heating. Another possibility is that the observed signal is the superposition of signals from different regions of the sample each having different local properties of strain broadening, quenching, and ion-ion interaction. This is not unreasonable considering the ferroelastic domains known to be present in the material [5]. With the experimental data presently available, it is not possible to choose between these various possibilities.

The change in the diffusion coefficient observed as the laser excitation is scanned through the absorption band is again consistent with site selection leading to spatial energy migration with weak spectral diffusion. Using (1) to analyze the data treats the diffusion coefficient as a phenomenological parameter without making any assumptions as to the microscopic details of the motion. It is important to note that this approach gives essentially the same value for D found from using (2) with the assumed value for the ion–ion interaction rate since a wide range of estimates for V can be found in the literature.

The presence of sequential two-photon excitation processes appears to be an important process in determining the properties of four-wave mixing signals produced by scattering from population gratings. Although this specific effect has not been reported previously, it is closely related to the "optically generated pseudo-Stark effect" seen in ruby [14] and to the recently reported effect of "photon gated holeburning" [15]. These can all be classified as photorefractive effects, and as is generally the case with this class of effects, it is difficult to identify the exact nature of the ionization and trapping process involved.

ACKNOWLEDGMENTS

REFERENCES

[1] C. M. Lawson, R. C. Powell, and W. K. Zwicker, "Measurement of exciton diffusion lengths in Nd,La$_{1-x}$P$_5$O$_{14}$ by four-wave mixing techniques," *Phys. Rev. Lett.*, vol. 46, pp. 1020–1023, 1981; ——, "Transient grating investigation of exciton diffusion and fluorescence quenching in Nd,La$_{1-x}$P$_5$O$_{14}$ crystals," *Phys. Rev. B*, vol. 36, pp. 4836–4844, 1982.

[2] J. K. Tyminski, R. C. Powell, and W. K. Zwicker, "Temperature dependence of the exciton diffusion in Nd,La$_{1-x}$P$_5$O$_{14}$ crystals," in *Proc. Int. Conf. Lasers '83*, R. C. Powell, Ed. McLean, VA: STS Press, 1984, pp. 272–274.

[3] ——, "Investigation of four-wave mixing in Nd,La$_{1-x}$P$_5$O$_{14}$," *Phys. Rev. B*, vol. 29, pp. 6074–6085, 1984.

[4] V. M. Kenkre and D. Schmid, "Coherence in singlet-exciton motion in anthracene crystals," *Phys. Rev. B*, vol. 31, pp. 2430–2436, 1985.

[5] R. D. Plattner, W. W. Kruhler, W. K. Zwicker, T. Kovats, and S. R. Chinn, "The growth of large, laser quality Nd,RE$_{1-x}$P$_5$O$_{14}$ crystals," *J. Cryst. Growth*, vol. 49, pp. 274–290, 1980.

[6] J. M. Flaherty and R. C. Powell, "Concentration quenching in Nd,Y$_{1-x}$P$_5$O$_{14}$ crystals," *Phys. Rev. B*, vol. 19, pp. 32–42, 1979; ——, "Laser site-selection time-resolved spectroscopy of NdP$_5$O$_{14}$," *Solid State Commun.*, vol. 26, pp. 503–506, 1978.

[7] J. R. Salcedo, A. E. Siegman, D. D. Dlott, and M. D. Fayer, "Dynamics of exciton transport in molecular crystals: The picosecond transient grating method," *Phys. Rev. Lett.*, vol. 41, pp. 131–134, 1978.

[8] G. J. Quarles, G. E. Venikouas, and R. C. Powell, "Sequential two-photon excitation processes of Nd^{3+} in solids," *Phys. Rev. B*, vol. 31, pp. 6935–6940, 1985.

[9] Y. M. Wong and V. M. Kenkre, "Extension of exciton-transport theory for transient grating experiments into the intermediate coherence domain," *Phys. Rev. B*, vol. 22, pp. 3072–3077, 1980.

[10] M. D. Fayer, "Exciton coherence," in *Spectroscopy and Exciton Dynamics of Condensed Molecular Systems*, V. M. Agranovich and R. M. Hochstrasser, Eds. Amsterdam: North-Holland, 1983, pp. 185–248.

[11] R. C. Powell and G. Blasse, "Energy transfer in Concentrated systems," in *Structure and Bonding, Vol. 42: Luminescence and Energy Transfer*. Berlin: Springer-Verlag, 1980, pp. 43–96.

[12] D. K. Garrity and J. L. Skinner, *J. Chem. Phys.*, vol. 82, p. 260, 1985.

[13] V. M. Kenkre and G. P. Tsironis, *J. Luminescence*, vol. 34, p. 107, 1985.

[14] P. F. Liao, A. M. Glass, and L. M. Humphrey, "Optically generated pseudo-Stark effect in ruby," *Phys. Rev. B*, vol. 22, pp. 2276–2281, 1980.

[15] A. Winnacker, R. M. Shelby, and R. M. Macfarlane, "Photon gated holeburning—A new mechanism using two-step photoionization," *Opt. Lett.*, vol. 10, pp. 3050–3052, 1985.

Richard C. Powell was born in Lincoln, NE, on December 20, 1939. He received the B.S. degree in 1962 from the United States Naval Academy, and the M.S. and Ph.D. degrees in physics from Arizona State University Tempe, in 1964 and 1967, respectively.

From 1964 to 1968 he was a Staff Scientist at the Air Force Cambridge Research Laboratories and from 1968 to 1971 he was a Research Staff member at Sandia National Laboratory. Since 1971, he has been a faculty member of the Department of Physics, Oklahoma State University, Stillwater, where he now serves as a Regents Professor and Director of the Materials Research Center. His contributions have been in the field of laser spectroscopy of solids, including four-wave mixing studies of exciton dynamics, holographic studies of photorefractive materials, and picosecond pulse multiphoton absorption studies of ions in crystals and glasses.

Dr. Powell is a Fellow of the American Physical Society and a member of the Optical Society of America.

Jacek K. Tyminski, photograph and biography not available at the time of publication.

Ali M. Ghazzawi, photograph and biography not available at the time of publication.

Christopher M. Lawson, photograph and biography not available at the time of publication.

PHYSICAL REVIEW B

CONDENSED MATTER

Sequential two-photon excitation processes of Nd^{3+} ions in solids

Gregory J. Quarles, George E. Venikouas,* and Richard C. Powell

Department of Physics, Oklahoma State University, Stillwater, Oklahoma 74078

(Received 7 November 1984)

The frequency-doubled and -tripled outputs of a high-power pulsed Nd-doped yttrium aluminum garnet laser were used to excite Nd^{3+} ions in hot crystals of $Y_3Al_5O_{12}$ and $Y_3Ga_5O_{12}$ and in a commercially available Nd-doped lithium silicate glass (ED-2). The fluorescence emission occurring as a result of two-photon excitation processes was studied for both of these excitation wavelengths. The variations of the intensities of the emission processes with laser pulse width show that the excitation processes are sequential stepwise absorption processes with real resonant intermediate states. A time-resolved spectroscopy technique developed previously was used to determine the excited-state absorption cross sections which are shown to be consistent with theoretically predicted values. The frequency-tripled laser excitation process terminates on a $5d$ level of Nd^{3+}, leading to a cross section over two orders of magnitude greater than that associated with the process occurring after frequency-doubled laser excitation which terminates on a level of the $4f$ configuration. Radiative and radiationless relaxation processes between $5d$ and $4f$ levels are also observed in these systems.

I. INTRODUCTION

High-power, picosecond-pulse lasers provide sources for studying spectroscopic properties of materials not easily observable under normal excitation conditions. Two important processes of this type are multiphoton absorption and intraconfigurational relaxation. Both of these processes are especially important in materials to be used in applications involving high levels of optical pumping. We recently reported initial results of studying the spectroscopic properties of $Y_3Al_5O_{12}:Nd^{3+}$ [neodymium-doped yttrium aluminum garnet (Nd-YAG)] after excitation with high-power pulses of 30-picosecond duration.[1] The properties of two new metastable states were characterized, two different types of two-photon absorption processes were identified, and the $5d$-$4f$ radiationless relaxation rate was measured for this material. The work described here extends this investigation to provide a detailed understanding of these excitation and relaxation processes and to characterize their properties in different materials.

Using the time-resolved spectroscopy technique developed previously,[1] the two-photon absorption cross sections were measured for Nd-YAG for excitation wavelengths of 532.0 and 354.7 nm as a function of laser pulse width between 30 and 200 ps. For both cases, the results are shown to be consistent with sequential two-photon excitation processes (STEP). Similar results were observed on $Y_3Ga_5O_{12}:Nd^{3+}$ neodymium-doped yttrium gallium garnet (Nd-YGaG) and on Nd-doped lithium silicate glass (ED-2), but not on other Nd-doped crystals. In addition, the $5d$-$4f$ radiationless relaxation rate in Nd-YGaG was measured to be similar to that found in Nd-YAG. In the glass host Nd^{3+}-Ce^{3+} energy transfer was observed.

II. EXPERIMENTAL PROCEDURE

Figure 1 shows a block diagram of the experimental setup. The Nd-YAG laser provides a pulse whose duration is controlled by changing the output coupler of the oscillator cavity and whose wavelength depends on the harmonic generation crystals used. The power of the excitation pulse incident on the sample is controlled by changing the laser power supply and by using neutral density filters. The sample fluorescence is analyzed by a $\frac{1}{4}$-m monochromator. For time-resolved spectroscopy measurements, an EG&G—Princeton Applied Research (EGG—PAR) gated optical multichannel analyzer with a silicon diode array is used for detection. For lifetime measurements, an EGG—PAR boxcar integrator/signal averager combination is used with an RCA C31034 photomultiplier tube for detection. A beam splitter picks off part of the pulse to monitor the shot-to-shot intensity variations of the laser.

Three samples were investigated in this work: YAG:Nd^{3+} (1.18×10^{20} cm^{-3}); YGaG:Nd^{3+} (3.24×10^{19}
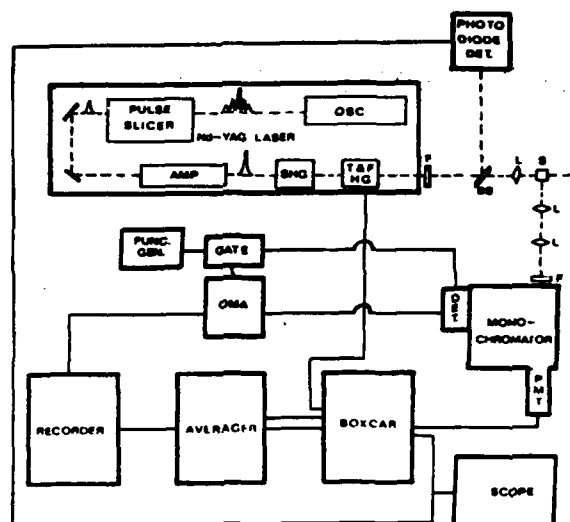
FIG. 1. Block diagram of experimental apparatus. The laser is a passively mode-locked Nd-YAG system with a single-stage amplifier and frequency-doubling, -tripling, and -quadrupling crystals. F, filter; BS, beam splitter; L, lens; and S, sample. Time-resolved fluorescence spectra are recorded using a silicon diode array detector and a gated optical multichannel analyzer (OMA). Fluorescence lifetimes are measured using a photomultiplier tube detector and a boxcar integrator/signal averager combination.

FIG. 2. Rate diagram for interpreting the spectral dynamics observed after high-power excitation at 532.0 nm. The W's represent excitation rates and the β's represent decay rates. The n's are the populations of the various energy levels and the I's are the fluorescence emission intensities.

cm^{-3}); and ED-2:Nd^{3+} (1.83×10^{20} cm^{-3}). The composition of the glass host in mole percent is 60SiO_2, 27.5Li_2O, 10CaO, and 2.5Al_2O_3 with 0.16CeO_2 and 0.35Nd_2O_3. Some of the general spectroscopic properties of these samples have been reported previously.[2-5]

III. RESULTS FOR 532.0 nm PUMPING

The frequency doubled output of the Nd-YAG laser was used to excite the samples at 532.0 nm. It was shown in Ref. 1 that this wavelength results in two-photon excitation of the $^2(F2)_{5/2}$ level which is the highest energy metastable state of the $4f^3$ electronic configuration of the Nd^{3+} ion. The properties of the fluorescence emission from this level are summarized in Ref. 1. A simplified rate diagram for describing the pumping and decay dynamics under this excitation condition is shown in Fig. 2. One of the Stark components of the $^4G_{7/2}$ level acts as a real intermediate state for the two-photon transitions. The ions excited to this intermediate state either relax radiationlessly to the $^4F_{3/2}$ metastable state or are re-excited to the $^2(F2)_{5/2}$ state. The W_k and β_k parameters represent the appropriate pumping and decay rates. The fluorescence emission can be monitored from level 3 after two-photon excitation and from level 1 after one-photon excitation. The rate equations describing the time evolution of these fluorescence emissions have been solved previously.[1]

Figure 3 shows the ratios of the measured integrated fluorescence intensities of the transitions from level 3 and level 1 for Nd-YAG using different excitation pulse

widths. These intensities have been corrected for quantum efficiencies, branching ratios, and the spectral sensitivity of the equipment. The observed exponential variation of the intensity ratio with time after the excitation pulse is consistent with the results reported previously.[1] The important new information shown in Fig. 3 is that the slope and intercept of this time evolution changes with the pulse width of the laser excitation. This type of varia-

FIG. 3. Time evolution of the ratios of the integrated fluorescence intensities of the emission from the $^4F_{3/2}$ and $^2(F2)_{5/2}$ metastable states after 532.0 nm excitation of different pulse widths for Nd-YAG.

tion will occur for two-photon transitions involving real resonant intermediate states but not for transitions involving virtual intermediate states. Therefore these results show that a sequential two-photon excitation process is responsible for the fluorescence from the $^2(F2)_{5/2}$ level.

The values of the fluorescence intensities immediately after the excitation pulse can be used to determine the excited-state absorption cross section for the STEP mechanism,

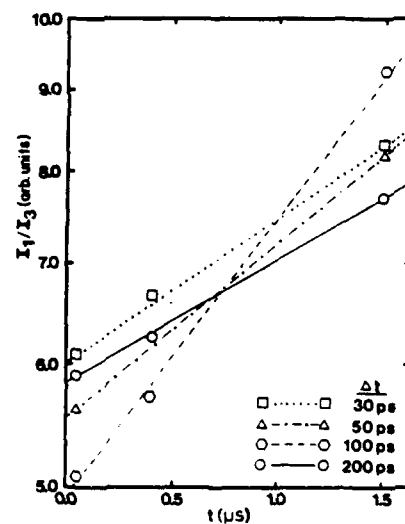$$\sigma_{i3}=[\beta_1'/\beta_3'][I_3(0)/I_1(0)][(h\nu_1)/(h\nu_3)][(\beta_i\,\Delta t)/(0.375I_p)]\;,\tag{1}$$

where again the corrected values for $I_k(0)$ are implied. The β_k' represent the radiative decay rates, Δt is the laser pulse width, and I_p is the photon flux per pulse. A major simplification which has been made in deriving the expression in Eq. (1) is using $P(t)=(0.375/\Delta t)$ for the pulse-time dependence instead of the full Gaussian expression

$$P(t)=(0.375/\Delta t)\exp\{-2.77[(t-t_0)/\Delta t]^2\}\;.\tag{2}$$

In order to evaluate the excited-state absorption cross section using Eq. (1), it is necessary to estimate a value for the decay rate of the intermediate state of the STEP transition. This can be done by considering the spectral line shape of the absorption transition from the ground state to the $^4G_{7/2}$ level. The absorption spectra in this region are shown in Fig. 4 for the three samples. The structure and asymmetry of these absorption lines are due to unresolved Stark components. An estimate of the full width at half maximum of an individual Stark component can be obtained by deconvoluting these spectral shapes. At room temperature, these linewidths should be dominated by lifetime broadening processes. Therefore the measured width of a level can be used to determine the decay rate from the level. This analysis gives a value of $\beta_i=8.4\times10^{12}$ Hz for the YAG:Nd sample. Using this value along with the measured values of the fluorescence intensities and the excitation pulse intensity, and the radi-

ative decay rates of the metastable states determined previously,[1] Eq. (1) gives the values of the excited-state cross section for the STEP transition.

Figure 5 shows the variation of σ_{i3} with excitation pulse width for the Nd-YAG sample. The results show a direct correspondence between σ_{i3} and Δt as predicted by Eq. (1). However the best fit to the data is a line with a slope slightly greater than the predicted value of one. This is probably associated with the simplification used in describing the pulse shape in Eq. (1).

Table I lists the values of the parameters obtained in this study. Experimental error in determining the corrected values of the intensities limits the accuracy of the σ_{i3} value to $\pm1\times10^{-19}$ cm^2. A similar analysis was made of the same STEP mechanism in Nd-YGaG and in Nd-ED-2. The values of β_i and σ_{i3} for Nd-YGaG are similar to those found for Nd-YAG. The extensive inhomogeneous line broadening in the glass host makes it impossible to use the spectrum shown in Fig. 4 to obtain a value for β_i for Nd-ED-2 and therefore the value of σ_{i3} cannot be determined by this method.
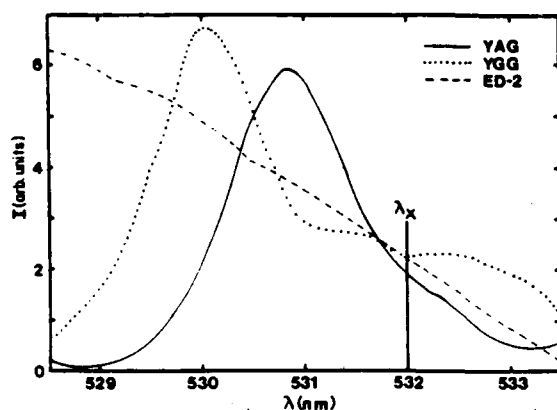

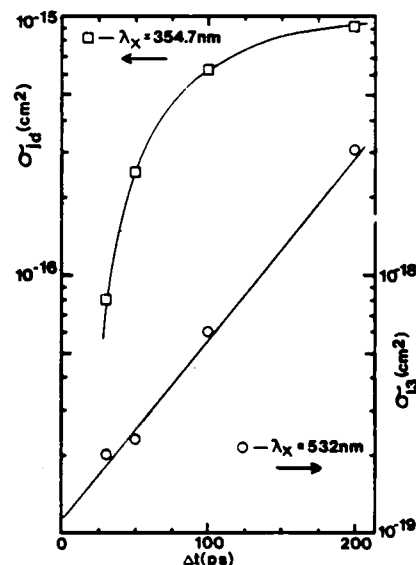FIG. 4. Absorption spectra of Nd^{3+} in three hosts in the region of 532.0 nm excitation.

FIG. 5. Variation of the excited state absorption cross sections σ_{i3} (532.0 nm excitation) and σ_{i4} (354.7 nm excitation) with excitation pulse width for Nd-YAG.

QUARLES, VENIKOUAS, AND POWELL

TABLE I. Summary of parameters ($\Delta t = 30$ ps; $T = 300$ K).

Parameter	Host		
	YAG	YGG	ED-2
τ_1 (μs)	220	264	320
τ_2 (μs)	0.3	0.3	0.4
τ_3 (μs)	3.0	2.0	1.0
τ_d (ns)	2.0	4.8	
β_i (Hz)	8.4×10^{12}	9.0×10^{12}	
β_j (Hz)	2.7×10^{13}	4.0×10^{13}	
σ_{13} (cm^2)	2.1×10^{-19}	3.5×10^{-19}	
σ_{jd} (cm^2)	8.2×10^{-17}	6.5×10^{-17}	

IV. RESULTS FOR 354.7 nm EXCITATION

The spectral dynamics are more complex after excitation by the frequency-tripled output of the Nd-YAG laser.[1] Figure 6 shows a simplified rate equation diagram to describe the results. The tripled output of the Nd-YAG laser is in resonance with a transition from the ground state to one of the Strak components of the $^4D_{3/2}$ level. Electrons excited to this level can either relax radiationlessly to the $^2P_{3/2}$ metastable state or undergo a second photon absorption process to one of the $5d$ levels. The properties of the $^2P_{3/2}$ metastable state for Nd-YAG were characterized in Ref. 1. The electrons excited to the $5d$ level relax back to the $^2(F2)_{5/2}$ metastable state and decay radiatively as described in the preceding section.

The various excitation and decay rates and the level populations are designated in Fig. 6. The rate equations for this model were solved in Ref. 1 and the results predict the time evolution of the ratio of the fluorescence intensities from level 2 to level 3 to decrease exponentially. Figure 7 shows the time dependence of I_2/I_3 for four different excitation pulse widths. An exponential decrease is seen for each case as predicted.

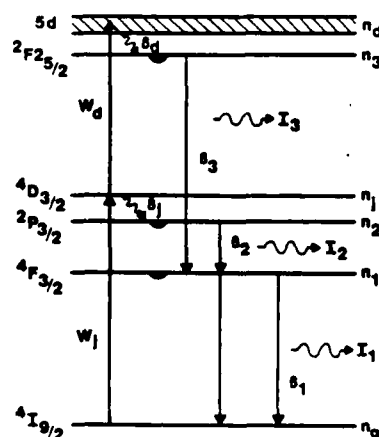The fact that the slopes and intercepts of the curves in

FIG. 7. Time evolution of the ratios of the integrated fluorescence intensities of the emission from the $^2P_{3/2}$ and $^2(F2)_{5/2}$ metastable states after 354.7 nm excitation of different pulse widths for Nd-YAG.

Fig. 7 are different for different pulse widths again shows that the two-photon excitation mechanism involves a resonant, real intermediate state. The cross section for the excited-state absorption part of this STEP mechanism is given by Eq. (1) with the subscripts designating levels 1 and i being replaced by 2 and j. The procedure described in the preceding section for estimating the relaxation rate of the intermediate level can be applied to find values for β_j using the absorption spectra in the region of the $^4D_{3/2}$ level shown in Fig. 8. The values obtained from this procedure are listed in Table I and σ_{jd} is plotted versus Δt for the Nd-YAG sample in Fig. 5. Experimental error in determining the corrected values of the intensities limits the accuracy of the σ_{jd} value to $\pm 8 \times 10^{-18}$ cm^2.

FIG. 6. Rate diagram for interpreting the spectral dynamics observed after high-power excitation at 354.7 nm. The W's represent excitation rates and the β's represent decay rates. The n's are the populations of the various energy levels and the I's are the fluorescence emission intensities.
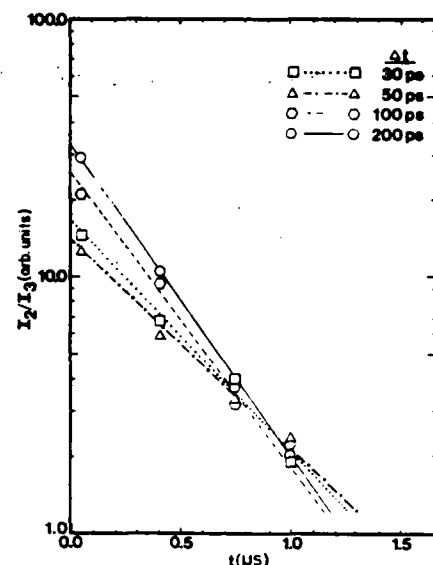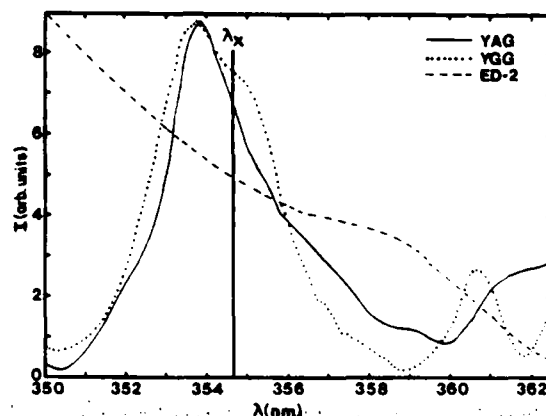

FIG. 8. Absorption spectra of Nd^{3+} in three hosts in the region of 354.7 nm excitation.

Similar measurements were made on the Nd-YGaG and Nd-ED-2 samples and the results are given in Table I. The magnitudes of both the σ_{jd} and the β_j parameters are similar for the two crystalline samples. However it was not possible to determine accurate values for these parameters for the glass sample due to the spectral characteristics shown in Figs. 8 and 9. The extremely broad, unresolved shape of the $^4D_{3/2}$ absorption band prevents accurate evaluation of β_j. Figure 9 compares the fluorescence emission of Nd-ED-2 in the 400 nm spectral region after 532.0 nm STEP excitation and after 354.7 nm STEP excitation. The former process leads to line emission from the $^2(F2)_{5/2}$ metastable state with a fluorescence decay time of 1.06 μs whereas the latter type of excitation results in broad band fluorescence with a 40 ns lifetime. The broad band is attributed to radiative emission from the $5d$ level of the Ce^{3+} ions present in the host glass excited by energy transfer from the Nd^{3+} ions.

The variation of σ_{jd} with excitation pulse width shown in Fig. 5 for Nd-YAG is generally in agreement with the prediction of Eq. (1). However, there appears to be an additional time dependence which causes the cross section to decrease more rapidly at smaller values for the excitation pulse width. This can be attributed to the finite value of β_d which has been ignored in the derivation of the simplified expression for σ_{jd} given in Eq. (1). The fluorescence emission from the $^2(F2)_{5/2}$ level exhibits an initial rise after 354.7 nm STEP excitation through the $5d$ level which is not observed after 532.0 nm STEP excitation or direct excitation of this metastable state. The time at which the fluorescence reaches its maximum value, t_m, can be related to the decay rates of the $5d$ and the $^2(F2)_{5/2}$ levels through the expression[6]

$$t_m = \tau_3 \tau_d \ln(\tau_d/\tau_3)/(\tau_d - \tau_3) . \qquad (3)$$

The values determined for the relaxation time of the $5d$ level for the two crystalline samples are of the order of a few nanoseconds as listed in Table I. This d-f relaxation

FIG. 9. Fluorescence spectra of Nd-ED-2 near 400 nm after high-power excitation at 532.0 nm (dashed line) and at 354.7 nm (solid line).

time can affect the value for $I_3(0)$ used in Eq. (1) to determine the magnitude of σ_{jd}.

V. DISCUSSION AND CONCLUSIONS

The results obtained in this study show that the spectroscopic properties of Nd^{3+} ions in YGaG and ED-2 hosts under high-power, picosecond-pulse excitation are similar to those observed in YAG.[1] The fluorescence lifetimes of the three metastable states of the $4f^3$ configuration observed in this investigation are listed in Table I. The nonradiative decay rate for the $5d$-$4f$ process in Nd-YGaG is similar to that found for Nd-YAG. However, in the ED-2 glass host Nd^{3+} multiphonon excitation with 354.7 nm pumping resulted in energy transfer to Ce^{3+} which decayed radiatively. The measured fluorescence decay time is similar to the $5d$ lifetime found previously by directly pumping Ce^{3+} in ED-2 (Refs. 7 and 8) and that measured for Ce^{3+} ions in YAG.[9] The band position shown in Fig. 9 appears to be shifted to longer wavelengths compared to the Ce^{3+} emission shown in Ref. 7. This can be attributed to the effects of reabsorption. The overlap of the fluorescence with the Ce^{3+} and Nd^{3+} absorption bands on the high-energy side of the emission cuts off the band in this region. The undistorted band shape can be observed only for very small samples with very small Ce^{3+} concentrations and observation of the fluorescence from the front face. To prove that the observed emission is associated with Ce^{3+}, we studied two other glass samples under the same excitation conditions. One contained Ce^{3+} only and the other contained only Nd^{3+}. The first exhibited the same broad band shown in Fig. 9 and the other showed the series of sharper lines.

Similar experiments performed on NdP_5O_{14} and YVO_4:Nd crystals with 532.0 nm excitation gave significantly different results from those reported above. In the former crystal no STEP mechanism was observed even with high excitation powers. In the latter crystal the STEP mechanism resulted in the fluorescence of the host vanadate emission band indicating delocalization of the excited electron. These different types of responses appear to be associated with the location of the $^2(F2)_{5/2}$ energy level with respect to the host band edge. This will be the subject of future investigations.

There have been several other investigations of multiphoton excitation processes of Nd^{3+} ions in solids.[10-13] However, these have each involved experimental conditions very different from the high-power picosecond-pulse excitation used here. Under some conditions, two-photon processes involving virtual intermediate states have been observed.[10] We were unable to observe such processes using the fundamental emission from the Nd-YAG laser with 30 ps pulses. Results of other studies have been interpreted using theoretical models involving virtual intermediate states even though resonant enhancement due to real intermediate states was present.[11,12] A model involving a STEP mechanism was employed in Ref. 13, but no unambiguous evidence was provided to justify this interpretation.

The time-resolved spectroscopy technique used here provides a sensitive experimental method for obtaining
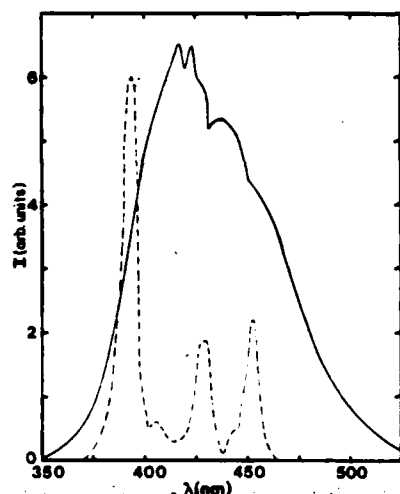
two-photon absorption cross sections for the crystalline materials investigated here. However, the problem of inhomogeneous broadening in the glass sample demonstrates the limitation of this technique. The more conventional pulse-probe technique is required to obtain the transition cross section in this case. The data obtained from these measurements can be interpreted either in terms of two-photon processes involving virtual intermediate states or the STEP mechanism. In Ref. 1 we arbitrarily chose to use the former approach since it is more general and no evidence supporting either type of mechanism was available. However, the variation of the two-photon excitation efficiency with excitation pulse width reported here conclusively demonstrates that STEP mechanisms are responsible for both types of two-photon transitions which were investigated. The cross sections for the first steps in these two sequential processes have been tabulated previously for Nd-YAG.[14] Cross sections for $4f$-$4f$ transitions of Nd^{3+} in glass hosts are known to be smaller by about an order of magnitude due to inhomogeneous broadening.[15] The magnitudes of the cross sections measured for the second steps in the two-photon processes excited by 532.0 nm pulses are similar to those of the first steps. Theoretical estimates for these cross sections can be obtained from the expression

$$\sigma_{kl} = (\beta^r_{lk} \lambda^2_{kl}) / (8\pi c n^2_0 \Delta \nu_{kl}) . \qquad (4)$$

This can be applied to the data obtained on Nd-YAG using the branching ratios for the $^2(F2)_{5/2}$ level[1] and treating the transition linewidth as the convolution of the widths of the intermediate and final levels. The theoretically predicted cross section is 4.5×10^{-19} cm^2 which is in good agreement with the measured values.

The magnitudes of the cross sections of the second steps of the two-photon transitions after 354.7 nm excitation are significantly greater than those measured for the STEP mechanism involving 532.0 nm excitation. This is because the $4f$-$5d$ transition involves states of different parity and therefore is an allowed transition. Equation (4) cannot be applied to the Nd-YAG data for this case since it uses the fluorescence lifetime of the final state of the absorption transition and the $5d$ level does not exhibit radiative emission for this material.

In conclusion, the results reported here provide evidence for two types of STEP mechanisms in Nd-doped materials and supply new information about $5d$ radiationless relaxation transitions. Enhancing our understanding of these processes can be important in determining the spectral dynamics of these laser materials under highpower, fast pulse excitation conditions. This may be relevant to developing uv or cascade laser pumping schemes.

*Present address: Electronics Division, Union Carbide Corporation, P.O. Box 6381, Washougal, WA 98671.

[1]G. E. Venikouas, G. J. Quarles, J. P. King, and R. C. Powell, Phys. Rev. B **30**, 2401 (1984).

[2]L. D. Merkle and R. C. Powell, Phys. Rev. B **20**, 75 (1979).

[3]M. Zokai, R. C. Powell, G. F. Imbusch, and B. DiBartolo, J. Appl. Phys. **50**, 5930 (1979).

[4]R. C. Powell, D. P. Neikirk, and D. Sardar, J. Opt. Soc. Am. **70**, 486 (1980).

[5]L. D. Merkle, R. C. Powell, E. E. Freed, and M. J. Weber, J. Lumin. **24/25**, 755 (1981).

[6]B. DiBartolo, *Optical Interactions in Solids* (Wiley, New York, 1968).

[7]R. R. Jacobs, C. B. Layne, M. J. Weber, and C. F. Rapp, J. Appl. Phys. **47**, 2020 (1976).

[8]S. E. Stokowski, 1979 Laser Program Annual Report, Lawrence Livermore National Laboratory Report No. UCRL-50021-79, 1979, p. 2–156 (unpublished).

[9]M. J. Weber, Solid State Commun. **12**, 741 (1973).

[10]S. Singh and J. E. Geusic, in *Optical Properties of Ions in Crystals*, edited by H. M. Crosswhite and H. W. Moos (Interscience, New York, 1967), p. 493.

[11]P. A. Apanasevich, R. I. Gintoft, V. S. Korolkov, A. G. Makhanek, and G. A. Skripko, Phys. Status Solidi B **58**, 745 (1973).

[12]M. A. Kramer and R. W. Boyd, Phys. Rev. B **23**, 986 (1981).

[13]B. R. Reddy and P. Venkateswarlu, J. Chem. Phys. **79**, 5845 (1983).

[14]W. F. Krupke, IEEE J. Quantum Electron. QE-7, 153 (1971).

[15]W. F. Krupke, IEEE J. Quantum Electron. QE-10, 450 (1974).

Investigation of Energy Transfer Processes in Nb-Compensated CaMoO₄ : Nd³⁺ Crystals

BRAHIM ELOUADI,* RICHARD C. POWELL, AND SMITH L. HOLT

*Department of Physics, Oklahoma State University,
Stillwater, Oklahoma 74078-0444*

The temperature dependence and time evolution of the fluorescence was studied for samples of $CaMoO_4 : YNbO_4$ and $CaMoO_4 : NdNbO_4$, and the results are used to characterize the thermal quenching and host-sensitized energy transfer properties of these materials. Doping with $YNbO_4$ is found to enhance the room-temperature luminescence yield of $CaMoO_4$. Efficient host-sensitized energy transfer to Nd^{3+} ions was observed in $CaMoO_4 : NdNbO_4$, and the fluorescence lifetime of Nd^{3+} was found to be close to its radiative lifetime in this host. © 1987 Academic Press, Inc.

I. Introduction

Molybdates are interesting materials for phosphor and laser applications. $CaMoO_4$ exhibits a green fluorescence emission band attributed to charge transfer transitions of the MoO_4^{2-} molecular ion (*1–3*). This is an intense luminescence at low temperatures but is strongly quenched at room temperature. Molybdates such as $CaMoO_4$ and $SrMoO_4$ doped with Nd^{3+} and charge compensated with Nb (*5*) have been shown to be good laser materials (*4–6*). We report here an investigation of the properties of thermal quenching and host-sensitized energy transfer in the materials $CaMoO_4 : YNbO_4$ and $CaMoO_4 : NdNbO_4$.

Single crystals were grown from congruent melts by the Czochralski method by

Brixner at DuPont (*7*). The coupled substitution $Ca^{2+} + Mo^{6+} = Ln^{3+} + Nb^{5+}$ keeps the Ln^{3+} dopant ions in the trivalent state. Our samples contained approximately 1.2 mole% $NdNbO_4$ or $YNbO_4$.

The absorption spectra were recorded on a Perkin–Elmer spectrophotometer. The fluorescence spectra and lifetimes were measured using a pulsed nitrogen laser as an excitation source at $\lambda = 337.1$ nm. The excitation pulse is less than 0.4 nm wide and 10 nsec in duration. The samples were mounted in a cryogenic refrigerator capable of controlling the temperature between 10 and 300 K. The fluorescence was analyzed by a 1-m monochromator, detected by a cooled RCA C31034 photomultiplier tube, averaged by a boxcar integrator triggered by the laser, and displayed on a strip-chart recorder. To investigate the characteristics of host-sensitized energy transfer, time-resolved spectroscopy (TRS) measurements were made by gating the boxcar to

* Permanent address: Applied Solid State Chemistry Laboratory, Faculty of Sciences, Charia Ibn Batota Rabat, Morocco.
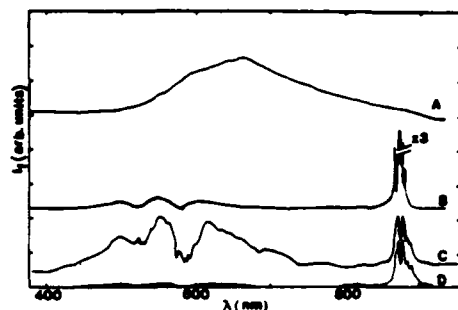
369

FIG. 1. Examples of fluorescence spectra of some rare earth-doped molybdate crystals. (A) CaMoO$_4$: YNbO$_4$ at 100 μsec after the laser pulse, T = 300 K; (B) CaMoO$_4$: NdNbO$_4$ at 100 μsec after the laser pulse, T = 11 K; (C) CaMoO$_4$: NdNbO$_4$ at 100 nsec after the laser pulse, T = 300 K; (D) CaMoO$_4$: NdNbO$_4$ at 30 μsec after the laser pulse, T = 300 K.

record the spectra at set times after the laser pulse.

II. Experimental Results

The absorption edge of these samples occurs near 340.0 nm, which is similar to undoped CaMoO$_4$ crystals. The temperature and time dependences of the fluorescence emission were studied in detail for both of the samples. Typical examples of the emission spectra taken under different experimental conditions are shown in Fig. 1. CaMoO$_4$: YNbO$_4$ has a broad fluorescence band in the region 400 to 800 nm similar to CaMoO$_4$, except that the emission intensity is stronger and the fluorescence lifetime longer at room temperature than in the undoped material (1–3). The structure of this band indicates the presence of two or more unresolved transitions contributing to the observed emission.

The Nd^{3+} absorption transitions in CaMoO$_4$: NdNbO$_4$ are a series of sharp lines associated with 4f–4f transitions

which are similar to Nd^{3+} spectral features in other host crystals. In Fig. 2 the Nd^{3+} emission lines in the visible region of the spectrum associated with the transitions from the $^4F_{3/2}$ metastable state to the crystal field components of the $^4I_{9/2}$ ground state manifold are seen between 850 and 900 nm. These transitions can be used to monitor the fluorescence quenching and energy transfer processes of interest to this study. The Nd^{3+} lines dominate the spectrum observed at 30 μsec after the excitation pulse, whereas the spectrum taken at 100 nsec after the laser pulse also shows the broad emission band of the host crystal. In this case the host emission band exhibits significant structure associated with radiative reabsorption of the fluorescence by the Nd^{3+} ions. The ratio of the integrated areas of the dips in the band caused by radiative energy transfer to that of the total band was found to remain constant at a value of about 0.2 with time after the excitation pulse for all temperatures. This is discussed further in the following section.

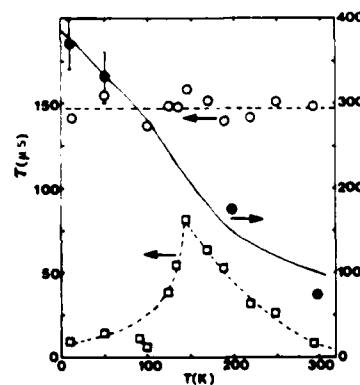The temperature dependences of the fluorescence lifetimes of the host emission

FIG. 2. Temperature dependence of the fluorescence lifetimes of CaMoO$_4$: YNbO$_4$ (solid circles), CaMoO$_4$: NdNbO$_4$ host emission (squares), and Nd^{3+} emission (open circles).

in both the $YNbO_4$- (τ_H°) and $NdNbO_4$- (τ_H) doped samples, and the Nd^{3+} emission (τ_A) in the latter sample, are shown in Fig. 2. τ_H° exhibits a significant decrease between 10 K and room temperature. The spread in data points at low temperature is associated with different values measured at different spectral positions across the broad emission band. This may be attributed to the effects of inhomogeneous broadening at low temperatures due to local disorder in the crystal. Phonon processes cause homogeneous broadening to dominate at high temperatures and a single lifetime is measured for all positions in the band. The temperature dependence of the host fluorescence lifetime in the $NdNbO_4$-doped sample is significantly different from that of the $YNbO_4$ sample, and the magnitude of τ_H is less than that of τ_H° at all temperatures. τ_H increases between 10 and 145 K and then decreases as temperature is raised to 300 K. These characteristics are the effects of host-sensitized energy transfer as well as the presence of thermal quenching, and are discussed further in the following section. The Nd^{3+} fluorescence lifetime is about 148 μsec at all temperatures, which is close to the radiative decay time of 152 μsec predicted by earlier measurements (8).

Figure 3 shows the temperature dependences of the fluorescence intensities of the host and Nd^{3+} emission bands in both the $YNbO_4$- and $NdNbO_4$-doped samples. The peaks of the host emission bands in both samples are normalized to a value of 10 at 300 K. These peak intensities generally decrease exponentially as temperature is lowered. The rate of decrease is greater for the host peak in the $NdNbO_4$-doped sample, which exhibits a slight initial increase as temperature is lowered from 300 K and then tends to become constant below 100 K. The integrated intensity of the Nd^{3+} fluorescence near 875 nm also decreases exponentially with decreasing temperature down to about 100 K and then
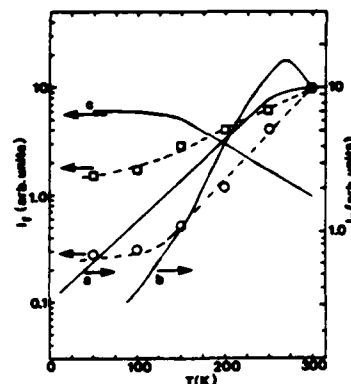
FIG. 3. Temperature dependences of the peak fluorescence intensities of (a) CaMoO₄:YNbO₄ and (b) CaMoO₄:NdNbO₄ host emission, the integrated fluorescence intensities of CaMoO₄:NdNbO₄ host emission (circles) and Nd³⁺ emission (squares), and the ratios of the integrated fluorescence intensities of the Nd³⁺ and host emission in CaMoO₄:NdNbO₄ (c).

tends toward a constant value. The ratio of the integrated intensities of the Nd^{3+} emission and the host emission in the $CaMoO_4$:$NdNbO_4$ sample is constant between about 50 and 150 K and then decreases exponentially as temperature is increased to 300 K.

III. Interpretation of Results

The independence of the absorption band edge on doping compositions has been observed previously (1, 9). The band edge absorption has been attributed to a charge transfer transition in which an oxygen $2p$ electron goes into one of the empty $4d$ orbitals of the molybdenum (9). The host emission band is associated with the Stokes shifted reverse of this transition. For the samples investigated here, the large spectral shift and long low-temperature lifetime suggest the presence of radiationless relaxation to a triplet excited state before a spin forbidden radiative emission to the singlet ground state (10).

The fact that the peak fluorescence intensity of the host emission band in $CaMoO_4:YNbO_4$ increases while the fluorescence lifetime decreases with increasing temperature indicates that thermal processes enhance the radiative emission. A comparison of these results with those published previously (1) for $CaMoO_4$ shows that the presence of $YNbO_4$ enhances the room-temperature luminescence. The mechanism for thermal quenching of the luminescence in the similar materials of $CaWO_4$ and YVO_4 has been identified as thermally activated migration of the excitation energy to quenching centers (11–13). The introduction of defects into the host crystal can either enhance the quenching if the defects act as additional quenching centers or decrease the quenching if the defects act as scattering or recombination centers to inhibit the exciton migration. If this model is valid for $CaMoO_4$, the presence of $YNbO_4$ appears to introduce recombination centers which cause the mobile excitons to have a higher radiative decay rate than the self-trapped excitons.

The temperature dependences of the fluorescence intensity and lifetime of the $CaMoO_4:YNbO_4$ sample can be attributed to the emission from both free and self-trapped excitons with a thermal equilibrium distribution of the relative population of the two states. These are described by the expressions

$$\tau^{-1}(T) = \tau_t^{-1} + \tau_f^{-1} \exp(-\Delta E/kT) \quad (1)$$

$$I(T) = I_t + I_f \exp(-\Delta E/kT), \quad (2)$$

where k is Boltzmann's constant and ΔE is the activation energy between the free and mobile exciton states. The solid lines in Fig. 2 and curve (a) of Fig. 3 represent the best fits to the data using these equations and treating the activation energy and the free exciton lifetime (τ_f) and emission intensity (I_f) as adjustable parameters. The

values giving the best fits are $\Delta E = 212.7$ cm^{-1}, $\tau_f = 50$ μsec, and $I_f = 17.9$. The values used for the trapped exciton lifetime (τ_t) and intensity (I_t) are found from extrapolating the experimental data to zero temperature.

Investigating the characteristics of energy transfer from the host crystal to an optically active impurity ion such as Nd^{3+} can provide further insight into the host energy migration and quenching processes. For $CaMoO_4:NdNbO_4$, host-sensitized energy transfer can take place both radiatively and nonradiatively. The contributions due to these two processes can be separated through their different effects on the host fluorescence properties. Radiative reabsorption does not change the observed lifetime of the host fluorescence while radiationless energy transfer produces lifetime quenching. In addition, the measurements of the structure in the host emission band due to reabsorption show that the radiative energy transfer contribution is independent of temperature and time after the excitation pulse. Radiationless energy transfer varies with both parameters. Our main interest here is understanding the mechanism of radiationless energy transfer and the following discussion deals only with this contribution to the total energy transfer.

The temperature variation of the fluorescence intensity ratios shown in Fig. 3 indicates a constant efficiency for host-sensitized energy transfer between 50 and 150 K, and then a decrease in transfer efficiency as temperature is raised to 300 K. The rate of energy transfer can be defined from the expression

$$\omega = \tau_H^{-1} - (\tau_H^o)^{-1}. \quad (3)$$

The values of ω obtained from the lifetime measurements are plotted versus T^{-1} in Fig. 4. Between 10 and 150 K, the energy transfer rate decreases, and then it increases as temperature is raised to 300 K.

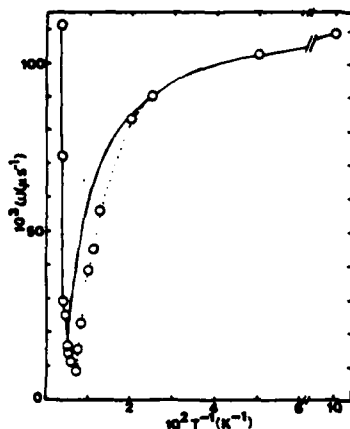Although both the transfer efficiency and

FIG. 4. Temperature dependence of the host-sensitized energy transfer rate. Circles with the dashed line represent values obtained from lifetime quenching measurements and the solid line is obtained from the results of TRS measurements.

FIG. 5. Time evolution of the integrated fluorescence intensity ratios of the Nd³⁺ and host emission in CaMoO₄:NdNbO₄ at 10 K. (open circles), 170 K (solid circles), and 300 K (squares). (See text for explanation of theoretical lines.)

transfer rate show changes in their properties at $T = 150$ K, they appear to give contradictory information about the temperature variation of the host-sensitized energy transfer. We attempted to resolve this apparent discrepancy through time-resolved spectroscopy measurements. The fluorescence spectra shown at two times after the laser pulse in Fig. 1 demonstrates the time dependence of the energy transfer from the host to the Nd³⁺ ions. The time evolution of this energy transfer was obtained at numerous temperatures by measuring the fluorescence spectra at many different times after the excitation pulse. Figure 5 shows examples of the time variation of the ratios of the integrated fluorescence intensities of the Nd³⁺ and host emission bands at several temperatures.

Different models were required to obtain the best fits to the TRS data at high and low temperatures. Above 200 K the rate equation model shown in Fig. 6 was used. n_H and n_A represent the concentrations of excited states of the host and Nd³⁺ activa-

tor ions, respectively, while β_H and β_A are their fluorescence decay rates. W_H and W_A are the direct pumping rates of the host and activators. The latter will include any excitation of the Nd³⁺ ions due to radiative energy transfer. ω and ω' are the energy transfer and back transfer rates, which for this model are taken to be time independent. The rate equations for the excited state populations are given by

$$dn_H/dt = W_H - \beta_H n_H - \omega n_H + \omega' n_A \quad (4)$$

$$dn_A/dt = W_A - \beta_A n_A + \omega n_A - \omega' n_A. \quad (5)$$

Solving these equations for a delta function excitation pulse gives the ratio of the excited state populations which is related to
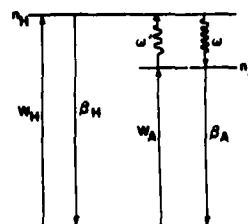
FIG. 6. Energy levels and rate parameters for interpreting host-sensitized energy transfer in CaMoO₄:NdNbO₄. (See text for explanation of notation.)

the observed ratio of the fluorescence intensities through a factor of the ratio of the radiative decay rates, β_A^r/β_H^r,

$$I_A(t)/I_H(t) = [I_A(0)/I_H(0)]$$
$$\{[1 + G_1 \tanh(Bt)]/[1 + G_2 \tanh(Bt)]\}, \quad (6)$$

where

$$B = \{[(\omega + \beta_H - \omega' - \beta_A)/2]^2 + \omega\omega'\}^{1/2}$$

$$G_1 = \{[n_H(0)/n_A(0)]\omega$$
$$+ [\omega + \beta_H - \omega' - \beta_A]/2\}/B$$

$$G_2 = \{[n_A(0)/n_H(0)]\omega'$$
$$- [\omega + \beta_H - \omega' - \beta_A]/2\}/B.$$

An example of the best fit to the data obtained using this equation and treating the initial intensity ratio, energy transfer, and back transfer rates as adjustable parameters can be seen by the solid line in Fig. 5. The parameters giving the best fits to the data at different temperatures are listed in Table I. The ratio of the radiative decay rates is approximated by the ratio of the measured fluorescence decay rates extrapolated to 0 K.

At temperatures of 150 K and less, the same general model shown in Fig. 6 can be used to interpret the TRS data, but the back transfer rate is zero and the energy transfer rate is time dependent. Solving the rate equations under these conditions leads to the expression (4)

$$I_A(t)/I_H(t) = \{[I_A(0)/I_H(0)]$$
$$+ 1\} \exp(\omega t^{3/q})^{-1}, \quad (7)$$

where $q = 6$, 8, or 10 for electric dipole–dipole, dipole–quadrupole, or quadrupole–quadrupole interaction. Examples of the best fits to the TRS data are shown as solid lines in Fig. 5 and the parameters needed to obtain the best fits for each temperature are listed in Table I.

The values obtained for ω from fitting the TRS data are used to plot the solid line in Fig. 4 for the purpose of comparing these results with the values of ω obtained from the lifetime quenching measurements.

TABLE I

ENERGY TRANSFER PARAMETERS FOR CaMoO$_4$: NdNbO$_4$

T (K)	Model	$I_A(0)/I_H(0)$	ω (μsec^{-1})	ω' (μsec^{-1})	ω (from τ_H) (μsec^{-1})
295	Eq. (6)	0.140	0.1109	0.0382	0.1109
275	Eq. (6)	0.185	0.0722	0.0248	0.0722
250	Eq. (6)	0.280	0.0577	0.0	0.0290
220	Eq. (6)	0.400	0.0619	0.0	0.0249
190	Eq. (7), $q = 8$	0.000	0.0408[a]	0.0	0.0136
170	Eq. (7), $q = 8$	0.000	0.0490[a]	0.0	0.0111
100	Eq. (7), $q = 10$	0.200	0.0662[a]	0.0	0.0383
90	Eq. (7), $q = 10$	0.720	0.0662[a]	0.0	0.0445
10	Eq. (7), $q = 10$	0.400	0.1069[a]	0.0	0.1083

[a] At $t = 15$ μsec.

Since the TRS analysis gives a time-dependent energy transfer rate in the low-temperature region, the values listed in Table I and plotted in Fig. 5 are for a specific time after the excitation pulse. For the purpose of this comparison we have chosen the values at 15 μsec. The general shapes of the curves of ω versus T obtained from the two different types of measurements are similar and show a distinct change in properties near 150 K. At the highest and lowest temperatures the magnitudes of ω obtained by the two methods are very similar, while at intermediate temperatures the values of ω obtained from TRS measurements are larger than those obtained from lifetime quenching measurements.

IV. Conclusions

The results reported here show that efficient host-sensitized energy transfer takes place in CaMoO$_4$: NdNbO$_4$. At low temperatures the characteristics of the transfer process are consistent with a single-step, multipole–multipole interaction mechanism. The rate of this process decreases as temperature is raised while the total amount of energy transfer remains constant. This is consistent with transfer from

localized excited states of MoO_4^{2-} molecular ions to their nearest-neighbor Nd^{3+} ions, with a statistical distribution of transfer distances. Increasing temperature causes the energy transfer to occur with a smaller rate but allows the same total amount of transfer to occur. This can be explained if the laser is preferentially exciting MoO_4^{2-} ions near Nd^{3+} ions. This is very probably the case since the laser excitation at 337.1 nm is just higher than the band edge of 340.0 nm, and it has been shown for other materials that excitation into the "red edge" of the host band preferentially excites regions of the host crystal near defects (12, 14). If there are extended trapping regions around each activator, increasing the temperature will allow excitons in the outer regions of the trap to migrate closer to the Nd^{3+} before transfer occurs.

At very high temperatures the host-sensitized energy transfer characteristics are consistent with a multistep energy migration process in which the energy migrates among several MoO_4^{2-} ions before transferring to a Nd^{3+} ion. This thermally activated exciton model has been used to characterize host-sensitized energy transfer in similar crystals (11–13). As temperature is raised in this range, the transfer rate increases while the total amount of transfer decreases. This indicates that the excitons have become mobile enough to migrate away from the Nd^{3+} trapping regions. As the rate of migration increases with temperature, the rate of energy transfer to Nd^{3+} ions will increase but the rate of interaction with other trapping centers will also increase, thus decreasing the total amount of energy transfer to Nd^{3+} ions.

The energy transfer characteristics in the Nd^{3+}-activated crystal indicate that thermally activated energy migration may be responsible for the quenching of luminescence in molybdate crystals. Then doping with $YNbO_4$, which is not optically active, can enhance the room-temperature luminescence of the host by providing recombination centers for the migrating excitons. The room-temperature quantum efficiency of the $CaMoO_4$:$YNbO_4$ crystal investigated here was approximately 18%. Although this is not high, it appears that this type of mixed crystal might be usable for broadband tunable laser applications. The efficient host-sensitized energy transfer observed here along with the optically pumped laser properties of $CaMoO_4$:Nd NbO_4 reported previously (4, 6) indicates that this type of mixed crystal may be a good laser material for nitrogen or eximer laser pumping.

Acknowledgments

References

1. F. A. KROGER, "Some Aspects of Luminescence of Solids," Elsevier, Amsterdam (1948).
2. G. BLASSE AND G. D. M. VAN DEN HEUVEL, J. Lumin. 9, 74 (1974).
3. J. A. GROENINK, C. HAKFOORT, AND G. BLASSE, Phys. Status Solidi A 54, 477 (1979).
4. R. C. DUNCAN, J. Appl. Phys. 36, 874 (1965).
5. L. F. JOHNSON, G. D. BOYD, K. NASSAU, AND R. R. SODEN, Phys. Rev. 126, 1406 (1962).
6. P. A. FLOURNOY AND L. H. BRIXNER, J. Electrochem. Soc. 112, 779 (1965).
7. L. H. BRIXNER, J. Electrochem. Soc. 111, 690 (1964); 113, 621 (1966); and 114, 108 (1967).
8. T. S. LOMHEIM AND L. G. DESHAZER, J. Appl. Phys. 49, 5517 (1978).
9. G. BLASSE, Structure and Bonding 42, 1 (1980).
10. C. J. M. COREMANS, J. H. VAN DER WAALS, J. KONUNENBERG, A. H. HUIZER, AND C. A. G. O. VARMA, Chem. Phys. Lett. 125, 514 (1986).
11. M. J. TREADAWAY AND R. C. POWELL, Phys. Rev. B 11, 862 (1975); J. Chem. Phys. 61, 4003 (1974).
12. R. C. POWELL AND G. BLASSE, Structure and Bonding 42, 63 (1980).
13. C. HSU AND R. C. POWELL, J. Lumin. 10, 273 (1975); D. K. SARDAR AND R. C. POWELL, J. Appl. Phys. 51, 2829 (1980).
14. R. G. PETERSON AND R. C. POWELL, J. Lumin. 16, 285 (1978).

Fluorescence and Energy-Transfer Characteristics of Rare Earth Ions in BaYF₅ Crystals

LIU XINGREN,* XU GANG, AND RICHARD C. POWELL

*Department of Physics, Oklahoma State University,
Stillwater, Oklahoma 74078*

Fluorescence spectra, excitation spectra, and fluorescence lifetimes are reported for a series of BaYF₅ crystals doped with Eu^{2+}, Er^{3+}, or Ho^{3+}, or codoped with Eu^{2+} and either Er^{3+} or Ho^{3+} ions. These data were obtained as a function of concentration of active ions and temperature. The rate and efficiency of energy transfer between pairs of ions is obtained and the mechanism for energy transfer is found to be electric dipole–dipole interaction. In addition, multiphonon radiationless decay rates are determined for Er^{3+} in this host. © 1986 Academic Press, Inc.

Introduction

Doped fluoride crystals of the type BaLnF₅ and BaLn₂F₈ (Ln = La, $\cdots$ Lu, and Y) are an important class of materials for laser, phosphor, and upconversion applications (1–5). These host crystals can be simultaneously doped with divalent and trivalent rare earth ions. The former have strong, broad absorption bands ideal for optical pumping while the latter have sharp emission lines with much longer lifetimes ideal for generating stimulated emission. To make optimum use of these properties in designing materials for specific applications, it is important to characterize the process of energy transfer taking place between these two types of ions. This paper describes the fluorescence properties of BaYF₅ : Eu^{2+}, BaYF₅ : Eu^{2+},Er^{3+}, and BaYF₅ Eu^{2+},Ho^{3+} and presents the char-

acteristics of energy transfer between Eu^{2+} and the trivalent rare earth ions in the latter two crystals.

The samples were prepared by solid state reaction of a stoichiometric mixture of fluorides in a pure nitrogen flow or N₂/H₂ mixture. The stoichiometric mixtures were loaded in graphite capsules and fired for about 20 hr at 1000°C. The BaYF₅ samples were checked by X-ray diffraction and found to be cubic with a unit cell dimension of 5.9 Å.

The samples were mounted in a cryogenic refrigerator capable of controlling the temperature between 10 and 300 K. For fluorescence spectra and lifetime measurements, excitation was provided by a nitrogen laser pulse 10 ns in duration and 1.0 Å in half width centered at 337.1 nm. The emission was focused onto the entrance slit of a 1-m Spex monochromator set for a resolution of 1 Å. The signal was detected by a cooled RCA C31034 photomultiplier tube and analyzed by an EGG/PAR boxcar inte-

* On leave from Changchun Institute of Physics, Chinese Academy of Science, Changchun, China.
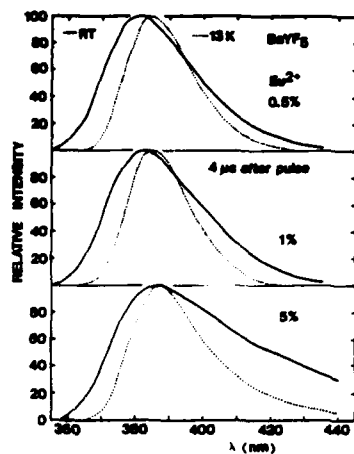
FIG. 1. Fluorescence spectra of Eu^{2+} in $BaYF_5$ at 4 μs after a nitrogen laser excitation pulse.

grator before being displayed on a strip-chart recorder. The boxcar window was either set to give time-resolved spectra or scanned to determine lifetimes. Excitation spectra were obtained with xenon lamp excitation.

Experimental Results

Spectra of $BaYF_5$: Eu^{2+}

The excitation spectra of the three Eu^{2+}-doped samples consist of two broad bands

at approximately 260 and 332 nm which are similar to Eu^{2+} absorption bands reported in other host crystals. The nitrogen laser excitation efficiently pumps the low-energy absorption band. Figure 1 shows the fluorescence spectra of Eu^{2+} in $BaYF_5$ at 4 μs after the excitation pulse for three doping concentrations at both high and low temperatures. Each spectrum consists of a broad band in the near UV spectral region as is common for Eu^{2+} in other strong crystal field hosts. This is due to the allowed transition from the lowest level of the $4f^65d^1$ configuration to the ground state of the $4f^7$ configuration. The emission bands shown in Fig. 1 are broadened and shifted to lower energy as temperature is increased and as concentration of Eu^{2+} is increased.

The fluorescence decays for these samples were observed to be single exponentials with lifetimes less than a microsecond. These are listed in Table I. They were found to be independent of temperature and are typical magnitudes for parity- and spin-allowed transitions.

Spectra of $BaYF_5$: Eu^{2+}, Er^{3+}

The room-temperature fluorescence spectrum of $BaYF_5$: Eu^{2+}, Er^{3+} after pulsed nitrogen laser excitation is shown in Fig. 2. The spectrum consists of two features: the first is the broad Eu^{2+} band similar to that

TABLE I

Eu^{2+}–Er^{3+} DECAY TIME AND ENERGY TRANSFER PARAMETERS (300 K)

Sample (mole %)		$\tau(\mu s)$		$t_r(\mu s)$			
Eu	Er	Eu	Er	Er	η	$\omega(\mu s^{-1})$	$R_0(Å)$
0.5	0.0	0.71					
1.0	0.0	0.50					
5.0	0.0	0.21					
0.5	0.5	0.55			0.225	0.41	9.0
0.5	1.0	0.50			0.296	0.59	7.6
0.5	3.0	0.34	370	54	0.521	1.53	7.7
0.5	5.0	0.24			0.662	2.56	6.8
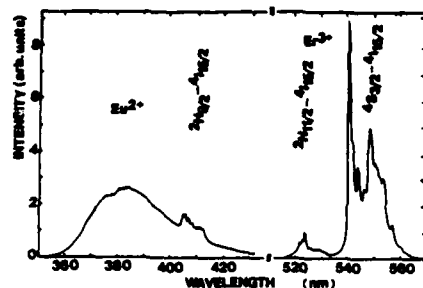
FIG. 2. Fluorescence spectrum of $BaYF_3$: Eu^{2+}, Er^{3+} at room temperature.

FIG. 4. Relative intensity of the Eu^{2+} emission at 380 nm and the Er^{3+} emission at 540 nm for samples of $BaYF_3$ containing 0.5 mole% Eu^{2+} as a function of X mole% Er^{3+} at room temperature.

seen in Fig. 1; the second is the series of sharp lines associated with the $4f$–$4f$ transitions of the Er^{3+} ions. The set of lines in the 540- to 560-nm spectral region corresponds to transitions between levels of the $^4S_{3/2}$–$^4I_{15/2}$ manifolds; those in the 522- to 535-nm region correspond to $^2H_{11/2}$–$^4I_{15/2}$ transitions; and the blue emission lines are associated with the $^2H_{9/2}$–$^4I_{15/2}$ transitions. The latter are weak but grow with increasing Er^{3+} concentration. The red emission of Er^{3+} associated with the $^4F_{9/2}$–$^4I_{15/2}$ transitions which is seen in other hosts is not observed in $BaYF_3$ at either high or low temperature under UV excitation. This may be due to reduced multiphonon relaxa-

tion rates in this host as discussed below. Infrared emission was not investigated.

Figure 3 compares the room-temperature excitation spectra of E_r^{3+} in $BaYF_3$ samples with and without Eu^{2+}. Several sets of sharp lines belonging to Er^{3+} absorption transitions are observed in both spectra while the broad Eu^{2+} absorption band appears only in the Eu^{2+}-doped sample. These results show that efficient energy transfer occurs from Eu^{2+} to Er^{3+} ions in $BaYF_3$.

Figure 4 shows the fluorescence intensities of the Eu^{2+} emission at 381 nm and the Er^{3+} emission at 540 nm plotted as a function of the Er^{3+} concentration in $BaYF_3$ a: room temperature. The Eu^+ concentration is fixed at 0.5 mole% in these samples. The intensity of Er^{3+} emission increases while that of Eu^{2+} decreases with increasing Er^{3+} concentration up to about 3 mole%. This can be attributed to increased energy transfer efficiency as the average separation between Eu^{2+} and Er^{3+} ions decreases. At higher concentrations, the Er^{3+} emission intensity also decreases due to interactions between neighboring Er^{3+} ions.
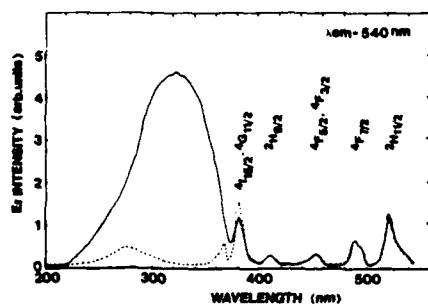

FIG. 3. Room-temperature excitation spectra of Er^{3+} emission of two samples at 540 nm with 0.5 mole% Er^{3+}. One sample contained no Eu^{2+} (broken line) and the other contained 0.5 mole% Eu^{2+}.
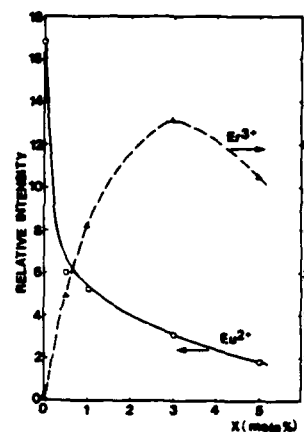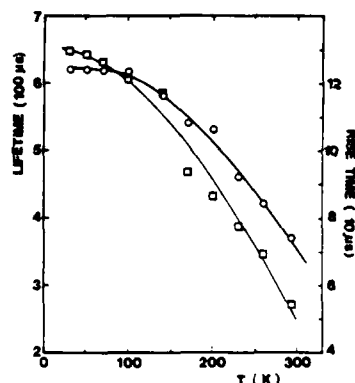
FIG. 5. Temperature dependence of the fluorescence lifetimes (circles) and rise times (squares) of Er^{3+} $^4S_{3/2}$ emission in $BaYF_5$: Eu^{2+},Er^{3+} containing 0.5 mole% Eu^{2+} and 3.0 mole% Er^{3+}.

The fluorescence decay patterns of Er^{3+} after nitrogen laser excitation exhibit an initial rise and then an exponential decay. The temperature dependences of the rise and decay times are shown in Fig. 5 and the measured values are listed in Table I. Above about 100 K, the rise and decay times decrease similarly with increasing temperature. As temperature is lowered below 100 K the rise time continues to increase while the lifetime tends toward a constant value. The temperature dependence of the fluorescence lifetime is associated with the change in the rate of the multiphonon radiationless relaxation process from the $^4S_{3/2}$ level to the $^4I_{9/2}$ level. This is described by (6-10)

$$W_f = W_r + W_{nr} \qquad (1)$$

with

$$W_{nr} = W(0)[e^{\hbar\omega/kT}/(e^{\hbar\omega/kT} - 1)]^p \qquad (2)$$

where

$$W(0) = Ce^{-\alpha\Delta E}. \qquad (3)$$

Here W_f, W_r, and W_{nr} are the fluorescence, radiative, and nonradiative decay rates, re-

spectively. The latter is treated as the emission of p phonons of energy $\hbar\omega$ needed to cross an energy gap $\Delta E = p\hbar\omega$. $W(0)$ is the zero temperature rate for the multiphonon process and C and α are parameters associated with the specific host material. For the case of interest here, the energy gap is approximately 3030 cm^{-1}. The value for the maximum phonon energy in $BaYF_2$ has not been measured but should be of the order of 350 cm^{-1} as found for other fluoride crystals. This assumption leads to a $p = 9$ phonon process. Using these values in Eqs. (1) and (2), a good fit to t. e observed temperature dependence of the fluorescence lifetime can be obtained for values of $W_r = 1.44 \times 10^3$ sec^{-1} and $W_{nr} = 0.17 \times 10^3$ sec^{-1}. For other fluoride crystals the value of α has been determined to be close to 4×10^{-3} cm (6). Using this value in Eq. (3) gives a value for C of 3.1×10^7 sec^{-1}. This is consistent with the results of Johnson and Guggenheim on BaY_2F_8 crystals (10). The fact that W_r is an order of magnetude larger than W_{nr} at low temperatures is consistent with the fact that no fluorescence is observed from the $^4I_{9/2}$ level.

There can be two possible origins for the observed rise times in the fluorescence emission patterns. The first is the process of energy transfer from Eu^{2+} to Er^{3+} and the second is the process of radiationless relaxation from the higher energy levels of Er^{3+} down to the $^4S_{3/2}$ metastable state. The dominant contribution to the observed rise time is due to the process having the smallest transition rate. In both cases the expression for the rise time t_r is

$$t_r = (W_2 - W_f)^{-1} \ln(W_2/W_f) \qquad (4)$$

where W_2 is either the energy transfer rate for the radiationless relaxation rate. The value for the energy transfer rate can be found from the quenching of the Eu^{2+} fluorescence lifetime as discussed below. If the value found in this way is substituted into Eq. (4) for W_2, the predicted value for t_r is
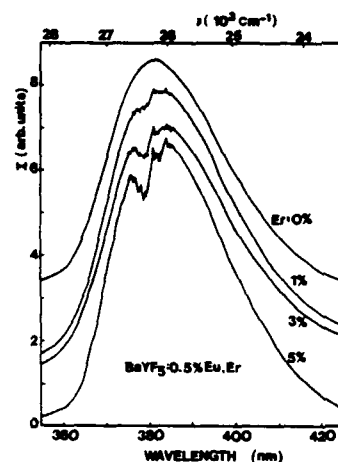
FIG. 6. Fluorescence spectra of Eu^{2+} in $BaYF_3$: Eu^{2+},Er^{3+} containing 0.5 mole% Eu^{2+} and various concentrations of Er^{3+} at room temperature.

much smaller than the observed value. Thus the rise time is associated with a bottleneck in the multiphonon decay from the excited states in Er^{3+} after energy transfer has occurred. Using the measured values of the fluorescence decay times and the risetimes in Eq. (4), values for the nonradiative decay rate can be determined. Extrapolating this to low temperatures gives $W'(0) = 1.6 \times 10^3$ sec^{-1}. Although this represents the combined results of several different multiphonon decay processes across different size energy gaps, the dominant contribution will come from the process with the largest energy gap. For relaxation after pumping through energy transfer from Eu^{2+}, the largest gap will be between the $^2H_{9/2}$ and $^4F_{3/2}$ levels which is approximately $\Delta E = 2500$ cm^{-1}. Using this in Eq. (3) along with the values of C and α found from analyzing the temperature dependence of the fluorescence decay time gives a predicted value for $W'(0)$ of 1.4×10^3 sec^{-1}. This is almost exactly the value determined from the rise-time data and is significantly smaller than the energy-transfer rate. Thus

the observed risetime is definitely associated with slow nonradiative relaxation processes and the assumptions made in analyzing the temperature dependence of the fluorescence decay time appear to be valid.

Figures 1 and 3 show that there is excellent overlap between the Eu^{2+} emission band and the $^4I_{15/2}$–$^4G_{11/2}$ absorption transitions of Er^{3+}. This can produce both radiative and radiationless energy transfer. Evidence for the radiative-transfer mechanism is provided by the reabsorption dips in the Eu^{2+} emission band corresponding to the $^4I_{15/2}$–$^4G_{4/2}$ absorption transitions of Er^{3+} as shown in Fig. 6. The area of the reabsorption dips increases with Er^{3+} concentration.

Evidence for radiationless energy transfer is provided by the change in the decay pattern of the Eu^{2+} fluorescence with increasing Er^{3+} concentration as shown in Fig. 7. The Eu^{2+} becomes nonexponential at high Er^{3+} concentrations and the lifetime becomes much shorter. The measured val-
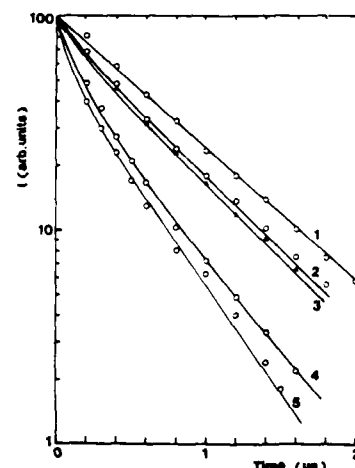
FIG. 7. Change in the Eu^{2+} decay patterns as a function of Er^{3+} concentration at room temperature in $BaYF_3$: Eu^{2+},Er^{3+} crystals containing 0.5 mole% Eu^{2+} and Er^{3+} concentrations of (1) 0.0 mole%; (2) 0.5 mole%; (3) 1.0 mole%; (4) 3.0 mole%; and (5) 5.0 mole%. (See text for explanation of theoretical lines.)
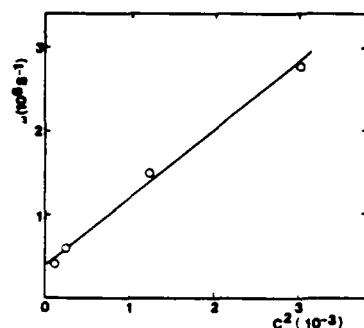
FIG. 8. Variation of Eu^{2+}–Er^{3+} energy-transfer rate with the square of the total concentration of doping ions at room temperature. The Eu^{2+} concentration was fixed at 0.5 mole% and the Er^{3+} concentrations were 0.5, 1.0, 3.0, and 5.0 mole%.

ues of the lifetimes are listed in Table I. The efficiencies (η) and rates (ω) of radiationless energy transfer were calculated from the lifetime data using the expressions

$$\omega = \tau^{-1} - \tau_0^{-1} \qquad (5)$$

$$\eta = \omega/\tau^{-1} \qquad (6)$$

where τ_0 is the intrinsic lifetime of the sensitizer and τ is the lifetime of the sensitizer in the presence of the acceptor. The lifetime of the sensitizer in the presence of the acceptor. The values obtained for ω and η are listed in Table I.

The mechanism for radiationless energy transfer between Eu^{2+} and Er^{3+} can be determined using the theory developed by Forster (11) and extended by Dexter (12) and Inokuti and Hirayama (13). In this theory the decay profile of the sensitizer after pulsed excitation is given by

$$I(t) = I(0)\exp[-t/\tau_{so}$$
$$- \Gamma(1 - 3/s)(C_a/C_0)(t/\tau_{so})^{3/s}] \qquad (7)$$

where τ_{so} is the intrinsic lifetime of the sensitizer emission, C_a is the activator concentration, C_0 is the critical energy-transfer concentration, and s is a number indexing the different types of electric multipole-

multipole interaction. This can be used to analyze the sensitizer decay patterns in Fig. 7. The best fits to the data found using Eq. (7) are shown as solid lines. For the four double-doped samples the best theoretical fits were found using a value of $s = 6$ which implies dipole–dipole interaction. The critical energy transfer concentration was treated as an adjustible parameter and fitting the data yields an average value of $R_0 = [(4/3)\pi C_0]^{1/3} = 7.6$ Å. This critical transfer distance is related to the transfer rate by

$$\omega = \tau_{so}(R_0/R_{sa})^6 \qquad (8)$$

where R_{sa} is the separation between sensitizer and activator ions. Using the values of ω listed in Table I obtained from lifetime quenching measurements and the value of R_0 obtained above, Eq. (8) gives an average sensitizer–activator separation ranging from 9.3 to 7.4 Å for these samples.

The values obtained for R_0 and ω are physically reasonable for energy transfer between a divalent and trivalent rare earth ion but it is not possible to obtain an accurate theoretical prediction for these values because a quantitative absorption spectrum cannot be obtained on the small crystallite samples presently available. An additional check on the interpretation of the energy
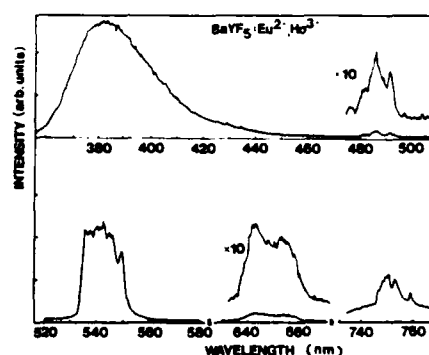

FIG. 9. Room-temperature fluorescence spectra of $BaYF_5:Eu^{2+}(1.0$ mole%),$Ho^{3+}(3.0$ mole%) after 337.1-nm excitation.

transfer mechanism as electric dipole–dipole interaction is obtained by plotting the transfer rate versus the square of the total concentration of doping ions as shown in Fig. 8. The fact that ω varies linearly with the square of the concentration is consistent with the square of the concentration is consistent with the predictions of dipole–dipole interaction (14).

Spectra of $BaYF_5: Eu^{2+}, Ho^{3+}$

The room-temperature fluorescence spectra of $BaYF_5: Eu^{2+}, Ho^{3+}$ after pulsed laser excitation at 337.1 nm is shown in Fig. 9. The broad band in the 380 nm spectral region is associated with the d–f transition of Eu^{2+}. The major emission from Ho^{3+} appears in four spectral regions: 478–497 nm ($^5F_3$–$^5I_8$); 530–560 nm ($^5S_2$–$^5I_8$); 635–663 nm ($^5F_3$–$^5I_7$ and $^5F_5$–$^5I_8$); and 746–764 nm ($^5I_4$–$^5I_8$).

The room-temperature excitation spectra of the 541 nm Ho^{3+} emission line for $BaYF_5$ samples with and without Eu^{2+} are similar to that of $BaYF_5: Eu^{2+}, Er^{3+}$. The broad band associated with the f–d absorption transition of Eu^{2+} appears in the excitation spectrum of Ho^3 which shows the presence of energy transfer from Eu^{2+} to Ho^{3+}.

Figure 10 shows the change in the relative intensities of the Eu^{2+} and Ho^{3+} fluorescence emission as a function of Ho^{3+} concentration. The Eu^{2+} emission is quenched by the addition of Ho^{3+} due to
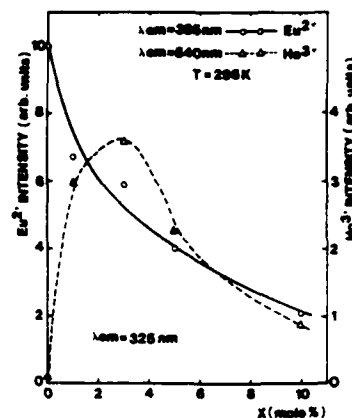
FIG. 10. Relative intensities of the Eu^{2+} (385 nm) and Ho^{3+} (541 nm) emissions at room temperature in $BaYF_5: Eu^{2+}(1.0\ mole\%), Ho^{3+}(x\ mole\%)$ as a function of x.

energy transfer. The Ho^{3+} emission intensity increases up to a concentration of about 3 mole% due to increased energy transfer from the Eu^{2+}. At higher concentration levels Ho^{3+} concentration quenching occurs. The Eu^{2+} fluorescence decay time is also quenched by the addition of Ho^{3+}. The values of these lifetimes are listed in Table II.

The quenching of the Eu^{2+} fluorescence intensity and lifetime by the addition of Ho^{3+} is due to the transfer of energy from the former to the latter type of ion. Using

TABLE II

Eu²⁺–Ho³⁺ Decay Time and Energy Transfer Parameters (300 K)

Sample (mole %)		$\tau(\mu s)$		$t_r(\mu s)$			
Eu	Ho	Eu	Ho	Ho	η	$\omega(\mu s^{-1})$	$R_0(\text{Å})$
1.0	1.0	0.34			0.32	0.94	9.8
1.0	3.0	0.30	102	13.5	0.40	1.33	5.7
1.0	5.0	0.26			0.48	1.85	5.3
1.0	10.0	0.20			0.60	3.00	5.3
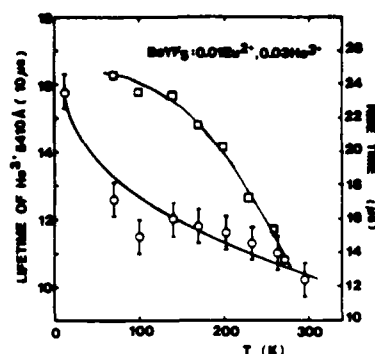
FIG. 11. Temperature dependences of the fluorescence lifetimes (circles) and rise times (squares) of Ho^{3+} in $BaYF_3$: Eu^{2+}(1.0 mole%),Ho^{3+}(3.0 mole%) after 337.1 pulsed excitation.

Eqs. (5) and (6) the transfer rate and efficiency can be determined and these are listed in Table II.

The decay profiles of the activator ions excited through energy transfer exhibit an

FIG. 12. Change in the Eu^{2+} decay patterns as a function of Ho^{3+} concentration at room temperature in $BaYF_3$: Eu^{2+}.Ho^{3+} crystals containing 0.01 mole% Eu^{2+} and Ho^{3+} concentrations of (1) 0.0 mole%; (2) 1.0 mole%; (3) 3.0 mole%; (4) 5.0 mole%; and (5) 10.0 mole%. (See text for explanation of theoretical lines.)

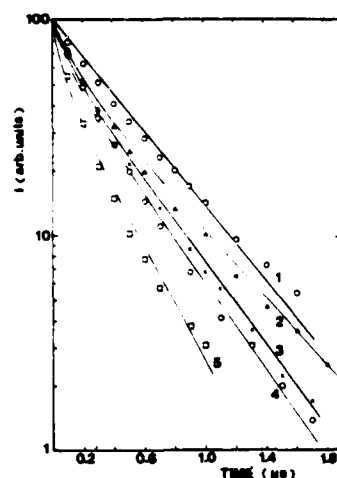initial rise followed by a single exponential decay. The temperature dependences of the fluorescence decay times and rise times of the Ho^3 are shown in Fig. 11 and the room-temperature values are listed in Table II. The measured rise times are again an order of magnitude larger than those predicted theoretically using Eq. (4) and the measured energy transfer rate for W_2. As before, we attribute this to a bottleneck in the radiationless relaxation processes due to weak multiphonon emission processes in this type of host crystal. However, the shape of the temperature dependence of the fluorescence lifetime can not be fit by using Eqs. (1) and (2) and thus the various parameters describing the relaxation processes cannot be determined. The different shape for the curve of the fluorescence lifetime versus temperature may be associated with the interaction between Ho^{3+} ions which occurs at the concentration present in this sample. This interaction may have an additional temperature dependence associated with it which contributes to the observed results.

The decay profiles of the sensitizer ions in the presence of activators are nonexponential due to energy transfer. These are shown in Fig. 12 for different activator concentrations. The curves are fit by the predictions of Eq. (7) assuming electric dipole–dipole interaction. The values of the critical interaction distances found from this procedure are listed in Table II. The transfer efficiency, transfer rate, and critical interaction distance for Eu^{2+}–Ho^{3+} energy transfer are smaller than the parameters found for Eu^{2+}–Er^{3+} energy transfer. This is due to the difference in spectral overlap for the two systems.

Acknowledgments

providing experimental facilities for some of these measurements.

References

1. H. J. GUGGENHEIM AND L. F. JOHNSON, *Appl. Phys. Lett.* **15**, 51 (1969); L. F. JOHNSON AND H. J. GUGGENHEIM, *Appl. Phys. Lett.* **19**, 44 (1971); **20**, 474 (1972).
2. L. F. JOHNSON, H. J. GUGGENHEIM, J. C. RICH, AND F. W. OSTERMAGER, *J. Appl. Phys.* **43**, 1125 (1972).
3. C. FOUASSIER, B. LATOURRETTE, J. PORTIER, AND P. HAGENMULLER, *Mat. Res. Bull.* **11**, 933 (1976).
4. B. LATOURRETTE, F. GUILLEN, AND C. FOUASSIER, *Mat. Res. Bull.* **14**, 865 (1979).
5. F. GAUME, A. GROS, AND J. C. BOURCET, *Rare Earths Mod. Sci. Technol.* **3**, 143 (1982).
6. L. A. RISEBERG AND M. J. WEBER, "Progress in Optics," Vol. 14, (E. Wolf, Ed.), p. 89, North-Holland, Amsterdam, 1977.
7. L. A. RISEBERG AND H. W. MOOS, *Phys. Rev.* **174**, 429 (1968); E. D. REED, JR., AND H. W. MOOS, *Phys. Rev. B* **8**, 980 (1973).
8. M. J. WEBER, *Phys. Rev.* **171**, 283 (1968).
9. F. K. FONG, S. L. NABERHUIS, AND M. M. MILLER, *J. Chem. Phys.* **56**, 4020 (1972).
10. L. F. JOHNSON AND H. J. GUGGENHEIM, *Appl. Phys. Lett.* **23**, 96 (1973).
11. TH. FORSTER, *Ann. Phys.* **2**, 55 (1948).
12. D. L. DEXTER, *Chem. Phys.* **21**, 836 (1953).
13. M. INOKUTI AND F. HIRAYAMA, *J. Chem. Phys.* **43**, 1978 (1965).
14. F. K. FONG AND D. J. DIESTLER, *J. Chem. Phys.* **56**, 2875 (1972).

III. SPECTROSCOPIC PROPERTIES OF TRANSITION METAL LASER CRYSTALS

In this thrust area, the work includes investigations of the properties of established laser materials and of new materials with potential for laser applications. One important aspect of the research involves the problems associated with nonrandom active ion distributions in the host crystals. Some of the common types of deviations from random distributions of active ions are listed in Table I while Table II lists some of the effects these nonrandom distributions have on the optical properties of the materials. An example of light scattering from clustered defects in ruby crystals is shown in Fig. 1. Developing methods for minimizing these problems will greatly enhance the development of new laser materials.

The first two manuscripts in this section describe the optical properties of titanium doped sapphire. This is an important tunable laser material in the near infrared spectral region. The tuning range is limited by parasitic absorption on the low energy side of the emission band. The results described here provide some insight into the origin of this absorption and also show the presence of some multiphoton absorption under high pumping powers. The next three manuscripts describe the details of the optical properties of alexandrite crystals. This is currently the most important tunable solid state laser crystal in systems applications. Along with providing conventional spectroscopic information, the results obtained by FWM indicate the presence of long range energy migration among the Cr^{3+} ions and give the pump band to metastable state relaxation rate. All of these results provide a better understanding of the pumping

dynamics of alexandrite which will be helpful in developing new vibronic laser materials.

The next four manuscripts survey the optical properties of novel materials with potential laser applications. The only one of these in which gain was observed was Ti^{4+} in lithium germanium oxide. This result was important because the material provided tunable emission in the blue-green spectral region and was the first observation of gain from a closed shell ion. However, the gain was found to be dependent on the pump pulse width and was only significant if the power was extracted very rapidly. This was attributed to quenching through intersystem crossing to a triplet state. Another important result of the work described here involved fiber crystal growth of Mn_2SiO_4. Bulk crystals of this material exhibited strong thermal quenching of the fluorescence and pulling fiber crystals from the same material improved the quenching properties by more than an order of magnitude.

TABLE I. TYPES OF DEVIATIONS FROM RANDOM DISTRIBUTIONS OF ACTIVE IONS

concentration gradients	banding
dislocation decoration	aggregates
defect pairing	special site occupancy

TABLE II. EFFECTS OF NONRANDOM DISTRIBUTIONS OF ACTIVE IONS

diffraction	light scattering
radiationless quenching	energy transfer
loss of lasing centers	parasitic absorption

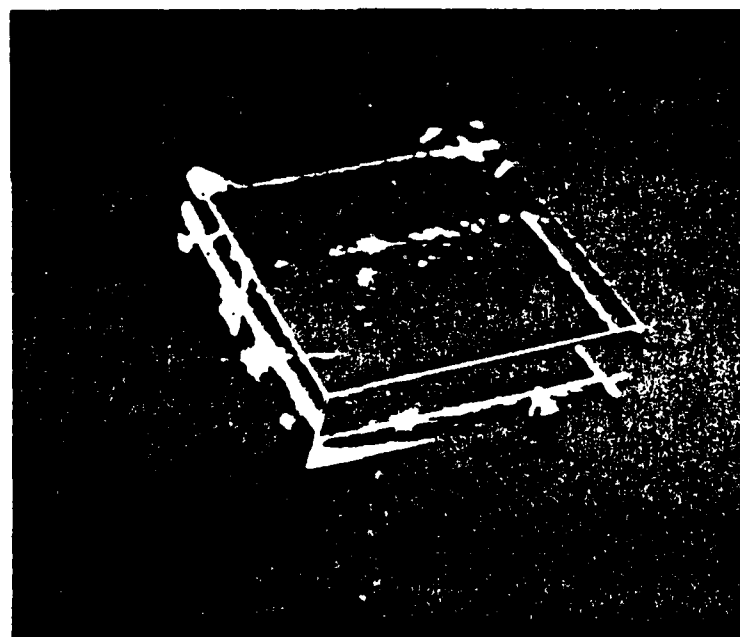Fig. 1. Laser light scattering from defects in a ruby laser crystal.

Growth, characterization, and optical spectroscopy of Al_2O_3:Ti^{3+}

Richard C. Powell
Department of Physics, Oklahoma State University, Stillwater, Oklahoma 74078

Jaroslav L. Caslavsky
Ceramics Research Division, Army Materials and Mechanics Research Center, Watertown, Massachusetts 02172

Zuhair AlShaieb and John M. Bowen
Department of Geology, Oklahoma State University, Stillwater, Oklahoma 74078

The process of growing large diameter single crystals of Al_2O_3:Ti^{3+} by vertical solidification of the melt is described, and some of the problems in producing high-optical quality material are discussed. The characterization of the distribution and valance state of titanium ions was performed by x-ray techniques and laser Raman microprobe methods. The presence of other impurity ions, specifically iron, was also determined. In some cases titanium was found in the grown crystal to be in the rutile form. In addition, Ti-Fe pairs, and concentrated regions of titanium on the surface of the boule were also observed. Some procedures for minimizing these problems are discussed. The results of optical absorption, fluorescence, and lifetime measurements are reported. The addition of Fe is shown to produce a broad absorption band in the red region of the spectrum, and two-photon laser excitation terminating in the ultraviolet spectral region produces a broad blue emission band.

I. INTRODUCTION

There is a significant interest in the application of Al_2O_3:Ti^{3+} crystals as tunable laser materials.[1,2] The broad, intense fluorescence emission band provides a wider tuning range and higher gain cross section than other transition metal ion tunable lasers. To develop this material to the point where it can be used in commercial laser systems requires the ability to produce large size, high-optical quality, high-purity single crystals. Moderately high concentrations of Ti^{3+} uniformly distributed throughout the entire crystal are also required. In addition, the dynamics of optical pumping and decay processes must be investigated to determine optimum system configurations. So far, most of the characterization of laser properties of Al_2O_3:Ti^{3+} has been performed with laser pumping, although some techniques for fast flashlamp pumping have been developed.[3] Some of the limitations encountered in trying to optimize laser parameters include scattering centers and parasitic absorption bands in the laser spectral region. Little work has been done in investigating upper excited states of the system which may be detrimental to the system through excited state absorption of pump or fluorescence light, or may be useful for alternate pumping mechanisms.

We report here a description of a crystal growth technique capable of producing laser quality crystals of Al_2O_3:Ti^{3+}, and describe the results of characterizing doping and impurity ion distributions using several different techniques. In addition, some spectroscopic properties of the system are reported including emission occuring after two-photon excitation into the ultraviolet spectral region.

II. CRYSTAL GROWTH

The Czochralski[4] method of crystal growth has been successful in producing different types of single crystals.

However, some factors limit the Czochralski technique in production of large diameter single crystals which have both high melting points and high-specific gravities. Viechnicki and Schmid[5] overcame some of these problems by developing a heat exchanger technique based on the original work of Strober.[6] This proved successful in growing large diameter single crystals only for single component, undoped systems. Recently, Caslavsky[7] overcame these problems by designing a crystal growth method using a sophisticated heating element which allows control of the heat flow during the process of solidification. This method is called vertical solidification of the melt (VSOM). The VSOM technique originated, and an apparatus was built for VSOM crystal growth, at the Army Materials and Mechanics Research Center in Watertown, Massachusetts.

When the propagation of the solid-liquid interface during crystal growth is achieved, by either pulling the crystal or moving the furnace, vibrations and thermal fluctuations are present during the process of growth and this can produce stress in the cooling crystal. Such stress not only lowers the optical quality of the crystals but generally results in microcracks, which are detrimental to the production of laser quality single crystals. To avoid this problem, large diameter single crystals have to be grown in a vibration-free environment, with a planar interface. In addition, if the crystal has both a high melting point and a high-specific gravity, it is necessary to support the crystal over its entire diameter during the entire period of growth. This can be achieved by confining the melt in a suitable container, rather than controlling the crystal diameter by balancing the heat flow during growth.

Although all of the problems discussed above cannot be eliminated entirely, their effects can be significantly minimized by use of the VSOM method. This technique eliminates the problem of vibrations by moving the thermal field
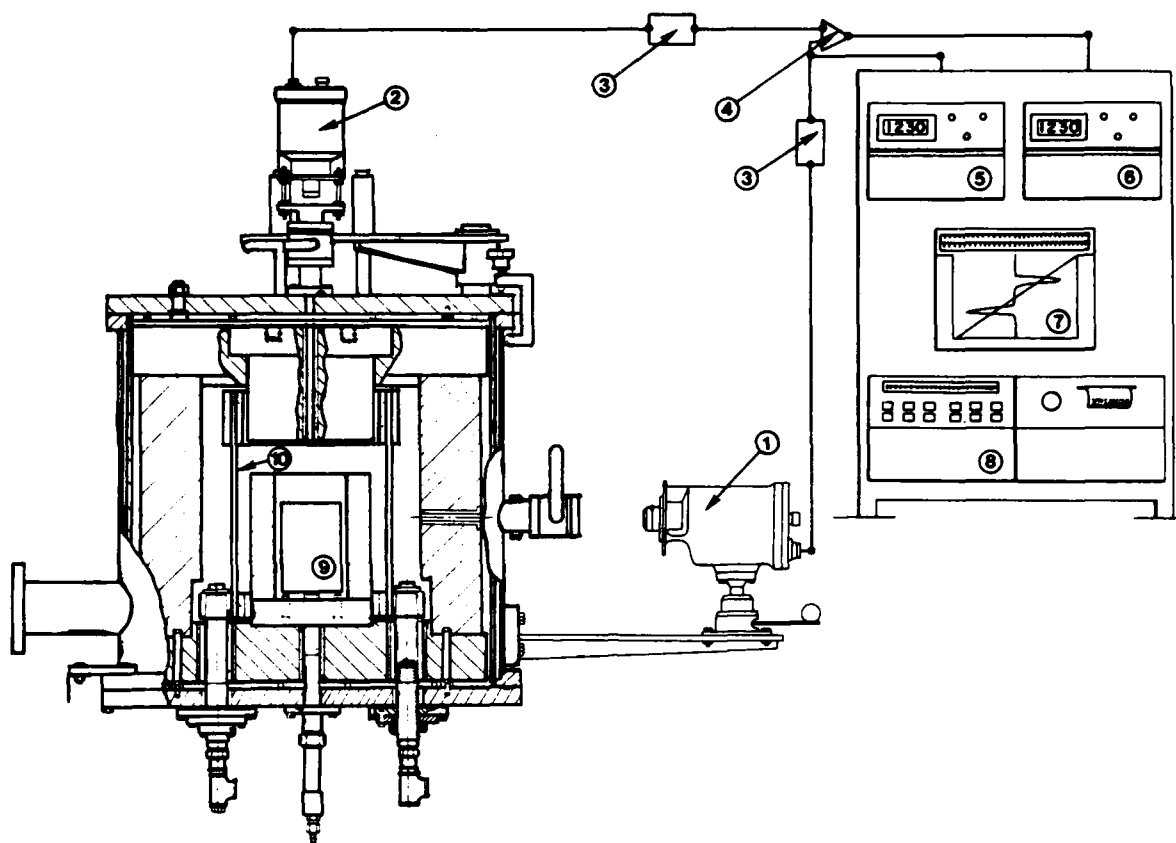
FIG. 1. Schematic diagram of crystal growth furnace for VSOM. (1) Two-color pyrometer; (2) single-color pyrometer; (3) signal conditioners; (4) differentiation of signals; (5) temperature readout from two-color pyrometer; (6) temperature readout from single-color pyrometer; (7) two pen recorder for recording ODTA curve and temperature of blackbody; (8) controlling microprocessor; (9) 10-cm-diam container in which crystal is grown; (10) heating element.

through the system, instead of moving the crucible or the furnace. A schematic diagram of the VSOM crystal growth apparatus is shown in Fig. 1, and the cross section of the heat sink depicted in Fig. 2. The material to be synthesized into a large single crystal is loaded into a cylindrical container with the diameter of the required crystal size. A seed crystal is placed in the center of the bottom of the crucible. Since the entire content of the crucible other than the seed crystal has to be melted, the crucible is rested on a cold finger, which is situated just below the seed crystal to protect it from melting. During the period of shaping the solid-liquid interface, and specifically during the entire period of crystal growth, this cold finger takes on the function of a heat sink, thus having crucial importance in controlling the crystal growth. In order to obtain the driving force for crystal growth, the thermal field is propagated throughout the system in the desired fashion and rate. To achieve this, precise readings of two optical automatic pyrometers are essential. (Positions of these pyrometes are illustrated in Fig. 1.) The system operates as follows: pyrometer no. 1 senses the temperature of the blackbody and thus controls the temperature of the whole system. Pyrometer no. 2 observes the temperature of the content of the crucible. In order to start the growth, the temperature of the blackbody has to be slightly lowered first. Since the heat capacity of the crucible generally is higher than the heat capacity of the blackbody, a temperature dif-
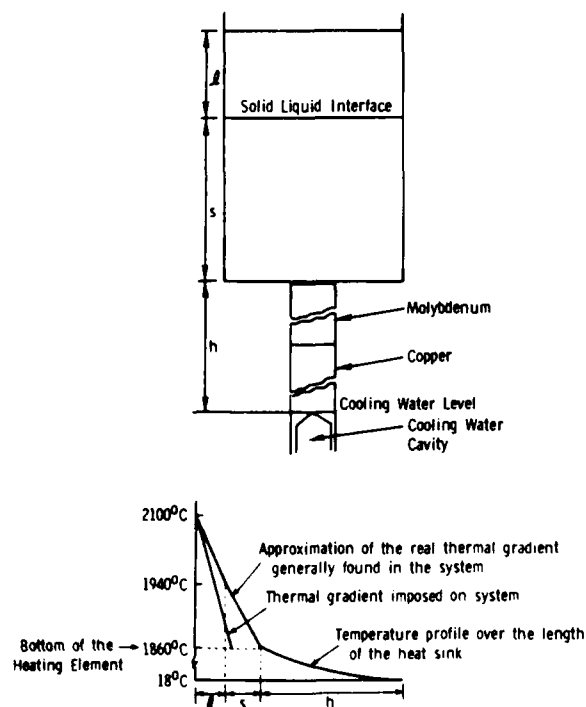

FIG. 2. Cross section of the crucible and heat sink, and diagram of the thermal gradient in the system.

ference ΔT between the blackbody and the melt occurs. This temperature difference creates an appropriate signal, which is fed to the microprocessor whose program is designed in such a way that on the occurrence of such a difference it starts to decrease the blackbody temperature as a function of ΔT. During solidification of large diameter crystals a significant amount of latent heat is developed on the solid-liquid interface. In turn, this heat influences the melt temperature. Occurrence of such a temperature increase is registered by pyrometer no. 2 which immediately corrects the signal of pyrometer no. 1, and as a consequence the melt temperature is not affected by the latent heat developed at the interface. This type of a temperature control enables programming of the thermal field propagation with an accuracy of ± 1 °C in the temperature range between 1600 and 2100 °C, and the rate of the temperature decrease between 0.1 and 2.0 °C/h. This is a very accurate control of the driving force for the crystal growth.

In order to keep the linear upward thermal gradient over the required vertical distance and to maintain the isotherms mutually parallel, as well as parallel to the bottom of the crucible, the latent heat of solidification has to be removed from the system, down through the already solidified material and into the heat sink. Therefore, in order to grow any single crystal by the VSOM method, in a controlled manner and on a flat interface, the net heat flow through the heat sink has to be equal at all times to the heat flux through the already solidified material. Such a heat flux is a sum of the latent heat of solidification and the heat absorbed due to the radiation from the element through the container wall. In the first approximation, the heat transferred through the system can be described as

$$K_h A_s (dT/dx_s) - K_l A_l (dT/dx_l) = ALp(dx/dt), \qquad (1)$$

where K is the thermal conductivity, A is the cross-section area of the charge, T is temperature, x is a coordinate measured along the vertical axis of the system, ρ is the density, and L is the latent heat of the crystallizing material. The subscripts s, l, and h, relate to the solid and liquid phases, and to the heat sink, respectively. Since the cross sections for the solid and liquid and that of the interface are all approximately equal, Eq. (1) becomes

$$K_s G_s - K_l G_l = RL\rho, \qquad (2)$$

where G is the temperature gradient and R the growth rate.

In this case, the growth rate is the movement of the interface, and the rate of growth of the crystal is governed by the rate at which the latent heat is extracted from the system by the heat sink. The heat flow ϕ through the heat sink can be expressed as

$$\phi = K_h A_h (dT/dx_h), \qquad (3)$$

and in the first approximation as

$$RL\rho = K_h A_h (dT/dx_h). \qquad (4)$$

Because of complicated boundary conditions and the practical impossibility of determining the exact position of the interface, Eq. (4) cannot be solved numerically. Therefore, ϕ has to be determined experimentally from the grown crystal. If the heat sink removes an insufficient amount of heat so that

$$RL\rho > K_h A_h (dT/dx_h), \qquad (5)$$

then a dendritic growth is observed. If the heat sink removes an excessive amount of heat so that

$$RL\rho < K_h A_h (dT/dx_h), \qquad (6)$$

the shape of the growth interface becomes convex. Adjusting for the proper heat flow capacity of the heat sink must be done through trial and error. Fine tuning of the ϕ value is achieved by adjusting the flow of cooling water through the heat sink.

For the crystals used for this study, a molybdenum crucible in a resistively heated graphite furnace was used and the crystals grown under a vacuum of approximately 5×10^{-2} Torr. The graphite elements were made in a bird cage design with the power feeds brought to the lower element ring. With this design, an upward gradient of 1.0°/mm over the 120-mm element height was achieved. Using this technique, single crystals of Al_2O_3:Ti^{3+} were grown up to 250 mm in diameter, free of cracks, with minimum phase segregation and dislocation structure similar to that found in undoped sapphire crystals grown by VSOM.[8,9]

III. OPTICAL SPECTROSCOPY

The optical absorption and emission spectra and the fluorescence lifetimes were measured for samples of Al_2O_3:Ti^{3+} cut from boules grown by the VSOM technique. Typical results are discussed below for a sample of high-optical quality and a Ti^{3+} concentration determined to be 0.054 wt. %.

The absorption spectrum of Al_2O_3:Ti^{3+} is shown in Fig. 3. The major features of this spectrum include a broad band with a peak near 580 nm, a shoulder to longer wavelengths, and a long tail extending past 900 nm. The absorption edge appears near 280 nm and has a distinct shoulder near 240 nm. The fluorescence emission produced by pumping in the 580-nm absorption band is shown in Fig. 4. It appears as a broadband peaking near 750 nm and extending past 1000 nm. The fluorescence lifetime of this band was found to be 4.0 μs and independent of temperature between 10 and 300 K.
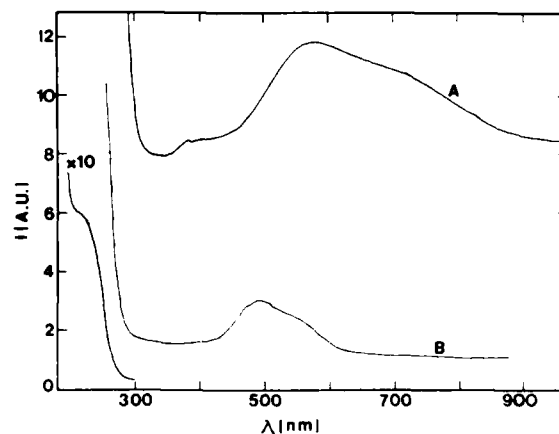

FIG. 3. Room temperature absorption spectra of Al_2O_3 (A) co-doped with Ti^{3+} and Fe^{3+} and (B) doped with Ti^{3+}. The intensity scale is relative.
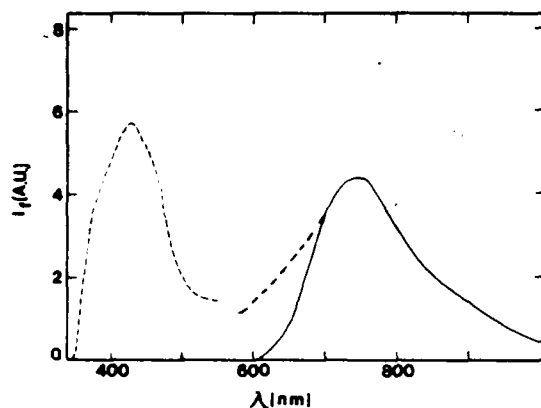
FIG. 4. Room temperature fluorescence spectra of $Al_2O_3:Ti^{3+}$. Solid line shows results obtained after low-power excitation with a nitrogen laser-pumped dye laser at 590 nm. Broken line shows results obtained after high-power Nd-YAG laser excitation at 532 nm.

FIG. 5. Raman microprobe spectra of Al_2O_3 and the perfect region of $Al_2O_3:Ti^{3+}$ with vibrational modes designated by their irreducible representations.

The major absorption and emission bands at 580 and 750 nm, respectively, are due to transitions between the $^2T_2$ ground state and the ^2E excited state of a single d electron ion occupying an aluminum site in the corundum lattice.[10-13] The large Stokes shift, indicates a strong coupling to the lattice in the excited state. The broad widths of these bands are due to the modulation of the crystal field splitting between the ^2E and $^2T_2$ levels by the lattice vibration of the ligands around the Ti^{3+} ions. This strong vibronic coupling produces a Jahn–Teller splitting in the excited state, which is responsible for the double peak seen in the absorption band. Spin-orbit interaction and the trigonal crystal field distortion cause an additional splitting of the ground state, which can be seen in the far infrared[13,14] and electron paramagnetic resonance spectrum.[15]

The other features of the optical spectra cannot be associated with transitions involving isolated Ti^{3+} ions. The long absorption tail in the 800-nm spectral region becomes more prominent for samples containing higher concentrations of titanium[16] and reabsorbs the fluorescence in this area. One well known type of defect transition producing an absorption band in this region is the charge transfer transition between coupled iron-titanium ion pairs, $Fe^{3+}Ti^{3+}$-$Fe^{2+}Ti^{4+}$. This is the origin of the color in "blue sapphire"[17] and the absorption spectrum of a crystal purposely co-doped with Fe^{3+} and Ti^{3+} is shown in Fig. 3. The presence of iron in $Al_2O_3:Ti^{3+}$ crystals is discussed in Sec. IV.

The fact that the absorption band edge of doped sapphire crystals is moved to lower energies from that of the undoped crystal has been attributed to the presence of ligand-metal ion charge transfer bands in the near UV spectral region.[18] Ti^{3+} is known to have a charge transfer band in the region of the 228-nm band edge shoulder shown in Fig. 3.[18]

In order to determine the effects of pumping in the charge transfer absorption bands, the sample was excited by a 30-ps pulse from a frequency doubled Nd-YAG laser. The experimental setup for this work has been described previously.[19] Part of the 532-nm light is directly absorbed by the
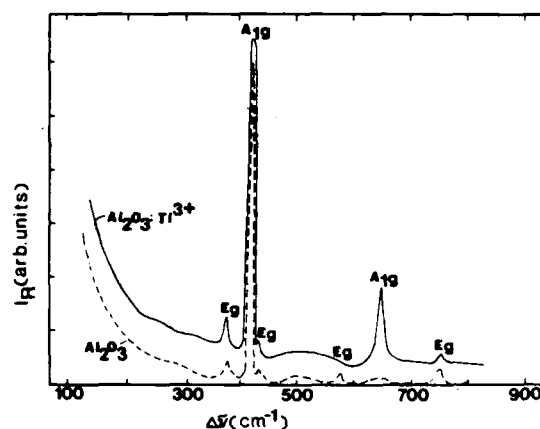
Ti^{3+} in one-photon processes and part is absorbed by two-photon processes in the charge transfer band at 266 nm. The fluorescence occurring after this type of excitation is shown as a broken line in Fig. 4. It consists of the normal Ti^{3+} emission band peaking near 780 nm but with an additional tail extending to higher energies, and a new fluorescence emission band peaking near 420 nm. This band is also seen after direct UV excitation.[20] The fluoroescence lifetime measured after this type of excitation is still $4.0 \mu s$ for the 740-nm emission band, but a rise time for the fluorescence of the order of 20 ns is observed implying the presence of an additional pumping mechanism for this fluorescence. The lifetime measured in the new high-energy tail of this band is 7.4 μs, while the lifetime of the 420-nm band is $2.3 \mu s$. The origin of these new emission bands is not known at the present time.

IV. CHARACTERIZATION OF CRYSTAL DEFECTS

In order to better understand the distribution and valence states of titanium ions and the effects of other chemical and structural defects in the samples, electron microscopy and Raman microprobe spectroscopy techniques were used. The scanning electron microscope used for this work was a Joel 355 with a Tracor Northern 2000 energy dispersive x-ray analyzer (EDAX) attachment for quantitative elemental analysis in selected microscopic regions of the sample. The Raman microprobe equipment included a Spectra Physics argon laser, and an Instruments S.A. Ramanor U-1000 equipped with computer-controlled data acquisition. This instrument allowed the direct acquisition of Raman spectra of specific areas of the sample as small as 1 μm in diameter. Four kinds of regions having different types of defect properties were identified. These included the "perfect" regions of the sample, inclusions, precipitates, and discolored regions on the surface of the sample.

In the "perfect" regions of the sample, no chemical impurities were detected by SEM/EDAX analysis. The micro-Raman spectrum in these regions is the same as that for undoped Al_2O_3 as shown in Fig. 5. In addition, a strong background fluorescence is observed in the spectral region consistent with Ti^{3+} emission as described in Sec. III. This
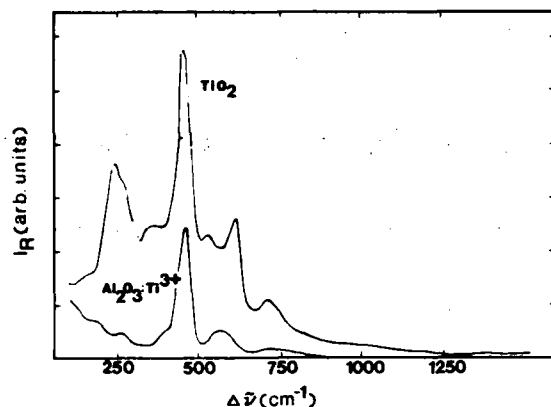
FIG. 6. Raman microprobe spectra of TiO_2 and a region with an inclusion in $Al_2O_3:Ti^{3+}$.

remains essentially constant in intensity as the microprobe is scanned throughout this type of region.

The inclusions appeared under the SEM as voids with diameters of a few microns. These are randomly distributed in the crystal. The precipitates are randomly distributed disturbed regions of the crystal having dimensions of the order of tens of microns. In many cases, an inclusion and precipitate are located in the same region of the crystal. The SEM/EDAX analysis of the voids did not indicate the presence of any chemical impurities. However, the precipitates were found to contain chemical impurities such as Ce, K, Cl, Fe, La, and Nd. Each precipitate had different compositions of these impurities in the level of several hundred parts per million. Raman microprobe analysis of the precipitates produced very noisy spectra with no additional peaks to those of the normal host spectrum shown in Fig. 5. The background Ti^{3+} fluorescence varied greatly in intensity as the microprobe was scanned throughout the precipitate region. When the microprobe was focused onto the surface of a void, the Raman spectrum shown in Fig. 6 was observed. This is shown in comparison to the Raman spectrum of a crystal of TiO_2. The peak positions in the two spectra are well correlated. The differences in relative intensities are due to the fact that the TiO_2 spectrum is from an oriented single crystal, while the inclusion spectrum is from unoriented crystallites. In addition, the background fluorescence from Ti^{3+} goes to zero in the region of the inclusion.

Finally, regions on the surface of the samples having a yellowish-brown color were investigated. Both EDAX and Raman microprobe analysis showed these to be regions with a high concentration of titanium, but the chemical composition could not be identified.

V. SUMMARY AND CONCLUSIONS

An ideal $Al_2O_3:Ti^{3+}$ laser crystal requires a uniform distribution of titanium in its trivalent state. In addition, it must be free of any chemical impurities and different phases. The results described above indicate that it is possible for titanium in sapphire to form inclusions of rutile, to form charge transfer pairs with iron, and to be rejected from the host to concentrated areas on the surface. These effects de-

grade the laser properties of the material by decreasing the number of optically active Ti^{3+} ions, by introducing an absorption band which absorbs potential laser active fluorescence, and by producing defect centers which scatter laser light. Using the methods discussed in Sec. II, to carefully adjust the crystal growth parameters in the VSOM technique, it has been possible to produce crystals which are free of scattering centers and free of the infrared absorption band. Rejection of titanium remains a problem when growing crystals with moderate concentrations of Ti^{3+}.

The origin of the additional fluorescence emission bands observed after two-photon excitation has not been identified. Their position is not the same as the bands observed from radiation-induced color centers in Al_2O_3[21–23] or those observed for other chemical impurities in sapphire.[18] It may be associated with a Ti-ligand charge transfer transition. The position of this band is consistent with transitions of Ti^{4+} ions after excitation in the same spectral region in other host crystals.[24] It is difficult to understand the presence of Ti^{4+} in Al_2O_3 crystals except as TiO_2 precipitates, as discussed above. However, recent work on the phase diagrams for this crystal system indicates that there may be a limited range of solubility of the mixed valence compound Ti_4O_7 in Al_2O_3.[25] If this proves to be true, the UV transitions of this filled shell ion might explain some of the optical features reported here. Also, it is known that iron impurities in sapphire give rise to many different optical bands depending on their local interaction with other ions.[26] This needs to be investigated further to help identify some of the weaker bands observed in the optical spectra of $Al_2O_3:Ti^{3+}$.

The position of the absorption band reached with the two-photon excitation used here is too far into the UV to be effective in excited state absorption of laser emission. However, the demonstration of the existence of high-energy absorption and emission bands in this system shows that using single d electron ions does not eliminate the possibility of excited state absorption in laser materials. It also shows that multiphoton absorption can be an important loss mechanism for laser-pumped $Al_2O_3:Ti^{3+}$ lasers.

ACKNOWLEDGMENTS

[1]P. F. Moulton, Opt. News 8, 9 (1982); Laser Focus 19, 83 (1983).
[2]P. F. Moulton, in Tunable Solid State Lasers, edited by P. Hammerling, A. B. Budgor, and A. Pinto (Springer, New York, 1985), p. 4.
[3]L. Esterowitz, R. Allen, and C. P. Khattak, in Tunable Solid State Lasers, edited by P. Hammerling, A. B. Budgor, and A. Pinto (Springer, New York, 1985), p. 73.
[4]J. Czochrlaski, Z. Phys. Chem. 8, 219 (1918).
[5]D. Viechnicki and F. Schmid, J. Cryst. Growth 26, 162 (1974).
[6]F. Strober, Z. Kristallog., Kristallgeom., Kristallphys., Kristallchem. 61, 299 (1925).
[7]J. L. Caslavsky, "The Growth of Large Diameter Single Crystals by Vertical Solidification of the Melt," Army Report AMMRC TR 84-34 (1984);

Proc. Fifth International Summer School on Crystal Growth and Material Research, edited by E. Kaldis (North-Holland, Amsterdam, 1984), Chap. 10.

[8]J. L. Caslavsky, C. P. Gazzara, and R. M. Middleton, Philos. Mag. 25, 35 (1972).

[9]J. L. Caslavsky and C. P. Gazzara, Philos. Mag. 26, 961 (1972).

[10]D. S. McClure, J. Chem. Phys. 36, 2757 (1962).

[11]B. F. Gachter and J. A. Koningstein, J. Chem. Phys. 60, 2003 (1974).

[12]E. D. Nelson, J. Y. Wong, and A. L. Schawlow, in Optical Properties of Ions in Crystals, edited by H. M. Crosswhite and H. W. Moos (Wiley-Interscience, New York, 1967), p. 375.

[13]R. M. Macfarlane, J. Y. Wong, and M. D. Sturge, Phys. Rev. 166, 250 (1968).

[14]R. R. Joyce and P. L. Richards, Phys. Rev. 179, 375 (1969).

[15]L. S. Kornienko and A. M. Prokhorov, JETP Lett. 38, 1189 (1960).

[16]G. F. Albrecht, J. M. Eggleston, and J. J. Ewing, in Tunable Solid State Lasers, edited by P. Hammerling, A. B. Budgor, and A. Pinto (Springer, New York, 1985), p. 68; Opt. Commun. 52, 401 (1985).

[17]K. Nassau, Am. Mineral. J. 63, 219 (1978).

[18]H. H. Tippins, Phys. Rev. B 1, 126 (1970).

[19]G. E. Venikouas, G. J. Quarles, J. P. King, and R. C. Powell, Phys. Rev. B 30, 2401 (1984).

[20]L. Esterowitz (unpublished).

[21]K. H. Lee and J. H. Crawford, Jr., Phys. Rev. B 15, 4065 (1977).

[22]B. D. Evans and M. Stapelbroek, Phys. Rev. B 16, 7089 (1978).

[23]J. D. Brewer, B. T. Jeffries, and G. P. Summers, Phys. Rev. B 22, 4900 (1980).

[24]R. C. Powell (unpublished).

[25]J. L. Caslavsky, G. Bryant, and R. Allen (unpublished).

[26]J. Ferguson and P. E. Fielding, Chem. Phys. Lett. 10, 262 (1971).

Thermal effects on the optical spectra of Al$_2$O$_3$:Ti^{3+}

Richard C. Powell, George E. Venikouas,[a] Lin Xi, and Jacek K. Tyminski[b]
Department of Physics, Oklahoma State University, Stillwater, Oklahoma 74078

Milan R. Kokta
Union Carbide Corporation, Washougal, Washington 98671

The results of an investigation of thermal effects on the fluorescence spectra of Ti^{3+} in sapphire are presented. As-grown samples synthesized by the Czochralski method were found to exhibit a fluorescence band characteristic of Ti^{4+}. After thermal annealing this band was greatly reduced and the Ti^{3+} fluorescence was seen. The fluorescence lifetime was found to be constant between 10 and 300 K and then to decrease significantly as temperature was raised to 500 K. This decrease is shown to be associated with thermal activation to the higher Jahn–Teller component of the excited state. The temperature dependences of the intensities, widths and lifetimes of the two zero-phonon lines were monitored between 10 and 80 K. The lifetimes remained constant as the widths broadened and intensities decreased with temperature. The intensity change is associated with the increased rate of vibronic emission while the line broadening is attributed to the phonon processes coupling spin-orbit components of the ground state and to Raman scattering of phonons.

I. INTRODUCTION

System requirements for tunable solid state lasers have generated an interest in materials exhibiting broad, vibronic emission bands. Al$_2$O$_3$:Ti^{3+} has been shown to be a promising laser material for this type of application.[1–3] Although the basic optical spectroscopy properties for Ti^{3+} in Al$_2$O$_3$ crystals have been reported previously,[4–10] many of the details of the spectra have not been characterized. We report here results of an investigation of the temperature dependences of the widths and intensities of the zero-phonon lines and of the lifetime of the fluorescence emission. The results are interpreted in terms of the various electron–phonon processes occurring in the material. In addition, changes in the fluorescence spectra due to thermal annealing are presented and discussed in terms of valence state changes of the Ti ion.

The samples used in this work were grown by the Czochralski technique and contained a titanium concentration of about 0.07 wt. %. These were mounted either in a cryogenic refrigerator for measurements down to 10 K or in a sample holder with a cartridge heater for measurements up to 500 K. The low temperature properties of the zero-phonon lines were studied using the 10 ns, 0.02 nm wide excitation pulses from a nitrogen laser-pumped tunable dye laser with Rhodamine-6G dye. A 1 m monochromator, RCA C31034, and EGG–PAR boxcar integrator were used to analyze the fluorescence. The high temperature lifetime quenching measurements were made using the train of 17 ps pulses from a Spectra Physics synchronously mode locked, cavity dumped, argon laser-dye laser combination with Rhodamine-6G dye for excitation. A 0.25-m monochromator, Hamamatsu PM435 photomultiplier tube, and single photon coincident counting techniques were used for data analysis. For UV excitation studies the 266 nm, 30 ps pulses of a quadrupled Nd–YAG laser were used. A 0.25-m monochromator with either an EGG–PAR silicon diode array detector in conjunction with an optical multichannel analyzer or a RCA C31034 photomultiplier tube in conjunction with an EGG–PAR boxcar integrator were used to record spectra or fluorescence lifetimes, respectively.

II. EFFECTS OF THERMAL ANNEALING

The fluorescence spectra at 300 K after 266 nm excitation is shown in Fig. 1 for an as-grown sample and a sample annealed for 24 h at 1800 °C. The spectrum of the as-grown sample is a broad band peaking near 420 nm with a fluorescence lifetime of 23 μs and a rise time of about 8 μ. The spectrum of the sample after annealing is dominated by a broad band peaking near 720 nm with a lifetime of 3 μs. It has a 20 μs rise time for UV excitation and a negligible rise time for excitation in the 500 nm region.

The fluorescence properties of the annealed sample are characteristic of Ti^{3+} while those of the as-grown sample
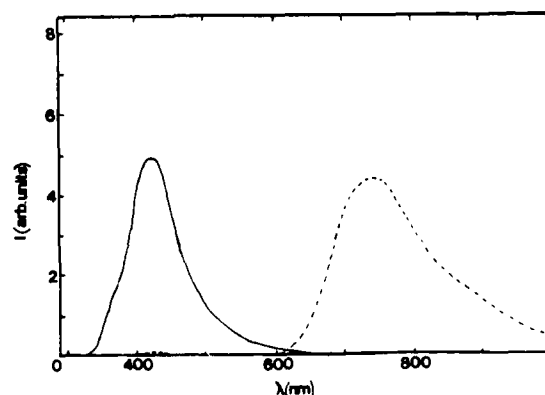

FIG. 1. Fluorescence spectra of Al$_2$O$_3$:Ti at 300 K with 266 nm excitation. Solid line for as-grown crystal and broken line for thermally annealed crystal.

[a] Present address: Union Carbide Corp., 750 S. 32 St., Washougel, WA 98671.
[b] Present address: Physics Dept., Center for Applied Quantum Electronics, North Texas State University, Denton, TX 76203.

can be attributed to Ti^{4+}. Thus it appears that during the normal Czochralski crystal growth process for Ti-doped sapphire, a significant amount of the titanium is incorporated in the lattice in the four-valent state and that the thermal annealing process tends to convert the doping ions to the trivalent state. The Ti^{3+} ions substitute for the Al^{3+} ions in Al_2O_3 but it is not clear where the Ti^{4+} are situated in the lattice or the mechanism of charge compensation.

III. TEMPERATURE DEPENDENCE OF THE FLUORESCENCE LIFETIME

Figure 2 shows the results of measurements of the fluorescence lifetime between 10 and 500 K. The observed time evolution of the fluorescence had a negligible rise and a single exponential decay over four decades at all temperatures. In addition, the lifetime was found to be the same at all wavelengths of fluorescence emission throughout the broad band and the zero-phonon lines observed at low temperatures.

The solid line in Fig. 2 represents the best fit to the data using an equation of the form

$$\tau^{-1} = \tau_r^{-1} + \beta \left[\exp(\Delta E / k_B T) - 1 \right]^{-1}, \qquad (1)$$

where τ_r represents the radiative decay rate of the level and second term describes radiationless quenching due to phonon absorption to a higher level. β is the rate constant for the radiationless transition and ΔE is the potential barrier for the process. The parameters used to obtain the fit shown in the figure are a radiative lifetime of $3 \mu s$, a radiationless quenching rate constant of $2.62 \times 10^6 \mu s^{-1}$, and a potential barrier of $4000 cm^{-1}$.

The optical activity of Ti^{3+} is associated with its single $3d$ electron. This gives a free ion ^2D term which splits in an octahedral crystal field into a $^2T_{2g}$ ground state and a ^2E_g excited state. In Al_2O_3 there is a trigonal distortion of the crystal field at the Al^{3+} site which does not split the ^2E level but does split the $^2T_2$ level into a lower ^2E and an upper $^2A_1$ level. Spin-orbit interaction further splits the ground state

into two sets of Kramers' degenerate pairs, the lower state designated as $E_{3/2}$ and the upper as $E_{1/2}$. The $^2A_1$ level becomes an $E_{1/2}$ Kramers' doublet with spin-orbit interaction. The excited state splitting is dominated by Jahn–Teller distortion instead of spin-orbit interaction. The observed fluorescence band is due to vibronic emission between the lowest Jahn–Teller component and the split components of the ground state manifold. As temperature is raised, thermal activation to the upper Jahn–Teller component of the excited state will become possible. If this is the process responsible for the observed shortening of the fluorescence lifetime, the activation energy for the transition is $4000 cm^{-1}$. Because of the Stokes shift occurring after excitation, it is difficult to determine exactly the energy from the bottom of the potential well for the lower Jahn–Teller component to the crossover point to the upper component. The absorption spectrum of Al_2O_3:Ti^{3+} consists of a broad band with two peaks near 488 and 556 nm.[10] These are due to transitions from the ground state to the two components of the excited state and these peak positions have been used to estimate an activation energy of $3000 cm^{-1}$ from the bottom of the lower potential well to the crossover point.[6] Considering the rough estimates involved in this method of determining ΔE, the thermal quenching of the lifetime appears to be consistent with this type of phonon absorption process.

IV. TEMPERATURE EFFECTS ON THE ZERO-PHONON LINES

The fluorescence emission at 10 K after pulsed dye laser excitation at 550 nm is shown in Fig. 3. The two sharp lines are labeled R_1 and R_2. These have the same $3 \mu s$ lifetime as measured for the broad emission band and are attributed to the zero-phonon transitions from the lower Jahn–Teller component of the excited state to the two spin-orbit split components of the ground state. The energy difference of these two lines is about $38 cm^{-1}$ which is consistent with the ground state splitting as measured by infrared absorption.[7]

As temperature is raised, the widths of the zero-phonon lines increase while their intensities decrease and their lifetimes remain constant. The R lines can not be observed above about 80 K because of the dominant vibronic emis-
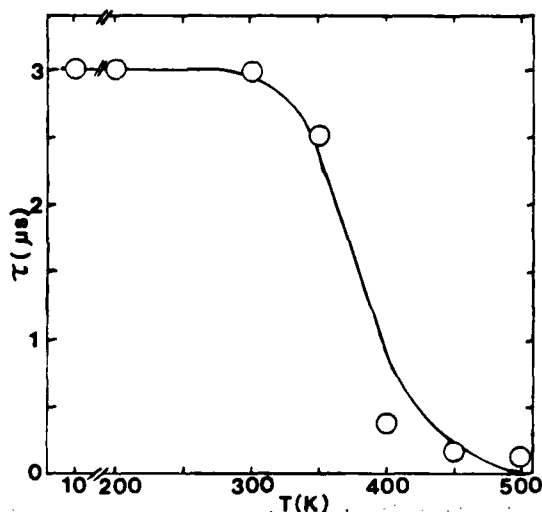
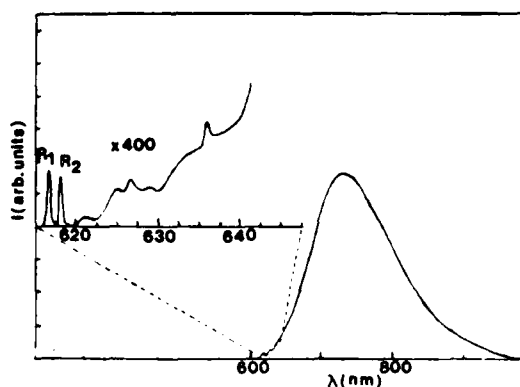FIG. 2. Temperature dependence of the fluorescence lifetime of Al_2O_3:Ti with 550 nm excitation. See the text for explanation of the theoretical line.

FIG. 3. Fluorescence spectrum of Al_2O_3:Ti at 10 K with 550 nm excitation.

data for the values of the parameters listed in Table I. The activation energy is found to be the same as the splitting of the ground state manifold. This indicates that the dominant broadening mechanism for the R lines in this temperature region is associated with stimulated phonon emission or absorption processes between the $E_{1/2}$ and $E_{3/2}$ levels. The contribution to the width of R_2 due to the spontaneous emission processes of this type has been included in $\Delta\bar{\nu}_0$ as described above. There is no contribution to the linewidth due to phonon processes in the excited state due to the large activation energy to the next higher electronic level as evidenced by the lifetime results.

V. DISCUSSION AND CONCLUSIONS

The results of this investigation can be divided into two separate categories. The first deals with the valence state of titanium in sapphire. Previous investigations of samples grown by the vertical solidification of the melt method also showed problems with titanium going into the 4 + state.[10] The annealing procedure described here appears to be effective in decreasing the concentration of isolated Ti^{4+} ions in the lattice and maximizing the concentration of titanium in the 3 + state. This is crucial to optimizing Al$_2$O$_3$:Ti^{3+} as a laser material.

The second category includes the results associated with the temperture dependence of the fluorescence spectrum 'of Ti^{3+} in Al$_2$O$_3$. The lifetime data show that the fluorescence is quenched at high tempertures due to thermally populating the upper Jahn–Teller component of the excited state. At low temperatures the zero-phonon lines associated with transitions from the lower Jahn–Teller component of the excited state to the lowest two spin-orbit components of the ground state decrease in intensity as temperature is in-creased due to enhanced vibronic emission processes. The homogeneous widths of these lines increase with temperature due to direct phonon processes coupling the two components of the ground state and to Raman scattering of phonons which can broaden both the excited level and ground state levels of the transition. A complete understanding of the electron–phonon interaction processes is important in the development of this material as a vibronic laser.

ACKNOWLEDGMENT

[1] P. F. Moulton, Opt. News **8**, 9 (1982); Laser Focus **19**, 83 (1984); in *Tunable Solid State Lasers*, edited by P. Hammerling, A. B. Budgor, and A. Pinto (Springer, New York, 1985), p. 4.

[2] L. Esterowitz, R. Allen, and C. P. Khattak, in *Tunable Solid State Lasers*, edited by P. Hammerling, A. B. Budgor, and A. Pinto (Springer, New York, 1985), p. 73; P. Lacovara, L. Esterowitz, and R. Allen, Opt. Lett. **10**, 273 (1985).

[3] G. F. Albrecht, J. M. Eggleston, and J. J. Ewing, in *Tunable Solid State Lasers*, edited by P. Hammerling, A. B. Budgor, and A. Pinto (Springer, New York, 1985), p. 68; Opt. Commun. **52**, 401 (1985).

[4] D. S. McClure, J. Chem. Phys. **36**, 2757 (1962).

[5] H. H. Tippins, Phys. Rev. B **1**, 126 (1970).

[6] B. F. Gachter and J. A. Koningstein, J. Chem. Phys. **60**, 2003 (1974).

[7] E. D. Nelson, J. Y. Wong, and A. L. Schawlow, in *Optical Properties of Ions in Crystals*, edited by H. M. Crosswhite and H. W. Moos (Wiley–Interscience, New York, 1967), p. 375.

[8] R. M. Macfarlane, J. Y. Wong, and M. D. Sturge, Phys. Rev. **166**, 250 (1968).

[9] R. R. Joyce and P. L. Richards, Phys. Rev. **179**, 375 (1969).

[10] R. C. Powell, J. L. Caslavsky, Z. AlShaieb, and J. M. Bowen, J. Appl. Phys. **58**, 2331 (1985); R. C. Powell, in *Tunable Solid State Lasers*, edited by P. Hammerling, A. B. Budgor, and A. Pinto (Springer, New York, 1985), p. 60.

[11] D. Hsu and J. L. Skinner, J. Chem. Phys. **81**, 1604 (1984).

Spectroscopic properties of alexandrite crystals

Richard C. Powell, Lin Xi, Xu Gang, and Gregory J. Quarles

Department of Physics, Oklahoma State University, Stillwater, Oklahoma 74078

John ·C. Walling

Allied Corporation, Mount Bethel, New Jersey 07060

(Received 11 March 1985)

Details of the optical-spectroscopic properties of alexandrite ($BeAl_2O_4$:Cr^{3+}) crystals were studied by different laser-spectroscopy techniques. The temperature dependences of the fluorescence lifetimes and widths of the zero-phonon lines were found to be quite different for Cr^{3+} ions in the mirror and inversion crystal-field sites. The results indicate that direct phonon-absorption processes dominate both thermal line broadening and lifetime quenching for ions in the mirror sites while phonon-scattering processes dominate the line broadening of inversion-site ions and leave their lifetime independent of temperature. Tunable-dye-laser site-selection methods were used to obtain the excitation spectra of the Cr^{3+} ions in inversion sites at low temperature and to identify six types of exchange-coupled pairs of Cr^{3+} ions in the lattice. Time-resolved site-selection spectroscopy was used to monitor the energy transfer between Cr^{3+} ions in mirror and inversion sites at both low and high temperature. Finally, high-power, picosecond pulse excitation was used to produce two-photon absorption, and the resulting emission spectrum was found to exhibit a new fluorescence band in the 400-nm spectral region.

I. INTRODUCTION

Alexandrite ($BeAl_2O_4$:Cr^{3+}) has become technologically important as a tunable solid-state laser material.[1-5] However, the properties of the optical spectra of alexandrite crystals have not been studied in great detail as they have for other important laser materials such as ruby (Al_2O_3:Cr^{3+}). The characteristics of the optical spectra provide important information for understanding the fundamental interactions between the optically active ions and the host lattice, and the interactions between two optically active ions. These interactions affect the optical pumping and decay dynamics relevant to the laser operation of the material. We report here the results of a series of different types of laser-spectroscopy measurements on alexandrite which provide new information concerning the crystal-field energy levels, ion-ion interaction, and electron-phonon interaction properties of this material.

The sample used for this investigation was an oriented, single-crystal cube of alexandrite with each edge measuring about 5 mm in length, containing 0.0897 at. % Cr^{3+} ions. The host crystal has the chrysoberyl, hexagonal-close-packed structure shown in Fig. 1.[6] The space group is orthorhombic *Pnma* with four molecules per unit cell and lattice parameters $a = 9.404$ Å, $b = 5.476$ Å, and $c = 4.427$ Å. The Al^{3+} ions are octahedrally coordinated by the oxygen ions and occur in two inequivalent crystal-field sites in this lattice. The Al^{3+} sites lying in the mirror-symmetry planes of the lattice have the site symmetry of the C_s point group, while the other Al^{3+} sites possess inversion symmetry and belong to the C_i point group. The Cr^{3+} ions enter the crystal substitutionally for the Al^{3+} ions, 78% replacing Al^{3+} ions in the mirror

sites and the rest going into the inversion sites.[7,8]

The energy-level diagram for Cr^{3+} ions in the mirror sites is shown in Fig. 2. The six oxygen ligands produce a crystal field which can be described as having O_h point-
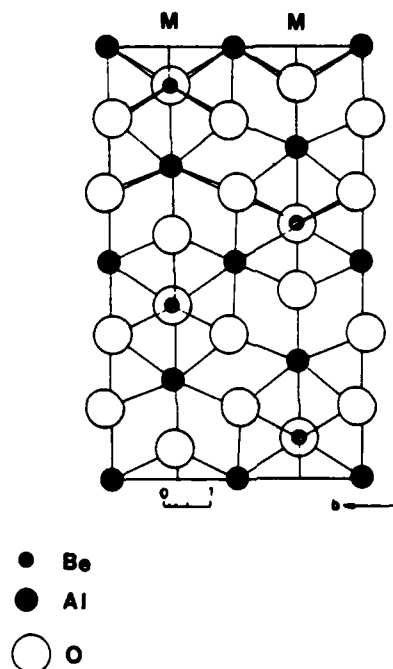
● Be

● Al

○ O

FIG. 1. *c*-axis view of chrysoberyl structure (from Ref. 6). *M* denotes mirror planes.

group symmetry slightly distorted to C_s. The O_h crystal field splits the free-ion wave functions of the $3d^3$-electron configuration of the Cr^{3+} ion into crystal-field wave functions having t^3- or t^2e-electron configurations, and either quartet or doublet multiplicities depending on the spin alignments of the electrons. The distortion to C_s symmetry causes a splitting of all of the orbitally degenerate T and E levels but not the orbital singlet A levels. Note that in performing the reduction from O_h to C_s symmetry it is important to take the diagonal mirror plane of the cube as the mirror element in the C_s group. The spin-orbit interaction of the electrons causes further splitting, leaving all levels designated as S_1, S_3 Kramers degenerate doublets.

Figure 2 also shows the electric-dipole-allowed absorption transitions. Since all transitions within states of the $3d^3$-electronic configuration are parity forbidden, crystal-field admixing with odd-parity configurations is required for any electric dipole transitions to be observed. These group-theoretical considerations are useful in understanding the qualitative features of the optical spectra, such as the number of lines and their relative intensities for different polarizations. A similar analysis of the ions in the inversion sites with C_i symmetry gives all A_g levels with no specific selection rules.

II. ABSORPTION, FLUORESCENCE, AND EXCITATION SPECTRA

Figure 3 shows the absorption spectra at room temperature. The absorption features consist of two broadbands centered at about 420 and 580 nm, three sets of sharp lines centered near 680, 650, and 470 nm, and the band edge appearing below 300 nm (not shown in the figure). The two bands are associated with transitions from the $^4A_{2g}$ ground state to the $^4T_{2g}$ and $^4T_{1g}$ excited states. These transitions involve changes in the crystal-field orbitals of the electrons and thus are highly sensitive to the crystal-field environment of the ion. Vibrational modulation of the field strength produces the broadbands. The 400-nm band peaks at higher energy and the 580-nm band peaks at lower energy for the $E||b$ polarization compared to the peak positions for the $E||a,c$ polarization directions. This is consistent with the selection rules and the level-splitting assignments for C_s symmetry shown in Fig. 2.

The three sets of sharp lines are associated with transitions from the ground state to the split components of the ^2E_g (R lines), $^2T_{1g}$ (S lines), and $^2T_{2g}$ (B lines) levels. These involve spin flips of the electron wave functions without changes in crystal-field states. Thus they are insensitive to vibrational modulation of the crystal field and therefore appear as sharp lines. The lines seen in Fig. 3 are associated with mirror-site ions. With the relatively low resolution of the spectra shown in the figure, it is difficult to ascertain the changes in intensity with different polarization for specific lines within a group. Results of this type for the R lines have been reported previously in Ref. 1 and are shown in the inset in Fig. 3. They show that the intensity of the transition to the lower component of the split ^2E_g level (R_{1m}) is significantly greater than the intensity of the transition to the upper component (R_{2m}) for $E||b$ polarization, and these relative intensities are reversed for the other two polarization directions. These results are consistent with the polarization selection rules shown for the R lines in Fig. 2.

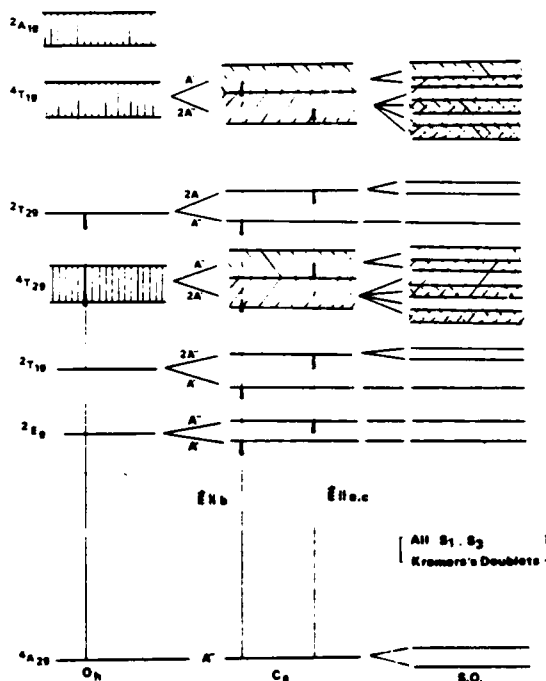The lines associated with the inversion-site ions are very

FIG. 2. Energy-level diagram for Cr^{3+} ions in mirror sites in alexandrite. Arrows show absorption transitions allowed by orbital-symmetry selection rules. All transitions between levels of the same parity require crystal-field admixture of levels of opposite parity, and all transitions between levels of different spin multiplicity require spin-orbit interaction to occur.
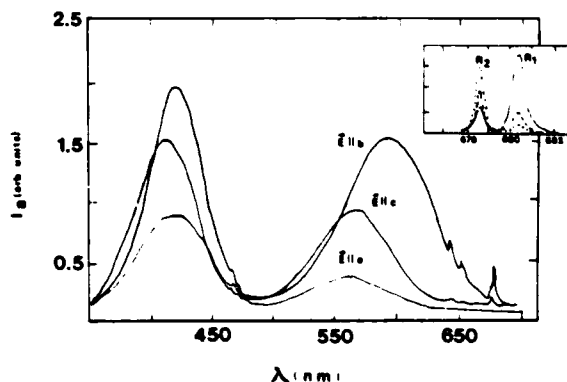

FIG. 3. Absorption spectra of alexandrite at room temperature. Inset shows R_m lines from Ref. 1. Solid line for $E||b$; dotted line for $E||c$ with sensitivity $\times 4$; dashed line for $E||a$ with sensitivity $\times 40$.

weak and difficult to observe in the absorption spectra and the broad absorption bands are hard to resolve from those associated with mirror-site ions. Some of the properties of transitions of ions in inversion sites obtained from other types of spectral measurements are discussed below. Polarization changes have been used to identify these as magnetic dipole transitions.[1]

The fluorescence emission at room temperature is shown in Fig. 4 for three excitation wavelengths. The major features of the spectra are the two sharp lines R_{1m} and R_{2m} and the broad, structured band peaking at lower energies. The latter is due the superposition of low-energy vibronic emission transitions from the components of the ^2E_g level and emission from the relaxed excited state of the $^4T_{2g}$ level which is Stokes-shifted to lower energy compared to the absorption transition involving this level. The structure in this sideband is a mixture of specific one-phonon vibronic peaks, and zero-phonon lines associated with transitions from the $^4T_{2g}$ and $^2T_{1g}$ levels. Tentative assignments have been made for the S_m lines,[1] but the other peaks have not been identified since no complete analysis of vibronic transitions has been done for Cr^{3+} ions in $BeAl_2O_4$ crystals. For certain excitation wavelengths, the R_{1i} and R_{2i} lines associated with Cr^{3+} ions in inversion sites can also be seen.

The spectra shown in Fig. 4 represent the $E||b$ polarization direction. For the other two polarization directions the broad emission band is significantly smaller in intensity relative to the R_m lines.[1] This is consistent with the absorption-band positions shown in Fig. 3 and with the crystal-field splittings and selection rules shown in Fig. 2 for the transitions involving the $^4T_{2g}$ level. The $E||b$ polarization involves allowed vibronic emission from the lowest crystal-field component of the split $^4T_{2g}$ level, which will have the greatest degree of occupancy in thermal equilibrium. The other two polarization directions have forbidden transitions from this component and allowed transitions from the higher component, which has a lower degree of occupancy. The observed fluorescence intensity will depend both on the selection rules and the degree of occupancy of the initial level of the transition.

FIG. 5. Excitation spectrum of R_{1i} line of alexandrite at room temperature.

The excitation spectra of the R_{1m} and R_{1i} lines are shown in Figs. 5 and 6. The spectrum for the mirror-site emission at room temperature is essentially the same as the absorption spectrum shown in Fig. 3. The two excitation bands for the inversion-site ions are seen in Fig. 5 to peak near 480 and 380 nm. The expanded spectral region shown in Fig. 6 at room temperature shows very different excitation characteristics for the ions in the two types of sites. This indicates that energy transfer between ions in the two nonequivalent types of sites is very weak for the
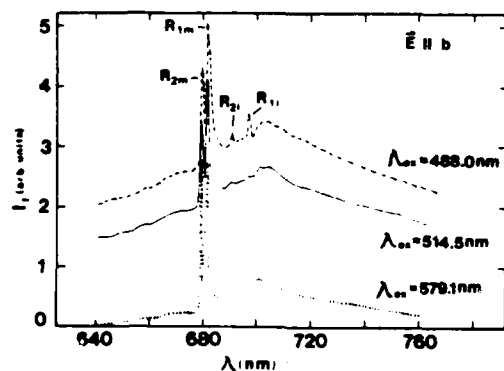

FIG. 4. Fluorescence spectra of alexandrite at room temperature.

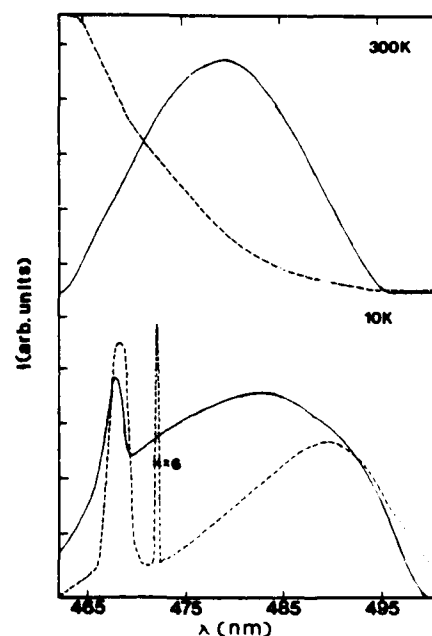FIG. 6. Excitation spectra of the R_1 lines of alexandrite in the spectral region between the major absorption bands at 300 and 10 K. The solid line is for the R_{1i} line and the dashed line is for the R_{1m} line.

chromium concentration level in this sample. The spectral features shown for these conditions are similar to those reported recently by Schepler.[9] The spectral features in this region change substantially as temperature is lowered to 10 K. A set of sharp lines appears which can be associated with the B_m lines and attributed to transitions terminating on the split components of the $^2T_{2g}$ level of ions in mirror sites. Also, ions in both mirror and inversion sites exhibit a similar excitation band in this spectral region. Since this is known from room-temperature results to be the region of inversion-site absorption, the results indicate the presence of energy transfer from ions in inversion sites to ions in mirror sites. This is discussed further in Sec. IV.

The final experiment on the absorption and fluorescence spectra of BeAl$_2$O$_4$:Cr^{3+} involved monitoring the fluorescence emission occurring after two-photon—absorption excitation. A 30-ps pulse from a frequency-doubled Nd-YAG laser (YAG denotes yttrium-aluminum-garnet) at 532 nm polarized parallel to the b direction was used for excitation. This has weak single-photon absorption by mirror-site ions in the visible spectral region and strong two-photon absorption in the uv region terminating on a shoulder of the band edge as seen in Fig. 7. The fluorescence observed after this type of excitation occurs in two regions: the normal emission in the 700-nm region as shown in Fig. 4 and a new emission band in the 400-nm region as shown in Fig. 7. This new, broad, structured emission band has not been reported previously and may be important in determining the excited-state absorption and dispersion properties of the material.

The broad luminescence band near 400 nm may be due to a $^2A_{1g}$-$^4A_{2g}$ transition. The initial state of this transition is a Stokes-shifted upper level of the $t^2_{2g}e_g$-electron configuration. The reciprocal transition in absorption should be a broadband shifted to higher energies. Howev-

er, it is difficult to observe because it is both spin and symmetry forbidden in O_h symmetry and thus will be a very weak, broadband on the tail of the absorption edge. The absorption-edge shoulder at higher energies is probably due to a charge-transfer transition. The structure observed in the band cannot be explained by crystal-field or spin-orbit splitting and may be due to the effects of radiative reabsorption by the $^4T_{1g}$ band.
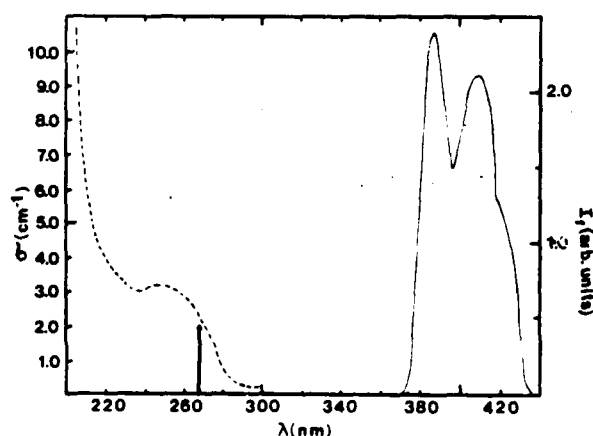
III. SPECTRAL EFFECTS OF ELECTRON-PHONON INTERACTIONS

Lattice vibrations interact with the electronic energy levels and transitions of the Cr^{3+} ions through the modulation of the local crystal field. The results of this interaction manifest themselves in the optical spectral properties through the initiation of vibronic transitions, radiationless transitions, and phonon-scattering mechanisms. The first of these produces the broad spectral bands described in the preceding section. The second leads to a temperature-dependent decrease of the fluorescence lifetime of the R lines and both the second and third can cause a thermal broadening of the R lines. The measurement of these last two effects are discussed in this section.

A. Fluorescence lifetimes

Figure 8 shows the temperature dependences of the fluorescence lifetimes of the R lines for Cr^{3+} ions in both mirror and inversion sites. The lifetime of the emission of the ions in the mirror sites decreases from about 2.3 ms at 10 K to about 290 μs at 300 K. The long lifetime at low

FIG. 7. Fluorescence emission in the 400-nm spectral region of alexandrite after two-photon excitation with a 30-ps pulse at 532 nm at room temperature. The dashed line shows the absorption-band edge ($E \| b$; sample thickness 0.6 cm) with the arrow at 266 nm showing the region excited by the two-photon transition.

FIG. 8. Temperature dependences of the fluorescence decay times of Cr^{3+} ions in mirror and inversion sites in alexandrite. The solid lines represent the best fits to the data using Eq. (1).

temperatures is the intrinsic lifetime of the ^2E_g state for ions in this type of site, while the reduced lifetime at high temperatures is due to thermal excitation to higher-lying levels with shorter intrinsic decay times. This quenching can be modeled by considering two excited levels in thermal equilibrium with intrinsic decay rates τ_E^{-1} and τ_T^{-1}. The common decay rate of the coupled levels is given by

$$\tau^{-1} = \tau_E^{-1} + \tau_T^{-1} \exp(-\Delta E_Q/k_B T) , \qquad (1)$$

where ΔE_Q is the splitting between the two levels and k_B is the Boltzmann constant. The solid line in Fig. 8 is the best fit to the data treating ΔE_Q and τ_T as ad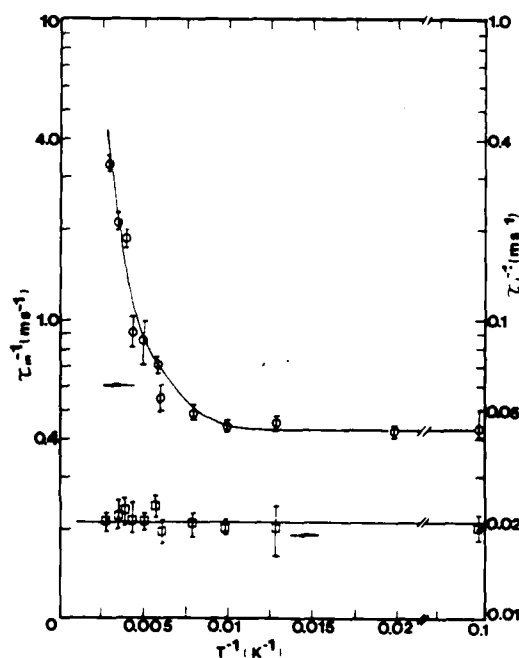justable parameters. The results give the energy-level splitting as 800 cm^{-1} and the lifetime of the upper level as 7.1 μs.

The inversion-site emission has a lifetime of about 48 ms and shows no change with temperature. The long lifetime is consistent with the forbidden nature of these transitions, and the lack of temperature dependence is consistent with the spectral observation that the upper energy levels are shifted to higher energy compared to the mirror sites, thus minimizing quenching of the ^2E_g levels through thermal-excitation processes to these higher levels.

The fluorescence lifetime of the broadband emission from Cr^{3+} ions in the mirror sites is the same after two-photon excitation, but the rise time of the fluorescence is measured to be about 20 μs. The broadband emission around 400 nm has a decay time of about 8 μs with a negligible rise time. The measured fluorescence lifetime of the 400-nm band is significantly shorter than expected for a spin-forbidden radiative transition which may indicate quenching due to radiationless relaxation. This is consistent with the observed rise time of the 700-nm emission after two-photon excitation, which implies the presence of an indirect pumping process of the normal fluorescence transitions. If this is due to relaxation from the 400-nm level, the rise time should be given by

$$t_r = (\tau_E^{-1} - \tau_{400\,\text{nm}}^{-1})^{-1}$$
$$\times \ln\{(\tau_{400\,\text{nm}}/\tau_E)$$
$$\times [1 - (\tau_E^{-1} - \tau_{400\,\text{nm}}^{-1})\tau_{nr}N_E/N_{400\,\text{nm}}]\} . \qquad (2)$$

Here, τ_{nr} is the nonradiative decay time of the upper level, while N_E and $N_{400\,\text{nm}}$ are the initial populations of the upper and lower level, respectively. Use of the measured fluorescence lifetimes with no direct pumping of the ^2E level results in a predicted value of 30 μs for t_r. The slightly shorter observed value can be attributed to the presence of some pumping of the ^2E_g level through one-photon—absorption processes to the $^4T_{2g}$ band. Setting $\tau_{nr}N_E/N_{400\,\text{nm}} = 17.94$ μs in Eq. (2) gives the observed result.

B. Linewidths

Electron-phonon processes also cause a temperature dependence of the widths of spectral lines. The width of a zero-phonon transition can have contributions from variations in the local static crystal field, direct phonon transitions, and Raman scattering of phonons. The first of these results in a temperature-independent Gaussian contribution to the linewidth due to inhomogeneous broadening. The second is a lifetime-broadening process which produces a temperature-dependent Lorentzian line shape. The third mechanism also gives a temperature-dependent Lorentzian contribution to the linewidth.

The temperature dependences of the full widths at half maximum of the R_1 lines from Cr^{3+} ions in mirror and inversion sites are shown in Fig. 9. Both lines approach a constant value at low temperature and broaden rapidly at high temperature. This is similar to the thermal broadening of the R lines in ruby.[10,11] The low-temperature linewidth is the inhomogeneous contribution due to local strains, while the temperature variation can be interpreted as being due to phonon-scattering processes and direct phonon transitions. In the Debye approximation the expression for line broadening due to Raman scattering of phonons is[12]

$$\Delta \nu = (\omega_D/4\pi^2) \int_0^1 dx \, \ln\{1 + 9\pi^2 W^2 x^6 \exp(xT_D/T)[\exp(xT_D/T-1)]^{-2}[g^2(x) + (9\pi^2/4)W^2 x^6]^{-1}\} , \qquad (3)$$

where

$$g(x) = 1 + W\{1 + 3x^2 + 1.5x^3 \ln[(1-x)/(1+x)]\} . \qquad (4)$$

The Debye temperature and frequency are given by T_D and ω_D, respectively, while W is the quadratic electron-phonon coupling constant. Using either velocity-of-sound measurements[3] or specific-heat data,[13] the Debye temperature for $BeAl_2O_4$ can be estimated and is found to be approximately 500 K.

The linewidth contribution due to a direct-phonon-absorption process is given by

$$\Delta \nu = \sum_i \beta_i \{\exp[(\Delta E_i/k_B T) - 1]\}^{-1} , \qquad (5)$$

where ΔE_i is the energy-level splitting spanned by the

phonon process and β_i is the coupling constant. The total broadening due to this type of process is the sum over all possible phonon transitions.

Attempts were made to use Eqs. (3) and (5) to fit the measured temperature-dependent widths of the R_1 lines after subtracting the low-temperature residual linewidths. For R_{1i} a good fit was obtained using Eq. (3) with values for W of either 0.79 or -0.2. This is shown as a solid line in Fig. 9. The perturbation-theory approach used in Ref. 10 gives an equally good fit to the data, but the value of the coupling coefficient does not justify use of the weak-coupling limit.

A good fit to the inversion-site data after subtracting the inhomogeneous contribution to the linewidth can also be obtained using Eq. (5) and treating β and ΔE as adjustable parameters. This is shown by a dotted line in the fig-
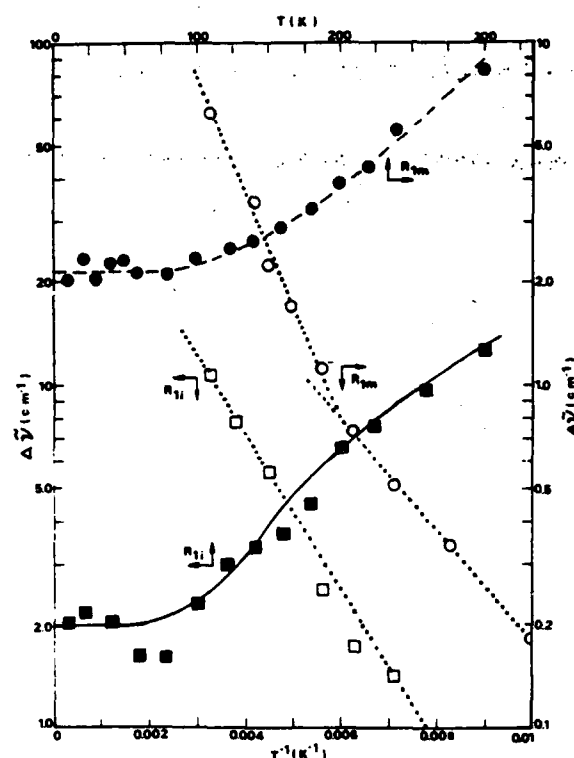
FIG. 9. *Temperature dependences of the full widths at half maximum of the R_1 lines in alexandrite. Circles are for R_{1m} and squares are for R_{1i} lines; solid symbols are measured data and open symbols represent the linewidths after subtraction of the temperature-independent inhomogeneous contributions. The solid line represents theoretical fit to the data using Eq. (3), while the dotted lines represent the best fits using Eq. (5). The parameters giving these fits are listed in Table I. The dashed line shows the general trend in the data and does not represent a theoretical fit.*

IV. ION-ION INTERACTION

The Cr^{3+} ions in the lattice can interact with each other through various electric or magnetic multipole interactions or through exchange. The mechanism for the interaction depends on the spacing and geometric arrangement of the ion pairs. Weak interaction can be treated as energy transfer between two isolated Cr^{3+} ions, whereas strong interaction produces coupled pairs with energy levels and transitions much different than those of isolated ions. In materials such as ruby it has been found that both types of interactions are present,[14-16] and we have observed both types of interactions in alexandrite crystals, as described below.

A. Energy transfer between Cr^{3+} ions

Site-selection time-resolved spectroscopy methods were used to investigate the transfer of energy from Cr^{3+} ions in mirror sites to Cr^{3+} ions in inversion sites. A 10-ns dye-laser pulse tuned to near 475 nm was used to selectively excite a nonequilibrium distribution of the ions in the two types of sites, and the time evolution of the fluorescence spectrum was monitored using a 1-m monochromator, an RCA C31034 photomultiplier tube, and an EGG-PAR boxcar integrator. Figure 10 shows the variation of the ratios of the integrated fluorescence intensities of the R_1 emission lines of Cr^{3+} ions in inversion and mirror sites as a function of time after the laser-excitation pulse at 10 K and room temperature.

The observed energy-transfer characteristics can be explained by assuming that the dominant transfer takes place from the ions in the higher-energy mirror sites to the ions in the lower-energy inversion sites with no back transfer. The time evolution of the sensitizer fluorescence intensity is described by an expression derived by Inokuti and Hirayama,[17] while the expression for the time evolution of the activator fluorescence intensity has been derived by Huber.[18] Assuming electric-dipole—dipole interaction, the ratio of these expressions has the form

$$I_i(t)/I_m(t) = At^{-1/2}\exp(Bt^{1/2}) , \qquad (6)$$

where

$$B = (4\pi^{3/2}/3)N_i\alpha^{1/2} , \qquad (7)$$

and A is a constant factor involving the radiative decay rates and initial concentrations of the ions in the two types of sites. The energy-transfer parameter can be expressed in terms of the critical interaction distance R_0 as

$$\alpha = R_0^6/\tau_m . \qquad (8)$$

ure with $\beta = 59$ cm^{-1} and $\Delta E = 365$ cm^{-1}. Since this activation energy does not correspond to a known splitting between inversion-site energy levels, it is concluded that the Raman scattering processes dominate the homogeneous line broadening for ions in the inversion sites.

No good fit to the data obtained on the temperature dependence of the linewidth for the R_{1m} line could be found using Eq. (3). After subtracting the inhomogeneous contribution to the linewidth of 2.15 cm^{-1}, the data can be fitted using Eq. (5) with two terms in the sum as shown by the dotted lines in Fig. 9. The first process has a coupling constant of 8 cm^{-1} and an energy splitting of 264 cm^{-1}, while $\beta = 202$ cm^{-1} and $\Delta E = 800$ cm^{-1} for the second process. The latter is consistent with direct phonon absorption to the $^4T_{2g}$ level, while the former may be associated with transitions to the components of the $^2T_{1g}$ levels.

The parameters obtained from these lifetime and linewidth measurements are summarized in Table I.

The dashed and solid lines in Fig. 10 show the best fits to the data found by using Eq. (6) and treating A and B as adjustable parameters. At room temperature a reasonable fit is obtained for an energy-transfer parameter of $\alpha = 6.1 \times 10^{-36}$ cm^{6}sec^{-1}. This implies a critical interaction distance of 35 Å. At low temperature the general shape of the time evolution of the fluorescence intensity ratios can be predicted by Eq. (6), but the data cannot be fitted exactly. The best simultaneous fit to the long-time and short-time parts of the data is shown in the figure.
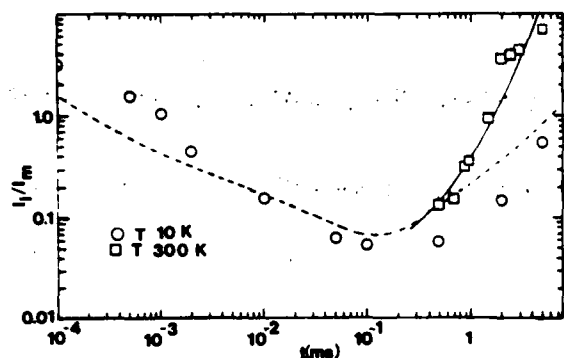
FIG. 10. Evolution of the ratios of the integrated fluorescence intensities of the R_1 lines in mirror and inversion sites as a function of time after the laser-excitation pulse at 300 and 10 K. The solid and dashed lines represent the best fits to the data using Eq. (6) with the parameters listed in Table I.

This was obtained using an energy-transfer parameter of $\alpha = 1.9 \times 10^{-36}$ cm^{6}sec^{-1}, which implies a critical energy-transfer distance of 40 Å. The poor fit to the data indicates that the simple model used for this interpretation is not adequate at low temperatures. The major difficulty is probably associated with the presence of a nonstatistically random distribution of Cr^{3+} ions as discussed in the following part of this section. The energy-transfer parameters obtained from fitting these time-resolved—spectroscopy data are summarized in Table I.

B. Exchange-coupled pairs of Cr^{3+} ions

When the chromium ions are located close enough to each other to interact strongly, they produce satellite lines in the optical spectra called N lines. Figure 11 shows the region of the fluorescence spectrum near the R_m lines for several different excitation wavelengths in this region. The tunable dye laser was used for excitation and an EGG-PAR optical multichannel analyzer (OMA) was used for data acquisition. The observed spectral lines can be attributed to transitions between levels of exchange-coupled pairs of Cr^{3+} ions. This type of pair spectrum has been observed for Cr^{3+} ions in other hosts.[16,19,20]

The interaction Hamiltonian describing the exchange coupling of the chromium ion pairs is

$$H_{ex} = -JS_1 \cdot S_2 , \tag{9}$$

where the coupling constant J is positive for ferromagnetic coupling and negative for antiferromagnetic coupling. The ground-state energy-level splitting due to ferromagnetic exchange coupling for two Cr^{3+} ions with spin $\frac{3}{2}$ is $\Delta E = 0, 1J, 3J, 6J$. For antiferromagnetic coupling of these ions the splitting is $\Delta E = 0, 3J, 5J, 6J$. The spectra in Fig. 11 can be associated with the energy-level diagrams of six different types of pairs shown in Fig. 12. Two are ferromagnetically coupled and four antiferromagnetically coupled. The small discrepancies in some of the observed

TABLE I. Summary of alexandrite spectral parameters.

Lifetime data	
$\tau_{R_m}(10 \text{ K}) = 2.3$ ms	$\tau_{R_m}(300 \text{ K}) = 290$ μs
$\Delta E_Q = 800$ cm^{-1}	$\tau_T = 7.1$ μs
$\tau_{R_i} = 48$ ms (all temperatures)	
$\tau_{400 \text{ nm}}(300 \text{ K}) = 8$ μs	$t_r = 20$ μs

Linewidth data	
Mirror site	Inversion site
$\Delta \nu_0 = 2.15$ cm^{-1}	$\Delta \nu_0 = 2.00$ cm^{-1}
$\beta_1 = 8.0$ cm^{-1}	$T_D = 500$ K
$\Delta E_1 = 264$ cm^{-1}	$W = 0.79$ or -0.2
$\beta_2 = 202$ cm^{-1}	
$\Delta E_2 = 800$ cm^{-1}	

Energy transfer	
$T = 300$ K	$T = 10$ K
$\alpha = 6.08 \times 10^{-36}$ cm^{6}sec^{-1}	$\alpha = 1.90 \times 10^{-36}$ cm^{6}sec^{-1}
$R_0 = 35$ Å	$R_0 = 40$ Å

Exchange-coupled pairs	
$J_1 = 4.3$ cm^{-1}	$J_4 = 4.3$ cm^{-1}
$J_2 = -6.2$ cm^{-1}	$J_5 = -7.3$ cm^{-1}
$J_3 = -6.5$ cm^{-1}	$J_6 = -4.4$ cm^{-1}
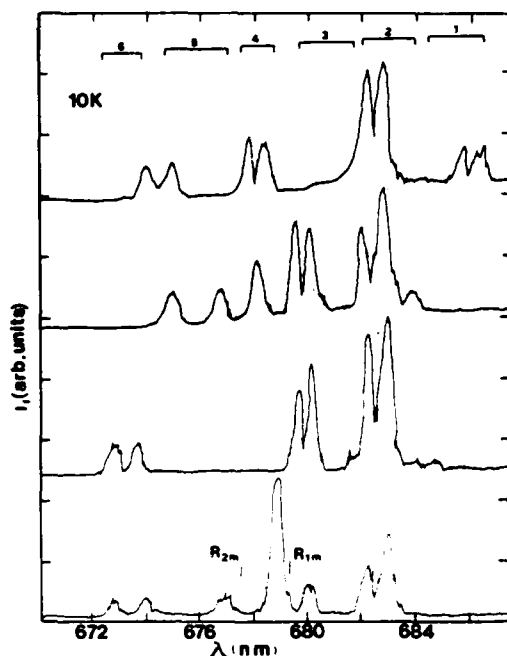
FIG. 11. Fluorescence spectra of N lines in alexandrite at 10 K for four different laser-excitation wavelengths between 670 and 680 nm.

FIG. 13. Excitation spectrum of the pair line at 683 nm in alexandrite at 10 K.

FIG. 12. Energy-level diagrams established for six exchange-coupled pairs of Cr^{3+} ions in alexandrite. The values for the coupling parameter J are listed in Table I.

energy-level values and those predicted by Eq. (9) may be due to effects of "superexchange" or "biquadratic exchange."[16] Table I gives the coupling parameter for each type of pair.

Figure 13 shows the excitation spectrum of the 683-nm pair line as an example of the excited-state splittings. This complex spectrum does not obey any simple splitting progression as seen in the ground-state manifold, and thus no attempt was made to establish excited-state energy-level diagrams for the pairs. The problem may be associated with a breakdown of the ion-ion interaction Hamiltonian given by Eq. (9) when the ions are in the excited state. A Hamiltonian coupling the spins of the individual electrons may be more appropriate in this case.[16]

It is difficult to identify the exact lattice sites involved in these different pairs without extensive investigation using tools such as electron paramagnetic resonance and uniaxial stress.[19] However, the lattice structure of chrysoberyl shown in Fig. 1 provides a variety of different combinations of close-neighbor pair sites involving both mirror and inversion locations.

V. DISCUSSION

The results of the group-theoretical analysis of the energy levels and selection rules for electric dipole transitions for Cr^{3+} ions in the mirror sites in alexandrite crystals presented in Sec. I provide an understanding of the changes in relative intensities and apparent peak positions of the sharp lines and broadbands seen in the absorption and fluorescence spectra for different polarization direc-

tions. The observation of the 400-nm emission band and its excitation through two-photon absorption terminating at 266 nm demonstrates the presence of several higher-lying levels in alexandrite crystals which have also been seen by other types of measurements. For example, the absorption-band edge in Cr^{3+}-doped $BeAl_2O_3$ is shifted toward the visible compared to that of the undoped material. Also, the magnitude of the refractive index change in alexandrite induced by four-wave mixing could be theoretically explained only by assuming the existence of high-oscillator-strength transitions to levels in the ultraviolet spectral region.[21] In addition, excited-state absorption measurements on alexandrite[4,22] show the presence of energy levels in the vicinity of 32000 cm^{-1}, which is between the absorbing and emitting levels associated with two-photon-excited fluorescence. The properties of these near-uv spectral transitions constitute an important area for future investigation.

The temperature-dependent variations in the spectral properties show the importance of electron-phonon interactions in determining the spectral dynamics of alexandrite. Direct-phonon-absorption processes dominate the temperature dependence of the R_{1m} zero-phonon line. The splitting of the ^2E_g and $^4T_{2g}$ energy levels ($\Delta E_Q = 800$ cm^{-1}) is small enough to be connected by direct-phonon-absorption process. This produces a temperature-dependent lifetime quenching and homogeneous line broadening. Similar phonon processes terminating on the $^2T_{1g}$ level contribute to the line broadening but not to the lifetime quenching. Recent results on the pressure dependence of the alexandrite mirror-site spectra have also been interpreted in terms of direct phonon processes to the $^4T_{2g}$ level for both line broadening and lifetime quenching.[23] It is interesting that no contribution to the line broadening due to Raman scattering of phonons is observed for the R_{1m} line.

The R_{1i} zero-phonon linewidth and lifetime are not affected by direct-phonon-absorption processes in the temperature range investigated because of the large excited-state splittings of the energy levels. Consequently, the lifetime is independent of temperature and the thermal line broadening is dominated by the Raman scattering of phonons.

The temperature variations of the homogeneous linewidths of the R_1 lines in alexandrite are similar to those observed for Cr^{3+} ions in ruby.[10,11,24,25] Contributions to the linewidth have been observed both from Raman scattering processes and from direct phonon processes between the excited-state levels.[11,21,22] The inhomogeneous linewidths observed at low temperatures in alexandrite are greater than those observed for ruby with equivalent Cr^{3+} concentrations. This indicates less random crystal-field environments in ruby than in alexandrite crystals.

The Cr^{3+} ions in alexandrite can interact to form exchange-coupled pairs. In this case the Cr^{3+} ions lose their individual identity and produce absorption and emission spectral lines associated with the energy levels of the pairs. The positions of the emission lines establish the splittings of the ground-state energy levels of each type of pair. The observed splitting progressions of the pair man-

ifolds are consistent with the predictions of the direct-exchange expressions given in Eq. (9). The values of J found for these alexandrite pairs are smaller than most of those reported for ruby and $YAlO_3$ hosts.[16,19,20] This may be due to differences in the pair geometries for the different host crystals or in the exact details of the exchange interaction involving contributions from superexchange or biquadratic exchange effects.[16] In studies of Cr^{3+} exchange-coupled pairs in ruby, it was found that the excited-state splittings are better described by an interaction Hamiltonian involving a summation over all individual electron spin-spin interactions instead of the total ion spin-spin interaction given by Eq. (9). This is probably also true for the pairs in alexandrite, but verification of this will require further work.

The presence of strongly coupled ion pairs complicates the interpretation of energy transfer between mirror- and inversion-site ions which are not strongly coupled. The fact that the Cr^{3+} ions in mirror and inversion sites have distinctly different excitation spectra at room temperature but not at low temperature is consistent with the results of time-resolved site-selection spectroscopy measurements which show very different energy-transfer characteristics at the two temperatures. The different excitation spectra explain why it was possible to establish laser-induced Cr^{3+} population gratings separately for the mirror- and inversion-site ions in alexandrite at room temperature.[21] Both excitation-spectra measurements and time-resolved site-selection spectroscopy results show that energy transfer from ions in inversion sites to ions in mirror sites takes place more strongly at low temperatures.

Normal assumptions concerning energy transfer between randomly distributed sensitizer and activator ions are not strictly valid for Cr^{3+} ions in alexandrite crystals because there is a region around each sensitizer within which strong coupling produces pair spectra instead of energy transfer. Thus the values of R_0 obtained from fitting Eq. (6) to time-resolved spectroscopy results should only be considered as effective interaction distances for comparing energy-transfer characteristics at different concentrations, temperatures, etc. The values listed in Table I are significantly larger than predicted from spectral overlap considerations assuming a uniform distribution of Cr^{3+} ions.[26] The apparent increase in energy transfer at low temperature is somewhat surprising since lowering the temperature generally quenches energy transfer instead of enhancing it. For the case of alexandrite it appears that the interaction causing the strong coupling decreases more at low temperature than the value of R_0 for energy transfer. This decreases the size of the strong-coupling sphere surrounding each sensitizer and allows activator ions closer to the excited sensitizer to take part in energy transfer instead of forming coupled pairs. Although this reasoning can account for the observed change in energy transfer with temperature, it is obviously a simplified picture of a very complex situation for ion-ion interaction in alexandrite.

The performance of alexandrite as a tunable solid-state laser material is critically dependent on the spectral dynamics of the Cr^{3+} ions. The two types of spectral information reported here most relevant to laser characteris-

tics concern the near-uv spectral bands and the ion-ion interaction. The former can contribute to degradation of lasing operation through excited-state absorption and nonlinear optical effects. The latter shows the importance of having a uniform distribution of Cr^{3+} ions in the crystal to minimize the presence of exchange-coupled pairs which do not contribute to laser emission. In addition, Cr^{3+} ions in inversion sites do not have the same lasing properties as ions in mirror sites and thus energy transfer from the mirror-site ions to inversion-site ions alters the laser operation. Therefore it is important to minimize the percentage of Cr^{3+} ions in inversion sites, which might be done through co-doping with ions which preferentially occupy these sites.

[1] J. C. Walling, O. G. Peterson, H. P. Jenssen, R. C. Morris, and E. W. O'Dell, IEEE J. Quantum Electron. QE-16, 1302 (1980); J. C. Walling and O. G. Peterson, ibid., 119 (1980).

[2] J. C. Walling, H. P. Jenssen, R. C. Morris, E. W. O'Dell, and O. G. Peterson, Opt. Lett. 4, 182 (1979).

[3] C. F. Cline, R. C. Morris, M. Dutoit, and P. J. Harget, J. Mater. Sci. 14, 941 (1979).

[4] M. L. Shand, J. Appl. Phys. 54, 2602 (1983); M. L. Shand, J. C. Walling, and R. C. Morris ibid. 52, 953 (1981).

[5] B. K. Sevast'Yanov, Yu. I. Remigailo, V. P. Orekhova, V. P. Matrosov, E. G. Tsvetkov, and G. V. Bukin, Dokl. Akad. Nauk SSSR 256, 373 (1981) [Sov. Phys.—Dokl. 26, 62 (1981)].

[6] E. F. Farrell, J. H. Fang, and R. E. Newnham, Am. Mineral. 48, 804 (1963); E. F. Farrell and R. E. Newnham, ibid. 50, 1972 (1965).

[7] R. E. Newnham, R. Santoro, J. Pearson, and C. Jansen, Am. Mineral. 449, 427 (1964).

[8] M. L. Shand, J. C. Walling, and H. P. Jenssen, IEEE J. Quantum Electron. QE-18, 167 (1982).

[9] K. L. Schepler, J. Appl. Phys. 56, 1314 (1984).

[10] D. E. McCumber and M. C. Sturge, J. Appl. Phys. 34, 1682 (1963).

[11] R. C. Powell, B. DiBartolo, B. Birang, and C. S. Naiman, J. Appl. Phys. 37, 4973 (1966).

[12] D. Hsu and J. L. Skinner, J. Chem. Phys. 81, 5471 (1984).

[13] Specific Heat of Nonmetallic Solids, edited by Y. S. Touloukios and E. H. Buyco (Plenum, New York, 1970), p. 1325.

[14] G. F. Imbusch, Phys. Rev. 153, 326 (1967).

[15] R. C. Powell, B. DiBartolo, B. Birang, and C. S. Naiman, Phys. Rev. 155, 296 (1967).

[16] R C. Powell and B. DiBartolo, Phys. Status Solidi A 10, 315 (1972), and references therein.

[17] M. Inokuti and H. Hirayama, J. Chem. Phys. 43, 1978 (1965).

[18] D. L. Huber, J. Lumin. 28, 475 (1983).

[19] W. Platz and J. Heber, Z. Phys. B 24, 333 (1976).

[20] J. P. van der Ziel, J. Chem. Phys. 57, 2442 (1972).

[21] A. M. Ghazzawi, J. K. Tyminski, R. C. Powell, and J. C. Walling, Phys. Rev. B 30, 7182 (1984).

[22] D. J. Harter, M. L. Shand, and Y. B. Band, J. Appl. Phys. 56, 865 (1984).

[23] W. Jia, Y. S. Shang, R. M. Tang, and Z. Y. Yao, J. Lumin. 31-32, 272 (1984).

[24] T. Kushida and M. Kikuchi, J. Phys. Soc. Jpn. 23, 1333 (1967).

[25] T. Muramoto, Y. Fukuda, and T. Hashi, Phys. Lett. 48A, 181 (1974).

[26] D. L. Dexter, J. Chem. Phys. 21, 836 (1953).

SPECTROSCOPIC PROPERTIES OF ALEXANDRITE CRYSTALS II

Andrzej B. SUCHOCKI, Guy D. GILLILAND, Richard C. POWELL and John M. BOWEN

Department of Physics, Oklahoma State University, Stillwater, Oklahoma 74078-0444, U.S.A.

John C. WALLING

Light Age, Inc., 6352 Castejon Drive, La Jolla, California 92037, U.S.A.

Several aspects of the optical spectroscopic properties of alexandrite crystals not previously investigated are reported here. For Cr^{3+} ions occupying the Al^{3+} lattice sites with mirror symmetry in $BeAl_2O_4$, the positions of the zero-phonon lines for absorption transitions to the $^2T_{1g}$ and $^4T_{2g}$ levels are identified, and vibronic transition peaks in the fluorescence spectrum are compared to transitions appearing in the Raman spectrum and Stokes excitation spectrum. In addition, the effects of radiation trapping are shown to lengthen the fluorescence lifetime of the $^2E_g - {}^4A_{2g}$ transition for ions in these sites at low temperatures. For Cr^{3+} ions occupying the Al^{3+} lattice with inversion symmetry, the ground state splitting of the $^2E_g - {}^4A_{2g}$ transition is reported and the decrease of the fluorescence lifetime with temperature is shown to be due to the increase in vibronic emission probability as well as increased probability of direct radiationless decay.

1. Introduction

Alexandrite ($BeAl_2O_4 : Cr^{3+}$) is important as a tunable solid state laser material [1,2]. We recently reported some of the spectroscopic properties of alexandrite crystals [3], and in this paper we present additional details of the optical spectroscopic characteristics of this material. The spectra are complicated by the presence of optical transitions associated with Cr^{3+} ions in two nonequivalent types of crystal field sites, one having mirror symmetry (C_s) and the other having inversion symmetry (C_i). In addition, nonuniform Cr^{3+} ion distributions produce transitions associated with exchange coupled pairs of Cr^{3+} ions [3–5], and the electron–phonon interaction gives rise to vibronic transitions. These properties have made it difficult to understand all of the details of the optical spectra of alexandrite. The results reported here include a comparison of the Raman spectra of alexandrite and chrysoberyl (undoped $BeAl_2O_4$) with the structure in the low-temperature absorption and fluorescence spectra, which allows the

identification of zero-phonon lines and specific phonon peaks in the vibronic sidebands for Cr^{3+} ions in sites of mirror symmetry. Also, the effect of radiative reabsorption on the fluorescence lifetime of the mirror site ions is discussed. In addition, the temperature dependence of the fluorescence lifetime of the Cr^{3+} ions in the inversion sites is presented.

The sample investigated was an oriented cube of alexandrite with each edge about 7 mm. It contained 0.0325 at% Cr^{3+} ions with 78% of these occupying aluminum sites with mirror symmetry and 22% occupying aluminum sites with inversion symmetry, as determined by the methods given in ref. [2]. The undoped chrysoberyl sample used for Raman spectroscopy was a cube of approximately the same dimensions.

2. Spectral properties of mirror site ions

2.1. Identification of spectral structure

The absorption spectra were measured on a Perkin–Elmer 330 UV visible spectrophotometer
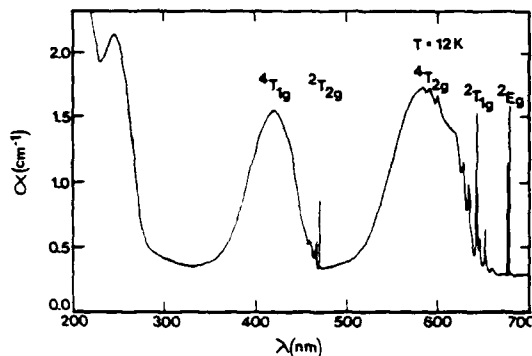
Fig. 1. Absorption spectrum of alexandrite at 12 K.

with the samples mounted in a cryogenic refrigerator to control the temperature. To obtain the fluorescence spectra, the sample was excited by a nitrogen laser-pumped dye laser with Rhodamine 6G dye tuned to excite the $^4T_{2g}$ band of the mirror site ions. A one-meter monochromator, RCA C31034 photomultiplier tube, and an EG & G/PAR boxcar averager were used for the detection system, and a cryogenic refrigerator was again used to control the temperature of the sample.

Figure 1 shows the absorption spectrum of alexandrite at 12 K with $E\|b$. The spectral features are dominated by transitions associated with Cr^{3+} ions in mirror sites both because of their higher concentration compared to inversion site ions and because the oscillator strengths of transitions of Cr^{3+} in sites with a center of symmetry are generally two orders of magnitude smaller than in sites without inversion symmetry. The two broad bands are associated with transitions to the $^4T_{1g}$ and $^4T_{2g}$ levels, while the shoulder on the band edge near 245 nm may either be due to a charge transfer transition or to a transition terminating on one of the higher levels of the $3d^3$ configuration such as the $^4T_{1g}(b)$ levels [3]. This is consistent with the crystal field splittings predicted by the Tanabe–Sugano diagram for this electronic configuration. The properties of this band will be the subject of future research. This spectrum is similar to the room temperature spectrum [3] except that at low temperatures the bands are narrower and there are more sharp peaks visible.

The sharp lines appearing on the low-energy side of the $^4T_{2g}$ band between about 580 and 670 nm include zero-phonon transitions to components of the $^2T_{1g}$ and $^4T_{2g}$ levels, and phonon peaks in the vibronic sidebands of both the R_{1m} line and the $^4T_{2g}$ zero-phonon lines. One of the goals of this investigation is to identify the origin of each of these peaks.

Figure 2 shows an expanded view of the absorption spectrum in the region of interest. Each peak in the spectral structure is labeled and its position is listed in table 1. The absolute positions of the peaks and the temperature dependences of their positions of the peaks and the temperature dependence of their positions and intensities are used to distinguish between zero-phonon lines and vibronic lines. Zero-phonon lines should appear in exactly the same position in the emission and absorption spectra whereas vibronic transitions appear as mirror images in absorption and emission about the zero-phonon line. Multiphonon transitions appear as uniform progressions in energy displacement from the zero-phonon lines.

Figure 3 shows the fluorescence on the anti-Stokes side of the R_{1m} line in the spectral region of interest, in comparison with the structure in the absorption spectra at different temperatures. From these spectra it is easy to identify the lowest two components of the $^2T_{1g}$ level split by the low symmetry contribution to the crystal field and by spin–orbit interaction. These are generally desig-
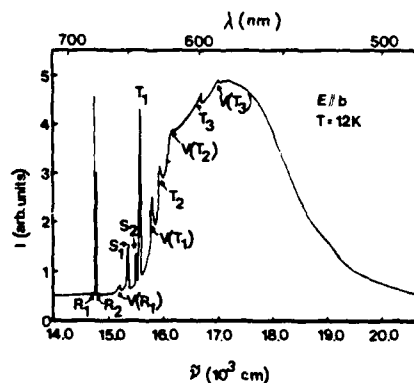

Fig. 2. Structure in the absorption spectrum of alexandrite near the R_m lines and on the low-energy side of the $^4T_{2g}$ band.

Table 1
Spectral structure of mirror site ions

Absorption spectra (12 K. $E\|b$)

λ (nm)	ν (cm⁻¹)	Assignment	Comment
678.68	14 734.5	R_{1m} (^2E_g)	$\Delta E_{ground\ state}$ = 0.54 cm⁻¹
677.11	14 768.6	R_{2m} (^2E_g)	ΔE_R = 34.1 cm⁻¹
661.50	15 117.0	R_{1m} vibronic	ν = 383.5 cm⁻¹
652.70	15 321.0	S_{1m} ($^2T_{1g}$)	
646.50	15 468.0	S_{2m} ($^2T_{1g}$)	
643.00	15 552.0	S_{3m} ($^2T_{1g}$)	
643.40	15 542.0	T_{1m} ($^4T_{2g}$)	
634.00	15 773.0	T_{1m} vibronic	ν = 231 cm⁻¹
629.00	15 898.0	T_{2m} ($^4T_{2g}$)	
620.00	16 129.0	T_{2m} vibronic	ν = 231 cm⁻¹
599.00	16 694.0	T_{3m} ($^4T_{2g}$)	
590.00	16 949.0	T_{3m} vibronic	ν = 255 cm⁻¹
470.95	21 234.0	B_{1m} ($^2T_{2g}$)	
467.30	21 400.0	B_{2m} ($^2T_{2g}$)	
465.30	21 492.0	B_{3m} ($^2T_{2g}$)	
460.00	21 739.0	T_{1m} ($^4T_{1g}$)	

Vibrational spectra (ν in cm⁻¹)

R_{1m} Fluorescence Vibronics (12 K)	Raman Alexandrite	Raman Chrysoberyl	Comment
41			Stokes excitation
246	240	240	Stokes excitation
257			
276			
315	326		
352	358	356	
378			
392			
410			
455	443	440	
459			
469			
473			
477			
481	482	482	
490			
501			
510			
520	524	524	
534			
560			
570	569	569	
586			
600			
610			
630			
660			

Table 1 (continued)
Vibrational spectra (ν in cm⁻¹)

R_{1m} Fluorescence Vibronics (12 K)	Raman Alexandrite	Raman Chrysoberyl	Comment
680	683	680	
700			
	749	749	
773			
	782	782	
816			
	938	938	

nated as S lines. The highest energy component of this level is superimposed on the lowest of the six components of the split $^4T_{2g}$ level (designated as T lines) at very low temperature. As temperature increases, the positions of the components from the two different levels shift in energy and vary in intensity differently, allowing them to be partially resolved as seen in fig. 3(A). Transitions involving the $^4T_{2g}$ levels appear in both absorption and emission spectra whereas transitions involving the
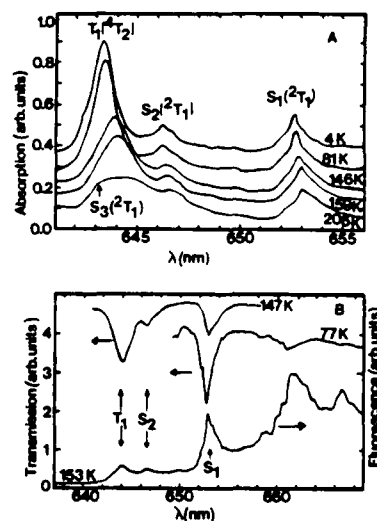

Fig. 3. Structural details in the alexandrite spectra in the 640 to 660 nm region. (A) Temperature variation of the absorption lines between 4 and 206 K. (B) Comparison of the line positions in the transmission spectrum and the anti-Stokes fluorescence spectrum.

$^2T_{1g}$ level appear only in the absorption spectra. Thus by comparing the two types of spectra shown in fig. 3(B) it is possible to identify the position of the T_1 line. Then the other component resolved in fig. 3(A) is assigned to S_3.

It is more difficult to identify unambiguously the zero-phonon absorption transitions terminating on the five upper components of the split $^4T_{2g}$ level. Since the first-order spin–orbit splitting is at most 50 cm^{-1} which is much less than the crystal field splitting for this level [6,7], there are expected to be three no-phonon lines with unresolved second-order spin–orbit splittings. The similar temperature dependences of the peak intensities favors the assignments given in table 1. Each of these zero-phonon lines has a satellite about 240 ± 10 cm^{-1} on its low-energy side which is attributed to strong coupling to a specific vibrational mode, as discussed below. The additional broad peak appearing at 661.5 nm is attributed to a vibronic transition of the R_{1m} line ($^2E_g-^4A_{2g}$ transition) involving a phonon of about 380 cm^{-1}. This transition also appears in the anti-Stokes sideband of the fluorescence spectrum shown in fig. 3. Because of the numerous possibilities for coupling to other phonon modes, the proposed assignments are not unambiguous.

The splitting between the R_{1m} and R_{2m} lines (i.e., the splitting of the ^2E_g level) is measured to be 34.1 cm^{-1} at 12 K. This splitting increases to over 40 cm^{-1} at higher temperatures.

The structure in the fluorescence spectrum was also investigated. Figure 4 shows the low-temperature fluorescence spectrum on the low-energy side of the R_{1m} line. The peaks in the anti-Stokes fluorescence spectrum shown in fig. 3(B) appear in the Stokes vibronic sideband in fig. 4 at approximately mirror image positions about the R_{1m} line. Most of the peaks within about 100 cm^{-1} of the R_{1m} line have been associated with transitions involving exchange coupled pairs of Cr^{3+} ions and are not discussed in this paper [3–5]. The remaining structure in the spectrum is associated with vibronic transitions involving the R_{1m} line and specific phonon modes. The positions of the vibronic transitions are listed in table 1.

In order to investigate the electron–phonon coupling with low-energy modes, we measured the
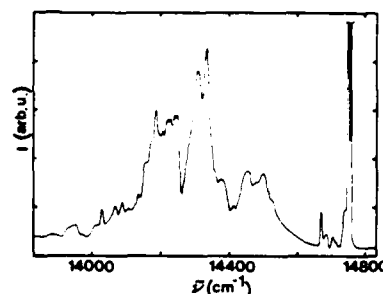
Fig. 4. Fluorescene vibronic sideband of the R_{1m} line in alexandrite at 12 K.

Stokes excitation spectrum in the region of the R_{1m} line (678.68 nm). The sample was mounted in a cryogenic refrigerator set for a temperature of 12 K. The emission intensity of the R_{1m} line was monitored during excitation with an argon pumped Rhodamine 6G dye laser tuned to selectively excite the mirror site ions in the $^4T_{2g}$ band. Then changes in the R_{1m} emission intensity were monitored as the sample was additionally excited by a nitrogen laser-pumped tunable dye laser containing Oxazine 720 dye. This laser was tuned between about 665.0 and 677.0 nm where there are no resonances with electronic transitions. Thus any additional excitation provided by this laser results from Stokes vibronic absorption transitions involving stimulated phonon emission. The simultaneous pumping with the Rhodamine 6G laser provides phonons for this process through radiationless relaxation from the $^4T_{2g}$ to the ^2E_g level. No R_{1m} emission was observed for excitation with only the Oxazine dye laser, but enhanced R_1 emission was observed when the Oxazine dye laser was tuned to certain wavelengths with the Rhodamine dye laser on.

The excitation spectrum was recorded point by point and although the resolution in this type of experiment is very poor, two distinct peaks were observed in the Stokes excitation spectrum. These were at approximately 40 and 240 cm^{-1} higher energy than the R_{2m} line. If the electronic part of the vibronic transition is associated with the R_{2m} line, this indicates the presence of a significant population of phonons of these energies generated

through cascade radiationless relaxation processes after pumping in the $^4T_{2g}$ band. Since 40 cm^{-1} is approximately the splitting between the R_m lines, these phonons are probably generated through the transitions from initial level of R_{2m} to the initial level of R_{1m}. There is additional evidence for the presence of a high density of 240 cm^{-1} phonons in the absorption spectrum (231 cm^{-1} vibronic peaks associated with the T_{1m} and T_{2m} zero-phonon lines and a 255 cm^{-1} vibronic peak associated with the T_{3m} zero-phonon line), the emission spectrum (246 cm^{-1} vibronic peak associated with the R_{1m} line), and the Raman spectra (240 cm^{-1} lines in both the alexandrite and chrysoberyl spectra). If these vibronic transitions were associated with the R_{1m} line rather than R_{2m} the phonon frequencies involved would have to be 74 and 274 cm^{-1}. Since there is no other spectral evidence of phonons with the former frequency and only a weak fluorescence vibronic peak of the latter frequency, the interpretation involving R_{2m} vibronic transitions appears to be correct.

Raman spectroscopy was used to identify the frequencies of other phonons in the lattice. The 514.5 nm line of an argon laser was used as the light source and an Instruments S.A. Ramanor U-1000 monochromator was used to analyze the scattered light. A computer controlled, single-photon counting system was used for data acquisition. Spectra were obtained for all crystallographic directions of polarization for the incident light while no polarizer was used in the scattered beam. Samples of both alexandrite and undoped chrysoberyl were analyzed. An example of the recorded spectra is shown in fig. 5, and the observed Raman lines are listed in table 1.

The Raman-active phonons can be classified in terms of the irreducible representations according to which they transform in the point group of the crystal. There are three possible types of vibrational modes in O_h symmetry, A_{1g}, E_g, and T_{2g} [8–10]. The reduction to C_s symmetry will cause a splitting into additional phonon modes and make it difficult to assign Raman peaks to specific vibrational modes through the observation of polarization intensity changes. Only the strongest Raman peaks are recorded in table 1, many other weaker peaks appear in the spectra. Group theory
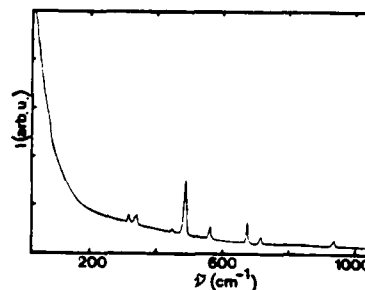
Fig. 5. Major peaks in the Raman spectrum of alexandrite.

analysis for the mirror site point group in the chrysoberyl crystal structure predicts the presence of over 90 vibrational modes, about half of which are Raman-active. More detailed Raman spectra of alexandrite have been reported recently [8]. The Raman spectra of alexandrite and chrysoberyl are essentially identical. There is some agreement between the Raman spectral peaks and the structure in the vibronic fluorescence sideband of the R_{1m} line.

2.2. Radiative energy transfer

Radiative energy transfer or "radiation trapping" is known to occur in Cr^{3+}-doped materials such as ruby [11]. This resonant reabsorption of the photons emitted from one Cr^{3+} ion by another Cr^{3+} ion in the crystal can change the shape and decay time of the fluorescence spectrum. We have determined the effects of reabsorption in alexandrite by measuring the variation of the fluorescence lifetime of the R_{1m} emission as a function of excitation position in the sample. The results are shown in fig. 6 along with the geometry of the experiment.

The mirror site Cr^{3+} ions were again selectively excited by the argon laser-pumped dye laser as described above. The light was polarized parallel to the a-axis of the crystal and the luminescence was observed perpendicular to the ac face, which is the direction of strongest absorption. The fluorescence was observed by the apparatus described in the previous section and processed by an EG & G/PAR 4202 signal averager. The laser excitation

Fig. 6. Variation of the fluorescence lifetime of Cr^{3+} ions in mirror sites as a function of excitation distance into the sample.

was chopped with a mechanical chopper in order to monitor the fluoresence decay kinetics.

Figure 6 shows the measured fluorescence lifetimes recorded at 30 K as a function of the distance of the laser beam from the edge of the sample observed by the photomultiplier tube. In order to eliminate the possible effects of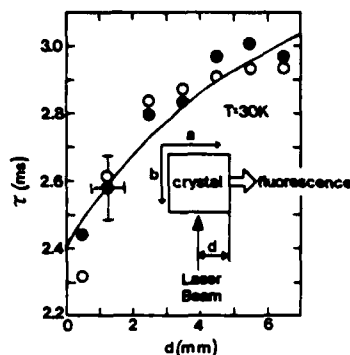 Cr^{3+} ion concentration gradients in the direction of observation, the measurements were repeated with the sample rotated 180° about the c-axis. The results for the two measurements are within the error bars of the experiment. The decay kinetics were observed to be nonexponential at early times, and to approach an exponential decay at long times. The relative importance of the nonexponential part of the decay curves increased with the excitation distance d into the sample. The decay times plotted in fig. 6 were measured in the long-time, exponential part of the decay curves.

The results shown in fig. 6 show that radiation trapping in the R_{1m} transition in alexandrite can influence spectral measurements even for samples with low Cr^{3+} concentrations, such as the 0.0325 at % sample used for this work. Exact theoretical models for the decay kinetics in the presence of radiation trapping are very complicated [12–14]. The simplest expression for the fluorescence lifetime of a crystal with thickness d, average absorption coefficient α_0, and intrinsic fluorescence de-

cay time τ_0 is given by Konobeev [14] as

$$\tau = \tau_0 \frac{(1 - q/2)}{(1 - q)} - 2qx^2$$
$$\times \left\{ \left\{ x(2x + 1)^2 - (2x - 1)^2 [\xi(2x + 1) + 1] \right\} \right.$$
$$\times \exp(-\xi/x) \right\} \left\{ x(2x + 1)^2 - (2x - 1)^2 \right.$$
$$\times [\xi(2x + 1) + 1] \exp(-2\xi/x) \right\}^{-1}, \qquad (1)$$

where $\xi = \alpha_0 d$, $x = 0.5(1 - q)^{-1/2}$, and $q = \int_0^\infty E(\nu)\eta(\nu) \, d\nu$. The function $E(\nu)$ is the normalized emission spectrum, and $\eta(\nu)$ is the quantum efficiency of the emission. This expression describes the physical situation of exciting one face of a sample and measuring the fluorescence emission from the opposite face. The thickness d is altered by working with samples of different sizes. In our experiment the excitation was created in a cylindrical shape within the sample parallel to the observing surface, and the effective thickness of the sample was controlled by changing the position of the laser excitation with respect to the sample surface through which the fluorescence was observed. Since this is not exactly the same configuration used in deriving eq. (1), this expression must be considered as only a rough approximation for interpreting the results. The solid line in fig. 6 represents the best fit to the data using eq. (1), treating τ_0 and q as adjustable parameters. The average absorption coefficient for R_{1m} in our sample was measured to be 1 cm^{-1}. The parameters obtained from this analysis are $\tau_0 = 2.4$ ms and $q = 0.45$.

The fit to the data shown in fig. 6 is good considering the simplified theoretical approach which has been used. At higher temperatures, the R_{1m} line broadens and the peak absorption coefficient decreases, thus decreasing the effects of radiative reabsorption.

3. Spectral properties of inversion site ions

Some of the spectroscopic properties of Cr^{3+} ions in the inversion sites in alexandrite crystals have been described previously [1–3,15]. We report here additional information on the zero-field

splitting of the R_{1i} line, and the temperature dependence of the fluorescence lifetime of the inversion site ions.

Figure 7 records the low-temperature fluorescence spectrum of alexandrite in the 670–700 nm in spectral region showing the positions of the R_{1m}, R_{2m}, R_{1i} and R_{2i} lines. The insert shows the change in the relative intensities of the components of the R_{1i} line for different polarization directions of the electric and magnetic field. These are consistent with a magnetic dipole transition [1]. The energy splitting between the R_{1i} and R_{2i} lines is about three times greater than the R line splitting for the ions in the mirror sites. This indicates a stronger low-symmetry component for the crystal field for the inversion site ions. Similarly, the ground state splitting for R_{1i} is about 1.15 cm^{-1}, as compared to 0.54 cm^{-1} for the R_{1m} line [1]. These splittings are listed in table 2.

The fluorescence decay time of the Cr^{3+} ions in inversion sites was monitored as a function of temperature between 25 and 490 K. The ions in the inversion sites were selectively excited in the $^4T_{2g}$ band by the 488 nm line of the argon laser where the mirror site absorption is weak [3,15].
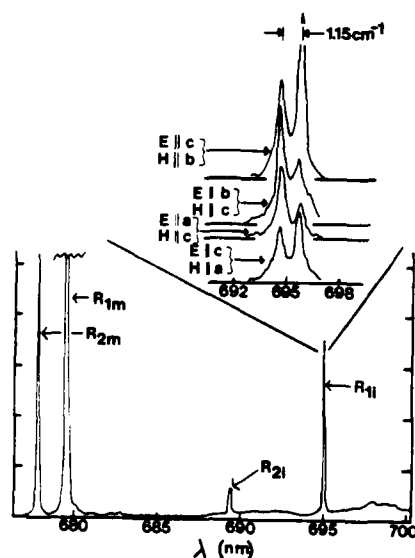
Table 2
Properties of inversion site ions (12 K)

R_{1i} = 14388.49 cm^{-1}	R_{2i} = 14513.79 cm^{-1}
$\Delta E_{ground\ state}$ = 1.15 cm^{-1}	ΔE_R = 124.30 cm^{-1}
τ_0 = 63 ms	τ_S = 1.5 ms
ΔE_S = 1430 cm^{-1}	$h\nu$ = 385 cm^{-1}

The rest of the experimental setup for lifetime measurements was the same as described in the previous section. The kinetics of the decay curves could be described very accurately as single exponentials for over two decades at all temperatures investigated. The measured decay rates are shown as a function of temperature in fig. 8. The decay rate is essentially constant below about 130 K and increases rapidly above this temperature.

For the Cr^{3+} ions in mirror sites, the variation of the fluorescence decay rate with temperature was attributed to having the ^2E_g and $^4T_{2g}$ levels in thermal equilibrium, so that the common decay rate was given by [3]

$$\tau^{-1} = \tau_E^{+1} + \tau_T^{-1} \exp(-\Delta E/kT). \qquad (2)$$

Here τ_E and τ_T are the intrinsic decay times of the ^2E_g and $^4T_{2g}$ levels, respectively, ΔE is the energy difference between these levels, and k is Boltzmann's constant. The broken curve in fig. 8 shows an attempt to fit the data for the inversion sites with this model. As seen from the figure, the resulting fit between theory and experiment is very poor. In addition, the parameters needed to obtain the closest fit (ΔE = 560 cm^{-1}; τ_T = 8.8 ms) are unphysical for inversion site ions.

Another contribution to the temperature dependence of the lifetime is the increase in vibronic emission probability. Modifying eq. (2) to include this possibility gives [16]

$$\tau^{-1} = \tau_0^{-1} \coth(h\nu/2kT) + \tau_S^{-1} \exp(-\Delta E/kT). \qquad (3)$$

Here the first term describes the results of phonon-induced transitions with phonons of energy $h\nu$ while the second term again describes the effects of thermalization between the ^2E_g level and a level ΔE above it. The fit between this equation and the measured data is quite good as

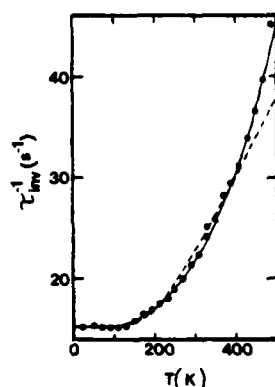Fig. 7. Fluorescence spectra of Cr^{3+} ions in inversion sites.

Fig. 8. Temperature dependence of the fluorescence lifetime of Cr^{3+} ions in inversion sites. (See text for explanation of theoretical curves.)

shown by the solid curve in fig. 9. The fitting parameters used in this analysis are listed in table 2. They are physically reasonable for inversion site ions. The nature of the direct phonon processes involved in the second term of eq. (3) is not known at the present time. These may be processes establishing thermal equilibrium with one of the split components of the $^2T_{1g}$ level if this level has a significantly shorter intrinsic decay time than the ^2E_g level. Another possibility is that these processes represent nonradiative decay out of the ^2E_g level through crossover to the ground state potential well. The spectroscopic information currently available on Cr^{3+} ions in inversion sites in alexandrite does not allow us to distinguish between these two possibilities. In addition it should be noted that it would also be possible to find good fits to the experimental data by including in eq. (3) the sum over several vibronic transitions involving phonons with different frequencies.

4. Summary and discussion

The spectral details of Cr^{3+} ions in mirror sites in alexandrite are similar to those seen in other Cr^{3+}-doped crystals such as ruby [6,7,12,17]. The crystal field splittings are significantly stronger for ions in the inversion sites compared to ions in the mirror sites. The vibronic sidebands of the R_1

fluorescence line in ruby and of the mirror site Cr^{3+} ions in alexandrite are similar [12,17] and do not show prominent local modes such as those observed for Cr^{3+} in $SrTiO_4$ [18]. The Raman-active phonons of about 240 cm^{-1} are important in the optical spectra of Cr^{3+} ions in the mirror sites. The presence of a high population of these phonons produces vibronic peaks in the absorption spectrum associated with the $^4T_{2g}$ zero-phonon lines and a vibronic peak of the R_{1m} line in the fluorescence spectrum. In addition, the results of the Stokes excitation experiment show these phonons to be generated by radiationless relaxation processes from the $^4T_{2g}$ level to the ^2E_g level. The generation of phonons with energy equal to the splitting of the ^2E_g level through the radiationless relaxation processes between the R_{2m} and R_{1m} levels as detected through the Stokes excitation results has also been observed previously in a different type of experiment [19].

Previous measurements of the fluorescence lifetime of the Cr^{3+} ions in the inversion sites in a more heavily doped sample have shown no temperature dependence up to room temperature [3]. The results reported here were obtained on a more lightly doped sample and show a strong temperature dependence between 200 and 500 K. It is possible that radiative trapping in the heavily doped sample obscured the onset of the temperature dependence of the lifetime. The fact that the temperature dependence is consistent with strongly coupled, vibronic emission processes as well as direct phonon processes is quite different from thermal quenching of the lifetime of mirror site ions. The relative importance of vibronic emission may be associated with the magnetic dipole nature of the R_{1i} transition of inversion site ions. This means that vibrational modes that break the inversion symmetry can result in higher oscillator strength transitions.

Acknowledgments

References

[1] J.C. Walling, O.G. Peterson, H.P. Jenssen, R.C. Morris and E.W. O'Dell, IEEE J. Quantum Electron. QE-16, (1980) 1302.

[2] J.C. Walling, D.F. Heller, H. Samelson, D.J. Harter, J.A. Pete and R.C. Morris, IEEE J. Quantum Electron QE-21 (1985) 1568.

[3] R.C. Powell, L. Xi, X. Gang, G.J. Quarles and J.C. Walling, Phys. Rev. B 32 (1985) 2788.

[4] J.C. Walling, unpublished results.

[5] D. Curie, unpublished results.

[6] D.S. McClure, J. Chem. Phys. 36 (1962) 2757.

[7] R.M. Macfarlane, J. Chem. Phys. 39 (1963) 3118.

[8] J. Weiyi, Z. Qingrong, S. Yusheng, W. Yanyun, Y. Zhenyi, H. Shouan, Z. Hetian and L. Liling, Kexue Tongbao 30 (1985) 452.

[9] M.T. Paques-Ledent and P. Tarte, Spectro Chimica Acta 29A (1973) 1007.

[10] J.L. Servoin and B. Piriou, Phys. Status Solidi (B) 55 (1973) 677.

[11] W. Jekeli, J. Opt. Soc. Am. 55 (1965) 1442.

[12] D.E. Nelson and M.D. Sturge, Phys. Rev. 137 (1965) A1117.

[13] T. Holstein, Phys. Rev. 72 (1947) 1212; ibid 83 (1951) 1159.

[14] Yu.V. Konobeev, Opt. i Spektr. sb. Specktroskopiya Tverdaga. Tela (1969) 208.

[15] K.L. Schepler, J. Appl. Phys. 56 (1984) 1314.

[16] R. Kubo and Y. Toyozawa, Prog. Theor. Phys. 13 (1955) 160.

[17] T. Kushida and M. Kikuchi, J. Phys. Soc. Japan 23 (1967) 1333.

[18] A. Kim, R.C. Powell, M. Mostoller and T.M. Wilson, Phys. Rev. B 12 (1975) 5627.

[19] R.J.G. Goossens, J.I. Dijkhuis and H.W. de Wijn (to be published).

Four-wave-mixing measurements of energy migration and radiationless relaxation processes in alexandrite crystals

Andrzej Suchocki, Guy D. Gilliland, and Richard C. Powell

Department of Physics, Oklahoma State University, Stillwater, Oklahoma 74078-0444

(Received 12 May 1986; revised manuscript received 18 August 1986)

Four-wave-mixing techniques were used to establish and probe population gratings of Cr^{3+} ions in both mirror and inversion sites in $BeAl_2O_4$:Cr^{3+} crystals as a function of temperature between about 6 and 300 K. The four-wave-mixing signal intensity and decay rate were monitored as a function of the crossing angle of the laser "write" beams. The variation of the signal intensity with crossing angle is explained theoretically with use of a model based on the interaction between the laser and a two-level atomic system. Theoretical fits to the results provide information concerning the relative importance of the absorption and dispersion contributions to the signal, and the dephasing time of the atomic system. The latter is found to be 2.2 psec for the mirror site ions and 80 psec for the inversion site ions. The signal decay rate of the inversion site ions was found to be independent of crossing angle at all temperatures, while the signal decay rate for ions in the mirror site increased with increasing crossing angle at temperatures below about 150 K. This indicates the presence of long-range energy migration, and the diffusion coefficient describing this process was found to increase to about 4.2×10^{-7} $cm^2 sec^{-1}$ at 6 K.

I. INTRODUCTION

The optical properties of alexandrite ($BeAl_2O_4$:Cr^{3+}) are of interest because of its importance as a tunable solid-state laser material.[1] We have recently reported some of the optical-spectroscopic properties of alexandrite, including the results of four-wave-mixing (FWM) measurements at room temperature.[2-4] In this paper we describe the results of extending our FWM measurements to low temperatures.

The mechanism of transient FWM in doped crystals is scattering from a laser-induced population grating. In alexandrite the Cr^{3+} ions can occupy two nonequivalent crystal-field sites, one having mirror symmetry and the other inversion symmetry. We have shown previously that population gratings can be established for Cr^{3+} ions in either type of site.[4] The grating can be associated with differences in either the absorption or dispersion properties of the Cr^{3+} ions when they are in the excited state instead of the ground state. We describe here a method for determining the contributions to the FWM signal from these two types of refractive-index modulation. The ratio of these two contributions is used to determine the dephasing time T_2 of the Cr^{3+} ions interacting with the laser excitation. For the experimental conditions used here, the dominant process in the dephasing is the pump-band—to—metastable-state radiationless relaxation process, which is of interest in understanding laser-pumping dynamics.

The transient dynamics of the FWM signal can be used to characterize the properties of energy migration among ions in crystals if the migration distance is of the order of the peak-to-valley separation of the laser-induced grating.[5-7] Our previous FWM results showed that no long-range energy transfer was taking place among the Cr^{3+} ions in alexandrite at room temperature.[4] This remains true for inversion-site ions at low temperatures. However, for ions in the mirror sites, the influence of long-range energy transfer on the FWM signal decay becomes evident below 150 K. The diffusion coefficient determined from these measurements increases to a value of 4.2×10^{-7} $cm^2 sec^{-1}$ at 6 K. This surprising result may be associated with nonuniform Cr^{3+}-ion distributions which are known to be present in alexandrite.[2]

II. EXPERIMENTAL APPARATUS AND SAMPLES

The crystal used for this work was an oriented cube of $BeAl_2O_4$:Cr^{3+} with each edge measuring approximately 7 mm. The concentration of Cr^{3+} ions is 0.0325 at. %. The Cr^{3+} ions enter the lattice substitutionally for the Al^{3+} ions, which occur in the chrysoberyl structure with octahedral coordination of oxygen ions. They can occupy two inequivalent types of crystal-field sites, one with mirror symmetry belonging to the C_s point group and one with inversion symmetry belonging to the C_i point group. It has been found previously that 78% of the Cr^{3+} ions occupy mirror sites and 22% inversion sites.[1] The mirror-site ions dominate the optical spectroscopy and lasing properties of the material.

The experimental setup used for the nondegenerate FWM measurements is shown schematically in Fig. 1. For temperature control, the sample was mounted in either a cryogenic refrigerator or a liquid-helium Dewar. The laser excitation was provided by either the 488.0-nm output from an argon laser or the output of a ring dye laser with Rhodamine-6(G) dye tuned to 589.0 nm. The former selectively excites the ions in the inversion sites while the latter selectively excites ions in the mirror sites.[2] The laser output was split with a beam splitter into two beams of equal power (write beams) which travel equal path lengths before crossing at an angle θ inside the sam-
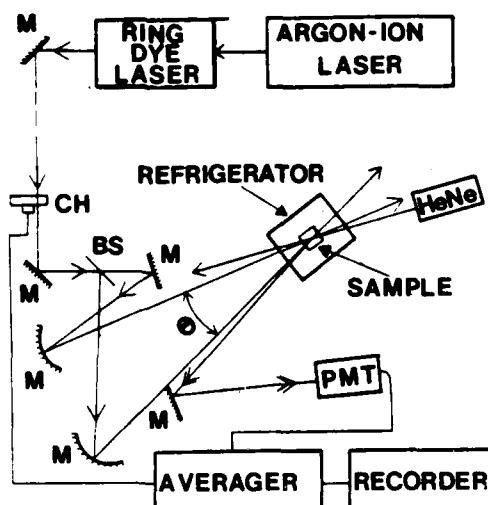
FIG. 1. Schematic representation of experimental apparatus for four-wave mixing. CH, chopper; PMT, photomultiplier tube; M, mirror; BS, beam splitter.

ple. Their interference forms a sinusoidal pattern which creates a spatial distribution of Cr^{3+} ions in the excited state with the same pattern. Due to the difference in the complex dielectric constant when the Cr^{3+} ions are in the ground and excited states, this population distribution acts as an index-of-refraction grating. Although the heat generated under these experimental conditions can also produce a change in the refractive index, thermal gratings have different magnitudes and angular dependences of the decay rates than population gratings. Thus it is easily possible to distinguish between contributions to the FWM signal from the two types of gratings. The properties of the FWM signal described in the following section show that the results reported here are associated with scattering from a population grating. No effects attributable to a thermal grating were observed. For nondegenerate FWM a He-Ne laser was used for a "read beam." This was aligned so it is almost counterpropagating to one of the write beams. It scatters from the index-of-refraction grating and produces a FWM signal leaving the sample almost counterpropagating to the other write beam. The signal beam was detected by an Amperex 2254B photomultiplier tube. To measure the intensity of the scattered light, the read beam was modulated with a mechanical chopper and an EG&G/PAR lock-in amplifier was used to enhance the signal-to-noise ratio. The decay rate of the signal was measured by chopping the write beams and storing the transient signal in an EG&G/PAR 4202 signal averager.

III. FWM STUDIES OF ENERGY TRANSFER

The decay of a FWM signal associated with a transient population grating is predicted to be a single exponential with a decay rate given by[5]

$$K = 2\tau^{-1} + [32(\pi/\lambda)^2 \sin^2(\theta/2)]D . \tag{1}$$

The first term describes the destruction of the grating due to the fluorescence decay of the ions in the excited state with a decay time of τ. The second term describes the destruction of the grating due to the migration of the excitation energy from ions in the peak to ions in the valley region of the grating. The latter term depends on the diffusion coefficient of the energy migration, D, and on the grating spacing $\Lambda = \lambda/[2\sin(\theta/2)]$, where λ and θ are the wavelength and crossing angle of the laser write beams in the crystal, respectively. Thus by measuring the FWM signal decay rate as a function of the write-beam crossing angle, it is possible to determine the energy-diffusion coefficient.

A. Experimental results

For gratings selectively established with Cr^{3+} ions in inversion sites, no angular variation was observed for the FWM signal decay rate at any temperature. Typical results are shown in Fig. 2. The signals were exponential and decayed with half the fluorescence lifetime of inversion-site ions, as measured independently.[2-4] This indicates that for Cr^{3+} ions in the inversion sites energy transfer does not take place over distances of the order of the grating spacing.

For gratings selectively established with Cr^{3+} ions in mirror sites, the FWM transient signals were nonexponential. A typical example is shown in Fig. 3. The decay rate of the long-time portion of the curve is equal to twice the fluorescence decay rate of the inversion-site ions. This long-time decay rate is independent of the write-beam crossing angle and power. Thus the long-time part of the nonexponential decay is associated with a population grating established with inversion-site ions due to energy transfer from mirror-site ions. In order to obtain an accurate decay rate for the mirror-site grating, the long-time decay curve is extrapolated to short times and subtracted from the measured curve as shown in Fig. 3. Although this procedure for separating the contributions to the signal due to the two types of gratings is not strictly correct for the case of energy transfer, the contribution due to the inversion-site grating is always less than 5% of the total
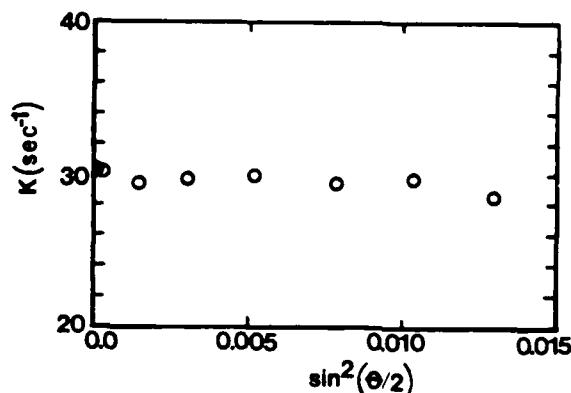

FIG. 2. Grating decay rate vs write-beam crossing angle for FWM in Cr^{3+} ions in inversion sites in alexandrite at 30 K. The solid point is twice the fluorescence decay rate.
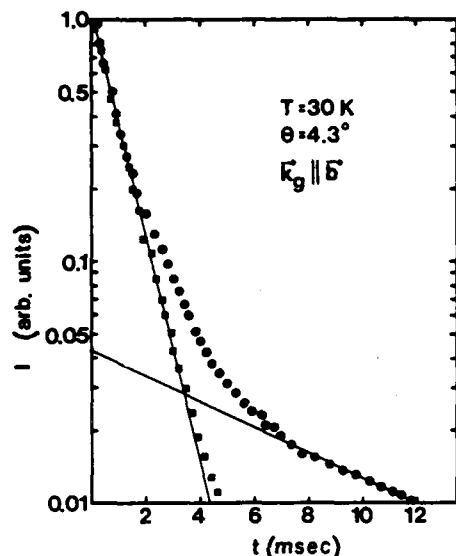
SUCHOCKI, GILLILAND, AND POWELL

FIG. 3. FWM signal intensity vs time for Cr^{3+} ions in mirror sites in alexandrite at 30 K.

FIG. 5. Grating decay rate vs write-beam laser power at 40 K for Cr^{3+} ions in mirror sites in alexandrite at $\theta=4.3°$.

signal and thus the error incurred by the use of this crude separation technique does not greatly affect the accuracy of the diffusion coefficient determined from these measurements as discussed below.

The values of the decay rates obtained in this way are shown plotted versus $\sin^2(\theta/2)$ in Fig. 4 for several temperatures. Above 150 K, no angular variation of K is observed as reported previously.[4] The data shown in Fig. 4 were obtained with the laser beams aligned so that the
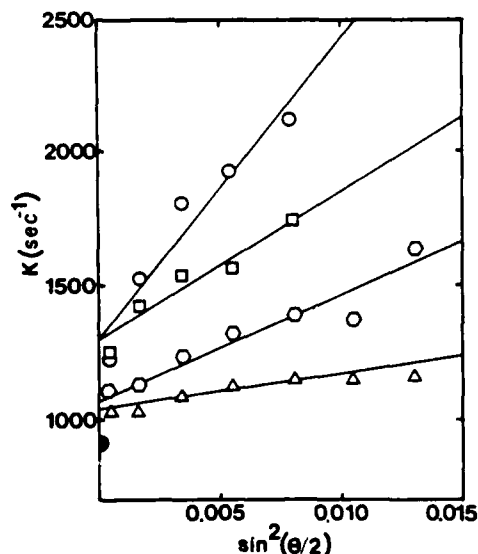

FIG. 4. Grating decay rate vs write-beam crossing angle for FWM in Cr^{3+} ions in mirror sites in alexandrite at several temperatures for 50 mW total write-beam laser power. Circles, 6 K; squares, 15 K; hexagon, 30 K; triangles, 60 K. The solid point represents twice the fluorescence decay rate. See text for explanation of theoretical curves.

grating wave vector was parallel to the crystallographic b axis. When similar measurements were made at low temperatures with the beams aligned so that the grating wave vector was parallel to the c axis, the observed variation of K with θ was much weaker.

One interesting aspect of the data shown in Fig. 4 is that the curves each extrapolate to values at $\theta=0°$ which are greater than the measured values of twice the fluorescence decay rates, $2/\tau$. Although these measurements were made at low laser powers in order to minimize effects of local heating, the discrepancy in the $\theta=0°$ value of K may be associated with the power dependence of the grating decay rate. Figure 5 shows the variation of K with laser power at 40 K for a crossing angle of 4.3°. No change was observed in the fluorescence lifetime as a function of laser excitation power. The increase in K with laser power indicates the presence of power-dependent effects that are not included in Eq. (1). Figure 6 shows the variation of FWM scattering efficiency with the square of the laser power in the write beams at 40 K for three crossing angles. The observed linear dependences are consistent with the room-temperature results reported earlier[4] and are consistent with theoretical predictions of laser interaction with a two-level atomic system.

The diffusion coefficient obtained from fitting Eq. (1) to the slope of curves such as those shown in Fig. 4 is plotted versus temperature in Fig. 7. The values obtained for D are zero above 150 K and increase as $T^{-1/2}$ to about 4.2×10^{-7} cm^2sec^{-1} at 6 K. From these values, the diffusion length can be determined using the relationship $L_d=(2D\tau)^{1/2}$. The values obtained for L_d and D are listed in Table I.

B. Interpretation of results

To interpret the data presented above, we need to obtain a theoretical estimate for the magnitude of D including its directional dependence, a model for explaining the relative change of D with temperature, and a model for explaining the variation of D with laser power.

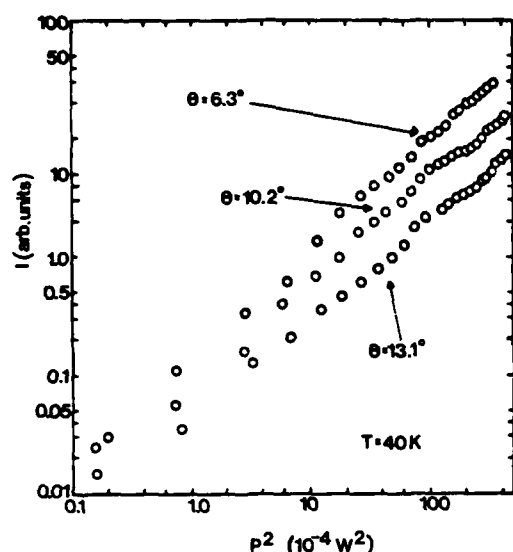FIG. 6. FWM signal intensity of Cr^{3+} ions in mirror sites in alexandrite as a function of the square of the laser power of the write beams at 40 K.

FIG. 7. Temperature dependence of the exciton-diffusion coefficient for Cr^{3+} ions in the mirror sites in alexandrite. (See text for explanation of theoretical line.)

The diffusion coefficient for exciton migration can vary with temperature due to various types of exciton-phonon interaction processes. For the temperature range of interest here, phonon absorption to higher-energy levels with stronger oscillator strengths is negligible[2,3] and the population of optical phonons at temperatures much less than the Debye temperature is very small. Exciton scattering by acoustic phonons[8] predicts a temperature dependence of the type shown in Fig. 7. For this long—mean-free-path model the diffusion coefficient can be expressed as[8]

$$D = \tfrac{1}{6}\langle \tau_s v^2 \rangle \approx \tfrac{1}{6}\langle \tau_s \rangle \langle v^2 \rangle , \qquad (2)$$

where $\langle \tau_s \rangle$ is the mean scattering time and $\langle v^2 \rangle$ is the mean-square group velocity of the excitons. The scattering time can be separated into a contribution due to acoustic phonons and a contribution due to exciton scattering from all other sources such as surfaces, crystal defects, and optic phonons.

$$\tau_s^{-1} = \tau_{ph}^{-1} + \tau_0^{-1} . \qquad (3)$$

The exciton—acoustic-phonon scattering time varies with

TABLE I. Energy-transfer parameters at 6 K for Cr^{3+} ions in mirror sites in alexandrite.

N_m (cm^{-3})	8.9×10^{18}
τ_r (msec)	63.2
τ_m (msec)	2.4
D (cm^{2}sec^{-1})	4.20×10^{-7}
D_{theory} (cm^2 sec^{-1})	1.80×10^{-7}
L_d (cm)	4.5×10^{-5}

temperature as $\tau \propto T^{-1/2}$ in the temperature range of interest, whereas the other scattering processes have a variety of different temperature dependences.[8] If the acoustic-phonon scattering time is much shorter than the scattering time for other processes, Eq. (3) can be expanded to give

$$\tau_s \approx \tau_{ph} - \tau_{ph}^2/\tau_0 , \qquad (4)$$

and Eq. (2) has the form

$$D = AT^{-1/2} - B , \qquad (5)$$

where A is a constant involving the exciton velocity and the matrix element for exciton—acoustic-phonon scattering. B contains a ratio of the rates of exciton scattering by acoustic phonons and by all other centers. The temperature dependence of B is unknown, but the solid line in Fig. 7 is consistent with Eq. (5), assuming B to be independent of temperature. This gives an excellent fit between theoretical predictions and experimental results.

The magnitude of the diffusion coefficient found from these experiments at low temperature is much greater than expected for exciton migration among randomly distributed Cr^{3+} ions with the level of concentration present in our sample. It is difficult to derive a theoretical estimate for D in the long—mean-free-path model since the details of the shape of the exciton band are not known. However, a rough theoretical estimate can be obtained for D by considering the rate of energy transfer between two Cr^{3+} ions. The mechanism of energy migration among Cr^{3+} ions in ruby crystals has been identified as exchange interaction.[9,10] In the simplest model for direct exchange, the energy-transfer rate between two ions separated by a distance R is given by[11]

$$P(R) = (2\pi\Omega Z^2/\hbar) \exp(-2R/L)$$

$$= P_0 \exp(-2R/L) , \qquad (6)$$

where Z depends on the spatial overlap of the electron wave functions, L is the average Bohr radius of the wave function, and the spectral overlap integral Ω includes the product of the normalized emission spectrum of the sensitizer ion ε_s and the normalized absorption spectrum of the activator ion α_a. For ruby, the value of P_0 has been estimated to be[12] 4.3×10^{14} sec^{-1}. For multistep energy migration, the diffusion coefficient can be expressed in terms of the ion-ion interaction rate as[13]

$$D = \frac{1}{6} \int_0^\infty R^2 P(R) \rho(R) dR , \qquad (7)$$

where the probability density of finding an ion at the distance R from the ion at the origin is given by[13]

$$\rho(R) = 4\pi N_m R^2 \exp(-4\pi N_m R^3/3) . \qquad (8)$$

The diffusion coefficient then becomes

$$D = (2\pi N_m P / 3) \int_a^\infty R^4 \exp\{-[(2R/L) + (4\pi N_m R^3/3)]\} dR . \qquad (9)$$

The lower limit of the integral is taken to be $a = 2.7$ Å, which is the smallest distance between Cr^{3+} ions in mirror sites. L is always close to 1 Å and has been estimated for ruby[9] to be 0.97 Å. This value for L, along with $N_m = 8.9 \times 10^{18}$ cm^{-3} for the concentration of mirror-site ions in our sample, can be used in Eq. (9) and the integral evaluated numerically to give 2.23×10^{-41} cm^5. Using this and the ruby value for P_0 gives a value for the diffusion coefficient of 1.8×10^{-7} cm^2 sec^{-1}, which is a factor of about 2.35 smaller than the diffusion coefficient obtained from analyzing the low-temperature FWM results. This represents excellent agreement between the magnitudes of D determined experimentally and theoretically, especially considering that Eq. (9) is strictly applicable for hopping migration and thus underestimates D for long–mean-free-path migration. In addition, nonuniform distributions of the Cr^{3+} ions can enhance the energy transfer enough to account for differences in the experimental and theoretical values of D. The effective diffusion coefficient in heavily doped ruby has been reported to be 2 orders of magnitude greater than the value found here for alexandrite.[14] Scaling for the difference in concentration brings these two results into agreement.

The fact that the diffusion coefficient for energy migration in the c direction is about an order of magnitude smaller than for migration in the b direction may be attributed to the anisotropy of the ion-ion interaction, or it may be associated with a nonuniform spatial distribution of Cr^{3+} ions since chromium-ion banding in c planes is known to be present in alexandrite crystals.[15]

The magnitude of the grating decay rate and its increase with laser power at low temperatures are more difficult to understand. The facts that the fluorescence decay rate is independent of power while the values of K at $\theta = 0°$ are greater than $2/\tau$ at low temperatures where diffusion is taking place but equal to $2/\tau$ at high temperatures, indicate that at high laser power there is an additional process that contributes to the decay of the grating without shortening the metastable-state lifetime. It is im-

portant to note that the fluorescence lifetimes measured with crossed-laser-beam excitation (identical conditions to grating decay measurements) are the same as those measured with standard single-beam excitation. Nonlinear diffusion and relaxation processes which could lead to the observed power dependence would also produce nonexponential decays in the fluorescence, which were not observed. One way to explain these observations is to postulate the presence of exciton trapping at centers which have fluorescence properties similar to the mirror-site ions but which have no difference in their complex refractive index when they are in the excited state instead of the ground state. These would act as quenching centers for the grating but not the fluorescence, while enhanced trapping through exciton-exciton or exciton-phonon processes could provide the observed power dependence of the grating decay rate. Finally, it should be pointed out that the simple expression given for K in Eq. (1) is strictly valid only for a limited region of the relative strength of the exciton scattering rate compared to the ion-ion interaction rate.[16] For values of these parameters outside of the allowed region, the exact expression for the dependence of K on θ deviates from a simple straight line at small values of θ and can actually be made to fit the low-temperature data shown in Fig. 4 with the measured value for $2/\tau$ at $\theta = 0°$. The usefulness of such a fit is limited at the present time by the lack of knowledge of the microscopic interaction parameters. This will be the subject for future investigations.

A similar discrepancy between the grating decay rate at zero crossing angle and twice the fluorescence decay rate was observed in FWM experiments on ruby crystals with high Cr^{3+} concentrations[6] and was attributed to the presence of exchange-coupled pairs of Cr^{3+} ions. No energy migration was observed by FWM measurements in heavily doped ruby. In alexandrite, the pairs are present even at low Cr^{3+} concentrations due to the nonuniform distribution effects.[2] It is not clear at the present time what role these pairs play in the grating dynamics, but their effects on the FWM results in concentrated ruby indicate that they may be responsible for the enhanced FWM signal decay and its power dependence observed in alexandrite at low temperatures.

IV. FWM MEASUREMENT OF DEPHASING TIME

The standard theoretical formalism used to interpret FWM signals is based on the interaction of three laser beams with a two-level atomic system.[17-19] Although there have been some attempts to extend the theory to account for the presence of additional levels of the atomic system, the results become extremely complicated and no model has been developed that is generally useful in the interpretation of experimental data. For the FWM experiments on alexandrite described here, the laser write beams interact directly with the $^4A_{2g}$-$^4T_{2g}$ transition of the Cr^{3+} ions. Fast radiationless relaxation occurs to the ^2E_g metastable state. The laser-induced population grating will be made up of ions in both the unrelaxed $^4T_{2g}$ level and the ^2E_g metastable state. In general, it is difficult to separate the contributions to the FWM signal due to the two types

of population gratings. Most of the FWM characteristics will be associated with the metastable state due to its greater population. However, the dephasing of an atomic system driven by coherent laser beams in generally associated with the unrelaxed excited state of the atomic transition in resonance with the laser frequency. Thus, in the alexandrite experiments described here, the dephasing time T_2 of the FWM signal should be attributed to phonon scattering and relaxation processes occurring in the $^4T_{2g}$ level. We describe below an analysis of the FWM scattering-efficiency data obtained on alexandrite, which results in the determination of the dephasing time of the $^4T_{2g}$ level. The normal two-level system model for FWM is used in this analysis since no appropriate multilevel model is available. Thus the results should be taken as a qualitative demonstration of the analysis technique, and the quantitative values should be considered as only approximations to the physical quantities. The comparison of the results of our analysis with values of the same parameters obtained by other experimental methods discussed below shows that the two-level model provides a

good approximation for this case. It should also be pointed out that recent accumulated photon-echo experiments on Nd^{3+} ions in glass have also used this type of two-level model to determine the radiationless relaxation time of a multilevel atomic system.[20]

The exact dependence of the FWM signal efficiency with the crossing angle of the write beams varies with the relative contributions to the laser-induced grating from the modulation of the absorption and dispersion components of the complex refractive index, $\Delta\alpha$ and Δn, respectively. The dephasing time of the atomic system depends on the ratio of these modulation depths. Thus, analyzing the angular dependence of the FWM signal efficiency provides a method for determining T_2.

A. Computer modeling of $\eta(\theta)$

Using the master-equation approach, the polarization of a two-level system in resonance with a laser driving field can be derived to be[17-19]

$$\tilde{P}=(\bar{\mu}^2\Delta N_0 T_2 E/\hbar)\{[\sin(\omega t)+(\omega_{21}-\omega)T_2\cos(\omega t)][1+(\omega-\omega_{21})^2 T_2^2+4\Omega^2 T_2\tau]^{-1}\}+\xi E\cos(\omega t) . \tag{10}$$

The first term represents the contribution due to the atomic transition near resonance with the laser frequency, while the second term (ξ) represents the combined effects of all other transitions in the sample.[21] Here, $\bar{\mu}$ is the dipole moment of the transition, ΔN_0 is the average equilibrium density of the population difference between the ground and excited states, τ is the fluorescence decay time of the excited state, E is the electric field of the laser beams in the crystal, ω is the angular frequency of the laser, ω_{21} is the resonant frequency of the atomic transition, and $\Omega=\bar{\mu}E/(2\hbar)$ is the precession frequency of the dipole moment. The polarization can be used to obtain the complex susceptibility

$$\chi=(\bar{\mu}^2\Delta N_0 T_2/\hbar)\{[T_2(\omega_{21}-\omega)-i]$$
$$\times[1+(\omega-\omega_{21})^2 T_2^2+4\Omega^2 T_2\tau]^{-1}\}\xi .$$
$$\tag{11}$$

The information concerning the physical characteristics of the system pertaining to absorption, dispersion, FWM, and saturation are contained in χ.

In cgs units, the wave equation describing the propagation of the laser beams in the atomic system is

$$\nabla^2 E=(\mu/c^2)\frac{\partial^2 E}{\partial t^2}+(4\mu\pi/c^2)\frac{\partial^2 P}{\partial t^2} . \tag{12}$$

The electric fields of the laser beams can be described as plane waves,

$$E_i(r,t)=(A_i/2)\exp[-i(\omega_i t-k_i\cdot r)]+c.c. ,$$
$$i=1-4 . \tag{13}$$

For degenerate FWM, all ω_i are equal, all $|k_i|=k$, and, to satisfy the Bragg scattering condition, $\sum_i k_i=0$. If E_1 and E_2 represent the write beams, the read beam E_3 is counterpropagating to E_1 and the signal beam E_4 is counterpropagating to E_2. To simplify the mathematical expressions, degenerate FWM is assumed. This will thus be only an approximation of our experimental condition in which the read beam had a different frequency than the write beams. Rough calculations using the exact readbeam frequency indicate that negligible error is introduced by this simplification as long as the read beam is weak enough that it does not affect the population grating. In addition, we make several assumptions relevant to our experimental conditions. The write beams are assumed to be more intense than the read and signal beams, the signal beam is assumed to be weaker than the read beam, and it is assumed that the weak beams have no beam depletion. Substituting the polarization and field expressions into the wave equation, using the "slowly varying envelope approximation," and equating like k-vector exponentials, a set of coupled, complex, differential equations are obtained. The scattering efficiency is defined as $\eta=|A_4|^2/|A_3|^2$, where the A_i represent the amplitudes of the beams. It is common practice to work with the normalized scattering efficiency, which depends only on A_4. In this case we need to consider only the coupled equations for A_2 and A_4, which can be separated into real and imaginary parts. Their variation with the write-beam crossing angle in the crystal θ is given by

$$\frac{dA_2^i}{d\theta} = [(A_2^rD_1^r - A_2^iD_1^i - A_2^rD_2^r - A_2^iD_2^i)k_1 \csc(\theta/2) - (D_2^rA_4^r - D_2^iA_4^i)(k_3^2/k_1)\csc(\theta/2)]/2 , \qquad (14)$$

$$\frac{dA_2^r}{d\theta} = [(-A_2^iD_1^r - A_2^rD_1^i + A_2^iD_2^r - A_2^rD_2^i)k_1\csc(\theta/2) - (D_2^iA_4^r + D_2^rA_4^i)(k_3^2/k_1)\csc(\theta/2)]/2 , \qquad (15)$$

$$\frac{dA_4^i}{d\theta} = [(-A_4^rD_1^r + A_4^iD_1^i + A_4^rD_2^r + A_4^iD_2^i)k_3\csc(\theta/2) + (D_2^rA_2^r - D_2^iA_2^i)(k_1^2/k_3)\csc(\theta/2)]/2 , \qquad (16)$$

$$\frac{dA_4^r}{d\theta} = [(A_4^iD_1^r + A_4^rD_1^i - A_4^iD_2^r + A_4^rD_2^i)k_3\csc(\theta/2) + (D_2^iA_2^i + D_2^rA_2^r)(k_1^2/k_3)\csc(\theta/2)]/2 , \qquad (17)$$

where the superscripts r and i refer to real and imaginary, respectively, and the coupling coefficients are

$$D_1 = D_1^r + iD_1^i = 2\pi\mu R(\kappa - \xi) , \qquad (18)$$

$$D_2 = D_2^r + iD_2^i = \pi\mu R \, \Delta\kappa . \qquad (19)$$

Here, R is the distance from the center of the overlap region of the beams, μ is the permeability of the material, κ is a complex parameter related to the complex index of refraction, and $\Delta\kappa$ is the laser-induced modulation in this parameter. The latter parameters are given by[17-19]

$$\kappa = \alpha_0(i + \delta)(1 + \delta^2)(1 + \delta^2 + |E/E_s|^2)^{-2} , \qquad (20)$$

$$\Delta\kappa^* = 2 |E/E_s|^2[\alpha_0(i + \delta)](1 + \delta^2 + |E/E_s|^2)^{-2} , \qquad (21)$$

where the detuning parameter is $\delta = (\omega - \omega_{12})T_2$, α_0 is the peak absorption coefficient, and E_s is the saturation field. The detuning parameter which accounts for the width of the resonant electronic transition contains the frequency dependence of the results. For laser fields much smaller than the saturation field, $\kappa \approx \chi + \xi$ and $\Delta\kappa^* \approx \Delta\chi$.

It is not possible to obtain a general analytic solution for η which has a simple enough form to be useful in fitting experimental data.[7] In order to understand the variation of scattering efficiency with write-beam crossing angle, it is necessary to either make several simplifying assumptions or to resort to numerical solutions. We compare here the results of both approaches.

Equations (14)–(16) can be solved numerically using a fourth-order Runge-Kutta method. Treating the real and imaginary parts of both coupling parameters as adjustable parameters, curves with various shapes can be obtained. Three examples are shown in Fig. 8. Although each of these show the FWM scattering efficiency rising sharply to a peak value and then decreasing at larger angles, the exact position of the peak and the rate of decrease with crossing angle vary greatly with choice of coupling parameters. The peak shifts to higher angles and the curve shape becomes broader as D_2^r or D_2^i are increased, whereas increases in D_1^r or D_2^i have the effect of raising the scattering efficiency at larger angles. The values of the components of the coupling parameters are related to the laser-induced modulations of the absorption and dispersion parts of the refractive index by

$$\Delta\alpha = (4\pi\omega/nc)\,\mathrm{Im}(\chi) = -2\alpha D_2^i/D_1^i , \qquad (22)$$

$$\Delta n = (2\pi/n)\,\mathrm{Re}(\chi) = (\alpha c/\omega)D_2^r/D_1^i , \qquad (23)$$

where α is the average absorption coefficient of the ma-

terial at the write-beam wavelength, ω. Thus as Δn or $\Delta\alpha$ increases, the peak of the curve shifts to higher angles, and an increase in α increases η at larger angles.

To obtain an approximate expression for $\eta(\theta)$, Eqs. (12)–(14) can be linearized by making the substitution $t = 2\ln[\tan(\theta/4)]$. Then the secular equation can be solved to obtain solutions for different special cases. For example, if

$$(D_2^i)^2 + (D_2^r)^2 - (D_1^i + D_2^i)^2 > 0$$

and

$$|D_1^r - D_2^r| \neq \begin{cases} 0 \\ [(D_2^i)^2 + (D_2^r)^2 - (D_1^i + D_2^i)^2]^{1/2} , \end{cases}$$

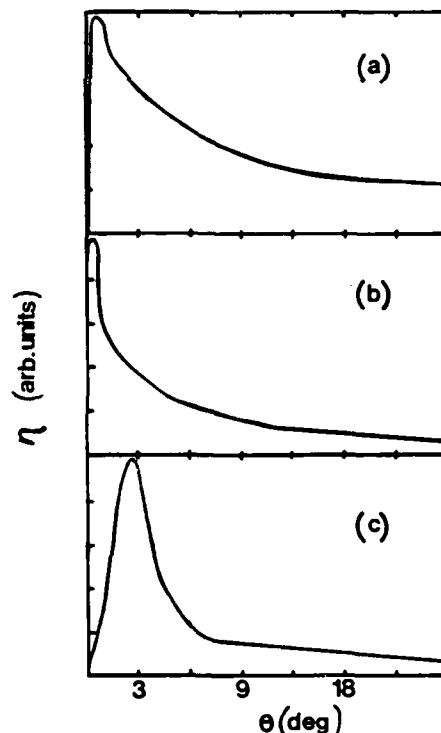the solution is

FIG. 8. Computer-generated plots of the FWM scattering efficiency vs the write-beam crossing angle for different values of the coupling parameters. (a) $D_1^r = 0.005$, $D_1^i = 0.100$, $D_2^r = 0.125$, and $D_2^i = 0.00002$. (b) $D_1^r = 0.006$, $D_1^i = 0.025$, $D_2^r = 0.090$, and $D_2^i = 0.00002$. (c) $D_1^r = 0.005$, $D_1^i = 0.075$, $D_2^r = 0.188$, and $D_2^i = 0.000096$.

$$\eta(\theta)=2[(\Gamma_2^i)^2+(D_2^r)^2][(D_2^i)^2+(D_2^r)^2-(D_1^i+D_2^i)^2]^{-1}\sin^2\{k[(D_2^i)^2+(D_2^r)^2-(D_1^i+D_2^i)^2]^{1/2}\ln[\tan(\theta/4)]\} . \qquad (24)$$

For the appropriate choices of the coupling parameters, Eq. (24) gives curves similar to those shown in Fig. 8. Other special cases will have significantly different forms for the solution of the coupled differential equations, but they predict the same general dependence of η on θ.

The advantage of the analytic solution is that it provides some insight into the origin of the angular dependence of the FWM scattering efficiency. The factor containing θ in the expression shown in Eq. (24) is related to the interaction length of the read beam with the grating, and the additional parameters in the argument of sine function describe the density of the grating fringes and the grating modulation depth. Evidently, it is the variation of these parameters that determines the shape of the curves of $\eta(\theta)$. The disadvantages of the analytic solution are that it is difficult to justify the assumptions necessary to define a specific case, and it is not possible to independently determine values for Δn and $\Delta\alpha$. Both of these disadvantages are overcome by using the numerical method of solution.

B. Interpretation of results

The numerical method for solving Eqs. (14)–(17) was applied to experimental data obtained on alexandrite and ruby crystals. Figure 9 shows the measured values of
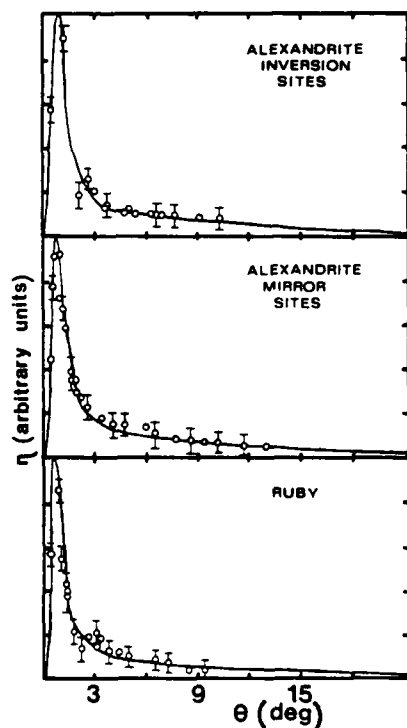

FIG. 9. FWM signal efficiency vs the write-beam crossing angle at 300 K for Cr^{3+} ions in the mirror sites and inversion sites in alexandrite and in ruby. (See text for explanation of theoretical lines.)

FWM scattering efficiency versus write-beam crossing angle for Cr^{3+} ions in both types of crystal-field sites in alexandrite and in ruby. The solid lines represent the best fits to the data using the numerical-solution technique and a nonlinear-regression least-squares-fitting routine, with the real and imaginary components of the coupling coefficients treated as adjustable parameters. The results were found to be independent of temperature between 30 and 300 K. The fitting parameters were substituted into Eqs. (22) and (23) to obtain values for the laser-induced modulation depths due to changes in absorption and dispersion. The values obtained from this procedure are listed in Table II.

Once these parameters are known, Eq. (21) can be solved for the dephasing time of the atomic system,

$$T_2 = (2\omega/c)(\Delta n/\Delta\alpha)(\omega-\omega_{12})^{-1} . \qquad (25)$$

The values of T_2 obtained for ruby and alexandrite are given in Table II.

For the two materials investigated here, the theoretical fitting of the angular dependence of the FWM scattering efficiency is very sensitive to changes in D_2^r but very insensitive to changes in D_2^i, since the magnitude of the latter parameter is very small. This results in an accurate determination of Δn but not $\Delta\alpha$. Previous approaches to calculating these components of the modulation depths provide an accurate method for determining $\Delta\alpha$ but not Δn.[19,22] The calculation of $\Delta\alpha$ based on a two-level system gives[4,19]

$$\Delta\alpha=N_0 I_0\sigma_1(\sigma_2-\sigma_1)(2I_0\sigma_1+h\nu/\tau)^{-1} , \qquad (26)$$

where N_0 is the concentration of active ions, I_0 is the energy density of the write beams with photon energy $h\nu$, and σ_1 and σ_2 are the ground- and excited-state absorption cross sections, respectively. Since excited-state absorption measurements have been made for both ruby[23] and alexandrite,[24] it is possible to obtain an accurate value of $\Delta\alpha$ using Eq. (26). The error bars listed in Table II are associated with estimates of the parameters used in Eq. (26) as well as with the curve-fitting procedure used to determine the coupling parameters.

TABLE II. FWM measurements of dephasing times in alexandrite and ruby at room temperature.

Parameter	Alexandrite Inversion sites	Alexandrite Mirror sites	Ruby
α (cm^{-1})	0.36	1.05	1.37
I_0 (W/cm^2)	60	50	60
η	10^{-4}	10^{-4}	10^{-4}
$\Delta\alpha$ (cm^{-1})	1.10×10^{-3}	1.90×10^{-2}	1.06×10^{-2}
Δn	2.52×10^{-5}	1.83×10^{-5}	8.16×10^{-5}
T_2 (psec)	80 ± 5	2.2 ± 4	4.5 ± 2
ΔE (cm^{-1})	6400	800	2300

The transverse relaxation time T_2 is related to the lifetime of the excited level T_1 and the pure dephasing rate due to scattering events γ by

$$T_2^{-1} = (2T_1)^{-1} + \gamma .\tag{27}$$

If the fast radiationless relaxation from the $^4\Gamma_{2g}$ "pump band" to the ^2E_g metastable state is the dominant process for dephasing the atomic system, the values determined for T_2 represent twice the relaxation times associated with this process. The value of 2.25 psec obtained in this way for T_1 in ruby is consistent with the upper limit of 7 psec found from pulse-probe measurements to be the $^4T_{2g}$-^2E_g relaxation rate.[25] The longer dephasing time found for alexandrite inversion-site ions which have a $^4T_{2g}$-^2E_g energy difference almost 3 times greater than in ruby, and the smaller dephasing time obtained for mirror-site ions in alexandrite which have a smaller energy-level difference between the pump band and metastable state, establish the existence of a relationship between the values of T_2 and the energy-level splitting of the excited states. This is shown explicitly in Fig. 10. The observed dependence of T_2 on ΔE is expected if the radiationless transitions between the $^4T_{2g}$ and ^2E_g levels are responsible for the dephasing of the system. Measurements made on alexandrite at 30 K gave the same value for T_2 as found at 300 K, indicating that strongly temperature dependent phonon scattering processes are not important.

From the preceding discussion, it appears that the $^4T_{2g}$-^2E_g relaxation process does dominate the dephasing for the FWM experiments on ruby and alexandrite. This decay process causes "lifetime broadening" of the $^4T_{2g}$ level. The zero-phonon lines of the lowest-lying crystal-field state of this level for ruby and the mirror-site ions in alexandrite have been observed[3,26] at low temperatures to have linewidths of the order of 25 cm^{-1}, which is significantly greater than the predicted contributions to the linewidth of a few wave numbers obtained from the measured values of T_2. This is due to the fact that these lines exhibit significant inhomogeneous broadening due to the

sensitivity of the $^4T_{2g}$ level to the local crystal field. Since these lines appear on the side of the broad vibronic band, it is difficult to accurately deconvolute the homogeneous and inhomogeneous contributions to the line shape.

These results imply that the $^2T_{1g}$ levels lying between the $^4T_{2g}$ and E_{2g} levels do not play a significant role in the pump-band—to—metastable-state relaxation process. This is consistent with previous theoretical predictions.[27]

V. DISCUSSION AND CONCLUSIONS

The observation of long-range energy migration among the mirror-site Cr^{3+} ions in alexandrite at low temperatures is a surprising result. Attempts to observe energy migration in ruby using FWM techniques have been repeated several times without success.[6,28,29] The observed energy-transfer characteristics are consistent with having a higher concentration of Cr^{3+} ions than predicted by assuming a uniform distribution of mirror-site ions. An increase by about a factor of 2.35 in the local density of Cr^{3+} ions over the average concentration will account for the observed characteristics. This is not unreasonable because of the chromium-ion banding that occurs in planes perpendicular to the direction of crystal growth in alexandrite.[15] Also, it should be emphasized that the simple exchange model used in Sec. III to analyze the FWM results underestimates the strength of the ion-ion interaction causing the energy transfer. The superexchange model used to explain transfer in ruby provides an interaction mechanism that is stronger and more directional than direct-exchange interaction.[9,10] Developing a superexchange model for ion-ion interaction in alexandrite is an important problem for future theoretical work.

The lack of any observed long-range energy transfer among the inversion-site Cr^{3+} ions is consistent with the lower concentration of these ions compared to the mirror-site ions. The evidence of enhanced energy transfer from mirror-site to inversion-site ions at low temperature is consistent with the results of time-resolved, site-selection spectroscopy measurements reported previously.[2] The temperature range in which nonexponential grating decays are observed is the same as the temperature range in which site-selection spectroscopy results show enhanced energy transfer to occur. The rate of diffusion-controlled energy transfer is given by

$$W_{mi} = 4\pi D R_i N_i ,\tag{28}$$

where R_i and N_i are the exciton-trapping radius and concentration of inversion-site ions. Using the nearest-neighbor distance between an inversion- and mirror-site ion for R_i and the diffusion coefficient found from FWM measurements, the transfer rate at 6 K is estimated to be of the order of 3×10^5 sec^{-1}. This value is consistent with the energy-transfer rate at 10 K determined by the site-selection spectroscopy measurements reported in Ref. 2 if the average separation between a mirror-site and inversion-site ion is about 12 Å. It is difficult to determine an accurate value for the average separation between mirror-site and inversion-site ions due to the nonuniform distribution of Cr^{3+} ions discussed previously. However, there appears to be both quantitative and qualitative
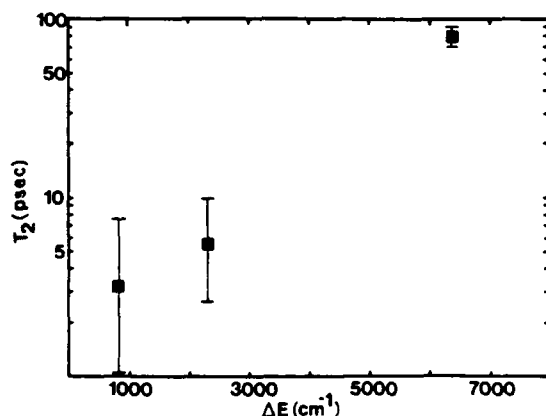

FIG. 10. Variation of dephasing time obtained from analysis of FWM measurements with the energy-level splitting of the $^4T_{2g}$ and ^2E_g levels for Cr^{3+} ions in alexandrite and ruby.

agreement in the results on energy transfer between mirror- and inversion-site ions obtained by the two different types of experimental techniques.

The investigation of the FWM scattering efficiency on the crossing angle of the write beams described here is important for two reasons. First, it demonstrates a method for determining the contributions to the laser-induced refractive-index gratings due to absorption changes and to dispersion changes. It is difficult to determine the relative contributions from these two types of gratings using other techniques. Second, it provides a measurement of the dephasing time of an atomic system driven by laser sources. Other coherent transient techniques for obtaining T_2, such as photon-echo measurements, have generally been used only for probing metastable states such as the ^2E_g level of ruby[30] where the dephasing time is much longer. The accumulated photon-echo technique recently applied to rare-earth-doped glasses[20] has provided the same type of information on T_2 of nonmetastable states as our experimental technique, and comparing the results of these two types of experiments on the same sample will be the subject of future research. Determination of T_2 through linewidth measurements is complicated by inhomogeneous broadening.

An important question concerning these results is the relationship between the values of T_2 determined from the analysis of the FWM data and the pump-band—to—metastable-state radiationless relaxation rate for the Cr^{3+}-doped laser crystals investigated here. This has been a parameter of interest for many years and has always been difficult to measure.[25−27,31−42] The actual relaxation process can be divided into several steps, including relaxation to the bottom of the vibronic potential well of the $^4T_{2g}$ level, crossover to an excited vibrational level of the ^2E_g level, and relaxation to the bottom of the ^2E_g level. The measured dephasing time may be associated with one specific step in this overall process and the total relaxation time may be longer. However, the data indicate a close relationship between these two times, especially in terms of the energy-gap dependence shown in Fig. 10 and the fact that the magnitudes of the relaxation times determined from the measured T_2's compare favorably with those determined from other measurements. The lack of any observed temperature variation of T_2 in the range investigated is consistent with the temperature dependence expected for phonon-emission processes involving large energy gaps of the size relevant to these data. Establishing the exact relationship between T_2 and the relaxation time requires additional work with direct picosecond pulse-probe measurements which will be the subject of future work.

ACKNOWLEDGMENTS

[1]J. C. Walling, O. G. Peterson, H. P. Jenssen, R. C. Morris, and E. W. O'Dell, IEEE J. Quantum Electron. QE-16, 1302 (1980); J. C. Walling, D. F. Heller, H. Samelson, D. J. Harter, J. A. Pete, and R. C. Morris, ibid. QE-21, 1568 (1985).

[2]R. C. Powell, L. Xi, X. Gang, G. J. Quarles, and J. C. Walling, Phys. Rev. B 32, 2788 (1985).

[3]A. B. Suchocki, G. D. Gilliland, R. C. Powell, J. M. Bowen, and J. C. Walling (unpublished).

[4]A. M. Ghazzawi, J. K. Tyminski, R. C. Powell, and J. C. Walling, Phys. Rev. B 30, 7182 (1984).

[5]J. R. Salcedo, A. E. Siegman, D. D. Dlott, and M. D. Fayer, Phys. Rev. Lett. 41, 131 (1978).

[6]H. J. Eichler, J. Eichler, J. Knof, and Ch. Noack, Phys. Status Solidi A 52, 481 (1979).

[7]C. M. Lawson, R. C. Powell, and W. K. Zwicker, Phys. Rev. Lett. 46, 1020 (1981); C. M. Lawson, R. C. Powell, and W. K. Zwicker, Phys. Rev. B 26, 4836 (1982); J. K. Tyminski, R. C. Powell, and W. K. Zwicker, ibid. 29, 6074 (1984).

[8]V. M. Agranovich and M. D. Galanin, Electronic Excitation Energy Transfer in Condensed Matter (North-Holland, Amsterdam, 1982); V. M. Agranovich and Yu. V. Konobeev, Opt. Spektrosk. 6, 242 (1959); 6, 648 (1959) [Opt. Spectrosc. (USSR) 6, 155 (1959); 6, 421 (1959)]; Phys. Status Solidi, 27, 435 (1968).

[9]R. J. Birgeneau, J. Chem. Phys. 50, 4282 (1969).

[10]J. Koo, L. R. Walker, and S. Geschwind, Phys. Rev. Lett. 35, 1669 (1975).

[11]D. L. Dexter, J. Chem. Phys. 21, 836 (1953); Phys. Rev. 126, 1962 (1962).

[12]G. F. Imbusch, Phys. Rev. 153, 326 (1967).

[13]S. Chandrasekhar, Rev. Mod. Phys. 15, 1 (1943).

[14]A. Monteil and E. Duval, J. Phys. C 13, 4565 (1980).

[15]S. C. Stotlar and L. B. Edgett, in Proceedings of the Optical Society of America Annual Meeting, Washington, D. C., 1985 (unpublished).

[16]V. M. Kenkre and D. Schmid, Phys. Rev. B 31, 2430 (1985).

[17]A. Yariv and D. M. Pepper, Opt. Lett. 1, 16 (1977).

[18]R. L. Abrams and R. C. Lind, Opt. Lett. 2, 94 (1978); 3, 205 (1978).

[19]K. O. Hill, Appl. Opt. 10, 1695 (1971).

[20]S. Asaka, H. Nakatsuka, M. Fujiwara, and M. Matusoka, Phys. Rev. A 29, 2286 (1984); H. Nakatsuka, M. Tomita, M. Fujiwara, and S. Asaka, Opt. Commun. 52, 150 (1984); M. Tomita and M. Matsuoka, J. Opt. Soc. Am. B 3, 560 (1986).

[21]A. Yariv, Quantum Electronics (Wiley, New York, 1975).

[22]K. A. Nelson, R. Cassalegno, R. J. D. Miller, and M. D. Fayer, J. Chem. Phys. 77, 1144 (1982).

[23]W. M. Fairbank, Jr., G. K. Klauminzer, and A. L. Schawlow, Phys. Rev. B 11, 60 (1975).

[24]M. L. Shand, J. C. Walling, and R. C. Morris, J. Appl. Phys. 52, 953 (1981).

[25]S. K. Gayen, W. B. Wang, V. Petricevic, R. Dorsinville, and R. R. Alfano, Appl. Phys. Lett. 47, 455 (1985).

[26]A. Misu, J. Phys. Soc. Jpn. 19, 2260 (1964).

[27]R. Englman, B. Champagnon, E. Duval, and A. Monteil, J. Lumin. **28**, 337 (1983).

[28]D. S. Hamilton, D. Heiman, J. Feinberg, and R. W. Hellwarth, Opt. Lett. **4**, 124 (1979).

[29]P. F. Liao, L. M. Humphrey, D. M. Bloom, and S. Geschwind, Phys. Rev. B **20**, 4145 (1979); P. F. Liao and D. M. Bloom, Opt. Lett. **3**, 4 (1978).

[30]I. D. Abella, N. A. Kurnit, and S. R. Hartmann, Phys. Rev. **141**, 391 (1966).

[31]B. Z. Malkin, Fiz. Tverd. Tela (Leningrad) **4**, 2214 (1962) [Sov. Phys.—Solid State **4**, 1620 (1963)].

[32]A. Kiel, in *Quantum Electronics, Proceedings of the Third International Conference, Vol. 1,* edited by P. Grivet and N. Bloembergen (Columbia University Press, New York, 1963), p. 535.

[33]J. Brossel and J. Margerie, in *Paramagnetic Resonance, Vol. II,* edited by W. Low (Academic, New York, 1963), p. 353.

[34]B. S. Tsukerblat and Yu. E. Perlin, Fiz. Tverd. Tela (Leningrad) **7**, 3278 (1965) [Sov. Phys.—Solid State **7**, 2647 (1966)].

[35]P. Kisliuk and C. A. Moore, Phys. Rev. **160**, 307 (1967).

[36]J. A. Calviello, E. W. Fisher, and Z. H. Heller, J. Appl. Phys. **37**, 3156 (1967).

[37]S. A. Pollack, J. Appl. Phys. **38**, 5083 (1967); IEEE J. Quantum Electron. QE-4, 703 (1968).

[38]M. Anson and R. C. Smith, IEEE J. Quantum Electron. QE-6, 268 (1970).

[39]P. N. Everett, J. Appl. Phys. **42**, 2106 (1971).

[40]W. H. Fonger and C. W. Struck, Phys. Rev. B **11**, 3251 (1975).

[41]J. E. Rives and R. S. Meltzer, Phys. Rev. B **16**, 1808 (1977).

[42]M. Montagna, O. Pilla, and G. Viliani, Phys. Rev. Lett. **45**, 1008 (1980).

1

OPTICAL SPECTROSCOPY OF Cr^{3+} AND Rh^{2+} IN SODIUM-BETA″-ALUMINA

Richard C. POWELL, George E. VENIKOUAS * and Lin XI

Department of Physics, Oklahoma State University, Stillwater, OK 74078, U.S.A.

J.B. BATES

Solid State Division, Oak Ridge National Laboratory, Box X, Oak Ridge, TN 37830, U.S.A.

Ion exchange techniques were used to substitute Cr^{3+} and Rh^{2+} ions for the sodium ions present in sodium-beta″-alumina single crystals. The optical absorption and fluorescence spectra were obtained and the fluorescence lifetimes measured for both types of samples. In each case the emission consisted of two bands having significantly different decay times. The temperature dependences of the fluorescence intensities and lifetimes were measured for these bands. The results are interpreted in terms of the energy level structures of these ions in different crystal field sites in this host lattice and the diffusion of ions in the conduction plane which changes these sites.

1. Introduction

The beta″-aluminas are important solid electrolytes because of their high ionic conductivity [1,2]. Recently it has been shown that single crystals of this material can be used as a host for various luminescent impurity ions [3,4] and a Nd^{3+}-exchanged sample has been operated as a laser [5]. The main interest in β''-alumina crystals as a laser host material is associated with the ability to diffuse high concentrations of active ions into the open planes of the crystal. It is speculated that the spacings between the sites in the conduction plane will allow only weak interactions between the active ions. This would result in the presence of high densities of active ions without strong concentration quenching, a condition which is necessary for efficient luminescent materials. We report here the optical spectroscopic properties of sodium-beta″-alumina with Cr^{3+} or Rh^{2+} ion exchange. Both are

known to be good luminescent ions in other crystals [6].

The conduction planes of Na-β''-alumina contain Na^+ ions and oxygen ions which act as a bridge between two spinel blocks [1–5]. There are two types of Na^+ sites in the plane. One is a site which is normally vacant called the mid-oxygen site since it is located between two bridging O^{2-} ions. The nearest neighbor oxygen ions provide octahedral coordination and bipyramidal symmetry for this site. The second type of site normally occupied by Na^+ ions is tetrahedrally coordinated with the O^{2-} ions on either side of the conduction plane and has T_d symmetry. Either of these types of sites may be occupied by exchanged transition metal ions. The distribution of sodium ions and vacancies around either of these sites will change the crystal field seen by an impurity ion occupying the site. The ions in the conduction planes are mobile, and the results reported here demonstrate the usefulness of transition metal ions as fluorescence probes for studying ionic rearrangements in the conduction plane of Na-β''-alumina.

The samples used were single crystals of

* Present address: Electronics Materials Division, Union Carbide Corp., 823 River St., Washougal, WA 02726, U.S.A.

$Na_{1.67}Mg_{0.67}Al_{10.33}O_{17}$ in the form of platelets a few millimeters square and about a millimeter thick. The unexchanged material had excellent optical quality and the absorption spectra showed no trace of optically active impurity ions. Ion exchange was accomplished by the standard technique of suspending the crystal by a wire in a crucible above a melt containing the ion desired for exchange ($CrCl_3$) or $RhCl_2$) [7]. The crucible was heated to 700 °C for 12 h. For both Cr^{3+} and Rh^{2+} the crystals colored deeply indicating a high percentage of ion exchange had taken place. Complete exchange would result in a concentration of active ions of the order of 1.5×10^{21} cm^{-3}. These conditions have been shown previously to produce 90% exchange, and X-ray diffraction has shown that the exchanged crystals retain the β''-alumina crystal structure [7]. However, the exchanged crystals had very poor optical quality and it was difficult to obtain a good surface polish because flaking occurred. This may be due to the strain induced in the lattice by the size differences and charge mismatch of the exchanged ions.

The absorption spectra were obtained on a Perkin–Elmer spectrophotometer. Fluorescence spectra and lifetime measurements were performed using a nitrogen laser to provide an excitation pulse 10 ns in duration and 0.1 nm in width at 337.1 nm focused to an energy density of 10^2 mJ/cm^2. Additional lifetime measurements were made using a Nd–YAG laser doubled to 532 nm to excite the sample with pulses 30 ps in duration and with energy densities of 10^4 mJ/cm^2. The samples were mounted in a cryogenic refrigerator to control the temperature between 10 and 300 K. The fluorescence was analyzed by a one meter monochromator, detected by an RCA C31034 photomultiplier tube, processed by an EGG–PAR boxcar integrator, and displayed on strip chart recorder. The boxcar window was either set to obtain the emission spectrum at a specific time after the excitation pulse or scanned to obtain the fluorescence lifetime.

2. Experimental results

The room temperature absorption spectra for Cr^{3+} and Rh^{2+} ions in Na-β''-alumina crystals
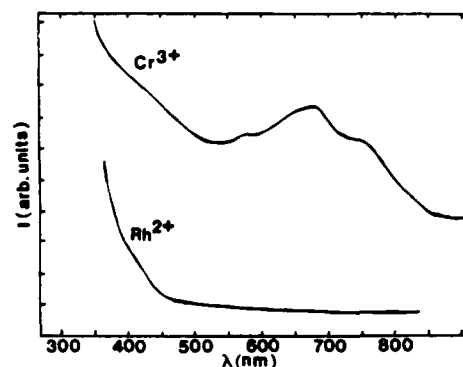
Fig. 1. Room temperature absorption spectra of Cr^{3+} and Rh^{2+} ions in Na-β''-alumina crystals.

are shown in fig. 1. The Cr^{3+}-exchanged crystal exhibits a broad band with three peaks centered near 680 nm. This is associated with the transitions to the crystal field split components of the
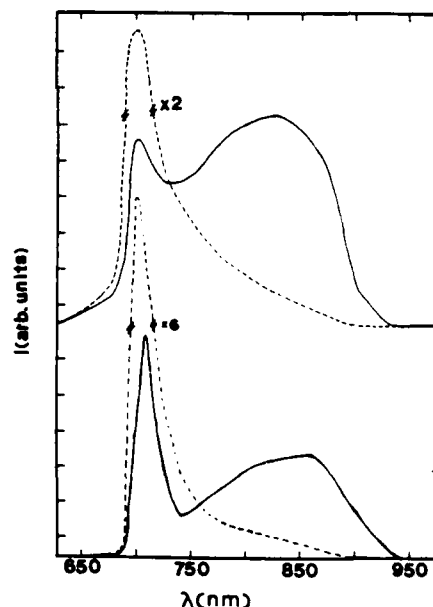
Fig. 2. Fluorescence spectra of Cr^{3+} in Na-β''-alumina crystals. Top: $T = 300$ K; solid line for 1 μs after the excitation pulse; broken line for 200 μs after the excitation pulse. Bottom: $T = 10$ K; solid line for 20 μs after the excitation pulse; broken line for 1 ms after the excitation pulse.

$^4T_2$ level which is generally the dominant absorption transition for Cr^{3+} in this spectral region. The band edge for this sample occurs near 350 nm with a broad tail extending to near 500 nm. This latter feature is attributed to transitions to the $^4T_1$ level. The Rh^{2+}-doped crystals have an absorption edge shifted to lower energy with a shoulder at about 420 nm and no absorption bands in the rest of the visible spectral region. This is consistent with the spectra of other Rh^{2+}-doped samples [6]. The low oscillator strength d–d transitions are difficult to detect in absorption and the band edge features are associated with strong charge transfer transitions.

The fluorescence spectra at two times after the nitrogen laser excitation pulse at both 300 K and 10 K are shown in figs. 2 and 3 for the two types of doped crystals. The spectra of both samples consists of broad, double peaked emission bands whose relative intensities evolve with time. For Cr^{3+}, the band at 700 nm is due to emission from the ^2E level of the $3d^3$ electronic configuration which appears at approximately the same position in all hosts. The width of this band in Na-β'''-alumina can be attributed to inhomogeneous braodening due to the significant amount of strain in the lattice. The lower energy emission near 820 nm comes from the Stokes shifted $^4T_2$ level and is broadened by vibronic interactions as well as inhomogeneous broadening. The Rh^{2+} fluorescence consists of two broad, overlapping bands with structure. The main peaks appear at about 600 and 700 nm. These are assigned to emission transitions from the lowest energy $^4T_2$ and ^2E levels of the $4d^7$ electronic configuration, respectively.

Figure 4 shows the results obtained from the measurements of the fluorescence lifetimes as a function of temperature with nitrogen laser excita-
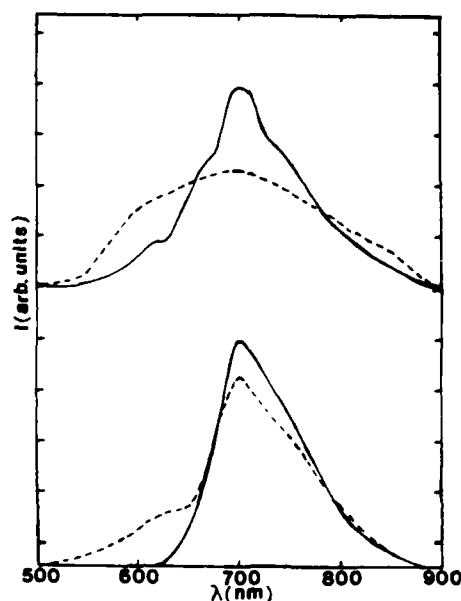
Fig. 3. Fluorescence spectra of Rh^{2+} in Na-β'''-alumina crystals. Top: $T = 10$ K: broken line for 25 μs after the excitation pulse: solid line for 1 ms after the excitation pulse. Bottom: $T = 300$ K: broken line for 25 μs after the excitation pulse: solid line for 700 μs after the excitation pulse.

Fig. 4. Temperature dependences of the fluorescence lifetimes of Cr^{3+} and Rh^{2+} emission bands in Na-β'''-alumina crystals. The open circles are for the 600 nm band of Rh^{2+} and the filled circles are for the 700 nm band of Rh^{2+}. The open squares are for the 700 nm band of Cr^{3+} and the filled squares are for the 820 nm band of Cr^{3+}.

tion. The 700 nm band of Cr^{3+} has a 2.3 ms lifetime at 10 K which decreases slightly to 1.2 ms at 300 K. The 820 nm band in this sample has a lifetime of about 54 μs independent of temperature. The 700 nm band in the Rh^{2+}-doped sample has a lifetime of about 8 ms independent of temperature, whereas the 600 nm band in this sample decreases from 192 μs at 10 K to 48 μs at 300 K. The magnitudes of these lifetimes are consistent with the transition assignments discussed in the previous paragraph. The long lifetimes involve spin forbidden transitions while the short lifetimes involve spin allowed transitions.
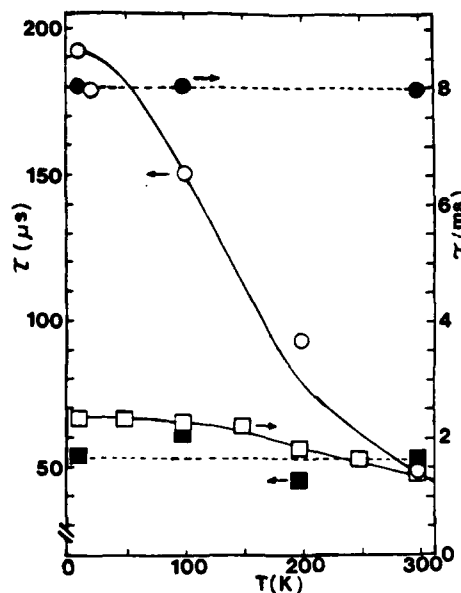
The fluorescence lifetimes of the Cr^{3+}-doped sample were also measured at room temperature after high power excitation with the frequency-doubled Nd–YAG laser. This 532 nm excitation directly pumps the d–d transitions in the visible region of the spectrum. Under these conditions the 820 nm band still exhibits a 54 μs lifetime, but it has a 26 μs risetime. However, 700 nm emission shows a strongly quenched lifetime of 4.5 μs.

The ratios of the integrated fluorescence intensities of the two bands are shown as a function of temperature in fig. 5 for the two samples. These are measured from the spectra taken at a long time after the excitation pulse when an equilibrium condition has been reached. For both samples, these ratios increase with temperature up to about 250 K and then decrease at room temperature.

3. Discussion and conclusions

In general, there are three types of physical processes which can be responsible for the type of spectral dynamics described in the preceding section. In some hosts, an optically active ion in a specific crystal field site can give fluorescence emission from two different excited states, and radiationless transitions coupling the two states can lead to a time evolution of the relative fluorescence intensities as well as a temperature dependence of the intensities and fluorescence lifetimes. If this were the case for Cr^{3+}-exchanged Na-β'''-alumina, the intensity of the $^4T_2$ emission would increase compared to the ^2E fluorescence as tem-
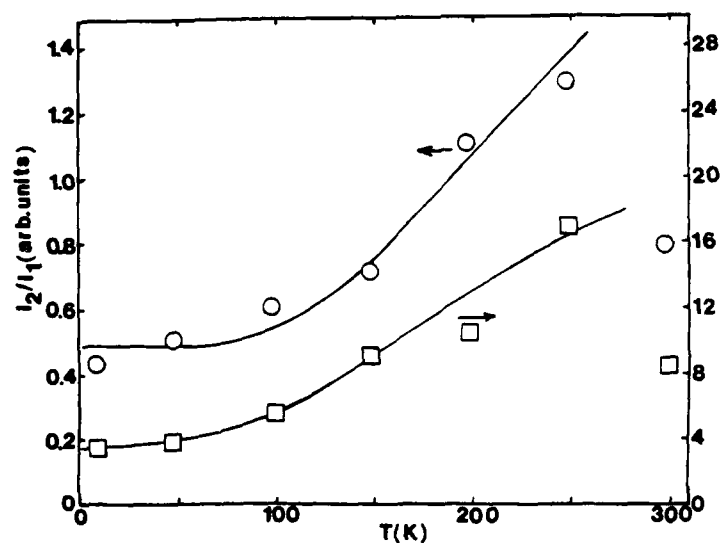

Fig. 5. Temperature dependence of the ratios of the integrated fluorescence intensities of the emission bands in Cr^{3+}- and Rh^{2+}-doped Na-β'''-alumina crystals at long times after the excitation pulse. Circles represent the ratios of the 700 nm band to the 820 nm band of Cr^{3+} and the squares represent the ratios of the 700 nm band to the 600 nm band of Rh^{2+}.

perature increases. This is opposite to the observed behavior. A similar argument can be made to rule out this model as an explanation for the Rh^{2+} data.

The second possibility is that the exchanged ions occupy two distinctly different types of crystal field sites in this lattice in which one site favors emission from the ^2E level while the other site favors fluorescence from the $^4T_2$ level. The spectral dynamics are then associated with energy transfer between ions in these nonequivalent types of sites. This model can be ruled out for the Cr^{3+}-exchanged sample because the ions in the site transferring the energy should exhibit a simultaneous decrease in their fluorescence intensity and lifetime as temperature is raised. Instead the $^4T_2$ band shows an intensity decrease with constant lifetime while the ^2E emission band has a temperature-dependent decrease in the lifetime. The same argument can not be made for the Rh^{2+}-exchanged sample since the $^4T_2$ band exhibits a decrease in both fluorescence intensity and lifetime as temperature is raised. However, it seems reasonable that the same types of processes should be responsible for the spectral dynamics for both types of ions in this material, and thus we must consider a different model for both sets of data.

The third possibility is that the active ions occupy two different types of crystal field sites, each having preferential emission from one of the two metastable states, and the high rate of diffusion of ions in the conduction plane changes the relative occupancy of the different types of sites. Although this is an unusual model for interpreting spectral data of the type reported here, it is appropriate for host crystals which are "superionic conductors" such as Na-β''-alumina. The lattice sites in the conduction plane contain Na^+, sodium ion vacancies, active ions substituted for Na^+, and bridging O^{2-} ions. The spectral properties of the active ions are determined primarily by the crystal field established by their near neighbor environment. Thermally activated ionic conductivity can cause the ions on the Na^+ sublattice to hop to new sites, thus changing the active ion environment.

In this model the temperature dependence of the relative fluorescence intensities of ions in two types of sites is given by

$$I_2/I_1 = A + B \exp(-\Delta E/kT). \qquad (1)$$

The observed band intensities are equal to the products of the concentrations of occupied sites giving rise to each type of emission and the radiative decay rates. The constant A represents the low-temperature equilibrium condition for site occupancy, which favors the lowest energy crystal field site (type 1 site). As the temperature is increased, ions in the conduction plane become mobile and hop to new lattice positions (type 2 sites) over a potential barrier with an activation energy ΔE. In order to explain the observed temperature dependence, the type 2 higher energy crystal field sites must have a greater probability of occupancy at high temperature leading to an increase in the relative emission from the band associated with ions in these sites as temperature is raised. The constant B represents the ratio of probabilities of occupying the two types of sites after factoring out the temperature dependent factor. This includes a diffusion coefficient describing the migration of ions through the lattice and a factor to account for the trapping of the ions in a specific type of site.

The fluorescence lifetime will not be quenched simply by the diffusion of ions with Cr^{3+} in the ground state. To account for the observed temperature dependences of the lifetimes it is necessary to assume that there are additional ion–lattice or ion–ion interaction mechanisms which change the radiative or radiationless emission rates and have a temperature-dependent probability of occurrence. The lifetimes can be described by the expression

$$\tau_i^{-1} = \tau_{ir}^{-1} + C \exp(-\Delta E'/kT). \qquad (2)$$

Here τ_{ir} is the intrinsic lifetime of the ith level and C is the rate of the quenching process with the temperature-dependent exponential factored out.

This model appears to explain the results obtained in this investigation. First consider the results obtained on Cr^{3+} in Na-β''-alumina. For type 1 sites, the crystal field is low enough that the Stokes shift of the $^4T_2$ level causes it to drop below the ^2E level and become the dominant level

for fluorescence emission. For type 2 sites the crystal field is greater so the relaxed $^4T_2$ level is higher in energy than the ^2E level causing the latter to be the dominant fluorescence level. The parameters used to fit eq. (1) to the data as shown by the solid line in fig. 5 are listed in table 1. The relevance of the magnitude for the activation energy is discussed later. The exact interpretation of the constants A and B is not possible because they depend on parameters such as the trapping rates and quantum efficiencies for each type of site. Although these parameters are not known, the values of A and B can be useful in comparing the two sets of data. The decrease in the observed intensity ratios between 250 K and room temperature may be due either to an increase in the radiationless decay rates of the Cr^{3+} ions or to the occupancy of a third type of site in which the Cr^{3-} ions do not have a fluorescence transition in this spectral region.

The constant fluorescence decay time observed for the 820 nm emission band indicates that the radiative and nonradiative decay rates of the $^4T_2$ level of ions in type 1 sites are both independent of temperature in the range investigated. The temperature dependence of the lifetime of the 700 nm emission band indicates a change in the ^2E decay rate of ions in type 2 sites. The parameters used to fit eq. (2) to the data as shown by the solid line in fig. 4 are listed in table 1. The activation energy for the lifetime quenching is significantly greater than that obtained from the intensity data, and the rate parameter C is significantly smaller than the $^4T_2$ emission rate. Thus the origin of the lifetime quenching of the ^2E level does not appear to be due either to phonon absorption to the $^4T_2$

level or to ionic diffusion. Two possible processes for the quenching are radiationless decay to the ground state and ion–ion interaction in which a Cr^{3+} ion in a type 2 site decays by radiationlessly transferring its energy to a neighboring Cr^{3+} ion. The observation that pumping at 532 nm at room temperature with power densities of 10^4 mJ/cm^2 causes the ^2E lifetime to be quenched from 1.2 ms to 4.5 μs with no risetime or double exponential decay suggests that ion–ion interaction is taking place. The fact that $^4T_2$ lifetime remains unchanged but the fluorescence exhibits a risetime of 26 μs under these pumping conditions indicates that at least part of the interaction is energy transfer from ions in type 2 sites to ions in type 1 sites.

Next consider the data obtained on Rh^{2+}-exchanged Na-β''-alumina. The broad, overlapping fluorescence bands indicate that the crystal fields at the Rh^{2+} ions in both types of sites is in the *low-field* region and slightly greater than the point where the decreasing ^2E level crosses the increasing $^4T_2$ level in the 4d^7 electron configuration in octahedral symmetry. Emission occurs from both levels with large Stokes shifts due to strong interactions with the lattice. In the lower crystal field type 1 sites the $^4T_2$ level is low enough to give fluorescence emission near 600 nm. In the higher crystal field type 2 sites the $^4T_2$ is shifted to higher energy and relaxes radiationlessly to the ^2E level which fluoresces near 700 nm. An alternate possibility is that the Rh^{2+} ions occupy sites with tetrahedral symmetry. However, in this case the emission from the ^2E level would have a narrower linewidth similar to the 700 nm band of Cr^{3+}.

The parameters used in eqs. (1) and (2) to fit the temperature-dependent intensity and lifetime data as shown by the solid lines in figs. 4 and 5 are listed in table 1. The activation energies found from lifetime and intensity data are the same. This implies that the interaction responsible for the lifetime quenching depends on the relative site occupancy and requires a thermal activation energy significantly less than that required for ionic diffusion. so that the latter processes controls the rate of the interaction. As before the specific meanings of the A and B parameters can not be determined from available information. Also the

Table 1
Summary of parameters

Parameter	Cr^{3+}	Rh^{2+}
τ_1 (μs)[10 K]	53	192
τ_2 (ms)[10 K]	2.3	8.0
$\Delta E'$ (cm^{-1})	556	203
ΔE (cm^{-1})	320	203
A	0.48	3.4
B	5.68	40.0
C (μs^{-1})	0.004	0.025

origin of the decrease in the intensity ratios between 250 and 300 K is uncertain. In this case lifetime of the ions in the type 2 sites is independent of temperature indicating that their decay processes are unaffected by ion–lattice and ion–ion interaction processes. One process consistent with these results is energy transfer from Rh^{2+} ions in type 1 sites to ions in type 2 sites. The rate of the energy transfer will increase as the concentration of acceptor ions increases.

An important question is the nature of the nonequivalent sites for the exchanged ions. The values of the ΔE and $\Delta E'$ for Cr^{3+} were found to be 320 cm^{-1} and 556 cm^{-1}, respectively, while a value of 203 cm^{-1} was found for both types of activation energies for Rh^{2+} (table 1). The magnitudes of these activation energies are consistent with the activation energy for diffusion of sodium ion vacancies that are not affected by superlattice ordering, which is about 242 cm^{-1} [2,8–10]. The vacancies in Na-β''-alumina tend to order on a superlattice at temperatures below 200°C which increases the activation energy for diffusion to about 2421 cm^{-1} [8,10]. Changes in composition have a pronounced effect on the low-temperature activation energy as a result of the change in extent of superlattice ordering [11]. The presence of Cr^{3+} as an impurity in the conduction layers may reduce the correlation length of the superlattice and therefore lower the activation energy of migration for the surrounding Na^+ ions and vacancies. Thermal energy to assist in the diffusion process is supplied by the vibrational modes of the lattice which have been characterized by Raman and infrared spectroscopy [12]. On the other hand, divalent impurity ions [3] have been found to have thermal activation energies for diffusion near 1000 cm^{-1}. The differences in the values of ΔE and B for Cr^{3+} and Rh^{2+} can be attributed to differences in the trapping processes at the two types of sites for the different active ions. The values obtained for C and $\Delta E'$ show that the energy transfer interaction is smaller for Cr^{3+} than for Rh^{2+} ions.

Because the sizes of the Cr^{3+} and Rh^{2+} doping ions are much smaller than that of the normal Na^+ lattice ions they replace, a significant amount of strain is introduced into the crystal, which

accounts for the decrease in the optical quality of the samples. Substitution of divalent or trivalent ions for monovalent sodium is accompanied by the production of one or two sodium ion vacancies, respectively. Different types of exchanged ions will have different preferences for occupation of the two different types of Na-sites. The mid-oxygen site is known to distort to noncentrosymmetric symmetry when occupied by some exchanged ions [13]. The amount of distortion is dependent on the distribution of Na^+ ions in the lattice. The distribution of sodium ions and vacancies around either of the two sites will change the crystal field seen by an impurity ion occupying the site. Our results do not provide information as to percentage of occupancy of these sites by Cr^{3+} and Rh^{2+} ions, but the presence of nonequivalent lattice sites is consistent with the model used to interpret the data. The magnitudes of the measured activation energies are consistent with attributing the two spectrally different sites to active ions in the same lattice site but with different local environments of sodium ions and vacancies which can change due to the mobility of the Na^+ ions.

The high power, picosecond pumping conditions used on the Cr^{3+}-exchanged β''-alumina crystal have produced stimulated emission in other materials [6]. Single-pass gain measurements on this sample showed no optical gain despite the strong lifetime quenching of the 700 nm band. Thus the lifetime quenching is associated with a loss mechanism for the excitation energy for ions in type 2 sites. Excited state absorption is one possible mechanism, but it should distort the time evolution pattern of the fluorescence of ions in type 2 sites to give a risetime or double exponential decay. This is not seen, and instead the time evolution pattern of the fluorescence of ions in type 1 sites is observed to have a risetime. Evidently this type of excitation produces a high concentration density of excited ions in type 2 sites which enhances the energy transfer to ions in the lower energy type 1 sites. The presence of energy transfer is not surprising with the high concentration of Cr^{3+} ions present in the lattice.

The spectral properties of Cr^{3+} in Na-β''-alumina have been reported previously [7]. The single lifetime reported for the fluorescence emis-

sion is intermediate between two values measured in this work. Concentration quenching of the lifetime was observed as well as a decrease in the lifetime over long time periods of the order of months. The latter effect was attributed to quenching impurities such as water absorbed into the conduction plane. The measurements in our work were made immediately after impurity exchange to minimize such effects.

Acknowledgments

References

[1] J.T. Kummer, in: Progress in Solid State Chemistry, Vol. 7, eds. H. Reiss and J.O. McCaldin (Pergamon, New York, 1972) p. 141.

[2] J.B. Bates, J.-C. Wang and N.J. Dudney, Physics Today 35 (1982) 46.

[3] G.C. Farrington and B. Dunn, Solid State Ionics 7 (1982) 267.

[4] B. Dunn and G.C. Farrington, Solid State Ionics 9 & 10 (1983) 223.

[5] M. Jansen, A. Alfrey, O.M. Stafsudd, B. Dunn, D.L. Yang and G.C. Farrington, Opt. Lett. 9 (1984) 119;
A.J. Alfrey, O.M. Stafsudd, B. Dunn, D.L. Yang and L. Salmon (to be published).

[6] R.C. Powell, in: Tunable Solid State Lasers, eds. P. Hammerling, A.B. Budgor and A. Pinto (Springer-Verlag, Berlin, 1985) p. 60;
R.C. Powell, R.H. Schweitzer, J.J. Martin, G.E. Venikouas and C.A. Hunt, J. Chem. Phys. 81 (1984) 1178;
R.C. Powell, G.J. Quarles, J.J. Martin, C.A. Hunt and W.A. Sibley, Opt. Lett. 10 (1985) 212.

[7] J.D. Barrie, B. Dunn and O.M. Stafsudd, Solid State Ionics 18/19 (1986) 677.

[8] H. Engstrom, J.B. Bates, W.E. Brundage and J.C. Wang, Solid State Ionics 2 (1981) 265.

[9] J.C. Wang, Phys. Rev. B 26 (1982) 5911.

[10] J.P. Boilot, G. Collin, P. Colomban and R. Comes, Phys. Rev. B 22 (1980) 5912.

[11] J.B. Bates, H. Engstrom, J.C. Wang, B.C. Larson, N.J. Dudney and W.E. Brundage, Solid State Ionics 5 (1981) 159.

[12] N.J. Dudney, J.B. Bates and W.E. Brundage, Solid State Ionics 9 & 10 (1983) 207;
R. Frech and J.B. Bates, Spectrochimica Acta 35 (1978) 685.

[13] W. Carrillo-Cabrera, J.O. Thomas and G.C. Farrington, Solid State Ionics 9/10 (1983) 245.

Optical spectroscopy of Mn$_2$SiO$_4$ crystals

Richard C. Powell, Brahim Elouadi,[a] and Lin Xi

Department of Physics, Oklahoma State University, Stillwater, Oklahoma 74078

G. M. Loiacono

Philips Laboratories, Briar Cliff Manor, New York 10510

Robert S. Feigelson

Center for Materials Research, Stanford University, Stanford, California 94305

The temperature dependences of the fluorescence intensities and lifetimes of Mn$_2$SiO$_4$ and the results of time-resolved spectroscopy measurements on this material are reported. A model is developed to explain the results in terms of thermally activated migration of Mn^{2+} excitons terminating on deep trapping centers. Fiber growth techniques are shown to decrease the concentration of fluorescence quenching centers in this material, and dilution with Mg or Ca ions is found to decrease the efficiency of the quenching process. Four-wave mixing results suggest the presence of laser-induced photoionization processes in these crystals.

I. INTRODUCTION

Divalent manganese ions have a strong intrinsic luminescence which is potentially useful for optical applications. However, in highly concentrated manganese systems strong concentration quenching occurs so that fluorescence emission is generally not observed at room temperature.[1-5] We reported recently the observation of room temperature luminescence from several new types of concentrated Mn^{2+} materials whose optical properties have not been previously characterized.[6] The results of studying the spectral dynamics of one of these materials, Mn$_2$SiO$_4$, are reported here. Laser-excited time-resolved spectroscopy techniques are used to characterize the time evolution of the fluorescence intensities and fluorescence decay profiles as a function of temperature. Using the information obtained from this study, a model is proposed to explain the concentration quenching of the luminescence in this material based on thermally activated exciton migration and trapping at quenching centers. The quenching is found to be reduced by diluting the Mn^{2+} concentration and by producing crystals with fewer imperfections. In addition, four-wave mixing experiments suggest the presence of laser-induced photoionization of the Mn^{2+} in this crystal.

The compound Mn$_2$SiO$_4$ (trephorite) is an orthosilicate of the olivine group of minerals. The phase diagram of the MnO–SiO$_2$ system indicates that Mn$_2$SiO$_4$ melts congruently at 1345 °C and crystalizes in the orthorhombic system. The compound was prepared[7] by direct melting (RF) of stoichiometric amounts of reagent grade MnO and SiO$_2$ in an iridium crucible under an argon atmosphere. Single crystals were grown at pulling rates between 1 and 5 mm/h and rotation rates of 12–18 rpm. During growth, an atmosphere of argon was maintained at a flow rate of 1 ℓ/h.

In order to investigate the effect of concentration quenching, solid solutions of the type Mn$_{2-x}$M$_x$SiO$_4$ were prepared with M = Mg or Ca. At high levels (> 15%) of Mg the melting point exceeded 1650 °C, while the composition

MnCaSiO$_4$ melted at 1350 °C. Crystal growth conditions for these solid solutions were similar to those for pure Mn$_2$SiO$_4$.

The crystals presently available from the standard synthesis process described above do not have a high optical quality. Visible scattering centers and strain patterns indicate the presence of a significant number of impurities and lattice defects in the material. In order to determine the effect of these imperfections on the spectral properties, small fiber crystals of Mn$_2$SiO$_4$ were produced by the laser-heated pedestal growth (LHPG) method.[8,9] The details of crystal growth have been described previously.[9] A 50 W CO$_2$ laser at 10.6 μm was used as the heating source. The laser emission is split into two beams and focused onto the sample material. As the material is melted in an argon atmosphere, a seed crystal is used to quickly pull a fiber from the melt at the rate of 1 mm/min. The starting material used to produce the Mn$_2$SiO$_4$ fiber was a crystal synthesized by the method described in the preceding paragraph. The resulting fiber was a single crystal about 500 μm in diameter and about 2 cm long. Characterization of other types of crystals grown by the LHPG method have shown that this fast growth technique produces crystals with greatly reduced chemical and structural imperfections compared to those grown by other methods.[9]

For measurements of the fluorescence spectra, the samples were mounted in a cryogenic refrigerator to control the temperature between 10 and 300 K. Excitation was provided by a nitrogen laser-pumped dye laser with a pulse width of 10 ns. The fluorescence was analyzed with a 1 m Spex monochromator and detected by an RCA C31034 photomultiplier tube. The signal was processed by an EGG-PAR boxcar integrator to obtain the fluorescence spectra at specific times after the laser pulse and to measure fluorescence lifetimes. Absorption spectra were obtained on a Perkin Elmer spectrophotometer.

II. EXPERIMENTAL RESULTS

The absorption spectrum of Mn$_2$SiO$_4$ at low temperature is shown in Fig. 1. The spectrum

[a] Permanent address: Applied Solid State Chemistry Laboratory, Faculty of Sciences, Charia Ibn Batota Rabat, Morocco.
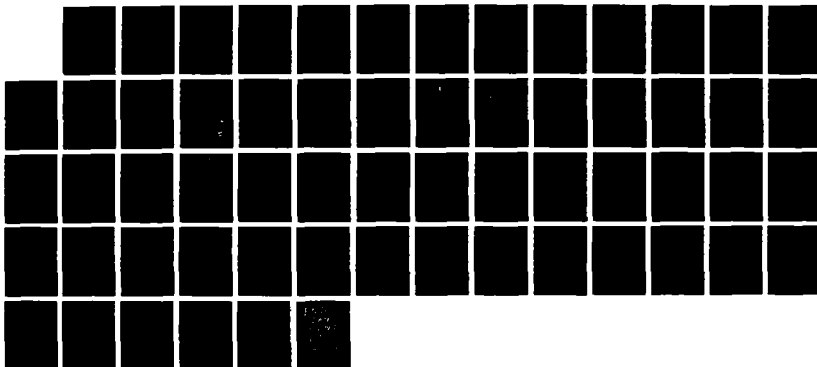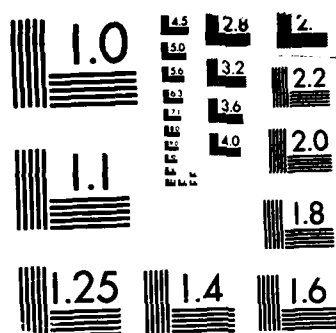
MICROCOPY RESOLUTION TEST CHART

BUREAU OF STANDARDS-1963-A
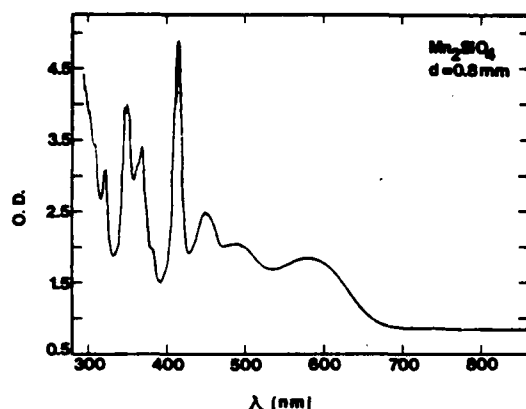
FIG. 1. Absorption spectrum of bulk Mn₂SiO₄ crystal at room temperature.

to those observed in other concentrated manganese systems.[1-5] They have been assigned[10-12] to transitions between levels of the $3d^5$ electron configuration of Mn^{2+}. In the approximation of octahedral site symmetry, these transitions originate on the $^6A_{1g}$ ground state and terminate on the $^4T_{1g}$, $^4T_{2g}$, $^4A_{1g}$, ^4E_g, $^4T_{2g}$, ^4E_g, and $^4T_{1g}$, listed in order of increasing energy.

The fluorescence spectra at three temperatures at two times after the laser pulse are shown in Fig. 2. The emission transition originates on the lowest $^4T_{1g}$ level Stokes shifted to lower energies from the absorption transition. At both 10 and 300 K there is no spectral evolution of the emission with time; it appears as a broadband peaked near 700 nm. How-

FIG. 3. Ratio of the integrated fluorescence intensities of the 800 nm to the 700 nm bands as a function of time after the laser pulse at 150 K. (See the text for an explanation of the theoretical line.)

ever, at intermediate temperatures, the spectrum evolves from a band peaked near 700 nm at short times after the excitation pulse to one peaked near 800 nm at long times. The time evolution of the ratios of the integrated fluorescence intensities of the two bands at 150 K is shown in Fig. 3.

Figure 4 shows the change in the fluorescence decay rates with temperature for both the 700 and 800 nm bands.

FIG. 2. Fluorescence spectra of bulk Mn₂SiO₄ crystal at 0.25 and 125 μs after the laser pulse at three temperatures (solid lines). At 150 K, the 700 nm bond appears at short times and the 800 nm bond at long times after the excitation pulse, whereas no time evolution appears in the spectra at 10 and 293 K. Fluorescence spectrum of CaMnSiO₄ crystal at 125 μs after the laser pulse at room temperature (dotted line). Fluorescence spectrum of Mn₂SiO₄ fiber at 125 μs after the laser pulse at room temperature (broken line).
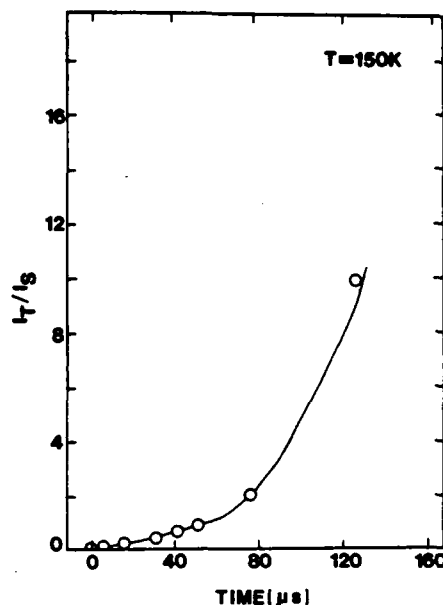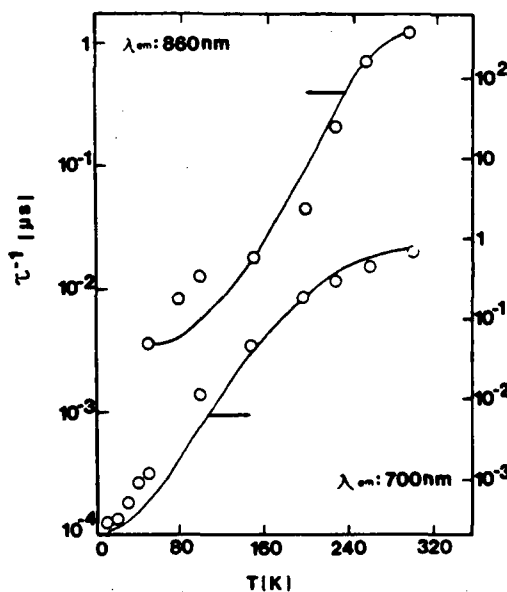

FIG. 4. Temperature dependences of the fluorescence decay rates of the 700 and 800 nm emission bands in Mn₂SiO₄. (See the text for an explanation of the theoretical line.)
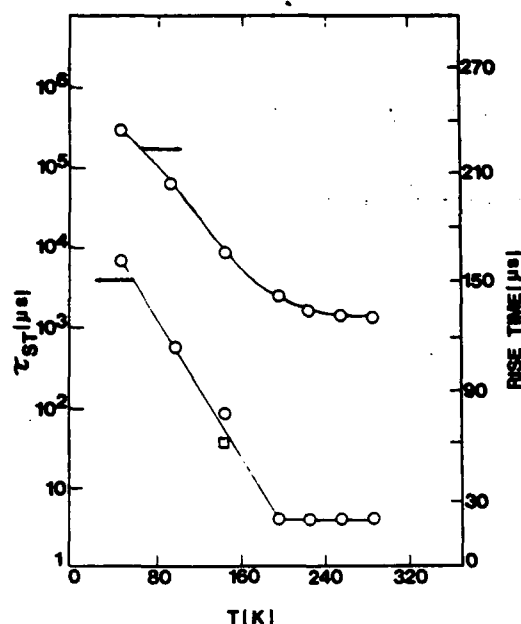
FIG. 5. Temperature dependences of the rise time of the 800 nm fluorescence band and the energy transfer rate. The square point is the energy transfer rate obtained by fitting the time-resolved spectroscopy data. (See the text for an explanation of the theoretical lines.)

FIG. 6. Model for explaining the spectral dynamics of Mn₂SiO₄ crystals. (See the text for a definition of parameters.)

The decay time of the former is 3.17 ms at 10 K and decreases to about 1.33 μs at 300 K. The lifetime of the latter is about 700 μs at 50 K decreasing to about 0.93 μs at 300 K. The emission profile of the 800 nm band also exhibits a rise time which decreases with increasing temperature as shown in Fig. 5.

III. INTERPRETATION OF RESULTS

The observed spectral characteristics described in the preceding section can be interpreted using a model based on exciton migration to quenching sites. Figure 6 shows a schematic representation of this model in terms of the energy levels, rate parameters, and activation energies involved in the spectral dynamics. The concentration of ions in the ith level is given by n_i and the rate of optical excitation is W_e. The majority of the Mn²⁺ ions are assumed to be in normal lattice sites in the crystal. The interaction between ions in this highly concentrated manganese system leads to the formation of an exciton band in the $^4T_{1g}$ metastable state. The excited ions decay nonradiatively to this level and at low temperatures lattice relaxation around the excited ions causes a self-trapping of the excitons. The 700 nm emission band is attributed to fluorescence from this self-trapped exciton level. As temperature is increased, the exciton can gain enough thermal energy to overcome the self-trapping barrier ΔE_{SB} and be excited into the exciton band. In this band the exciton is mobile and its diffusion through the lattice can be described by a thermally activated hopping processes, where k_D is the rate of diffusion and ΔE_D is the activation energy for hopping. The exciton band is assumed to have an intrinsic lifetime given by τ_B. However, because of efficient trap-
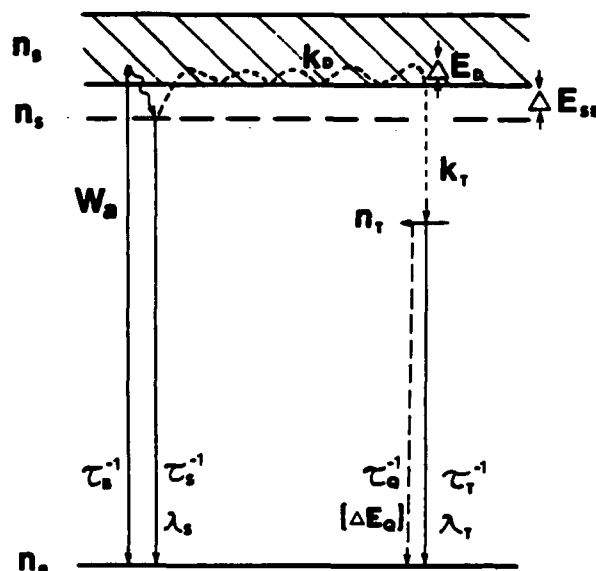
ping of the excitons at defect sites no band fluorescence is observed. The rate describing the trapping process is k_T. It is assumed that the traps are Mn²⁺ ions near to lattice defects which perturb their surroundings enough to shift their energy levels to lower energies. The observed 800 nm band is attributed to emission from these perturbed manganese sites. As temperature is raised further, the Mn²⁺ in the perturbed sites undergo radiationless relaxation to the ground state with an activation energy ΔE_Q and a rate τ_Q^{-1}.

The rate equations can be written for the populations of the energy levels shown in Fig. 6 and solved with the assumption of time independent rate parameters. The fluorescence intensity of a specific level is equal to the product of the population and the radiative decay rate of the level. In this model, the ratio of the fluorescence intensities of emission from the perturbed Mn²⁺ sites to emission from the self-trapped excitons at time t is given by

$$\frac{I_T(t)}{I_S(t)} = \left(\frac{\tau_S'}{\tau_T'}\right)\left[\left(\frac{n_T(0)}{n_S(0)} + \frac{\tau_{ST}^{-1}}{\tau_S^{-1} + \tau_{ST}^{-1} - \tau_T^{-1}}\right)\right.$$
$$\left. \times e^{(\tau_S^{-1} + \tau_{ST}^{-1} - \tau_T^{-1})t} - \frac{\tau_{ST}^{-1}}{\tau_S^{-1} + \tau_{ST}^{-1} - \tau_T^{-1}}\right], \quad (1)$$

where

$$\tau_{ST}(T) = k_T^{-1} + k_D^{-1}. \quad (2)$$

The temperature dependence of the fluorescence lifetime of the 700 nm band can be explained in this model by assuming that the populations of the self-trapped level and the exciton band are in thermal equilibrium with each other. Then

$$\tau_S^{-1}(T) = \tau_{SO}^{-1} + \tau_B^{-1}\exp(-\Delta E_{SB}/k_B t), \quad (3)$$

where τ_{SO} is the intrinsic decay time of the self-trapped excitons and k_B is Boltzmann's constant. The temperature de-

TABLE I. Spectral parameters for Mn₂SiO₄.

Transition times (s)	Activation energies (cm^{-1})
$\tau_S^0 = 3.17 \times 10^{-3}$	$\Delta E_{SB} = 612$
$\tau_B = 6.7 \times 10^{-8}$	$\Delta E_Q = 938$
$\tau_T^0 = 7.0 \times 10^{-4}$	$\Delta E_D = 15$
$\tau_Q = 2.1 \times 10^{-8}$	
$k_T^{-1} = 4.0 \times 10^{-6}$	Initial population ratio
$k_D(150\text{ K}) = 7.6 \times 10^{-5}$	$n_T(0)/n_S(0) = 0.1$

Secondary parameters

$R_0^H(150\text{ K}) = 28$ Å	$R_0^T = 12$ Å
$D(150\text{ K}) = 1.1 \times 10^{-8}$ cm^2 s^{-1}	$D_0 = 1.2 \times 10^{-5}$ cm^2 s^{-1}
$l(150\text{ K}) = 1.4 \times 10^{-5}$ cm	$t_H(150\text{ K}) = 2.4 \times 10^{-8}$ s
$n(150\text{ K}) = 1.3 \times 10^5$	

pendence of the 800 nm band can be described by

$$\tau_T^{-1}(T) = \tau_{TO}^{-1} + \tau_Q^{-1} \exp(-\Delta E_Q/k_B T), \qquad (4)$$

where τ_{TO} is the intrinsic decay time for the excitons trapped in perturbed manganese sites. The rise time of the fluorescence profile of the 800 nm band is given by

$$t_{Tm} = (\tau_T^{-1} - \tau_S^{-1})^{-1} \ln\{(\tau_S/\tau_T)$$
$$+ [n_T(0)/n_S(0)](\tau_S/\tau_T)[(\tau_S^{-1} - \tau_T^{-1})/\tau_{ST}^{-1}]\}. \quad (5)$$

Here $n_i(0)$ represents the concentration of ions in the *i*th level at zero time after the laser pulse.

The expressions given in Eqs. (1)–(5) can be used to fit the data shown in Figs. 3–5. The solid lines in Fig. 4 represent the best fits to the data using Eqs. (3) and (4) for the lifetimes of the 700 and 800 nm band, respectively. Table I lists the parameters used to obtain these fits. This analysis gives values for the intrinsic decay rate of the exciton band, the quenching rate of the perturbed Mn²⁺ ions, and the activation energies for lifting the exciton to the band from the self-trapped state and for radiationless quenching in the perturbed sites. The solid line in Fig. 3 represents the best fit to the data on the time evolution of the fluorescence intensity ratios using Eq. (1). The energy transfer rate τ_{ST}^{-1} and product

$$\{(\tau_S'/\tau_T')[n_T(0)/n_S(0)]\},$$

are found as adjustable parameters from this analysis and listed in Table I. The measured rise time observed in the fluorescence profile of the 800 nm band also provides information about the energy transfer rate. Using Eq. (5) with the measured values of the lifetimes of the two bands and the rise time of the 800 nm band at each temperature along with the ratio of the zero time populations obtained from the time-resolved spectroscopy results gives a value for the energy transfer time at each temperature. This is plotted in Fig. 5. The value for τ_{ST} obtained from the time-resolved spectroscopy measurement at 150 K is shown on the same plot and demonstrates the consistency of the results.

The transfer time decreases exponentially with increasing temperature up to about 190 K and then remains constant at higher temperatures. Since the time for energy trans-

fer is made up of the time of migration of the exciton up to the trapping site plus the time of the trapping interaction itself, the results are consistent with a phonon-assisted energy migration processes with a temperature independent trapping process. Due to the increased rate of phonon assisted hopping processes, the exciton migration time decreases as temperature is increased up to about 190 K above which it is faster than the trapping time. Thus at higher temperatures we are dealing with trap limited energy transfer and the observed transfer time is the time of the trapping step in the overall energy transfer processes.

The above description of energy transfer can be put on a quantitative basis by treating the exciton migration in a diffusion model with a temperature dependent diffusion coefficient. The time of the trapping step is found from the experimental results to be 4.0 μs. At $T = 150$ K the time for diffusion of the exciton to the trapping site is 76 μs. The energy transfer rate in this model can be expressed as[13]

$$k_D = 4\pi DRN_T, \qquad (6)$$

where D is the diffusion coefficient, R is the trapping radius, and N_T is the concentration of traps. A rough estimate for the value of D at 150 K can be obtained by assuming typical values of 4×10^{-8} cm and 2.5×10^{18} cm^{-3} for R and N_T, respectively. This gives $D(150) = 1.1 \times 10^{-8}$ cm^2 s^{-1}. At this temperature, the diffusion length, hopping time, and number of steps in the random walk can be found from

$$l = (6D\tau_S^0)^{1/2}, \qquad (7)$$

$$t_H = a^2/(6D), \qquad (8)$$

$$n = \tau_S^0/t_H. \qquad (9)$$

Here the parameter a represents the average lattice spacing between nearest neighbor manganese ions. The values determined in this way are listed in Table I.

For thermally activated diffusion of localized excitons, the temperature dependence of the diffusion coefficient is given by[13]

$$D(T) = D_0 \exp(-\Delta E_D/k_B T).$$

Using this expression, the data in Fig. 5 gives a value for the activation energy for diffusion of $\Delta E_D = 15$ cm^{-1} and $D_0 = 1.2 \times 10^{-5}$ cm^2 s^{-1}.

The critical interaction distances for the hopping and trapping steps in the random walk, R_0^H and R_0^T, can be found from the expressions

$$R_0^H = a(\tau_S^0/t_H)^{1/6}, \quad R_0^T = a(\tau_S^0/t_H)^{1/6}, \qquad (10)$$

assuming electric dipole–dipole interactions for the mechanisms causing the migration and trapping. The value of R_0^T for the trapping processes is found to be 12 Å. The critical interaction distance for hopping at $T = 150$ K is 28 Å.

An attempt was made to directly measure the exciton migration in Mn₂SiO₄ using degenerate four-wave mixing techniques. This has been successful in stoichiometric rare earth pentaphosphate crystals and the details of the experimental setup are described elsewhere.[14] Using the 488 nm line of an argon laser, four-wave mixing signals could be obtained in Mn₂SiO₄ crystals. However, the signal intensity decayed away within a few seconds and it was necessary to realign the laser beams in a different region of the crystal in order to reestablish the signal. The characteristics of a slowly

varying signal accompanied with a "permanent" change in the optical properties of the material are consistent with a photorefractive process. Under the experimental conditions used here, this must be associated with photoionization of the Mn^{2+} ions with subsequent trapping of the electrons at defect centers. As is usually the case with photorefractive processes, the nature of the trapping centers is difficult to identify.

If the model used to describe the spectral properties is accurate, the quenching of the Mn^{2+} fluorescence should be reduced if the number of trapping sites is reduced or if the exciton migration is inhibited. To test the model we measured the fluorescence spectra and lifetimes of Mn_2SiO_4 fibers and $CaMnSiO_4$ crystals. Figure 2 shows the room temperature emission spectra of these two samples which is similar to the bulk Mn_2SiO_4 crystals. The room temperature fluorescence decay profile of $CaMnSiO_4$ was found to be a double exponential with decay constants of 25 and 39 μs. The Mn_2SiO_4 fiber exhibited a single exponential decay with a decay time of 23 μs at room temperature.

Since fiber crystals are known to have reduced defect concentrations compared to bulk crystals, the order of magnitude difference in lifetime between the two samples can be attributed to decreased trapping of excitons at quenching sites in the fiber as predicted. In the $CaMnSiO_4$ crystal there are only half as many Mn^{2+} ions present to support exciton migration compared to the Mn_2SiO_4 crystal. This will reduce the diffusion coefficient and result in less efficient quenching by migration to traps as reflected by the increase in the fluorescence lifetime. Similar results were obtained using crystals diluted with Mg ions.[6]

IV. SUMMARY AND CONCLUSIONS

The results reported here show that the thermal quenching temperature of Mn^{2+} ions in normal lattice sites in Mn_2SiO_4 is above room temperature and the observed fluorescence quenching is associated with exciton migration to trapping sites with strong room temperature quenching. The exciton migration properties are consistent with a thermally activated hopping model. Above about 190 K the energy transfer becomes a trap limited process. The values of the critical interaction distances for hopping and trapping steps indicate that the former is a significantly stronger process than the latter which is consistent with the condition of trap limited energy transfer. In order to have efficient trapping under these conditions, the exciton must become localized in a distorted region around the trapping center so that it can not escape before trapping occurs. This type of extended

trapping region has been characterized in other materials.[15] Since the defects producing the perturbed Mn^{2+} sites are unknown at the present time, it is not possible to determine further characteristics of the trapping region.

The model for explaining fluorescence quenching involving energy migration to trapping sites is consistent with that used previously for other concentrated manganese systems.[3,5] The parameters describing thermal quenching of the high energy band are similar to those found for $RbMnF_3$. The parameters describing the energy migration part of the process are different. The activation energy between the self-trapped exciton and the mobile exciton band is significantly greater for the case studied here. The details of the energy migration mechanism have not been determined in previous investigations. Therefore it has not been possible to tell if the energy transfer process is diffusion limited or trap limited.

The fact that the fluorescence quenching is reduced by using the fiber growth process is of significant practical interest. This shows that if bulk single crystals can be produced with low concentrations of defects and impurities, the luminescence efficiency should be high enough to make them useful in practical applications such as phosphors or lasers.

[1] R. Greene, D. Sell, R. Feigelson, G. Imbusch, and H. Guggenheim, Phys. Rev. 171, 600 (1968).

[2] W. Holloway, E. Prohofsky, and M. Kestigian, Phys. Rev. A 139, 954 (1965).

[3] K. Gooen, B. DiBartolo, M. Alam, R. Powell, and A. Linz, Phys. Rev. 177, 615 (1969).

[4] S. Stokowski, D. Sell, and H. Guggenheim, Phys. Rev. B 4, 3141 (1976).

[5] J. Danko, D. Pacheco, and B. DiBartolo, Phys. Rev. B 28, 2382 (1983).

[6] L. Xi, R. H. Schweitzer, R. C. Powell, G. M. Loiacono, and G. Mizell, in Proceedings of the International Conference on Lasers '84, edited by K. M. Corcoran, D. M. Sullivan, and W. C. Stwalley (STS, McLean, VA, 1985), p. 540.

[7] F. P. Glasser, Am. J. Sci. 256, 405 (1958).

[8] R. S. Feigelson, in Tunable Solid State Lasers, edited by P. Hammerling, A. B. Budgor, and A. Pinto (Springer, Berlin, 1985), p. 129.

[9] R. S. Feigelson, in Crystal Growth of Electronic Materials, edited by E. Kaldis (Elsevier, Amsterdam, 1985), p. 127.

[10] J. W. Stout, J. Chem. Phys. 31, 709 (1959).

[11] R. Stevenson, Can. J. Phys. 43, 1732 (1965).

[12] L. L. Lohr, Jr., J. Chem. Phys. 45, 3611 (1966).

[13] R. C. Powell and G. Blasse, Struct. Bonding (Berlin) 42, 43 (1980).

[14] J. K. Tyminski, R. C. Powell, and W. K. Zwicker, Phys. Rev. B 29, 6074 (1984); C. M. Lawson, R. C. Powell, and W. K. Zwicker, ibid. 26, 8436 (1982).

[15] Z. G. Soos and R. C. Powell, Phys. Rev. B 6, 4035 (1972); R. C. Powell and Z. G. Soos, J. Lumin. 11, 1 (1975).

Spectroscopy and four-wave mixing in $Li_4Ge_5O_{12}:Mn^{4+}$ crystals

Andrzej Suchocki,[*] J. D. Allen, and Richard C. Powell

Physics Department, Oklahoma State University, Stillwater, Oklahoma 74078-0444

G. M. Loiacono

Philips Laboratories, Briarcliff Manor, New York 10510

(Received 4 May 1987)

The absorption and fluorescence spectra of Mn^{4+} in $Li_4Ge_5O_{12}$ crystals are reported and the temperature dependences of the fluorescence intensity and lifetime are described. The spectral features are consistent with the presence of two types of sites for the Mn^{4+} ions, and radiationless decay and vibronic transitions are shown to be responsible for the variation of the spectral properties with temperature. Four-wave mixing measurements were performed with the laser excitation wavelength in resonance with an absorption transition of the Mn^{4-} ions. The characteristics of the four-wave mixing signal are consistent with scattering from a laser-induced population grating and the temperature dependence of the signal is correlated with the temperature dependence of the fluorescence lifetime.

I. INTRODUCTION

Mn^{4+} has a $3d^3$ electron configuration which is isoelectronic with Cr^{3+}. Although there is extensive literature describing the optical properties of the latter ion due to its importance in laser applications, very little research has been reported on Mn^{4+} ions.[1-4] We report here the results of optical spectroscopy and four-wave mixing (FWM) experiments on Mn^{4+} in $Li_4Ge_5O_{12}$ crystals. The spectral features indicate the presence of two types of crystal-field sites for Mn^{4+} in this host, and the temperature dependence of the FWM signal is shown to be correlated with the temperature dependence of the fluorescence lifetime.

There are several possible forms of lithium germanium oxide having different chemical formulas and crystallographic structures. Crystals of the particular compound studied here were grown by the Czochralski technique and found from x-ray crystallography studies to have a triclinic structure with a $P\bar{1}$ space group.[5] The germanium atoms occupy at least two different types of sites in this crystal structure, one with tetrahedral point symmetry and one with octahedral symmetry. The distance between the Ge ions and oxygen ligands is 1.749 Å in the former type of site and 1.903 Å in the latter. The ratio of the relative number of these types of sites is 4:6. The Mn^{4+} ions enter the lattice substitutionally for the Ge^{4-}

ions. The sample used in this work contained 0.1 at.% Mn. It was 3 mm thick and had a yellowish color.

II. OPTICAL SPECTROSCOPY OF Mn^{4+} IN $Li_4Ge_5O_{12}$

The absorption spectra were recorded on a Perkin-Elmer model 330 spectrophotometer. Fluorescence spectra were obtained using a Spex 1-m monochromator, an RCA C31034 photomultiplier tube, an EG&G-PAR lock-in amplifier, and a strip chart recorder. The excitation was provided by the 488-nm line of a Spectra Physics argon laser. For fluorescence lifetime measurements, a Molectron nitrogen laser was used to provide excitation pulses 10 ns in duration at 333.7 nm and the signals were processed with either an EG&G-PAR boxcar averager or signal averager. The sample was mounted in a cryogenic refrigerator capable of controlling the temperature between 12 K and room temperature.

The absorption spectrum of $Li_4Ge_5O_{12}:Mn^{4+}$ at 12 K is shown in Fig. 1. The presence of Mn^{4+} introduces a broad band peaked near 420 nm which is probably associated with transitions from the $^4A_{2g}$ ground state to the $^4T_{2g}$ level. This band showed very little change as temperature was raised to 300 K. The absorption edge of the material near 300 nm is also changed by the presence of the Mn^{4-}. This is probably associated with transi-
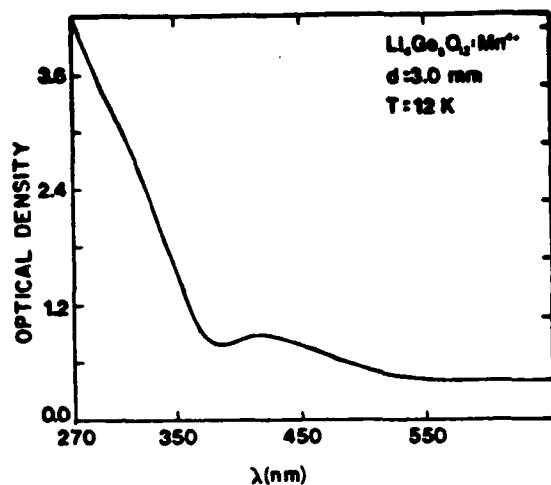
FIG. 1. Absorption spectrum of $Li_4Ge_5O_{12}:Mn^{4+}$ crystal at 12 K.

tions from the ground state to the $^4T_{1g}$ level. No sharp lines were observed in the absorption spectrum even at low temperatures.

The fluorescence spectrum at 12 K obtained by exciting into the $^4T_{2g}$ absorption band with the 488-nm line of an argon laser is shown in Fig. 2. The general features consist of two intense, sharp lines and a weak, broad band at lower energies. These characteristics are typical for a $3d^3$ ion in a relatively strong crystal field environment, and thus the standard designations of R_1 and R_2 are used for transitions from the two components of the ^2E_g level to the ground state. The broad band is the vibronic sideband of these zero-phonon lines. An expanded view of the spectra in the region of the R lines is shown for two temperatures in Fig. 3. Both R_1 and R_2 are split into two components with the splitting being 2.55 cm^{-1} for the former and 2.04 cm^{-1} for the latter.

Computer fits were generated for the curves in Fig. 3 assuming Lorentzian line shapes with variable intensities, full width at half maximum $\Delta\lambda$, and peak positions. The best fits are shown as broken lines in Fig. 3 and the
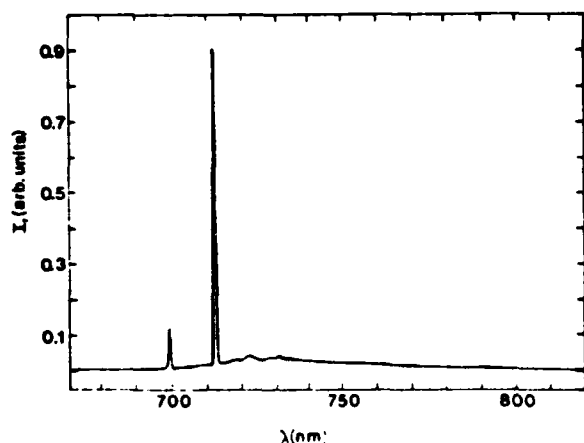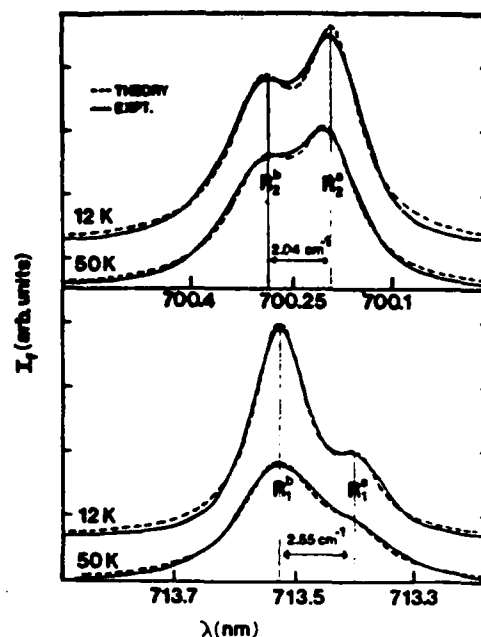
FIG. 3. Fluorescence spectrum in the region of the R lines (solid lines) and theoretical fits of Lorentzian curves (broken lines).

ratios of the total intensities of the low energy to the high energy components are plotted as a function of temperature in Fig. 4. For both the R_1 and R_2 lines, these ratios are approximately constant up to about 70 K and then increase significantly. Above 100 K the individual components broaden to the extent that they cannot be resolved.

Details of the vibronic sideband are shown in Fig. 5. The positions of the vibronic peaks with respect to the R_1 and R_2 lines are listed in Table I.

The temperature dependence of the fluorescence inten-

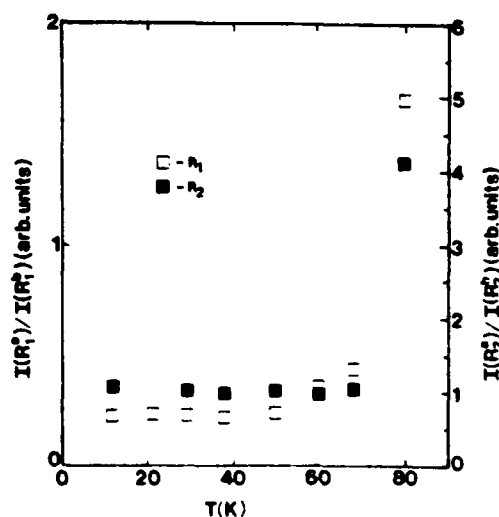FIG. 2. Fluorescence spectrum of $Li_4Ge_5O_{12}:Mn^{4+}$ crystal at 12 K.

FIG. 4. Temperature dependence of the relative total intensities of the two sets of R lines.
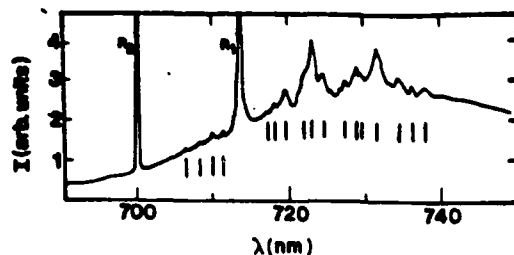
FIG. 5. Vibronic emission band of $Li_4Ge_5O_{12}:Mn^{4+}$ at 12 K with the main vibronic peaks marked by vertical lines.

sity at the peak of the vibronic emission band is shown in Fig. 6. It is constant from 12 to about 40 K and then decreases to about 20% of its initial value. This decrease can be described as an exponential with an activation energy of 360 cm^{-1}. The intensity then increases slightly between about 90 and 180 K, which is probably associated with an increase in the vibronic transition probability. Above 180 K there is a strong quenching of the fluorescence, which is probably associated with an increase in the radiationless decay probability.

The fluorescence decay profiles at the maximum of the vibronic sideband were monitored for various temperatures, and examples are shown in Fig. 7. The decay kinetics can be described by double exponential functions below 80 K. The fast component has a characteristic decay time of about 260 μs below 40 K. This decreases at higher temperatures and the decay curves become single exponentials with the longer decay component remaining above 80 K. The decay time of the longer component is constant at about 1.06 ms up to 150 K and then decreases. The temperature dependences of these decay times are shown in Fig. 8. These spectral characteristics are summarized in Table II.

FIG. 6. Temperature dependence of the peak fluorescence intensity.

III. FOUR-WAVE MIXING

Four-wave mixing (FWM) techniques have been useful in characterizing nonlinear optical properties and exciton dynamics of doped crystals and glasses.[6-9] In these types of experiments, laser-induced population gratings of the metastable states of the dopant ions are established and probed by crossed laser beams tuned to resonance with one of the absorption transitions of the ion. The experimental details for FWM measurements have been described previously.[7-9] In the work described here, the 488-nm line of an argon laser was used to write the gratings and a helium-neon laser was used to read the gratings. For measuring the FWM signal efficiency the laser beams were chopped and lock-in detection was used to improve the signal-to-noise ratio. The signal de-

TABLE I. Vibronic emission peaks in the fluorescence spectrum of $Li_4Ge_5O_{12}:Mn^{4+}$.

λ (nm)	v (cm^{-1})	$\Delta v(R_2)$ (cm^{-1})	$\Delta v(R_1)$ (cm^{-1})
706.4	14 156	126	
708.1	14 122	160	
709.8	14 088	195	
711.2	14 061	222	
715.4	13 979		37
718.2	13 924		92
719.7	13 895		121
722.2	13 847		168
723.7	13 818		198
724.9	13 795		220
727.6	13 744		272
729.1	13 716		300
729.8	13 702		313
731.9	13 663		352
734.7	13 611		404
736.5	13 578		438
738.2	13 546		460

FIG. 7. Fluorescence decay kinetics of $Li_4Ge_5O_{12}:Mn^{4+}$ at 138.4 K (solid circles) and 35.2 K (open circles). The open squares represent the initial decay at 35.2 K after subtraction of the longer decay component.

TABLE II. Spectroscopic properties of Mn^{4+} in $Li_4Ge_5O_{12}$ crystals.

Parameter	Site a	Site b
R_1 line (nm)	713.40	713.53
R_2 line (nm)	700.19	700.29
$\Delta\lambda$ for R_1 at 12 K (Å)	0.84	1.04
$\Delta\lambda$ for R_2 at 12 K (Å)	0.97	1.25
Splitting of the ^2E level (cm^{-1})	264.50	265.00
τ at 12 K (ms)	1.08	0.26
Quenching temperature (K)	180	40

cay kinetics were measured with a signal averager.

The results of the FWM measurements are shown in Figs. 8 and 9. The temperature dependence of the scattering efficiency is shown in Fig. 8. It follows closely the fluorescence lifetime and intensity with a decrease between 30 and 60 K, a constant value up to about 150 K, and a decrease above this temperature.
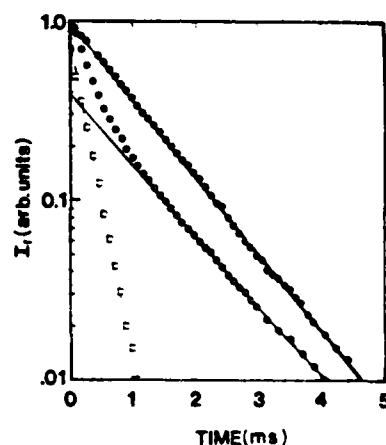
The decay kinetics of the FWM signals were found to be described by double exponentials at 42 K and single exponentials at 210 K. Figure 9 shows the variation of the signal decay rate on the crossing angle of the write beams. For both temperatures, the FWM signal decay rates are independent of crossing angles and approximately equal to twice the fluorescence decay rates.

IV. DISCUSSION AND CONCLUSIONS

The spectroscopic properties of Mn^{4+} in $Li_4Ge_5O_{12}$ crystals can be explained by assuming that the Mn^{4+} ions occupy two nonequivalent types of crystal field sites. The observed doublet structure of the R lines cannot be associated with the ground-state splitting of an ion in a single type of site since the magnitude of the splitting is different for the R_1 and R_2 lines. The ions in one type of site produce the transitions labeled R_1^a and R_2^a which have the 1.06 ms lifetime at low temperatures. The fluorescence of this center undergoes radiationless quenching above 180 K. The ions in the other type of
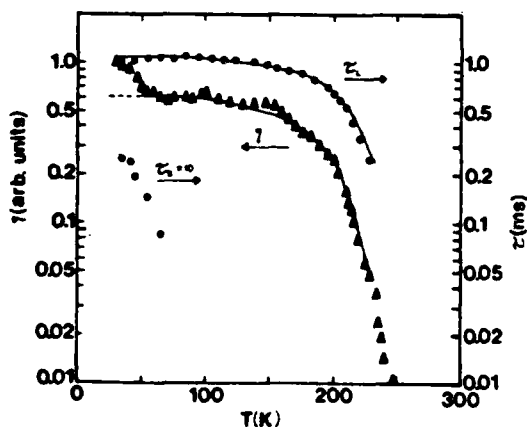

FIG. 8. Temperature dependences of the short (open circles) and long (solid circles) components of the fluorescence lifetimes, and of the FWM scattering efficiency at $\theta = 4.13°$ (solid triangles). The solid lines represent theoretical fits to the data.
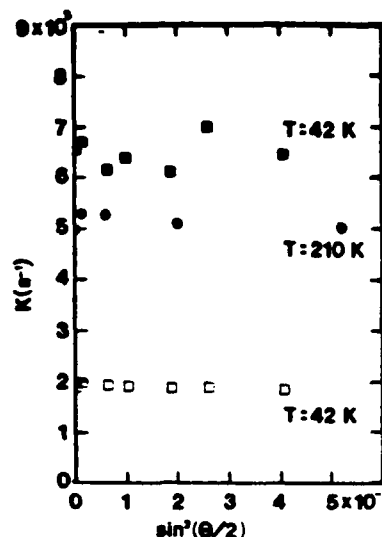
FIG. 9. FWM grating decay rate for $T = 210$ K (circles) and for 42 K (short component—solid squares; long component—open squares).

site produce the transitions labeled R_1^b and R_2^b which have the 260 μs lifetime at low temperature. The fluorescence of this center undergoes radiationless quenching above about 40 K. From optical data alone, it is not possible to identify the exact nature of the two types of sites. However, it is reasonable to expect that they are the two types of Ge^{4+} sites in this crystal lattice structure.

The temperature dependence of the fluorescence decay rate of ions in site a, τ^{-1}, can be described as the sum of the contributions from vibronic and nonradiative transitions,

$$\tau^{-1} = \tau_{vib}^{-1} + \tau_{non}^{-1} . \tag{1}$$

The vibronic contribution can be represented by an average phonon frequency $\langle \omega \rangle$ which leads to a temperature dependence given by

$$\tau_{vib}^{-1} = \tau_{vib}^{-1}(0) \coth(\langle \hbar\omega \rangle / 2kT) . \tag{2}$$

There are several types of nonradiative transitions that can contribute to the thermal quenching of the fluorescence decay time. For Cr^{3+} ions in relatively weak crystal field sites, the nonradiative contribution to the fluorescence lifetime is usually associated with the thermal population of the $^4T_2$ level. However, in this case the energy gap between the ^2E and $^4T_2$ levels is too large for this process to contribute significantly to the fluorescence lifetime in the temperature range of interest. The type of nonradiative transition which appears to be more important in this case is the direct decay process between the ^2E level and the ground state through the emission of p phonons each having an effective energy of $\hbar\omega$, where $p\hbar\omega$ is the energy gap crossed by the transition. The temperature dependence of this contribution to the fluorescence decay rate is[4,10]

$$\tau_{non}^{-1}(T) = RI_p(2s\sqrt{n(n+1)})[(n+1)/n]^{p/2}$$

$$\times \exp[-s(1+2n)] , \tag{3}$$

where

$$n = \{\exp[\hbar\omega/(kT)]-1\}^{-1}$$

is the phonon occupation number, s is the Huang-Rhys parameter, $I_p(x)$ is the modified Bessel function, and R is a temperature-independent prefactor.

The solid line in Fig. 8 represents the best fit to the data obtained from Eqs. (1)–(3) treating the parameters describing the electron-phonon coupling as adjustable parameters. The good fit between theory and experiment shown in the figure is obtained using $\hbar\omega = 325$ cm^{-1}, $\tau_{vib}^{-1}(0) = 924$ s^{-1}, $s = 0.2$, $p = 43$, and $R = 4.89 \times 10^{83}$ s^{-1}. These results are consistent with those described in Ref. 4 for Mn^{4+} in $Y_3Al_5O_{12}$. The value of the Huang-Rhys parameter is smaller for our case than that found in Ref. 4.

The characteristics of the FWM signal are consistent with scattering from a population grating of excited Mn^{4+} ions. The double exponential behavior of the grating decay kinetics at low temperatures is consistent with establishing population gratings independently in the two subsets of manganese ions in nonequivalent crystal field sites having different fluorescence lifetimes. The lack of dependence of the grating decay rates on the crossing angle of the write beams indicates that there is no long-range energy diffusion in this material. In addition, we performed time-resolved spectroscopy measurements exciting selectively in either site a or site b transitions. The time evolution of the fluorescence emission after selective excitation shows that no energy transfer takes place between ions in different types of sites. Thus the temperature dependence of the intensity ratios shown in Fig. 4 is due to differences in radiationless quenching and not site-to-site energy transfer.

The theoretical expression for the FWM signal is given by[8]

$$\eta = \exp[-2\alpha d/\cos\theta]\{\sinh^2[d\,\Delta\alpha/(2\cos\theta)]$$

$$+ \sin^2[d\pi\Delta n/(\lambda\cos\theta)]\} , \quad (4)$$

where d is the grating thickness and θ the crossing angle of the write beams in the sample. α is the average absorption coefficient at wavelength of the write beams λ. The first term represents the contribution to the signal due to an absorption grating of modulation depth $\Delta\alpha$, and the second term represents the contribution due to a dispersion grating of modulation depth Δn. For population gratings, the modulation depths can be expressed in terms of products of the concentration of ions in the peak regions of the gratings N_{2p}, with the differences in

either the absorption or dispersion of the ions in the ground and excited states. Using the rate equations describing the dynamics of a simple two-level system,[11]

$$N_{2p} = 2I_0 N_0 \sigma_1 / [2I_0\sigma_1 + (h\nu/\tau)] , \quad (5)$$

where I_0 is the intensity of the laser pump beam, N_0 is the total concentration of active ions, σ_1 is the absorption cross section for ions in level 1, $h\nu$ is the photon energy, and τ is the fluorescence lifetime of the metastable state. The parameter that dominates the temperature dependence of the four-wave mixing signal for population gratings is the fluorescence lifetime. For weak gratings, the functions in Eq. (4) can be expanded and the signal expressed as

$$\eta = C[1/(A + B/\tau)]^2 , \quad (6)$$

where the temperature independent constants A, B, and C have different meanings for absorption gratings and dispersion gratings.

Equation (6) can be used to relate the temperature dependences of the fluorescence lifetimes and the four-wave mixing signal intensity. At temperatures below 80 K, the four-wave mixing signal has contributions due to scattering from Mn^{4+} ions in both types of crystal field sites, as indicated by the double exponential kinetics of the signal. Fluorescence quenching occurs for the ions in one type of site above 40 K resulting in a decrease in the scattering efficiency. Above 80 K the FWM signal is due to scattering only from Mn^{4+} in the other type of site. Using the measured values of the fluorescence lifetimes in Eq. (3) and treating A, B, and C as adjustable constants results in the solid line fitting the FWM data shown in Fig. 8. This good fit confirms the relationship between the FWM signal and the metastable state lifetime for a population grating. Not enough independent information is available to interpret the values of the adjustable constants in terms of the contributions to the grating modulation depths and thicknesses. Four-wave mixing measurements on the several other host crystals doped with Cr^{3+} which is isoelectronic with Mn^{4+} have shown that dispersion gratings make the dominant contribution to the scattering efficiency.[7,9,11-14] However, for this case Fig. 1 shows a significant difference in absorption strength for light at the laser wavelength for ions in the ground and excited metastable states, and thus the possibility of a strong contribution from an absorption grating cannot be ruled out.

where

$$n = \{\exp[\hbar\omega/(kT)] - 1\}^{-1}$$

is the phonon occupation number, s is the Huang-Rhys parameter, $I_p(x)$ is the modified Bessel function, and R is a temperature-independent prefactor.

The solid line in Fig. 8 represents the best fit to the data obtained from Eqs. (1)–(3) treating the parameters describing the electron-phonon coupling as adjustable parameters. The good fit between theory and experiment shown in the figure is obtained using $\hbar\omega = 325$ cm^{-1}, $\tau_{vib}^{-1}(0) = 924$ s^{-1}, $s = 0.2$, $p = 43$, and $R = 4.89 \times 10^{83}$ s^{-1}. These results are consistent with those described in Ref. 4 for Mn^{4+} in Y$_3$Al$_5$O$_{12}$. The value of the Huang-Rhys parameter is smaller for our case than that found in Ref. 4.

The characteristics of the FWM signal are consistent with scattering from a population grating of excited Mn^{4+} ions. The double exponential behavior of the grating decay kinetics at low temperatures is consistent with establishing population gratings independently in the two subsets of manganese ions in nonequivalent crystal field sites having different fluorescence lifetimes. The lack of dependence of the grating decay rates on the crossing angle of the write beams indicates that there is no long-range energy diffusion in this material. In addition, we performed time-resolved spectroscopy measurements exciting selectively in either site a or site b transitions. The time evolution of the fluorescence emission after selective excitation shows that no energy transfer takes place between ions in different types of sites. Thus the temperature dependence of the intensity ratios shown in Fig. 4 is due to differences in radiationless quenching and not site-to-site energy transfer.

The theoretical expression for the FWM signal is given by[8]

$$\eta = \exp[-2\alpha d/\cos\theta]\{\sinh^2[d\Delta\alpha/(2\cos\theta)]$$

$$+ \sin^2[d\pi\Delta n/(\lambda\cos\theta)]\}, \quad (4)$$

where d is the grating thickness and θ the crossing angle of the write beams in the sample. α is the average absorption coefficient at wavelength of the write beams λ. The first term represents the contribution to the signal due to an absorption grating of modulation depth $\Delta\alpha$, and the second term represents the contribution due to a dispersion grating of modulation depth Δn. For population gratings, the modulation depths can be expressed in terms of products of the concentration of ions in the peak regions of the gratings N_{2p}, with the differences in

either the absorption or dispersion of the ions in the ground and excited states. Using the rate equation describing the dynamics of a simple two-level system,[11]

$$N_{2p} = 2I_0 N_0 \sigma_1 / [2I_0 \sigma_1 + (h\nu/\tau)], \quad (5)$$

where I_0 is the intensity of the laser pump beam, N_0 is the total concentration of active ions, σ_1 is the absorption cross section for ions in level 1, $h\nu$ is the photon energy, and τ is the fluorescence lifetime of the metastable state. The parameter that dominates the temperature dependence of the four-wave mixing signal for population gratings is the fluorescence lifetime. For weak gratings, the functions in Eq. (4) can be expanded and the signal expressed as

$$\eta = C[1/(A + B/\tau)]^2, \quad (6)$$

where the temperature independent constants A, B, and C have different meanings for absorption gratings and dispersion gratings.

Equation (6) can be used to relate the temperature dependences of the fluorescence lifetimes and the four-wave mixing signal intensity. At temperatures below 80 K, the four-wave mixing signal has contributions due to scattering from Mn^{4+} ions in both types of crystal field sites, as indicated by the double exponential kinetics of the signal. Fluorescence quenching occurs for the ions in one type of site above 40 K resulting in a decrease in the scattering efficiency. Above 80 K the FWM signal is due to scattering only from Mn^{4+} in the other type of site. Using the measured values of the fluorescence lifetimes in Eq. (3) and treating A, B, and C as adjustable constants results in the solid line fitting the FWM data shown in Fig. 8. This good fit confirms the relationship between the FWM signal and the metastable state lifetime for a population grating. Not enough independent information is available to interpret the values of the adjustable constants in terms of the contributions to the grating modulation depths and thicknesses. Four-wave mixing measurements on the several other host crystals doped with Cr^{3+} which is isoelectronic with Mn^{4+} have shown that dispersion gratings make the dominant contribution to the scattering efficiency.[7,9,11–14] However, for this case Fig. 1 shows a significant difference in absorption strength for light at the laser wavelength for ions in the ground and excited metastable states, and thus the possibility of a strong contribution from an absorption grating cannot be ruled out.

ACKNOWLEDGMENT

[*]Permanent address: Institute of Physics, Polish Academy of Sciences, Al. Lotnikow 32/46, 02-668 Warszawa, Poland.

[1]S. Geschwind, P. Kisliuk, M. P. Klein, J. P. Remeika, and D. L. Wood, Phys. Rev. **126**, 1684 (1962).

[2]B. Henderson and T. P. P. Hall, Proc. Phys. Soc. London **90**, 511 (1967).

[3]L. A. Riseberg and M. J. Weber, Solid State Commun. **9**, 791 (1971).

[4]J. F. Donegan, T. J. Glynn, G. F. Imbusch, and J. P. Remeika, J. Lumin. **36**, 93 (1986).

[5]G. M. Loiacono and B. L. Greenberg (unpublished).

[6]J. R. Salcedo, A. E. Siegman, D. D. Dlott, and M. D. Fayer, Phys. Rev. Lett. **41**, 131 (1978).

[7]A. M. Ghazzawi, J. K. Tyminski, R. C. Powell, and J. M. Walling, Phys. Rev. B **30**, 7182 (1984).

[8]H. Kogelnik, Bell Syst. Tech. J. **48**, 2909 (1969).

[9]H. J. Eichler, J. Eichler, J. Knof, and Ch. Noeck, Phys. Status Solidi A **52**, 481 (1979).

[10]F. Auzel, in *The Luminescence of Inorganic Solids*, edited by DiBartolo (Plenum, New York, 1978), p. 67.

[11]K. O. Hill, Appl. Opt. **10**, 1695 (1971).

[12]D. S. Hamilton, D. Heiman, J. Feinberg, and R. W. Hellwarth, Opt. Lett. **4**, 124 (1979).

[13]P. F. Liao, L. M. Humphrey, D. M. Bloom, and S. Geschwind, Phys. Rev. B **20**, 4145 (1979); P. F. Liao and D. M. Bloom, Opt. Lett. **3**, 4 (1978).

[14]H. Eichler, G. Salje, and H. Stahl, J. Appl. Phys. **44**, 5383 (1973).

Tunable single pass gain in titanium-activated lithium germanium oxide

G. M. Loiacono, M. F. Shone, and G. Mizell

Philips Laboratories, North American Philips Corporation, Briarcliff Manor, New York 10510

Richard C. Powell, G. J. Quarles, and B. Elouadi

Department of Physics, Oklahoma State University, Stillwater, Oklahoma 74078

Laser-pumped single pass gain measurements were made on crystals of titanium-activated lithium germanium oxide between about 388 and 524 nm. Gain was observed throughout this spectral region with a peak cross section of about 1.7×10^{-19} cm^2 near 450 nm.

The development of tunable solid state lasers has generated significant interest and has potentially important electro-optic systems applications. Previous research has centered around 3d, 4d, and 5d transition metal ions in suitable hosts which has resulted in laser operation only in the red or infrared spectral regions.[1-7]

The general spectroscopic properties and features of Ti^{+4} ions have been known since the late 1930's and a compendium of experimental data was presented by Kröger in 1948.[8] However, little of the underlying physics was known of the luminescence before the work of Macke, and Blasse and Dirksen.[9-11] It is now believed that luminescence is caused by a charge transfer mechanism between the surrounding oxygen ligands and the central Ti^{+4} ion. Given a proper low symmetry site, these electric dipole allowed transitions can be activated to provide a new and potentially strong mechanism for laser transitions. We have observed strong, broadband fluorescence emission in titanium-activated lithium germanium oxide crystals and report here the first observation of tunable single pass gain in this type of material.

The Ti^{+4} doped lithium germanate crystal was grown by the Czochralski method from stoichiometric amounts of Li_2CO_3, GeO_2, and doping levels of TiO_2 between 0.05 and 1.0 mole %. All starting materials were of greater than 99.99% purity (AESAR). Ti ions can substitute directly for Ge without the need for charge compensation due to the identical ionic charge M^{+4} and similar ionic radii (0.60 vs 0.54). Samples used for measurements contained some scattering centers which did not affect the spectroscopic studies but do produce losses that significantly affect the accurate determination of laser parameters.

The experimental setup used for the single pass gain measurements has been described previously.[7] The crystal was pumped by the quadrupled output of a mode-locked Nd-YAG laser. This produced an excitation pulse at 266 nm with a half-width of about 30 ps and an energy variable up to a few millijoules. The probe beam was the collimated emission from a xenon lamp passed through a 0.50-m monochromator. Several iris diaphragms and a monochromator were used to block any fluorescence from the photomultiplier detector during the gain measurements.

The changes in the fluorescence spectra and lifetime as a function of pump energy per pulse are shown in Figs. 1 and 2,

respectively. The emission for low excitation energy is a band peaked at about 450 nm, with a half-width of about 100 nm and a lifetime of about 9 μs. As the pump energy is increased above about 0.7 mJ, the fluorescence decay time abruptly decreases to about 35 ns and the half-width of the emission band narrows to about 70 nm. These characteristics are indicative of the onset of stimulated transitions from the metastable level.

To determine if stimulated emission processes are occurring at high excitation energies, single pass gain measurements were made at pump pulse energies slightly above the threshold level determined from the lifetime data in Fig. 2. The results are shown by the points in Fig. 1. By tuning the probe beam across the fluorescence emission band, tunable gain is demonstrated in this material between 388 and 524 nm.

Using the measured peak gain coefficient (γ) and the pulsed energy threshold, the peak transition cross section can be determined from

$$\sigma_p = \gamma h \nu_{pump} / E_{threshold} , \tag{1}$$

where $E_{threshold}$ is the absorbed pump energy per pulse which is converted into fluorescence photons.[12] The results of this
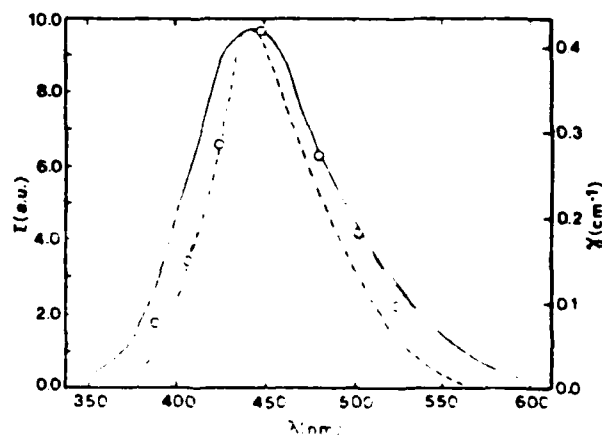

FIG. 1. Room temperature fluorescence emission of titanium-activated lithium germanium oxide after pulsed excitation at 266 nm. Below threshold (solid line) above threshold (broken line). The points represent the results of single pass gain measurements with the scale for the gain coefficient plotted on the right.
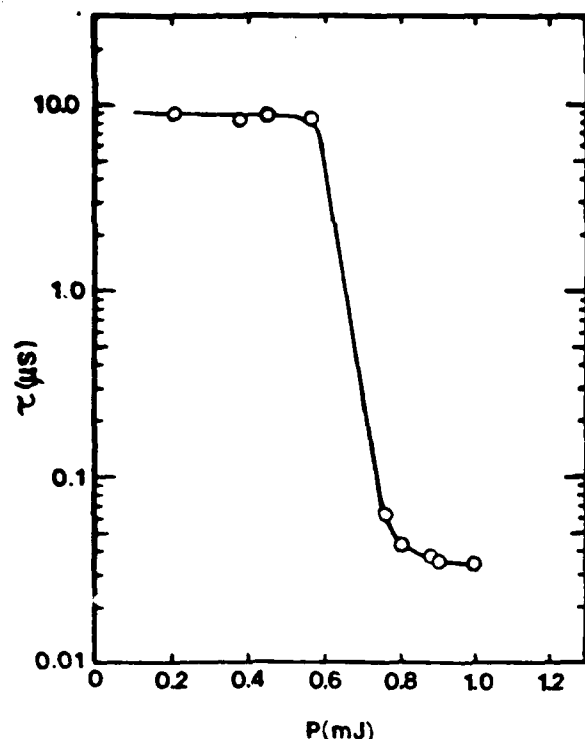
FIG 2 Variation of the fluorescence lifetime with pump pulse energy. The excitation wavelength is 266 nm and the pump pulse width is about 30 ps

calculation give a measured peak cross section of 1.7×10^{-19} cm^2. This is consistent with the theoretically predicted value if the effects of the large stokes shift are taken into account.[13,14]

These results represent the first observation of optical gain from a host activated with a closed shell transition metal ion. The spectral region, tuning width, and transition cross section demonstrate the potential importance of this material for laser applications.

Other materials of this type, improved crystal quality, and different pumping schemes are currently being investigated for determining optimum characteristics for laser performance.

[1] L. F. Johnson, H. J. Guggenheim, and R. A. Thomas, Phys. Rev. 149, 179 (1966).
[2] B. C. Johnson, P. F. Moulton, and A. Mooradian, Opt. Lett. 10, 116 (1984).
[3] J. Drube, B. Struve, and G. Huber, Opt. Commun. 90, 45 (1984).
[4] U. Brauch and U. Durr, Opt. Commun. 49, 61 (1984).
[5] J. Walling, O. G. Peterson, H. P. Jenssen, R. C. Morris, and E. W. O'Dell, IEEE J. Quantum Electron. QE-16, 1302 (1980).
[6] M. L. Shand and J. C. Walling, IEEE J. Quantum Electron QE-18, 1829 (1982).
[7] R. C. Powell, G. J. Quarles, J. J. Martin, C. A. Hunt, and W. A. Sibley, Opt. Lett. 10, 212 (1985).
[8] F. A. Kröger, Some Aspects of the Luminescence of Solids (Elsevier, New York, 1948).
[9] A. J. H. Macke, Phys Status Solidi A 39, 117 (1977); J. Solid State Chem. 18, 337 (1976).
[10] G. Blasse and G. J. Dirksen. Chem Phys. Lett. 62, 19 (1979).
[11] G. Blasse, Structure and Bonding (Berlin) 42, 1 (1980).
[12] W. Koechner, Solid-State Laser Engineering (Springer, New York, 1976).
[13] W. B. Fowler and D. L. Dexter, Phys. Rev. 128, 2145 (1962); J. Chem. Phys. 43, 1768 (1965).
[14] D. E. McCumber, Phys. Rev. A 136, 945 (1964).

IV. CHARACTERISTICS OF PHOTOREFRACTIVE CRYSTALS

One important aspect of research on photorefractive materials is characterizing the effects of different types of doping ions on the photorefractive response. The first three manuscripts in this section describe the results studying the effects of Mg ions in lithium niobate crystals. This is important since the addition of large quantities of Mg quenches the photorefractive effect and thus allows this material to be used in high power nonlinear optical and laser host applications. Several techniques were used in this investigation including small angle scattering pattern analysis and anisotropic self-diffraction. The former allows accurate determination of the modulation depth of the laser-induced grating and the latter allows accurate determination of charge diffusion properties without modulation by photovoltaic effects.

The final manuscript in this section describes results obtained on BSO crystals. This is different from the lithium niobate work in that the most important aspect of the photorefractive effect in BSO is the fast dynamic response of the material. The work described here deals with the effects of temperature on the response characteristics. Understanding this response is important in developing photorefractive materials for specific optical applications.

Analysis of holographic grating scattering patterns in LiNbO₃

H. C. Chow,* Michael L. Kliewer, Jacek K. Tyminski,† and Richard C. Powell

Department of Physics, Oklahoma State University, Stillwater, Oklahoma 74078

The properties of the photorefractive effect were investigated using the holographic grating technique in nominally pure LiNbO₃ crystals. Gratings were created with different write-beam crossing angles between 2.5° and 8.0°, and the angular distributions of the scattered probe-beam intensity were measured. Scattering maxima were observed at several different angles, and each spot was found to have a different erasure-decay rate. This is attributed to diffraction from a complex grating having multiple Fourier components. A theoretical method is presented for analyzing these types of data and obtaining information concerning the refractive-index modulation of each component of the grating. Computer fits of small-angle-scattering patterns for each diffraction maximum are shown to provide accurate values for the grating thickness and the grating depth. A comparison is made between results obtained from this technique and those obtained by measurements of the scattering efficiency at the Bragg angle with special attention focused on the importance of beam geometries in laser-induced grating experiments.

1. INTRODUCTION

The photorefractive effect (PRE) is an extremely important property for materials used in applications requiring the transmission of laser beams. Holographic images can be formed through the PRE for optical storage and information processing. On the other hand, the scattering of laser beams by the PRE inhibits the use of materials as waveguides and laser host crystals. Therefore it is important to have a detailed understanding of the physical processes underlying the PRE so that materials can be produced with optimum characteristics for specific applications. LiNbO₃ is an important material for numerous electro-optic and nonlinear-optic systems applications. Although the general characteristics of the PRE in LiNbO₃ have been well documented,[1] many specific details concerning the process are still not understood. The research discussed here describes a new technique for obtaining information on the properties of the PRE based on computer fits of small-angle-scattering patterns. The results obtained on LiNbO₃ crystals demonstrate the detailed information that can be obtained using this technique compared with other methods. In addition, the theoretical analysis of the grating properties presented here is applicable to a wide variety of laser-induced grating experiments used to study spectroscopic and nonlinear-optical properties of materials.

In the holographic technique, photorefractive patterns in the form of gratings are produced in the material by using crossed laser beams. The information concerning the grating has generally been obtained by monitoring the efficiency of scattering a laser probe beam off the grating at the Bragg diffraction angle or by measuring the decay time of the scattering efficiency while the grating is being erased by another source of light. It is assumed that the grating is in the form of a purely sinusoidal pattern with a well-defined Bragg condition so that a theoretical analysis of the data gives the modulation depth of the refractive-index grating. The properties of the charge-carrier generation, dynamics of relocation, and trapping underlying the PRE that produces the grating are determined by measuring the changes in

scattering efficiency that occur when sample properties, such as defect content and temperature, are changed or when experimental conditions, such as grating spacing and erasure-beam intensity, are changed.

Although recent advances have been made in obtaining fundamental properties of the charge-carrier-defect dynamics in some photorefractive materials,[2-4] there is still much to be understood about these processes, which are nonlinear because of the coupling between the electrostatic field and the migrating charges. These nonlinearities are bound to produce complex grating shapes in the photorefractive medium.[1] One problem with the experimental method described above is that absolute measurements of scattering efficiencies are not sufficiently accurate because of additional surface- and bulk-scattering processes as well as limitations that are due to the angular distribution of the fields present in the probe and scattered beams. Also, nonlinearities of the charge relocation within the volume of the crossed Gaussian beams make the assumption of a purely sinusoidal grating with a well-defined Bragg condition highly questionable for most conditions. Finally, the magnitude of the scattering efficiency found from this type of measurement is proportional to the square of the product of the grating depth and grating thickness. Thus, in order to obtain the desired value for the grating depth, an estimate for the grating thickness must be used. The latter can not be determined directly by this experimental technique, and the exact thickness of the grating is generally difficult to determine.

In the following sections, we describe a different technique for obtaining detailed information about the properties of laser-induced gratings. The gratings are established, and the sample and experimental conditions are varied as in a number of previously reported experiments.[1] However, in these studies, the complete small-angle-scattering pattern is measured. The thickness of the grating can be obtained directly and accurately from analyzing these patterns, and a value can be determined for the index-of-refraction modulation depth. In addition, details concerning the shape of the grating can be obtained with this method that cannot be

obtained by the methods used previously. In Section 4 the results of applying this technique to LiNbO$_3$ crystals under different experimental conditions are presented. It is shown that nonsinusoidal grating patterns can be important in determining the photorefractive properties of the material.

2. THEORETICAL DEVELOPMENT

In this section the expression describing the diffraction efficiency of light by a nonlinear optical material whose dielectric constant and conductivity are aperiodically spatially modulated is derived. In general, the aperiodic modulation of the material constants cannot be accurately described by a simple sinusoidal pattern with a single spatial frequency. The complex gratings are better described by the superposition of several sinusoidal patterns with different grating vectors. Clearly, with two or more grating vectors present simultaneously, it is not possible for a given incident beam to satisfy Bragg's condition for all the grating vectors at the same time. Light scattering off Bragg's condition has been analyzed by Kogelnik[6] for the case of a single-grating vector (i.e., a sinusoidal grating), and it is important to determine whether his results are valid for the various diffraction maxima that appear for multicomponent gratings. To justify such a procedure and to go beyond this level of accuracy requires explicit consideration of diffraction by a nonsinusoidal grating, which is the subject of this section. Roughly speaking, the basic qualitative conclusion of the present study is as follows: If the modulated index-of-refraction pattern is resolved into its Fourier components as characterized by different grating vectors, then, under the Bragg condition for a given grating vector, the diffracted light is largely independent of the other grating vectors, but off the Bragg condition the diffraction is influenced by the presence of the other grating vectors. It is shown that this feature is borne out by experimental observations. Insofar as the present study represents an extension of Kogelnik's theory,[6] his notations will be followed with as slight modifications as possible.

The situation to be studied is shown schematically in Fig. 1. An incident light beam R is brought into a medium containing a photorefractive grating. The average dielectric constant and conductivity of the medium are ϵ and σ, respectively. Let the z axis be chosen normal to the surface of the medium, let the x axis be chosen in the plane of incidence, and let the material be infinite in extent in the y direction (so that no physical quantities involved have any v dependences). The incident light enters a region ($0 \leq z \leq d$) where the material constants are modulated and emerges as S_1, S_2 after suffering changes in the propagation direction.

Actually the experiments to which the theory is intended to apply can be carried out during the erasure time of the grating. This means that the dielectric constant and the conductivity of the medium are not only spatially modulated but can also be time dependent. Under such circumstances Maxwell's equations, together with Ohm's law, dictate that the behavior of the electric field E associated with the light is governed by

$$\nabla^2 E - \mu\sigma(\partial E/\partial t) - \mu(\partial\sigma/\partial t)E - \mu\epsilon(\partial^2 E/\partial t^2)$$
$$- 2\mu(\partial\epsilon/\partial t)(\partial E/\partial t) - \mu(\partial^2\epsilon/\partial t^2)E = 0, \quad (1)$$

where μ, σ, and ϵ are, respectively, the permeability, conductivity, and dielectric constant of the medium. Let the E field be monochromatic with angular frequency ω and let the time variations of the dielectric constant and conductivity be slow compared with time variations of the field. Then in Eq. (1) the third and last two terms may be disregarded. If, in addition, the incident light is polarized perpendicular to the plane of incidence, only the y component of the E field, denoted by $E(x, z)$, will be of interest. This obeys the Helmholtz equation

$$(\nabla^2 + k^2)E(x, z) = 0, \quad (2)$$

where the complex propagation constant k is given by

$$k^2 = v\epsilon\omega^2 - i\mu\sigma\omega. \quad (3)$$

The dielectric constant and the conductivity in the modulated region are written, respectively, as

$$\epsilon = \epsilon_0 + \sum_{i=1}^{N} \epsilon_i \cos \mathbf{K}_i \cdot \mathbf{x},$$

$$\sigma = \sigma_0 + \sum_{i=1}^{N} \sigma_i \cos \mathbf{K}_i \cdot \mathbf{x}, \quad (4)$$

where the summation over i contains the N terms needed to describe the grating modulation, $\mathbf{x} = (x, y, z)$ is a position vector, $\mathbf{K}_i = K_i (\sin \phi_i, 0, \cos \phi_i)$ is the grating vector of the ith modulation component, and ϵ_i and σ_i are the cosine transforms associated with the $\mathbf{K}_i$ contribution to the spatial modulation of the dielectric constant and conductivity, respectively, and may themselves be time dependent (albeit slowly compared with the field time variation).
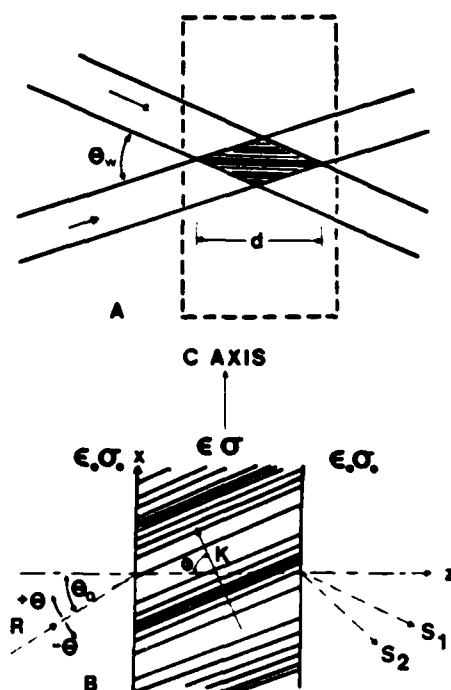

Fig. 1. Beam geometry for writing and reading laser-induced gratings.

Related to these modulations are the modifications of the index of refraction and the absorption constant of the medium. If one denotes the index of refraction by

$$n = n_0 + \sum_{i=1}^{N} \Delta n_i \cos(\mathbf{K}_i \cdot \mathbf{x}),$$

where n_0 is the average value and Δn_i is the change in the index of refraction that is due to the ith modulation, and similarly denotes the absorption constant by

$$\alpha = \alpha_0 + \sum_{i=1}^{N} \Delta \alpha_1 \cos(\mathbf{K}_i \cdot \mathbf{x}),$$

then, under the conditions of weak modulations,

$$n_0 \approx \epsilon_0^{1/2}, \qquad \Delta n_1 \approx \epsilon_i/2\epsilon_0^{1/2}; \qquad (5)$$

and

$$\alpha_0 = c\mu\sigma_0/2\epsilon_0^{1/2}, \qquad \Delta\alpha_i = c\mu\sigma_i/2\epsilon_0^{1/2}. \qquad (6)$$

On introducing the average propagation constant β through

$$\beta = 2\pi\epsilon_0^{1/2}/\lambda \approx 2\pi n_0/\lambda, \qquad (7)$$

where λ is the wavelength in vacuum, and the coupling constants κ_i through

$$\kappa_i = (1/4)\{[2\pi\epsilon_i/(\lambda\epsilon_0^{1/2})] - i(c\mu\sigma_i/\epsilon_0^{1/2})\}$$
$$\approx \pi\Delta n_i/\lambda - i\Delta\alpha_i/2, \qquad (8)$$

Eq. (3) may be rewritten as

$$k^2 = \beta^2 - 2i\alpha_0\beta + \sum_{i=1}^{N} 2\beta\kappa_i[\exp(i\mathbf{K}_i \cdot \mathbf{x}) + \exp(-i\mathbf{K}_i \cdot \mathbf{x})].$$

$$(9)$$

The electric field inside the modulated region of the photorefractive material is the superposition of the incident and diffracted waves:

$$E = R(z)\exp(-i\mathbf{r} \cdot \mathbf{x} + \sum_{i=1}^{N} S_i(z)\exp(-i\mathbf{s}_i \cdot \mathbf{x}). \qquad (10)$$

Here $\mathbf{r} = \beta(\sin\theta, 0, \cos\theta)$ is the propagation vector of the incident wave; $\mathbf{s}_i$ are the propagation vectors associated with the diffracted waves and are related to the incident wave vector through the grating vector $\mathbf{K}_i$,

$$\mathbf{s}_i = \mathbf{r} - \mathbf{K}_i, \qquad (11)$$

with Cartesian components $(\beta\sin\theta - K_i\sin\phi_i, 0, \beta\cos\phi - K_i\cos\phi_i)$. The condition for exact Bragg scattering for grating vector $\mathbf{K}_i$ is specified by

$$2\beta\cos(\phi_i - \theta_B) = K_i \qquad (12)$$

for angle $\theta = \theta_B$, while a convenient measure of the departure from this exact condition is given by the dephasing parameters ζ_i defined by

$$\zeta_i = (\beta^2 - s_i^2)/2\beta. \qquad (13)$$

These are zero at exact Bragg condition for $\mathbf{K}_i$.

Substituting Eqs. (9) and (10) into Eq. (2) and comparing the terms proportional to $\exp(-i\mathbf{r} \cdot \mathbf{x})$ and $\exp(-i\mathbf{s}_i \cdot \mathbf{x})$, the equations for the complex-wave amplitudes become

$$R'' - 2ir_zR' - 2i\alpha_0\beta R + 2\beta \sum_{i=1}^{N} \kappa_i S_i = 0,$$

$$S_i'' - 2is_{iz}S_i' - 2i\alpha_0\beta S_i + (\beta^2 - s_i^2)S_i + 2\kappa_i\beta R = 0, \qquad (14)$$

where i runs from 1 to N and the primes indicate derivatives with respect to z. Equations (14) indicate that the energies associated with the incident and diffracted waves can be depleted through absorption, that there is a direct energy interchange between the incident and diffracted waves through the coupling constants, and that there is only an indirect energy interchange between the diffracted waves through sharing the same incident wave (R). Following Kogelnik's analysis,[6] we neglect the second space derivatives of the R and S_i fields, which is justified insofar as the field envelopes change slowly. This approximation leaves us with a set of differential equations of the form

$$-2ir_zR' - 2i\alpha_0\beta R + 2\beta \sum_{i=1}^{N} \kappa_i S_i = 0,$$

$$-2is_{iz}S_i' - 2i\alpha_0\beta S_i + (\beta^2 - s_i^2)S_i + 2\kappa_i\beta R = 0. \qquad (15)$$

In the first of Eqs. (15) the second term originates from the absorption of the fields propagating in the lossy medium, while the third term describes the coupling between the R and S_i fields. Similarly, in the second of Eqs. (15) the second term is due to absorption, the third term is due to phase changes of the wave diffracted from the grating, and the fourth term is due to the coupling between the R and S_i fields. The term describing the phase change that is due to diffraction reflects only directional relationships among probe, diffracted, and grating wave vectors. At the same time, the terms describing the coupling between the R and S_i fields are dependent on the coupling constant κ_i, which depends on the depth of the index-of-refraction grating (both real and imaginary parts). Thus the validity of simplifying Eqs. (14) to Eqs. (15) requires that the second derivative R'' must be smaller than $2\beta \Sigma_{i=1}^{N} \kappa_i S_i$ and that the second derivative S_i'' must be smaller than $2\kappa_i\beta R$. These conditions set up a lower limit on the refraction-index depth (or coupling parameter κ_i) for which Eqs. (15) can be used to give a physically meaningful description of observed diffraction patterns.

Equations (15) can be rewritten in the following form:

$$c_R R' + \alpha_0 R = -i \sum_{i=1}^{N} \kappa_i S_i, \qquad (16)$$

$$c_{si}S_i' + (\alpha_0 + i\zeta_i)S_i = i\kappa_i R, \qquad i = 1, 2, \ldots, N, \qquad (17)$$

where $c_R = r_z/\beta = \cos\theta$ is the direction cosine with respect to the normal of the incident light and $c_{Si} = s_{iz}/\beta = \cos\theta - K_i\cos\phi/\beta$. These equations are supplemented with the boundary conditions

$$R(0) = 1, \qquad S_i(0) = 0, \qquad i = 1, 2, \ldots, N. \qquad (18)$$

Equations (16)–(18) constitute the basic equations for determining the diffraction efficiencies η_i in the directions of s_i. With the incident-wave amplitude normalized to unity and the power flow being normal to the surface, the requisite diffraction efficiencies, which are the fractional energy flows associated with the diffracted waves on emerging from the modulated region, are given by

$$\eta_i = (c_{Si}/c_R)S_i(d)S_i^*(d). \tag{19}$$

Since the shape of the grating is not known *a priori*, the knowledge of the number of coupled differential equations in Eqs. (16) and (17) to be solved is not available. Even if that were known and the required number of equations were solved exactly, the final results would be too complicated to be physically transparent and useful. Thus it is more advantageous to solve them approximately. The procedure for approximate solutions may be illustrated by considering the situation in which two grating vectors, K_1 and K_2, are pertinent. The extension to other situations is obvious.

Two cases may be distinguished. The first case occurs when one diffracted wave (say, S_1) takes precedence over the other (S_2). This happens if $\kappa_1 \gg \kappa_2$ or when the coupling constants are comparable if the Bragg condition for K_1 is nearly fulfilled. In this case it is permissible to ignore all the S_i terms in Eq. (16) except S_1. The resulting equation together with the two Eqs. (17) (for $i = 1$ and 2) can then be solved. The solutions that are in accord with the boundary conditions of Eq. (18) are

$$S_1(z) = \{i\kappa_1/[c_{s1}(\lambda_a - \lambda_b)]\}[\exp(\lambda_b z) - \exp(\lambda_a z)], \tag{20}$$

$$\begin{aligned}
S_2(z) = \{i\kappa_2/[c_R(\lambda_a - \lambda_b)]\}\{[(\alpha_0 + c_R\lambda_b)/ \\
(c_{s2}\lambda_a + \alpha_0 + i\zeta_2)]\exp(\lambda_a z) \\
- [(\alpha_0 + c_R\lambda_a)/(c_{s2}\lambda_b + \alpha_0 + i\zeta_2)]\exp(\lambda_b z) \\
- [(\alpha_0 + c_R\lambda_b)/(c_{s2}\lambda_a + \alpha_0 + i\zeta_2) \\
- (\alpha_0 + c_R\lambda_a)/(c_{s2}\lambda_b + \alpha_0 + i\zeta_2)] \\
\times \exp[-(\alpha_0 + i\zeta_2)z/c_{s2}]\},
\end{aligned} \tag{21}$$

where

$$\begin{aligned}
\lambda_{a,b} = (1/2)(-(\alpha_0/c_R) - (\alpha_0/c_{s1}) - i(\zeta_1/c_{s1}) \pm \{[(\alpha_0/c_R) \\
- (\alpha_0/c_{s1}) - i(\zeta_1/c_{s1})]^2 - (4\kappa_1^2/c_R c_{s1})\}^{1/2}).
\end{aligned} \tag{22}$$

Note that the expression for S_1 is identical to Kogelnik's result for the amplitude of a singly diffracted wave but that the S_2 result is different.[6] These results provide the quantitative basis for the statement made earlier that, under the Bragg condition for a given grating vector, the diffraction is largely independent of the presence of other grating vectors, and the same is not true for scattering off the Bragg condition. Since Eqs. (16)–(18) are symmetric with respect to an interchange of subscripts 1 and 2, the situation opposite what has just been described is realized if $\kappa_2 \gg \kappa_1$, or when the coupling constants are comparable, if the Bragg condition is fulfilled for K_2. The solutions for this situation are obtainable from Eqs. (20)–(22) by interchanging subscripts 1 and 2.

The final case to consider is when the departure from the Bragg condition of the coupling constants and phases for the two grating vectors is comparable. Under these conditions, $\kappa_1 \approx \kappa_2, c_{s1} \approx c_{s2} \equiv c_s$, and $\zeta_1 \approx \zeta_2 \equiv \zeta$, and the solutions to Eqs. (16)–(18) are

$$\begin{aligned}
S_i(z) = i(1/c_R)\{\kappa_1/(\gamma_a - \gamma_b)\}\{[(\alpha_0 + \gamma_b c_R)/(c_s\gamma_a + \alpha_0 + i\zeta)] \\
\times \exp(\gamma_a z) - [(\alpha_0 + \gamma_a c_R)/(c_s\gamma_b + \alpha_0 + i\zeta)]\exp(\gamma_b z) \\
- [(\alpha_0 + \gamma_b c_R)/(c_s\gamma_a + \alpha_0 + i\zeta) - (\alpha_0 + \gamma_a c_R)/ \\
(c_s\gamma_b + \alpha_0 + i\zeta)]\exp[-(\alpha_0 + i\zeta)z/c_s]\},
\end{aligned} \tag{23}$$

with $i = 1, 2$ and

$$\begin{aligned}
\gamma_{a,b} = (1/2)(-(\alpha_0/c_R) - (\alpha_0/c_s) - i(\zeta/c_s) \pm \{[(\alpha_0/c_R) - (\alpha_0/c_s) \\
- i(\zeta/c_s)]^2 - 4(\kappa_1^2 + \kappa_2^2)/(c_R c_s)\}^{1/2}).
\end{aligned} \tag{24}$$

For comparison of these theoretical predictions with experimental results, some geometrical simplifications consistent with typical experimental situations can be imposed. Consider the first case treated above and let K_1 and K_2 lie along the same direction (e.g., the c axis of a LiNbO$_3$ crystal) perpendicular to the normal as shown in Fig. 2. Then $\phi_1 = \phi_2 = \pi/2$ and $c_R = c_{s1} = c_{s2} = \cos\theta$. Introducing the dimensionless coupling constants

$$\nu_i = \kappa_i d/\cos\theta \qquad (i = 1, 2) \tag{25}$$

and the dimensionless dephasing parameters

$$\xi_i = \zeta_i d/(2\cos\theta) \qquad (i = 1, 2), \tag{26}$$

where $\zeta_i = \Delta\theta K \cos\theta$, the expression in Eq. (20) for the amplitude of the primary wave at the exit surface becomes

$$\begin{aligned}
S_1(d) = -i\exp(-\alpha_0 d/\cos\theta - i\xi_1)[\sin(\nu_1^2 + \zeta_1^2)^{1/2}]/ \\
[1 + \xi_1^2/\nu_1^2]^{1/2}.
\end{aligned} \tag{27}$$

The diffraction efficiency is then given by

$$\eta_1 = \nu_1^2/(\xi_1^2 + \nu_1^2)\exp(-2\alpha_0 d/\cos\theta)\sin^2(\nu_1^2 + \xi_1^2)^{1/2}. \tag{28}$$

For the second spot, the wave amplitude at $z = d$ is

$$\begin{aligned}
S_2(d) = (1/2)[\nu_2/(\xi_1^2 + \nu_1^2)^{1/2}]\exp(-\alpha_0 d/\cos\theta) \\
\times \{A\exp[-i\xi_1 + i(\xi_1^2 + \nu_1^2)^{1/2}] \\
+ B\exp[-i\xi_1 - i(\xi_1^2 + \nu_1^2)^{1/2}] \\
- (A + B)\exp(-i2\xi_2)\},
\end{aligned} \tag{29}$$

where

$$A = [(\xi_1^2 + \nu_1^2)^{1/2} + \xi_1]/[(\xi_1 - 2\xi_2) - (\xi_1^2 + \nu_1^2)^{1/2}], \tag{30}$$

$$B = [(\xi_1^2 + \nu_1^2)^{1/2} - \xi_1]/[(\xi_1 - 2\xi_2) + (\xi_1^2 + \nu_1^2)^{1/2}]. \tag{31}$$

The diffraction efficiency for the second spot is
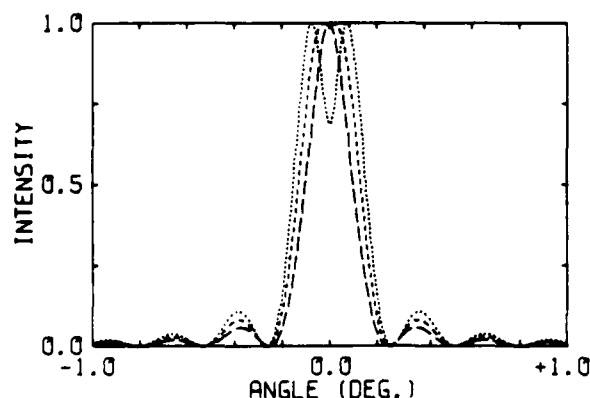

Fig. 2. Computer-simulated small-angle-scattering patterns for $\theta_B = 3°$ and $d = 400\ \mu m$. The broad dashed line is for $\Delta n = 4 \times 10^{-4}$, the short dashed line for $\Delta n = 3 \times 10^{-4}$, and the dotted line for $\Delta n = 2 \times 10^{-4}$.

$$\eta_2 = [\nu_2{}^2/(\xi_1{}^2 + \nu_1{}^2)]\exp(-2\alpha_0 d/\cos\theta)(A(A + B)$$
$$\times \sin^2\{[2\xi_2 - \xi_1 + (\xi_1{}^2 + \nu_1{}^2)^{1/2}]/2\}$$
$$+ B(A + B)\sin^2\{[2\xi_2 - \xi_1 - (\xi_1{}^2 + \nu_1{}^2)^{1/2}]/2\}$$
$$- AB \sin^2(\xi_1{}^2 + \nu_1{}^2)^{1/2}). \tag{32}$$

At the exact Bragg condition for K_1 or when $\xi_1 \ll \nu_1$, Eq. (32) is reduced to

$$\eta_2 = [\nu_2{}^2/(4\xi_2{}^2 - \nu_1{}^2)]\exp(-2\alpha_0 d/\cos\theta)$$
$$\times \{[4\xi_2/(2\xi_2 + \nu_1)]\sin^2[(2\xi_2 + \nu_1)/2]$$
$$+ [4\xi_2/(2\xi_2 - \nu_1)]\sin^2[(2\xi_2 - \nu_1)/2] - \sin^2\nu_1\}. \tag{33}$$

3. COMPUTER SIMULATIONS

In this section we focus our attention on the properties of lossless phase gratings predicted by the theoretical model described above. Most of the conclusions drawn from this analysis are applicable to (or have analogous cases for) amplitude gratings having purely imaginary coupling constants κ_i, and for combined amplitude and phase gratings where the κ_i are complex numbers. In the case of a phase grating, the coupling constant defined by Eq. (8) has only a real part, which is related to the depth of modulation of the index of refraction Δn by Eq. (5). The latter varies sinusoidally in a direction perpendicular to the z axis, thus producing a non-uniform modulation of the phases of the electric field of the probe beam in this direction causing diffraction to occur.

Figures 2 and 3 demonstrate several different angular diffraction profiles predicted by Eq. (28) under a variety of conditions relevant to our experimental studies of LiNbO₃. These patterns are for the case of unslanted gratings close to the Bragg condition where the scattering is dominated by a single spatial-frequency component of the grating. A Bragg angle of $\theta_B = 3°$ is assumed, and the computer-simulated diffraction patterns between $\pm 1°$ of the Bragg angle are generated by Eq. (28). These are normalized to a peak intensity of 1.0.

In Fig. 2 the grating thickness is fixed at 400 μm, while the modulation depth is varied between 2×10^{-4} and 4×10^{-4}. The diffraction patterns all have a pronounced central peak with sidelobes on both wings. The shape of the central peak is sensitive to changes in Δn. For a deep grating the central peak is sharp, whereas the shallow-grating diffraction pattern exhibits a broad, split central peak. The splitting of the diffraction pattern that causes the maximum scattering to occur off Bragg condition is a real physical effect[7] and not a theoretical artifact of the computer-generated pattern. In addition, for a given grating thickness, the angular separation of the sidelobes is constant, while their amplitudes decrease with an increase in grating depth.

The scattering profiles generated for a fixed grating depth of $\Delta n = 3 \times 10^{-4}$ and grating thicknesses between 300 and 500 μm are shown in Fig. 3. Again the width and the shape of the pronounced central peak change with changes in d. For thick gratings the central peak is sharp, whereas thin gratings produce a broad, split central peak. In addition, both the amplitude and the angular separation of the side-lobes are strongly dependent on the grating thickness.

The computer-generated diffraction patterns show that, as gratings become deeper or thicker, the intensity of the scat-

tered wave becomes concentrated in a well-defined region at the Bragg angle. In the limit of an infinitely thick or infinitely deep grating, the scattering pattern has the form of a delta function in the direction satisfying the Bragg phase-matching condition. For most real experimental situations, laser-induced gratings will produce scattering patterns with a significant amount of intensity at angles slightly varying from θ_B. Since the probe and signal beams are never perfectly collimated, it is important to determine how the signal seen by a detector with a small acceptance angle compares with that predicted for perfect Bragg scattering. This comparison is shown in Figs. 4 and 5 as a function of grating depth and grating thickness, respectively. The scattering efficiency at the Bragg angle is found from Eq. (28) to be

$$\eta_B = \exp[-2\alpha_0 d/\cos\theta_B]\sin^2[\pi\Delta n d/(\lambda\cos\theta_B)]. \tag{34}$$

The scattering efficiency averaged over a small angle $\Delta\theta$ around the Bragg angle is

$$\langle\eta\rangle = \int_{\theta_B-\Delta\theta}^{\theta_B+\Delta\theta} \eta(\theta')d\theta'/(2\Delta\theta), \tag{35}$$

where $\eta(\theta')$ is given by Eq. (28). The curves in the figures were generated for $\Delta\theta = \pm 0.025°$ and a Bragg angle of 3°.

Figure 4 compares the dependence of scattering efficiency on grating modulation depth for a grating thickness of 400 μm for a well-collimated probe beam versus a slightly converging or diverging beam. For deep gratings, an oscillatory dependence is observed for both collimated and averaged scattering efficiencies because of the interference effects of the phase-modulated signal contributions scattered from different parts of the grating. At smaller modulation depths, the curve for the collimated signal obeys the simple relationship

$$\eta_B \propto |\Delta n|^2 d^2, \tag{36}$$

which is frequently used in describing the results of laser-induced grating experiments. It is interesting to note that the deviation from this quadratic dependence occurs above a scattering efficiency of 90%, indicating that the validity of expression (36) is not limited to small values of η_B. For large values of Δn, the curve for the averaged scattering efficiency follows closely the curve for η_B. This is not sur-
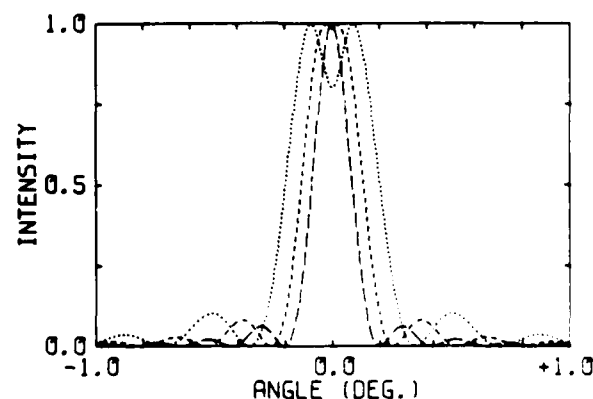

Fig. 3. Computer-simulated small-angle-scattering patterns for $\theta_B = 3°$ and $\Delta n = 3 \times 10^{-4}$. The broad dashed line is for $d = 500$ μm, the short dashed line for $d = 400$ μm, and the dotted line for $d = 300$ μm.
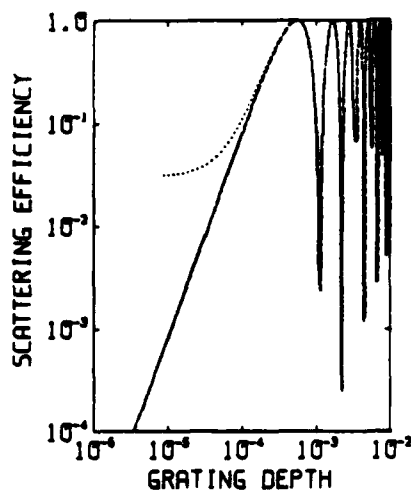
Fig. 4. Computer-simulated scattering efficiency as a function of grating depth Δn for $\theta_B = 3°$ and $d = 400 \,\mu m$. The broken line is for exact Bragg scattering, and the dotted line is the average value ±0.025° about θ_B.
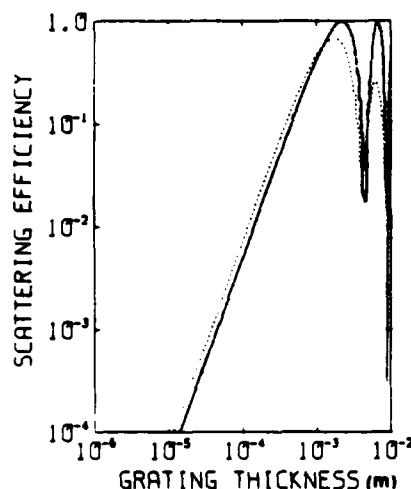

Fig. 5. Computer-simulated scattering efficiency as a function of grating thickness d for $\theta_B = 3°$ and $\Delta n = 1 \times 10^{-4}$. The broken line is for exact Bragg scattering, and the dotted line is the average value ±0.025° about θ_B.

prising, since for deep gratings most of the light is scattered in the Bragg direction, leading to

$$\eta_B \approx \langle \eta \rangle. \tag{37}$$

However, at small values for Δn, $\langle \eta \rangle$ departs from the quadratic dependence predicted by expression (36) because of the splitting of the central peak as seen in the diffraction patterns. Averaging the signal over small angles around the Bragg peak includes more of the scattered light intensity than seen at the exact Bragg angle, leading to

$$\langle \eta \rangle > \eta_B. \tag{38}$$

The curve in Fig. 4 tends toward a constant value of $\langle \eta \rangle$ for small Δn. Although the deviation from a quadratic dependence is real, the exact dependence shown is unphysical and

is due to the simplifications made in deriving Eqs. (14) and (15), in which the second derivatives of the fields R'' and S_i'' were neglected compared with the coupling constant κ_i.

Figure 5 compares the dependence of scattering efficiency on grating thickness for a grating of depth $\Delta n = 1.0 \times 10^{-4}$ for a well-collimated probe beam versus a slightly diverging or converging beam. The angular average is again taken for $\Delta\theta = \pm 0.025°$ around $\theta_B = 3°$. For thick gratings both η_B and $\langle \eta \rangle$ show an oscillatory behavior that is due to interference effects of light scattered from different parts of the grating. For thin gratings both η_B and $\langle \eta \rangle$ vary quadratically with d, as predicted by expression (36). The magnitude for the angular average scattering efficiency is greater than the exact Bragg scattering efficiency because of the splitting of the central peak. The smaller the value of d, the greater the range of Δn for which expression (37) will be valid.

The above discussion of computer-simulated scattering results shows that the simple expression given in relation (36), which is generally used to interpret scattering data from laser-induced gratings, is valid only for restricted conditions. One condition is having a simple sinusoidal grating that is produced only if the laser beams writing the grating are exactly collimated beams with uniform intensity throughout the region to be probed and if the charge-relocation dynamics are simple enough to replicate the shape of the laser-interference pattern. Another condition is having the modulation depth and thickness large enough to have most of the scattered light concentrated in the central Bragg peak but not so large that interference effects occur from light scattered from different parts of the grating. In addition, the probe and signal beams must be well collimated so that the detector sees only light scattered at the exact Bragg condition. Finally, fitting the curves obtained from angular scattering-pattern measurements provides a method for obtaining accurate values of grating thickness as well as grating depth. This cannot be found from the results of Bragg scattering-efficiency measurements. In the Section 3 experimentally measured scattering patterns are reported and compared with these theoretically predicted patterns in order to determine the physical properties of the gratings.

3. EXPERIMENTAL PROCEDURE

Samples of good-optical-quality single crystals of poled LiNbO$_3$ obtained commercially were used in this investigation. This was nominally pure material containing a total concentration of transition-metal-ion impurities of between 25 and 50 parts in 10^6.

Photorefractive gratings were established and probed using the experimental setup shown as a block diagram in Fig. 6. The 442-nm emission from a 16-mW He–Cd laser was used to write and erase the photorefractive holograms. The 633-nm emission from a 6-mW He–Ne laser was used to probe the grating without damaging the hologram. The scattered signal beam was detected by an RCA C31034 photomultiplier tube and recorded with the help of a lock-in amplifier to improve the signal-to-noise ratio.

In these experiments the write beam was split into two components, which were superimposed inside the sample, producing an interference pattern in the shape of a grating. The charge relocation associated with the PRE in the peak regions of the grating reached steady-state conditions in 20
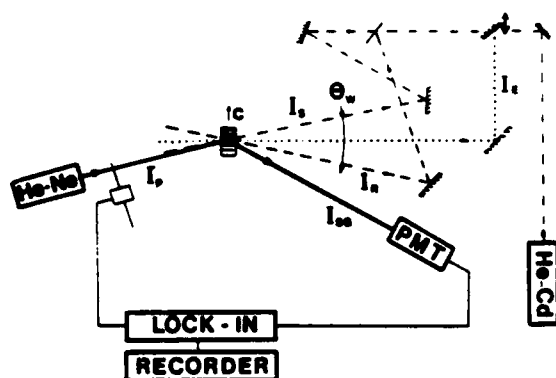
Fig. 6. Block diagram of the experimental setup. He–Cd and He–Ne are the lasers used to write (and erase) and probe the gratings, respectively. PMT, photomultiplier tube.

sec to 15 min. The properties of the resulting holographic grating were investigated by monitoring the scattering efficiency of the probe beam as a function of scattering angle. This was accomplished by slight rotations of the base on which the sample was mounted, which is equivalent to varying the angles of the probe and signal beams with respect to the induced grating. The details of this geometry are shown in Fig. 6.

The phase grating that develops in $LiNbO_3$ because of the interference pattern of the laser beams originates from de-trapped charges that migrate because of drift, diffusion, and the bulk photovoltaic effect.[1] As a result of this charge transport, a periodic electrostatic field develops inside the crystal, causing a modulation of the index of refraction of the material. However, the coupling between the static electric field and the velocity of the charges in the crystal leads to nonlinearities in the charge-transport characteristics, which can cause the final shape of the refractive-index grating to be significantly different from the sinusoidal interference pattern of the crossed laser beams.

Additional properties of the PRE in these samples were studied by monitoring the erasure of the holograms and by comparing the scattering properties for holograms with different grating spacings. Erasure was accomplished by inserting the movable mirror in the path of the He–Cd beam, as shown in Fig. 6. This produced uniform illumination of the sample, which relocated the trapped charges in a random distribution, thus erasing the photorefractive grating hologram. To avoid problems with partially erased gratings, the samples were thermally annealed in air at 500°C for 1 h after each measurement of the diffraction pattern.

4. EXPERIMENTAL RESULTS

The diffraction pattern developed in $LiNbO_3$ as a result of charge relocation induced by the interference pattern of the laser write beams was observed to consist of three primary maxima. The directions of these three diffracted beams show that they originate from different spatial frequencies contributing to the refractive-index grating consisting of the fundamental, first, and second harmonics of the write beams' interference pattern. The presence of the harmonic frequencies is caused by the nonlinearities in the charge

transport induced by the interaction between the light interference pattern and the space-charge field, which is built up by the charge relocation. Different erasure times of the different frequency components of the grating are observed by measuring the different time dependences of the three scattering maxima under uniform illumination of the sample, causing grating erasure.

Figure 7 shows examples of the small-angle-scattering patterns around the three primary scattering maxima measured on $LiNbO_3$ at a write-beam crossing angle of 2.5° and a write time of 2 min. Computer fits to the observed data were obtained from Eq. (28), treating the grating modulation depth and thickness as adjustable parameters. A good fit is obtained from the scattering pattern associated with the fundamental grating frequency, as shown in Fig. 7A. This was obtained for values of $\Delta n_1 = 3.48 \times 10^{-4}$ and $d_1 = 370$ μm and is extremely sensitive to the choice of both parameters. The fit between theory and experiment is poorer for the pattern associated with scattering from the grating component associated with the first harmonic of the laser-interference pattern, as shown in Fig. 7B. However, the best fit gives estimates for the depth and thickness of this component of the grating as $\Delta n_2 = 4.62 \times 10^{-4}$ and $d_2 = 401$ μm. The scattering from the grating component associated with the second harmonic of the laser-interference pattern, shown in Fig. 7C, has an asymmetric central peak and therefore cannot be described by Eq. (28).

The results of comparing experimentally observed scattering patterns with computer-generated patterns for multi-Fourier-component gratings, as shown in Fig. 7, demonstrate that the assumptions underlying the derivation of Eq. (28) are valid for scattering from the fundamental grating
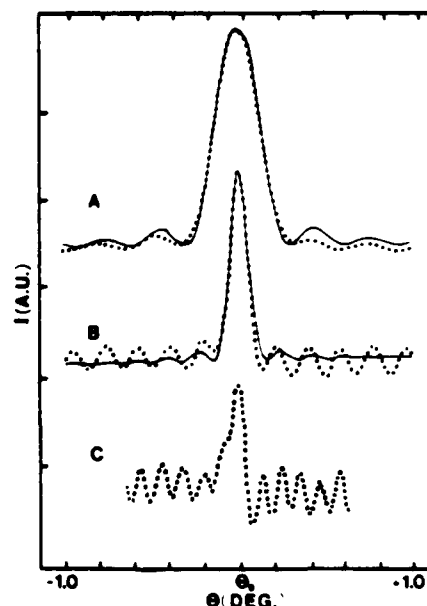
Fig. 7. Small-angle-scattering patterns around the three scattering maxima for $LiNbO_3$ after a 2-min write time at $\theta_W = 2.5°$. The dotted lines are the experimental measurements, and the solid lines are computer-simulated fits to the data. A, First spot $\theta_B = 2.8°$; $d = 370$ μm; $\Delta n = 3.48 \times 10^{-4}$. B, Second spot $\theta_B = 4.69°$; $d = 401$ μm; $\Delta n = 4.62 \times 10^{-4}$. C, Third spot $\theta_B = 6.3°$.
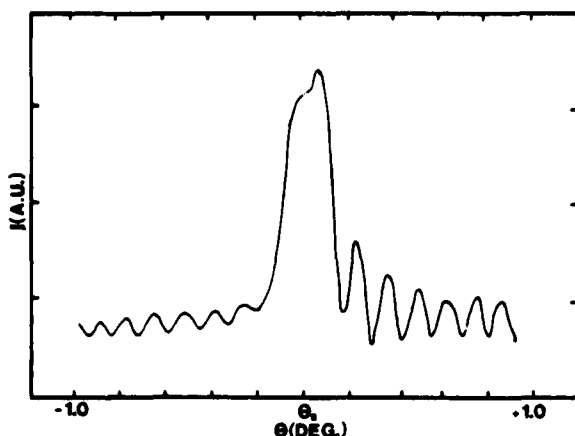
Fig. 8. Small-angle-scattering pattern for the first spot in LiNbO$_3$ after a 15-min write time at $\theta_W = 8°$. $\theta_B = 7.5°$.
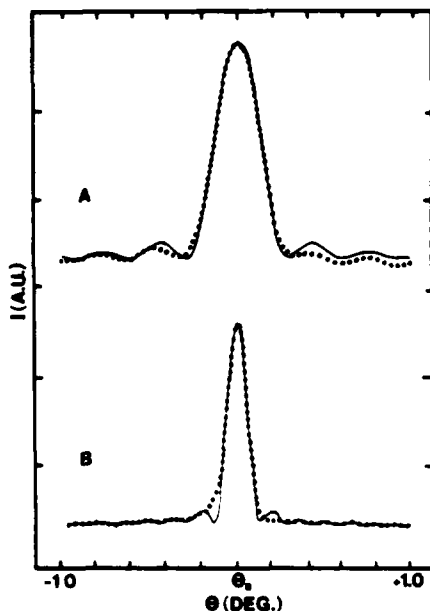

Fig. 9. Small-angle-scattering patterns for the first spot in LiNbO$_3$. A, $\theta_W = 2.5°$; $\theta_B = 2.79°$; $\Delta n = 3.48 \times 10^{-4}$; $d = 370$ μm; write time is 2 min. B, $\theta_W = 8°$; $\theta_B = 7.5°$; $\Delta n = 4.4 \times 10^{-4}$; $d = 300$ μm; write time is 20 sec.

component but become less valid for scattering from progressively higher-order frequencies of the grating. This is because the nonlinear interaction between the migrating charges and the induced space-charge field is greater for higher spatial frequencies. This results in a greater departure from a sinusoidal grating shape that breaks down the assumption that the probe and scattered waves couple through a single frequency of the Fourier series of the refractive-index grating. The experimentally observed pattern shown in Fig. 7C has large phase-correlated contributions associated with scattering from different spatial frequencies of the grating. These show up as the large oscillations in the

wings of the pattern with nondecaying amplitudes. This type of pattern is predicted by Eq. (32) describing the case of a grating with two spatial frequencies probed off Bragg conditions and with comparable coupling constants for the probe and scattered fields for both grating components. This effect appears to a smaller extent in the pattern shown in Fig. 7B. However, the pattern in Fig. 7A exhibits the predicted decaying amplitude sidelobes, indicating that, near Bragg condition for scattering from the grating frequency component associated with the fundamental of the write-beam interference pattern, the effects of scattering from other grating frequency components are negligible.

The results discussed above indicate that deviations from theoretically predicted scattering patterns will be observed when the interaction between the migrating charges and the electrostatic field is strong. This will occur for deep gratings and those with small spatial frequencies. The experimental conditions producing these conditions are long write times and large write-beam crossing angles, respectively. Figure 8 shows an example of a scattering profile obtained after writing a grating for 15 min at a write-beam crossing angle of 8.0°. The asymmetry of the pattern and the strong sidelobes resemble the shape of the pattern in Fig. 7C. Again, this can be attributed to phase-correlated contributions associated with scattering originating from different spatial-frequency components of the grating interfering with the scattering from the fundamental component near its Bragg condition.

One way to reduce the interference effects produced by scattering from multi-Fourier-component gratings is to create gratings with only a small population of charge relocation. This can be accomplished by reducing the writing time of the gratings. Figure 9 shows the small-angle-scattering patterns obtained for small amounts of charge relocation. For the small-write-angle results shown in Fig. 9A, a write time of 2 min could be used and still produce a good fit between the experimental results and the predictions of Eq. (28). For longer write times, discrepancies between theory and experiment begin to occur. Figure 9B shows similar results for a larger write angle. In this case the good fit shown between theory and experimental results could be obtained for write times of only 20 sec or less. This demonstrates that the smaller grating spacing produced at larger write angles results in significant electrostatic field effects for smaller numbers of charges relocated compared with the effects seen for gratings with larger spacings.

5. SUMMARY AND CONCLUSIONS

The analysis of the total angular scattering patterns from laser-induced refractive-index gratings in LiNbO$_3$ reveals intensity maxima in several directions associated with scattering from different components of a multi-Fourier-component grating. This is not a surprising result, considering the complexity of the charge-relocation dynamics in this material,[3] but it has not been investigated previously. Extension of Kogelnik's theory to a two-frequency-component grating predicts that the scattering efficiency at exactly the Bragg condition for one component is not significantly affected by the presence of the other components, but scattering at other angles shows interference effects associated with scattering from different grating frequency components. Anal-

ysis of the small-angle-scattering patterns around the multiple-scattering maxima observed for $LiNbO_3$ shows this prediction to be true for the lowest-frequency grating component but not for the highest-frequency component. In the latter case, a more rigorous theoretical treatment is needed to describe the nonlinear interaction between the migrating charges and the induced space-charge field.

The variation in the shapes of the small-angle scattering patterns with different write times was observed previously.[7] However, the technique of fitting computer-simulated scattering patterns to experimentally observed patterns has not been used before to obtain information about laser-induced grating parameters. The results presented above show this technique to be a sensitive way to measure the grating thickness and modulation depth. This method has significant advantages over the normal technique of measuring the scattering efficiency at the Bragg angle and relating the result to the index-modulation depth by assuming a value for the effective thickness of the grating. In addition, it was shown that scattering-efficiency measurements at an exact Bragg condition also suffer from experimental geometry problems, such as a limited detector acceptance angle and a slightly converging or diverging signal beam. This problem becomes crucial in the case of shallow gratings.

Laser-induced grating spectroscopy has become an important tool in studying the properties of solids in areas such as exciton, charge-carrier, and thermal transport as well as in studies of third-order nonlinear optical effects. Also, laser-induced gratings are being used in practical applications such as phase conjugation. The results reported here may have important consequences in any of these experiments or applications.

ACKNOWLEDGMENTS

* Permanent address, Department of Physics, Southern Illinois University at Edwardsville, Edwardsville, Illinois 90218.

† Present address, Department of Physics, Center for Applied Quantum Electronics, North Texas State University, Denton, Texas 76203.

REFERENCES

1. P. Gunter, Phys. Rep. **93**, 199 (1982). (An extensive survey of previous literature is contained in this review.)
2. J. Feinberg, D. Heiman, A. R. Tanguay, Jr., and R. W. Hellwarth, J. Appl. Phys. **51**, 1279 (1980); J. Appl. Phys. **52**, 537 (1980); J. Feinberg, in *Phase Conjugation*, S. J. Fisher, ed. (Academic, New York, 1983), p. 218.
3. J. K. Tyminski and R. C. Powell, J. Opt. Soc. A. B **2**, 440 (1985).
4. M. B. Klein and G. C. Valley, J. Appl. Phys. **57**, 4901 (1985).
5. J. Jackal, A. M. Glass, G. E. Peterson, C. E. Rice, D. A. Olson, and J. J. Veselka, J. Appl. Phys. **55**, 269 (1984).
6. H. Kogelnik, Bell Syst. Tech. J. **48**, 2909 (1969).
7. D. L. Staebler, W. Burke, W. Phillips, and J. J. Amodei, Appl. Phys. Lett. **26**, 182 (1975); D. L. Staebler, in *Holographic Recording Materials*, H. H. Smith, ed. (Springer-Verlag, Berlin, 1977), p. 101.

Laser-induced grating characteristics in doped lithium niobate crystals

Luis Arizmendi,[a] Michael J. Kliewer, and Richard C. Powell

Physics Department, Oklahoma State University, Stillwater, Oklahoma 74078-0444

The properties of laser-induced gratings were characterized in doped LiNbO$_3$ crystals using small-angle scattering pattern analysis, the analysis of erasure decay patterns, and two-beam mixing. The results show the usefulness of each of these types of experimental techniques in obtaining different types of information about the photorefractive response of the material. The samples investigated included crystals doped with copper, erbium, magnesium, and hydrogen. The results obtained on a series of Mg-doped crystals showed a strong increase in the charge relocation rate at high concentration levels resulting in a decrease in the grating modulation depth. The results of the two-beam mixing experiments are consistent with increased conductivity in the samples with high Mg concentrations.

I. INTRODUCTION

There is currently a renewed interest in understanding the details of the photorefractive effect in LiNbO$_3$ crystals because of the potential use of this material in optical switching, storage, waveguide, and phase-conjugation applications. Although the general properties of the physical mechanism leading to the photorefractive response of the material are known to be associated with light-induced charge relocation,[1] the individual processes of defect ionization, charge migration, and trapping have not been well characterized. In order to produce material with the desired photorefractive response for a specific application, it is essential that these processes be understood. Since the photorefractive effect (PRE) is an extrinsic property, it is necessary to investigate how *different types of defects* alter the photorefractive response of the material.

The laser-induced holographic grating technique provides a powerful method for investigating the properties of the PRE in a material.[1,2] We recently used this technique in two different types of experimental studies of "nominally pure" LiNbO$_3$ crystals. The first was an analysis of the dynamics of the erasure decay of the holographic gratings which provided information concerning the charge relocation rates and trap densities contributing to the PRE after different thermal treatments.[3] The second was an analysis of the total angular scattering patterns from the holographic gratings which provided information concerning the grating depths and widths as well as showing the presence of multiple Fourier components under different grating writing conditions.[4] The information obtained in both types of experiments is important in obtaining a complete understanding of the photorefractive process in the material. In addition, two-beam mixing is a useful method of characterizing the transport properties of photorefractive materials.[1]

In this paper we extend the measurements of the erasure decay analysis, scattering pattern analysis, and two-beam mixing to the study of doped crystals. Since it is known that impurity ions can either enhance or decrease the PRE in LiNbO$_3$, we have investigated the properties of both type of

doped materials. The impurity ions in the former category include Cu and Er, while those in the latter category include Mg and H$^+$. Emphasis is placed on the variation of the PRE properties as a function of Mg concentration since LiNbO$_3$:Mg crystals are finding important applications for "photorefractive-free" materials.[5,6]

II. EXPERIMENT

Eleven samples were used in this investigation. Five samples were cut from a boule of "nominally pure" LiNbO$_3$ obtained from Crystal Technology which contained a total concentration of transition-metal ion impurities of between 25 and 50 ppm. One of these was left undoped while the other four were doped with H$^+$ by heating them to 240 °C in sealed tubes containing benzoic acid for varying amounts of time ranging between two and fourteen days. These crystals were then annealed at 400 °C for six days in sealed tubes and then annealed in air for nine days at the same temperature. This procedure has been developed for H$^+$ exchange with the Li$^+$ in producing waveguides with controlled changes in the refractive index of the material.[6-9] Crystals of LiNbO$_3$:Cu (1 wt. %) and LiNbO$_3$:Er (0.05 wt. %) were also obtained from Crystal Technology. The remaining samples were obtained from Union Carbide and contained four different concentrations of MgO ranging from 1.8 to 8.8 mol %).

The details of the experimental procedures used in this work have been described previously.[3,4] The gratings are formed by crossing two laser beams in the sample from a 16-mW He-Cd laser at 442 nm, and probed by a He-Ne laser at 632 nm. The light-induced charge relocation reached steady-state conditions in times between 30 s and 2 min depending on the sample, laser intensity, and crossing angle of the write beams. The gratings can be erased by a single beam from the He-Cd laser. To analyze the grating decay dynamics, the decay of the intensity of the scattered probe beam under Bragg scattering conditions is monitored as a function of time during erasure. To analyze the shape of the angular scattering patterns, the scattering efficiency of the probe beam was monitored as a function of scattering angle. To characterize the two-beam mixing properties, the changes in *the intensities of the two write beams were monitored as a* function of time after exiting the sample.

---

[a] Permanent address: Departmento de Optica y Estructura de la Materia, Universidad Autonoma de Madrid, 28049 Madrid, Spain.
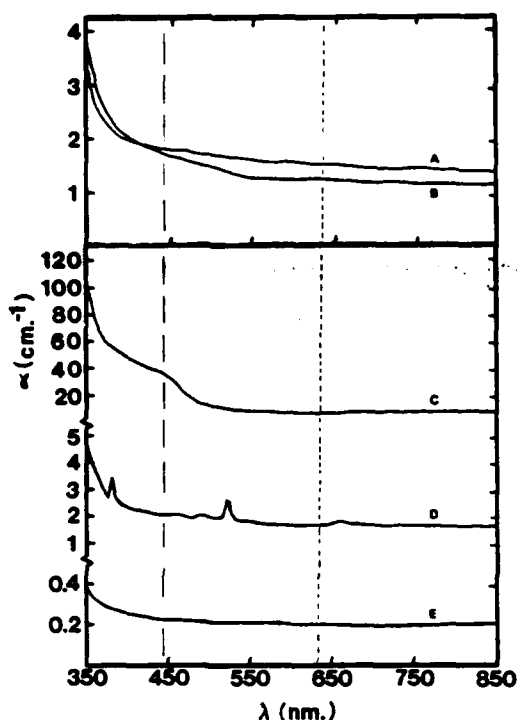
FIG. 1. Absorption spectra of (A) LiNbO$_3$:H$^+$, (B) LiNbO$_3$, (C) LiNbO$_3$:Cu, (D) LiNbO$_3$:Er, and (E) LiNbO$_3$:Mg.

Figure 1 shows the absorption spectra of the five types of samples used for this investigation with the broken vertical lines indicating the wavelengths of the laser beams used to write and probe the gratings. Note tha$^+$ Cu significantly en-

hances and Mg significantly decreases the absorption coefficient of the material at the wavelength of the He-Cd laser. This implies that light absorption in LiNbO$_3$:Cu crystals can produce Cu$^+$-Cu^{2+} valence changes contributing to the photorefractive response while the Mg^{2+} valence state remains unchanged by light absorption. The presence of H$^+$ causes little change in the absorption of the host crystal at the wavelength of the He-Cd laser. The LiNbO$_3$:Er sample shows additional absorption bands associated with *f-f* transitions of Er^{3+}, but there is no evidence that these play any direct role in changing the photorefractive response of the material.

III. ANALYSIS OF ANGULAR SCATTERING PATTERNS

The information concerning the details of the laser-induced grating is obtained by generating a computer fit to the angular scattering patterns measured by the procedure described above. The theory for generating the computer fits to the data was derived in detail in Ref. 4. This is based on the theory of Kogelnik[10] extended to include the possible presence of two components to the grating described as the superposition of two sine-wave patterns with different wave vectors. By resolving the refractive-index grating into its Fourier components, it was shown that under the Bragg scattering condition for a given grating vector, the diffracted light is essentially independent of the presence of the other Fourier components of the grating, but outside the Bragg condition interference effects among the different grating components influence the shape of the scattering pattern.

The expression derived for the scattering efficiency of a specific Fourier component of the grating is[4]

$$\eta = \{(\Delta n \lambda_w)^2 / [(\Delta n \lambda)^2 + (\lambda_p \Delta\theta \sin\theta_B \cos\theta_B)^2]\} \exp[-(2\alpha d/\cos\theta)]$$
$$\times \sin^2\{[(\lambda_w \pi \Delta n d)^2 + 2(\pi\Delta\theta\lambda_p d \sin\theta_B \cos\theta_B)^2]/(\lambda_p \lambda_w \cos\theta)^2\}^{1/2}. \tag{1}$$

Here, λ_w and λ_p are the wavelengths of the write and probe beams in the crystal, Δn is the grating depth (laser-induced *change in the refractive index*), d is the grating thickness, α is the absorption coefficient at the wavelength of the probe beam, and $\theta = \theta_B + \Delta\theta$ where θ is the scattering angle and θ_B is the Bragg angle. At Bragg condition this reduces to

$$\eta_B = \exp[-(2\alpha d)/\cos\theta_B]\sin^2[(\pi\Delta n d)/(\lambda_p \cos\theta_B)]. \tag{2}$$

This shows that for small arguments of the sin function, the scattering efficiency is proportional to $(\Delta n d)^2$.

Typical results of the analysis of angular scattering patterns are shown in Fig. 2. These were obtained for the strongest diffraction spot using a write beam crossing angle of 4°. For the Mg- and H$^+$-doped samples, write times of 2 min were found to provide the best scattering pattern, while 30-s write times gave the best patterns for the Cu- and Er- doped samples. The shapes of the patterns in terms of the widths of the Bragg peaks, the intensities of the Bragg peaks relative to the

side lobes, and the angular separation of the side lobes are approximately the same for the H$^+$- and Mg-doped samples. However, these characteristics change significantly for the Er and Cu samples, as seen in Fig. 2. The values of Δn and d obtained from fitting Eq. (1) to the experimental results are listed in the figure caption.

One result of special interest is to determine how the laser-induced refractive-index change varies with concentration of H$^+$ and Mg under similar grating formation conditions. These results are shown in Fig. 3. For both sets of samples, the grating thicknesses ranged between 688 and 624 μm for the patterns analyzed. The H$^+$-doped samples exhibited a decrease by a factor of about 0.6 in Δn compared to the value obtained for the "nominally pure" sample, and appeared to saturate at this level for acid treatments of four days and longer. Small levels of Mg doping increase the magnitude of the laser-induced change in the refractive index, but at high concentration levels Δn is reduced by a factor of about 0.03 of its value in the "nominally pure" sample.
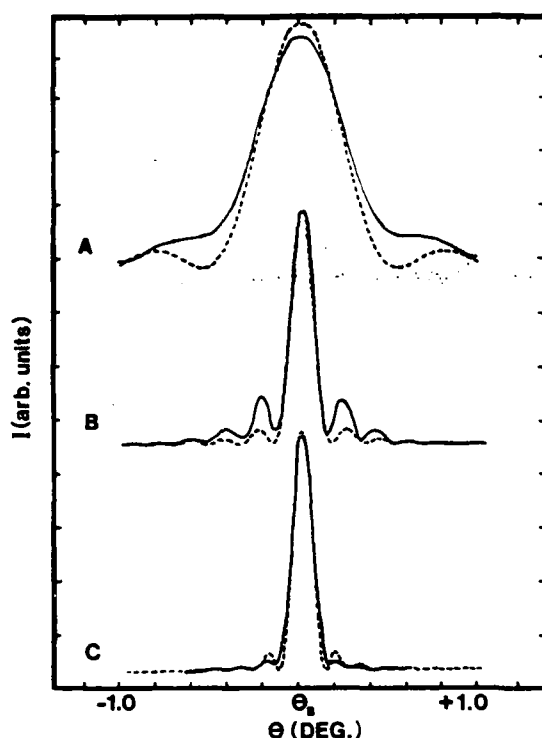
FIG. 2. Measured angular scattering patterns (solid lines) and computer simulations (broken lines) for doped LiNbO$_3$. (A) Cu doped, $\Delta n = 1.08 \times 10^{-3}$, $d = 197$ μm. (B) Er doped, $\Delta n = 5.5 \times 10^{-4}$, $d = 600$ μm. (C) H$^+$ doped, $\Delta n = 4.03 \times 10^{-4}$, $d = 688$ μm.
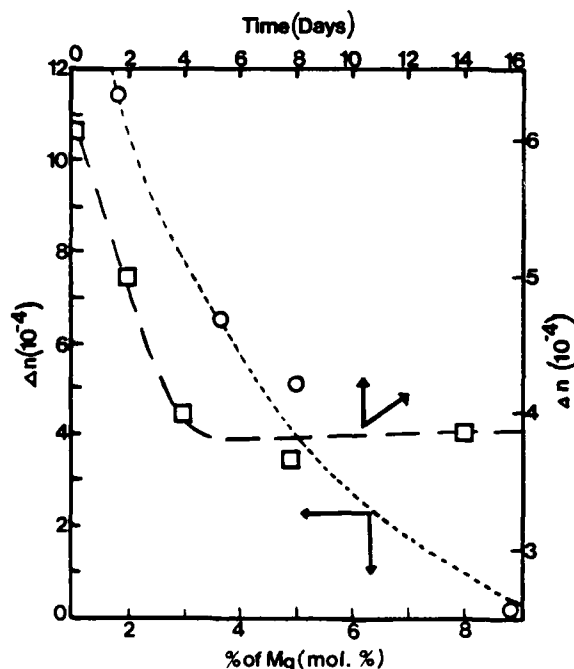

FIG. 3. Variation of Δn with Mg concentration (circles) and with H$^+$ concentration determined by the time used for the acid treatment (squares).

A final experiment was performed on grating erasure in "nominally pure" LiNbO$_3$. Gratings were formed at 4° write beam crossing angles and write times of 1 min. Scattering patterns were recorded after partial erasure times of between 0 and 3 min. Computer analysis of these patterns was performed to determine the variation of Δn and d as a function of erasure time. For short partial erasure times, the product of $(\Delta nd)^2$ was found to decrease with time in the same way as the scattering efficiency at Bragg condition, as predicted theoretically. However, at longer partial erasure times η continues to decrease with time while the value of $(\Delta nd)^2$ obtained from scattering pattern analysis becomes independent of time. This represents a lower limit of the sensitivity of this technique which occurs for small grating modulation depths.[4] The value of Δn at which this limit occurs depends on the grating thickness and grating fringe spacing.

IV. ANALYSIS OF GRATING DECAY DYNAMICS IN LiNbO$_3$:Mg CRYSTALS

In addition to knowing the effects of specific impurity ions on the thickness and modulation depth of laser-induced gratings, it is important to determine the mechanisms through which the impurity ions are affecting the PRE in the material. This can be associated with changes in the charge migration, trapping, or detrapping rates and can be investigated by analyzing the erasure decay dynamics of the scattering efficiency at the Bragg condition.[3] Because of the effectiveness of Mg in changing the PRE in LiNbO$_3$, we analyzed the grating erasure decays of the four samples with different concentrations of Mg.

The approach used in this analysis is based on a model developed by Feinberg et al.[11] which assumes that the grating wavelength is greater than the charge relocation distance and that the relocation of charges can be described by a single parameter, the average charge relocation rate. The decay of the scattered signal intensity during erasure is predicted to be exponential with the decay rate given by

$$K = K_0 + K_\theta \sin^2(\theta/2) . \qquad (3)$$

The first term describes the contribution to the erasure rate due to the trapping and detrapping of charges and is independent of the grating spacing. It is given by $K_0 = 2(RL^2)Nq^2/(\epsilon\epsilon_0 k_B T)$, where ϵ and ϵ_0 represent the dielectric constants of the material and a vacuum, respectively, k_B is Boltzmann's constant, T is the temperature, N is the average concentration of the photocarriers contributing to the PRE, and q is their charge. The charge relocation parameter $(RL)^2$ is the product of the square of the distance over which the charges relocate, L, and the R is the rate of relocation. The latter is given by the product of the effective photon density creating the free charge carriers and their diffusion coefficient. The second term in Eq. (3) is given by $K_\theta = 2(RL^2)(4\pi/\lambda)^2$. This describes the contribution to the erasure due to charge relocation over the distance $\Lambda/2\pi$. where the grating wavelength is given by $\Lambda = \lambda/[2\sin(\theta/2)]$.

Information on the charge concentrations contributing to the PRE and their relocation rate can be obtained by measuring the erasure decay rate of the scattered signal intensity
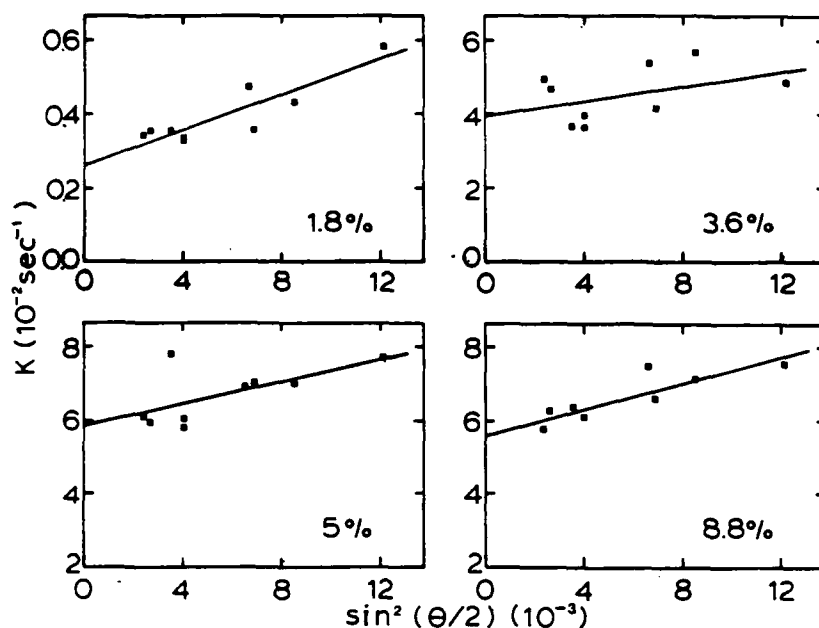
FIG. 4. Variation of the erasure decay rate of laser-induced gratings as a function of crossing angle of the write beams for LiNbO₃:Mg with different doping levels of Mg.

as a function of the crossing angle of the write beams used to create the grating. The slope and $\theta = 0°$ intercept of these results give the values of K_0 and K_θ, respectively. From the definitions given in the previous paragraph, information on the charge carrier density and relocation rate can then be obtained. Figure 4 shows the data obtained on the four samples of Mg-doped LiNbO₃. The erasure was accomplished by illuminating the sample with the He-Cd laser beam expanded in the c direction to cover all the sample. The intensity of the erasure beam was approximately 90 mW/cm². The solid lines in the figure represent the least-squares fits to the data. The values of K_0 and K_θ obtained from fitting these data are listed in Table I.

The values obtained from this analysis for the concentration of charge carriers and the charge relocation rate for each of the four samples are also listed in Table I. The latter parameter shows a significant increase with Mg concentration while no distinct concentration variation is observed for the former. The concentrations of charge carriers contributing to the PRE is approximately the same for the Mg-doped samples as that reported previously for the "nominally pure" sample, while the relocation rates are significantly larger in the doped samples.[3] Figure 5 shows a plot of (RL^2)

versus Mg concentration. The greatest change in the relocation rate occurs between concentration levels of 2 and 5 mol % MgO.

These results show that the effect that large doping levels of Mg have on reducing the laser-induced change in the refractive index in LiNbO₃ is associated with increasing the charge carrier relocation rate and not with decreasing the concentration of charge carriers contributing to the PRE. Since the same light intensity was used for obtaining the data on each of the samples, and any changes in the relocation distance L should be reflected in changes in the concentra-

TABLE I. PRE parameters for Mg²⁺-doped LiNbO₃.

| Parameter | Mg concentration (mol %) | | | |
	1.8	3.6	5.0	8.8
K_0 (s⁻¹)	0.0026	0.040	0.059	0.057
K_θ (s⁻¹)	0.24	0.99	1.50	1.75
N (10¹⁴ cm⁻³)	0.7	2.5	2.4	2.0
RL^2 (10⁻¹² cm² s⁻¹)	2.0	6.1	9.3	10.8
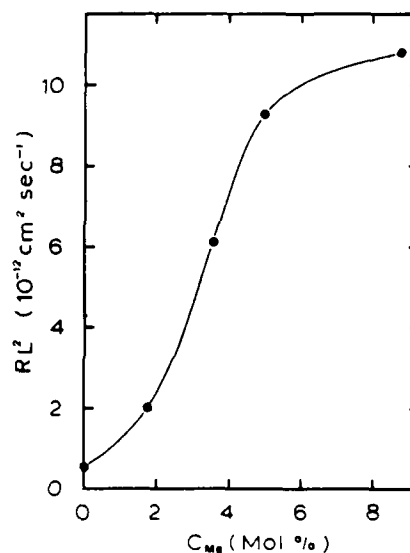
FIG. 5. Variation of the charge relocation parameter as a function of Mg concentration in LiNbO₃:Mg.

tion of defect centers contributing charges to the PRE, the observed concentration dependence of the relocation rate can be associated with changes in the diffusion coefficient of the charge carriers.

V. RESULTS OF TWO-WAVE MIXING EXPERIMENTS IN LiNbO₃:Mg CRYSTALS

Charge relocation due to diffusion forms a component of the laser-induced grating which is out of phase with the laser interference pattern. This causes energy transfer to occur between the two laser write beams as they go through the sample. Thus, monitoring this two-wave mixing effect can provide information on the transport properties of the sample. To determine the effects of Mg doping on the charge transport properties of LiNbO₃, we performed two-wave mixing experiments on our four LiNbO₃:Mg crystals and one pure crystal as a function of the grating spacing.

The samples used for these experiments were all in a well-oxidized state. The experimental setup was the same as that described previously except that no probe beam was needed. The intensities of the two write beams entering and exiting the sample were monitored as a function of the crossing angle. Since energy transfer occurs in the direction of the poled c axis, the beams exiting the crystal with $+c$ and $-c$ directional component were labeled the signal beam and the reference beam, respectively. The grating spacing was controlled by changing the crossing angle of the two beams in the crystal. In order to avoid changes in the size of the crossing region for different angles, the reference beam was expanded to about 3 mm in diameter. The reference beam entered the sample with a power density about 50 times greater than that of the signal beam. With these conditions, the effects of the decrease of the reference beam due to energy transfer can be neglected.

The magnitude of the beam coupling determined by two-wave mixing experiments is generally expressed in terms of the gain parameter Γ, which is related to the measured ratios of the signal and reference beam intensities I_S and I_R through the expression

$$\Gamma = d^{-1}\ln\left[(I_{S1}/I_{S0})(I_{R0}/I_{R1})\right], \qquad (4)$$

where the 0 and 1 subscripts refer to the entrance and exit faces of the sample, respectively. Figure 6 shows the results obtained on the 5.0 mol % Mg-doped sample. The gain resulting from beam coupling in this sample decreases approximately linearly as the grating fringe spacing increases. The samples containing 3.6 and 8.8 mol % Mg were observed to have approximately the same magnitude of gain and the same linear dependence on grating spacing as the 5.0-mol % sample. On the other hand, the 1.8-mol % Mg-doped sample had the same very weak beam coupling reported previously[3] for undoped LiNbO₃ which produced a gain of about 1 order of magnitude smaller than that seen in the 5.0-mol % sample. Under these conditions accurate measurements of Γ as a function of fringe spacing were not possible.

The theory of Kukhtarev et al.[12] with ordinary light polarization, in the small charge transport length limit, predicts a gain dependence on fringe spacing of $\Gamma \propto \Lambda^{-1}$. This limit is valid for undoped LiNbO₃. In this approximation,

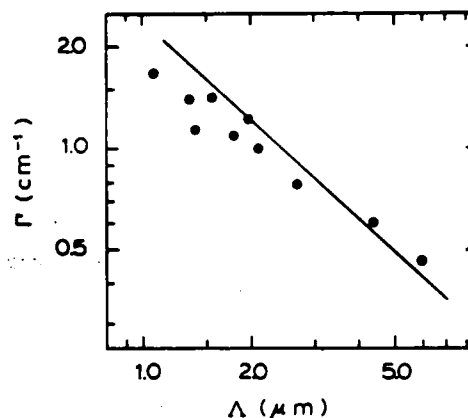FIG. 6. Two-wave mixing gain coefficient for a 5.0 mol % Mg-doped LiNbO₃ crystal as a function of grating spacing. The points represent experimental results and the line represents the prediction of the Kukhtarev theory.

the only material properties which effect the gain appear as a ratio of the photoconductivity and dark conductivity. Taking these data from Huafu, Guotong, and Zhongkang,[13] it is possible to calculate the gain as a function of fringe spacing with no adjustable parameters. This is shown as a solid line in Fig. 6. The good agreement between theory and experiment confirm that the small transport length approximation is still valid for concentrated Mg-doped LiNbO₃ crystals. The photoconductivity for 5.0 mol % Mg-doped LiNbO₃ crystals has been found to be about 6 times greater than that for undoped crystals. Thus, the gain predicted theoretically for the undoped sample is much smaller than for the heavily doped sample and the time to reach steady-state conditions for the beam intensities will be much longer for the undoped sample. This is consistent with our experimental observations.

VI. SUMMARY AND CONCLUSIONS

The results described here show the usefulness and limitations of the scattering pattern analysis technique for obtaining information about laser-induced photorefractive gratings. This technique provides a method for determining the modulation depth and thickness of the grating, and observing any interference effects due to the presence of multiple Fourier component gratings. Although values of Δn can be obtained by other techniques, they generally require assumptions concerning grating thickness and pattern shape. These results demonstrate the significant changes in scattering patterns produced by impurities which enhance the PRE and those which decrease the PRE. Unfortunately, the sensitivity of the pattern analysis technique depends on the grating modulation depth, and thus it is not useful for very small values of Δn such as those encountered in erasure experiments.

The most important results reported here involve the effects of Mg doping on the PRE in LiNbO₃. Scattering pattern analysis showed that the modulation depth of the laser-induced grating decreased significantly with increasing Mg concentration while the grating thickness did not change appreciably. Analysis of the erasure decay dynamics showed

that this change is associated with an increase in the charge carrier diffusion coefficient at high Mg concentrations while the total concentration of carriers contributing to the PRE is not changed. Theoretical interpretation of two-wave mixing results confirm this conclusion. Similar conclusions have been reached through the results of other types of experimental studies of LiNbO₃:Mg.[13–16] The reason that higher charge carrier conductivity reduces the PRE is that the magnitude of Δn depends on the magnitude of the local electric field established in the crystal by the light-induced charge relocation. This latter value depends on the ratio of the photovoltaic current due to the anisotropic potential at the site of the defects at which the charges are produced, and the reverse photocurrent driven by the space-charge field built up at the boundary of the light beam in the crystal. The final field established is much lower for materials with high conductivity. The mechanism by which high concentrations of Mg increases the photoconductivity of LiNbO₃ is not yet established. It has been shown that the presence of Mg changes the local defect environment of optical impurities in the material.[16] Since shallow traps have been shown to affect the relocation rate of charge carrier in LiNbO₃,[3] it may be possible that doping with Mg decreases the concentration of these traps and thus increases the mobility of the migrating charges.

ACKNOWLEDGMENTS

[1]P. Gunter, Phys. Rep. 93, 199 (1982).

[2]A. M. Glass, Opt. Eng. 17, 470 (1978); M. E. Lines and A. M. Glass, *Principles and Applications of Ferroelectrics and Related Materials* (Oxford University Press, Oxford, 1979).

[3]J. K. Tyminski and R. C. Powell, J. Opt. Soc. Am. B 2, 440 (1985).

[4]H. C. Chow, M. J. Kliewer, J. K. Tyminski, and R. C. Powell, J. Opt. Soc. Am. B 3, 688 (1986).

[5]Gi-Guo Zhong, Jin Jian, and Zhong-Kang Wu, in *Proceedings of the 11th International Quantum Electronics Conference*, IEEE Cat. No. 80 CH 1561-0, p. 631 (1980).

[6]R. L. Byer, Y. K. Park, R. S. Feigelson, and W. L. Kway, Appl. Phys. Lett. 30, 17 (1981); M. Digonnet, M. Fejer, and R. L. Byer, Opt. Lett. 10, 235 (1985).

[7]M. Demicheli, P. Sibillot, D. B. Ostrowsky, and M. Papuchon, Opt. Commun. 42, 101 (1982).

[8]R. G. Smith, D. B. Fraser, R. T. Denton, and T. C. Rich, J. Appl. Phys. 39, 4600 (1968).

[9]J. L. Jackel, D. H. Olsen, and A. M. Glass, J. Appl. Phys. 52, 4855 (1981).

[10]H. Kogelnik, Bell Syst. Tech. J. 48, 2909 (1969).

[11]J. Feinberg, D. Heiman, A. R. Tanguay, Jr., and R. W. Hellwarth, J. Appl. Phys. 51, 1279 (1980); 52, 537 (1980); J. Feinberg, in *Phase Conjugation*, edited by S. J. Fisher (Academic, New York, 1983), p. 218.

[12]N. V. Kukhtarev, V. B. Markov, S. G. Odulov, M. S. Soskin, and V. L. Vinetskii, Ferroelectrics 22, 949 (1979); 22, 961 (1979).

[13]Wang Huafu, Shi Guotong, and Wu Zhongkang, Phys. Status Solidi A 89, K211 (1985).

[14]D. A. Bryan, R. Gerson, and H. E. Tomaschke, Appl. Phys. Lett. 44, 847 (1984).

[15]K. L. Sweeney, L. E. Halliburton, D. A. Bryan, R. R. Rice, R. Gerson, and H. E. Tomaschke, Appl. Phys. Lett. 45, 805 (1984).

[16]D. A. Bryan, R. R. Rice, R. Gerson, H. E. Tomaschke, K. L. Sweeney, and L. E. Halliburton, Opt. Eng. 24, 138 (1985).

Anisotropic self-diffraction in Mg-doped LiNbO₃

Luis Arizmendi[a] and Richard C. Powell

Department of Physics, Oklahoma State University, Stillwater, Oklahoma 74078-0444

The characteristics of anisotropic self-diffraction were studied for undoped LiNbO₃ crystals and LiNbO₃:Mg at doping levels of a few mole percent. From the absolute magnitude and the time dependence of the signal, it was possible to determine the induced refractive-index change and the conductivity of the charges involved in the photorefractive effect for each sample. For these excitation conditions, only charge migration perpendicular to the c axis contributes to laser-induced grating, and thus the conductivity is associated with charge diffusion. The results show that the total refractive-index change causing the self-diffraction is only slightly smaller for the Mg-doped samples than for undoped LiNbO₃ while the conductivity is 1 order of magnitude greater for the Mg-doped samples.

I. INTRODUCTION

Understanding the details of laser-induced refractive-index changes in doped and undoped LiNbO₃ crystals is important because of the application of these materials in systems based on optical technology.[1] Several methods have been developed for studying the photorefractive effect. The most powerful of these are based on characterizing the properties of laser-induced holographic gratings through monitoring the erasure decay dynamics, measuring the small-angle scattering patterns, and measuring the energy transfer between the laser beams writing the grating.[2-4] In the last of these methods, the interference pattern of the light intensity of two laser beams crossing in the sample causes a spatial modulation of the refractive index through the photorefractive effect, and this causes a self-diffraction of these write beams. The most common type of self-diffraction occurs when the grating is written along the c axis. This isotropic self-diffraction (or two-wave mixing) produces changes in the energy and phase of each of the write beams. These effects can be useful for image amplification[5,6] and evaluation of crystal parameters.[7,8] In special circumstances a different type of self-diffraction may be observed which causes a change in the polarization of the write beams.[9] This is called anisotropic self-diffraction and is characterized by two crossed write beams with one polarization direction and two diffracted beams with their polarization direction rotated 90° with respect to the write beams. Anisotropic self-diffraction requires special experimental geometry to satisfy phase-matching conditions, and the strength of the effect is determined by the size of the off-diagonal elements of the electro-optic coefficient connecting the two polarization directions. In BaTiO₂ the large value of the r_{42} tensor component of the electro-optic coefficient was observed to produce anisotropic self-diffracted beams with about half the intensity of the incident write beams.[9]

We report here the observation of anisotropic self-diffraction in LiNbO₃ crystals and Mg-doped LiNbO₃. The experimental geometry needed to observe this effect involved a laser-induced grating with a direction perpendicular to the c axis of the crystal. Since the photovoltaic effect in LiNbO₃ acts in the c direction, the characteristics of anisotropic self-diffraction are independent of the photovoltaic properties of the crystal. Thus, the only process involved in writing the holographic grating in this geometry is the diffusion of charge carriers. Therefore, the results of this investigation provide information about the diffusion contribution to the photorefractive effect in LiNbO₃ generally masked by the drift contribution induced by the photovoltaic effect. This is of special interest in understanding the effects of Mg doping which is known to reduce the photorefractive effect and increase the photoconductivity in LiNbO₃.[4,10,11]

II. EXPERIMENT

The samples used for these experiments were a nominally pure crystal of LiNbO₃ obtained from Crystal Technology and four Mg-doped crystals with doping levels ranging between 1.8 and 8.8 mol % obtained from Union Carbide. All of the samples were in a well-oxidized state.

The experiments were carried out with the geometry shown in Fig. 1. Two beams from a He-Cd laser were crossed inside the sample. The laser had a total power of about 5 mW at a wavelength of 442 nm and the beam diameters were about 1 mm. The plane of incidence was perpendicular to the c axis of the sample and the beams entered with an extraordinary polarization ($E \parallel c$). The intensities of the two transmitted write beams and the two diffracted beams were each
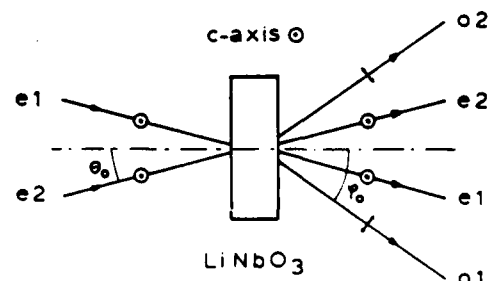

FIG. 1. Experimental geometry for anisotropic self-diffraction experiments. *e* refers to the extraordinary polarization direction and *o* to the ordinary polarization direction.

[a] Permanent address: Departamento de Optica y Estructura de la Materia, Universidad Autonoma de Madrid, 28049 Madrid, Spain.

TABLE I. Summary of experimental results.

| Parameter | Sample (dopant) | | | |
	Undoped	3.6 mol % Mg	5.0 mol % Mg	8.8 mol % Mg
θ (deg)	14.05	14.35	14.03	12.20
n_o	2.2844	2.2800	2.2847	2.3092
Δn (10^{-5})	8.29	2.28	5.65	1.04
E_{sc} (V/m)	39.6	40.9	27.0	4.9
N_A (cm^{-3})	1.29×10^{12}	3.62×10^{11}	8.78×10^{11}	1.40×10^{11}
τ (s)	20.85×10^2	1.53×10^2	1.62×10^2	1.81×10^2
l_D (μm)	61	1.15×10^2	74	1.85×10^2
σ $(\Omega^{-1} cm^{-1})$	5.78×10^{-19}	2.94×10^{-18}	7.07×10^{-18}	1.32×10^{-18}
σ/I $(\Omega^{-1} W^{-1} cm)$	4.62×10^{-18}	2.83×10^{-17}	5.99×10^{-17}	1.20×10^{-17}

measured using a calibrated silicon photodiode. All of the light intensities used in the calculations described below were those inside the crystal. Reflections at the surfaces were taken into account using the measured refractive indices and the usual formulas for reflection.

In order to generate the anisotropic self-diffracted beams, it is necessary to adjust the crossing angle of the write beams to fulfill the phase-matching condition given by[9]

$$\sin \theta = [(n_o^2 - n_e^2)/8]^{1/2}, \qquad (1)$$

where θ is the half-angle of the write beams intersecting outside the crystal and n_o and n_e are the ordinary and extraordinary refractive indices, respectively. To obtain a rough estimate of what θ should be, we extrapolated the data reported[12] on the refractive indices of LiNbO$_3$ to a wavelength of 442 nm. This gave $n_o = 2.3853$ and $n_e = 2.2869$. Substituting into Eq. (1) predicts $\theta = 13.85°$. Since the exact values of the refractive indices are known to depend strongly on the [Li]/[Nb] ratio of the specific crystal[12] and may also be sensitive to high concentrations of Mg, it was necessary to experimentally adjust θ near this predicted value in order to obtain the maximum diffraction efficiency for each sample. The anisotropic self-diffracted beams appear at an angle ϕ given by[9] $\sin \phi = 3 \sin \theta$. The appearance of the diffracted beams is extremely critical with respect to the crossing angle.

III. RESULTS AND DISCUSSION

The crossing angles required to obtain anisotropic self-diffraction are listed in Table I for each of the samples. The sample with 1.8 mol % Mg had such a low diffraction efficiency that it was impossible to determine accurately the phase-matching angle. This is consistent with the results of other types of photorefractive measurements on this sample which indicate that the concentration of active traps is lower than that present in the other samples.[4] Since the ordinary refractive index is not very sensitive to the stoichiometry of the crystal,[12] we used the value of n_o given above and the measured phase-matching angles in Eq. (1) to calculate values of n_e for each sample. These are also listed in Table I. There appears to be no direct correlation between n_e and the Mg concentration in the samples. The undoped, 3.6-mol % Mg-doped, and 5.0-mol % Mg-doped samples all have values of n_e consistent with crystals grown under congruent melting conditions. The most heavily Mg-doped sample has a higher value of n_e consistent with a richer Li concentration than the congruent [Li]/[Nb] composition.[13]

According to the theory of Kukhtarev et al.[9] the intensity of the anisotropic self-diffracted beams is related to the laser-induced change in the refractive index Δn by the expression

$$I_{o1}/I_{e1}(0) = (n_o/n_e)\{1 + [|\Delta n|kf(I)d]^{-1/2}\}^{-1}, \qquad (2)$$

where $k = \omega/c$, d is the grating thickness, and $f(I) = [I_{e1}(0)I_{e2}(0)]^{1/2}/[I_{e1}(0) + I_{e2}(0)]$ with the meaning of the different beam intensities shown in Fig. 1. We monitored the time dependence of the buildup of the anisotropic self-diffracted beam intensities after the write beams were turned on for each sample. By substituting the results into Eq. (2) the time dependence of the induced change in the refractive index was obtained. Examples of the results are shown in Fig. 2 for the undoped and 5.0-mol % Mg-doped samples. For both samples, the change in refractive
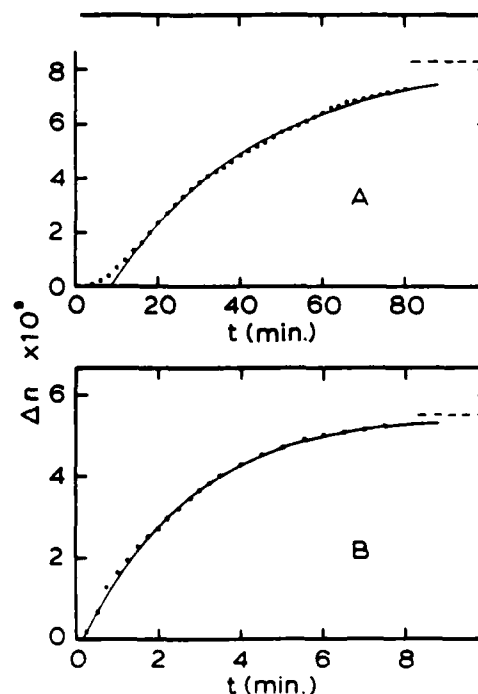

FIG. 2. Time evolution of the induced refractive-index change in (A) undoped LiNbO$_3$ and (B) LiNbO$_3$:Mg (5.0 mol %) for anisotropic self-diffraction.

index tends toward constant values at long times with the growth in Δn being about 10 times faster for the doped sample. The other doped samples exhibit a similar time dependence as the 5.0-mol % sample but the maximum changes in Δn are different for each sample.

The theory of Kukhtarev et al.[9] predicts a time dependence of the form

$$\Delta n = \Delta n_{max} [1 - \exp(-t/\tau)] . \qquad (3)$$

The characteristic time constant is given by

$$\tau = (\epsilon_0\epsilon_{11}/\sigma)(L^2 + l_d^2)/(L^2 + l_D^2), \qquad (4)$$

where σ is the total conductivity, ϵ_{11} is a component of the static dielectric constant, L is the grating wavelength, l_d is the diffusion length, and l_D is the Debye screening length. The latter two quantities are given by

$$l_d = 2\pi\sqrt{D/(\gamma_R N_A)} \qquad (5)$$

and

$$l_D = [(4\pi^2\epsilon_0\epsilon_{11}k_B T)/(N_A e^2)]^{1/2}. \qquad (6)$$

Here γ_R is the trapping rate per unit volume, N_A is the density of charge traps, and ϵ_{11} has been reported[14] to be 85.2. The solid lines in Fig. 2 represent the best fits of Eq. (3) to the data treating τ as an adjustable parameter. The values obtained for τ and Δn_{max} for each sample are listed in Table I.

The values obtained for Δn_{max} in these experiments are very low compared with those obtained for laser-induced gratings oriented along the c direction.[1] This is due to the fact that the major contribution to the photorefractive process along the c axis in LiNbO$_3$ is the photovoltaic effect and this does not affect the results in our experimental geometry. The space-charge electric field producing the change in the index of refraction for our experimental geometry can be calculated from[9]

$$\Delta n = - [(r_{51}n_o^2 n_e)/(2\cos\theta_i)]E_{sc}, \qquad (7)$$

where θ_i is the crossing angle of the write beams inside the crystal and r_{51} is the electro-optic tensor component appropriate for this experimental geometry. Using[15] $r_{51} = 32\times10^{-12}$ m/V along with the measured values of Δn_{max}, θ_i, and n_e, Eq. (7) gives the values of E_{sc} listed in Table I.

The saturation space-charge electric field can be expressed in terms of the Debye screening length[9] using the equation

$$E_{sc} = [(2\pi k_B T)/(eL)]/(1 + l_D^2/L^2). \qquad (8)$$

The numerator in Eq. (8) is the diffusion field. Using the values of E_{sc} determined previously, Eq. (8) was used to calculate values for the Debye screening lengths, and these were then substituted into Eq. (6) to find the concentration of traps available for the excited charges. The resulting values for N_A are listed in Table I for each sample. The concentrations of traps found for this set of samples are very small and appear to have no direct correlation with the concentration of Mg doping. These values of N_A are about 3 orders of magnitude smaller than the average density of photocarriers measured in the same samples by erasure decay experiments.[4]

The diffusion length generally satisfies the condition $l_d \ll L \approx 1 \mu m$ for most photorefractive materials including LiNbO$_3$.[1,16] Thus in the expression for the time constant given in Eq. (4), l_d can be neglected and the values obtained above for l_D can be used along with the measured values of τ to obtain values for the conductivity. The values obtained for σ are listed in Table I for each sample.

The conductivity determined by this procedure is the sum of the dark conductivity and the photoconductivity. The values of σ listed in Table I for the Mg-doped samples are about 10 times higher than that obtained for the undoped sample. There is no direct correlation of conductivity with the level of Mg doping. This may be due to other differences in the samples which also affect the conductivity such as the concentration of other chemical impurities. The magnitude we obtained for the total conductivity with this technique is consistent with the values of dark conductivity of the order of $10^{-19} \Omega^{-1}$ cm^{-1} determined from the decay times of recorded holograms in the dark.[17] Direct measurements of dark conductivity have produced much greater values,[11] of the order of $10^{-15} \Omega^{-1}$ cm^{-1}. The cause of this discrepancy between the values of dark conductivity found by direct measurements and those inferred by the characteristics of photorefractive properties is not understood. The magnitude of the conductivity is dependent on the impurity content and on the oxidation-reduction state of the sample.[18] In addition, directly measured conductivity has contributions from surfaces and internal macroscopic defects which do not play a role in the bulk conductivity involved in the photorefractive effect. Thus, it is not surprising that the two types of measurements produce quite different results.

The results reported here show that anisotropic self-diffraction is a useful technique for determining the nonphotovoltaic contribution to the photorefractive effect in photovoltaic crystals. In addition, the sensitivity diffraction efficiency to the phase-matching condition provides a good technique for determining the crystal composition. The addition of Mg at concentration levels of a few mole percent was found to increase the conductivity by an order of magnitude, which confirms previous results obtained from different types of measurements.

ACKNOWLEDGMENTS

[1]P. Gunter, Phys. Rep. 93, 199 (1982).

[2]J. K. Tyminski and R. C. Powell, J. Opt. Soc. Am. B 2, 440 (1985).

[3]H. C. Chow, M. J. Kliewer, J. K. Tyminski, and R. C. Powell, J. Opt. Soc. Am. B 3, 688 (1986).

[4]L. Arizmendi, M. J. Kliewer, and R. C. Powell, to be published in J. Appl. Phys.

[5]N. Kukhtarev, V. Markov, S. Odulov, M. Soskin, and V. Vinetskii, Ferroelectrics 22, 961 (1979).

[6]F. Laeri, T. Tschudi, and J. Albers, Opt. Commun. 47, 387 (1983).

[7]R. Orlowski and E. Kratzig, Solid State Commun. 23, 338 (1977).

[8]P. Gunter and A. Kurmins, Appl. Phys. 23, 199 (1980).

[9]N. V. Kukhtarev, E. Kratzig, H. C. Kulich, R. A. Rupp, and J. Albers, Appl. Phys. B 35, 17 (1984).

[10]R. L. Byer, Y. K. Park, R. S. Feigelson, and W. L. Kuay, Appl. Phys. Lett. **38**, 17 (1981); M. Digonnet, M. Fejer, and R. L. Byer, Opt. Lett. **10**, 235 (1985).

[11]W. Huafu, S. Guotang, and W. Zhangkang, Phys. Status Solidi (A) **89**, K211 (1985).

[12]D. F. Nelson and R. M. Mikulgak, J. Appl. Phys. **45**, 3688 (1974).

[13]J. G. Bergman, A. Ashkin, A. A. Ballman, J. M. Dziedzic, H. J. Levinstein, and R. G. Smith, Appl. Phys. Lett. **12**, 92 (1968).

stein, and R. G. Smith, Appl. Phys. Lett. **12**, 92 (1968).

[14]R. T. Smith and F. S. Welsh, J. Appl. Phys. **42**, 2219 (1971).

[15]E. Bernal, G. D. Chen, and T. O. Lee, Phys. Lett. **21**, 259 (1966).

[16]L. Young, M. G. Moharam, F. El Guibaly, and E. Lun, J. Appl. Phys. **50**, 4201 (1979).

[17]R. Orlowski, E. Kratzig, and H. Kurz, Opt. Commun. **20**, 171 (1977).

[18]E. Kratzig, Ferroelectrics **21**, 635 (1978).

Temperature dependence of the dynamic response of the photorefractive signal in $Bi_{12}SiO_{20}$

Luis Arizmendi[a] and Richard C. Powell

Department of Physics, Oklahoma State University, Stillwater, Oklahoma 74078

The dynamic response of the photorefractive signal in $Bi_{12}SiO_{20}$ with no external electric field was studied as a function of temperature. At low temperatures, the response follows the predicted exponential behavior. At temperatures higher than 220 °C with the writing beams on, the signal increases to a peak intensity and decays with time, with a time constant that varies with temperature. When the write beams are turned off and no erasure beam is present, the signal exhibits a sharp decrease and then increases to a secondary maximum before the final decay occurs. When an erasure beam is present, the same general signal pattern is observed but the secondary peak can be significantly greater at high temperatures. The theory of Kukhtarev satisfactorily describes the signal patterns observed at low temperatures. The more complex signal patterns observed at high temperatures are explained by postulating the presence of mobile positive charges which compensate the electric fields established by the negative charges participating in the photorefractive response of the material.

I. INTRODUCTION

There has been a significant amount of interest in characterizing the photorefractive effect (PRE) in sillenite-type crystals such as $Bi_{12}SiO_{20}$ (BSO) and $Bi_{12}GeO_{20}$ (BGO). Some of the recent work describes various aspects of the dynamic response of these crystals during the buildup and erasure of photorefractive gratings under different experimental conditions.[1-11] Important material parameters relevant to the PRE have been obtained[1] through studies of the erasure time constant as a function of the grating period. The dependence of the PRE erasure decay time constant on an applied electric field has been measured[2] and the effect of reversing the electric field on the dynamic photorefractive response has been described.[3] A fast photorefractive process associated with the presence of shallow traps has been reported in BSO (Ref. 4) and a fixing behavior of the holograms associated with the presence of space-charge compensation by positive charges has been found.[5] The dynamic response of the PRE in BSO with an applied electric field at room temperature has been analyzed using the theory of Kukhtarev[12,13] and the results indicate the presence of a complex rate parameter.[7] Preliminary results have been reported on the temperature dependence of the dynamic PRE in BSO at 633 nm.[8]

Although the dependence of the photorefractive response of BSO on an applied electric field has been well characterized, little work has been done in determining the variation of the photorefractive response with temperature. We report here the results of investigating the dynamics of the PRE in BSO using 514.5-nm light. The signal response shape, erasure decay rate, and dark decay rate were recorded as a function of temperature with no applied electric field. At low temperatures the theory of Kukhtarev provides a satisfactory interpretation for the results, but an anomalous time response is observed above 220 °C. The latter is explained by

postulating the presence of mobile positive charges which partially compensate the photorefractive grating field.

II. EXPERIMENT

A block diagram of the experimental setup used for this work is shown in Fig. 1. The sample was an oriented crystal of BSO obtained from Crystal Technology. The sample thickness was about 3.9 mm parallel to the ⟨110⟩ crystallographic direction.

An argon laser at 514.5 nm was used to produce laser-induced refractive index gratings (primary holograms) in the sample. The laser output was split into two beams which were expanded and crossed inside the sample. This produced uniform illumination of the entire sample and the interference pattern of the intensity formed a sine wave. The crossing angle of the beams outside the sample was 12° and the grating wave vector was oriented in a ⟨110⟩ direction. This is referred to as the perpendicular sample orientation ($K_g \perp \langle 001 \rangle$) which gives the optimum diffraction efficiency.[14,15]
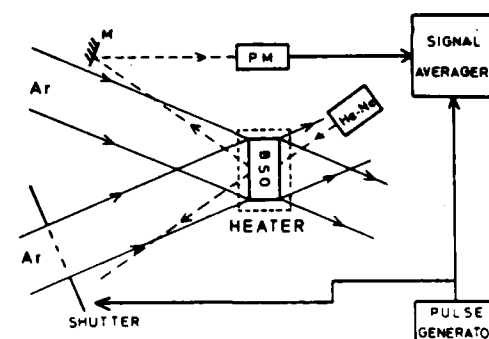

FIG. 1. Block diagram of experimental apparatus. Ar refers to the argon laser beams; He-Ne refers to the helium-neon laser; and PMT is the photomultiplier tube. The results are sent from a signal averager to a stripchart recorder.

[a] Permanent address: Departamento de Optica y Estructura de la Materia, Universidad Autonoma de Madrid, 28049 Madrid, Spain.

The intensities of the two write beams were 14.1 mW/cm^2 and 4.4 mW/cm^2. This resulted in a contrast ratio for the interference pattern of

$$m = [I_1 I_2 / (I_1 + I_2)] = 0.43.$$

An electromechanical shutter was used to shut off the write beams and allow the writing-decay cycle to be repeated several times. For erasure decay measurements, only the more intense write beam was cut off while the other beam was left on to erase the grating. Due to the low diffraction efficiency, no effects of coupling are expected to affect the erasure dynamics.[1] For dark decay measurements, the shutter was placed to cut off both write beams.

The probe beam was provided by a He-Ne laser incident on the opposite face of the sample at the Bragg angle to the grating formed by the write beams. Part of the probe beam was diffracted by the grating and detected as the signal beam by an RCA C31034 photomultiplier tube. By using a red probe beam (633.0 nm) with a low intensity (<3 mW/cm^2), the grating was left undisturbed by the reading process.[7,8,15] The signal was averaged over 100 cycles by an EG&G/PAR signal averager and recorded on a stripchart recorder.

The sample was mounted in a holder with a cartridge heater and a chromel-alumel thermocouple allowing the temperature to be controlled up to 350 °C. No electric field was applied to the sample so that charge transport occurs only through thermal diffusion of the carriers and internal field effects.

III. RESULTS AND DISCUSSION

The time evolution of the photorefractive signal efficiency was recorded during the writing and decay cycles between room temperature and 350 °C. Both dark and erasure decays were recorded. At temperatures up to about 220 °C the buildup and decay patterns were exponential except for a slight deviation near steady-state conditions associated with beam depletion within the sample.

The band transport model of the PRE[6,12,13] predicts an exponential increase in the change in the refractive index during writing with the form $\Delta n \propto [1 - \exp(-\Gamma t)]$ and a decrease during the decay with the form $\Delta n \propto \exp(-\Gamma t)$. The diffraction efficiency of a phase grating is $\eta \propto \sin^2[(\pi d / 2\lambda)\Delta n]$, where λ is the wavelength of write beams in the crystal and d is the thickness of the grating. For BSO crystals the argument of the sine is small so the function can be expanded to give $\eta \propto (\Delta n)^2$. Thus, the time evolution patterns of the PRE signal are described by

$$\eta \propto [1 - \exp(-\Gamma t)]^2 \qquad (1)$$

during writing and

$$\eta \propto [\exp(-\Gamma t)]^2 \qquad (2)$$

during decay. The rate constant Γ in a nonferroelectric crystal depends on the diffusion length of the carriers and their drift length in an electric field, the Debye screening length connected with the number of traps, the dark and photoconductivities, and the light intensities used to write or erase the grating.[6,13]

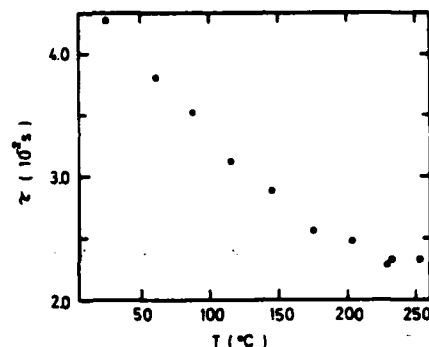The values of Γ were obtained by fitting Eqs. (1) and

FIG. 2. Time constant for the decay of holographic gratings in BSO as a function of temperature.

(2) to the experimentally observed signal patterns. Figure 2 shows the temperature dependence of $\tau = \Gamma^{-1}$ obtained from the decay part of the PRE cycle. The magnitude of τ decreases by about a factor of 2 between room temperature and 250 °C. The values of Γ^{-1} obtained from the writing part of the PRE cycle at temperature of 180 °C or less are the same as those shown in Fig. 2, after correcting for the difference in light intensity between writing and erasure. At higher temperatures, anomalous writing patterns were observed as discussed below.

The PRE decay constant can be expressed explicitly in terms of material and experimental parameters as[6,12,13,16]

$$\tau = [e\mu/(\sigma_T \gamma_R)] \frac{[(\gamma_R N_A/\mu) + (K_g^2 K_B T/e)]}{[(4\pi e N_A/\epsilon) + (K_g^2 K_B T/e)]}, \qquad (3)$$

where the external applied field has been set equal to zero. The total conductivity is the sum of the dark and photoconductivities, $\sigma_T = \sigma_d + \sigma_p$, μ is the mobility, γ_R is the recombination rate coefficient, N_A is the number of acceptors, and K_g is the magnitude of the grating wave vector.

If the room-temperature values for the parameters given in Ref. 6 are substituted into Eq. (3), it is found that the first term in the denominator is much greater than the second term. This will be true throughout the temperature range of interest to this study and thus the second term in the denominator is neglected. The two terms in the numerator are of the same order of magnitude for BSO with the experimental conditions of interest to this work. Thus, with this approximation, Eq. (3) has an explicit temperature dependence which predicts a direct linear relationship between τ and T. Since the observed temperature dependence of the time constant plotted in Fig. 2 shows an inverse relationship between τ and T, one of the parameters in Eq. (3) must have a strong enough temperature dependence to offset the explicit dependence on T. Although several of these parameters can vary with temperature, it is expected that the temperature dependence of τ is dominated by the temperature variation of σ_T.

It is well known that dark conductivity increases exponentially with temperature when occupied traps exist below an energy band. Occupied shallow traps have been reported in BSO.[17] However, the dark decay results discussed below indicate that for our experiments the contribution due to dark conductivity is very small compared to the contribution
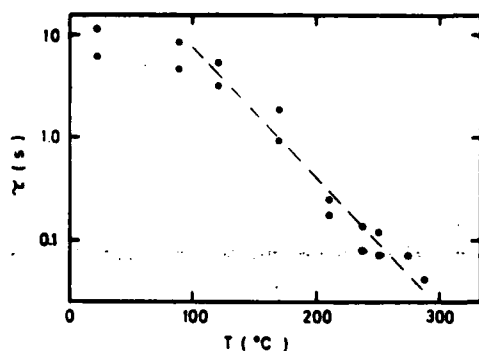
FIG. 3. Dark decay times of holographic gratings in BSO as a function of temperature. The two data points at each temperature represent the time constants for both parts of the double exponential decays.

FIG. 4. Time evolution of the signal patterns for writing and optical erasure of holographic gratings in BSO at (a) 291 °C and (b) 313 °C.

due to photoconductivity. It has been suggested[8] that the stronger dependence observed using light of 633 nm is due to changes in the photoionization cross section of the photorefractive centers. In order to understand all of the contributions to the observed temperature dependence, it is necessary to know the temperature behavior of all of the parameters such as the mobility, carrier recombination constant, and the photoconductivity at this wavelength.

To determine the importance of the dark conductivity contribution to the grating erasure, we monitored the decay of the signal when both writing beams were turned off. The analysis of the dark decay patterns showed the presence of two exponentials. Figure 3 shows the time constants associated with these two exponentials as a function of temperature. Both of the time constants appear to have the same temperature dependence.

The dark decay time constants shown in Fig. 3 decrease more than two orders of magnitude between room temperature and 285 °C. Previous results of this type were reported using red illumination of about 30 times greater power density than that used here.[8] Using the results of Ref. 8 to determine Γ^{-1} as defined by Eqs. (1) and (2) gives values about an order of magnitude smaller than the values we found for the time constant in the temperature range between room temperature and 100 °C. This difference between the two sets of results decreases at higher temperatures and is only a factor of 2 at 250 °C. The reason for the discrepancy in these results is probably associated with the high level of the power density used for the probe beam in Ref. 8 since this will contribute to the erasure of the grating.

At temperatures above about 220 °C the time evolution of the diffraction efficiency for both writing and erasure processes can not be fit by simple exponential functions. Figure 4 shows the time response pattern for the photorefractive signal during a cycle of writing and erasing the grating at two temperatures. A maximum in the signal is reached after a short time in the writing cycle and a slower decay ensues. During the erase cycle one of the write beams is turned off and the other serves as the erase beam. The signal exhibits an initial fast decay and then increases to a broad maximum before slowly decreasing to zero. This general description of the time evolution of the signal during write and erase cycles
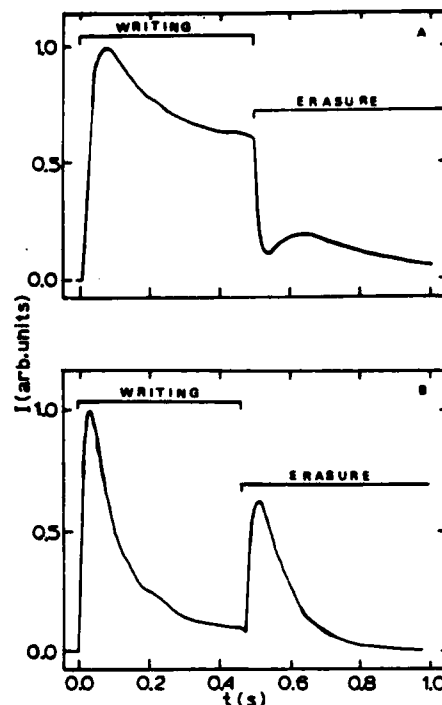
is the same at higher temperatures but the time constants for buildup and decay become faster and the secondary peak becomes more intense as shown in Fig. 4(b).

Patterns of the time evolution of the photorefractive signal similar to those shown in Fig. 4(a) have been observed for BSO under the different experimental conditions of an external electric field of about 2 kV/cm applied to the sample at room temperature.[7] These results were explained using Kukhtarev's theory.[12,13] The effect of an applied electric field causes the photorefractive hologram to be phase shifted with respect to the interference pattern of the writing beams due to diffusion of the charge cariers. In the absence of the field, the carriers move by drift alone and the hologram remains unshifted. This is accounted for by allowing the rate parameter Γ to become complex and the imaginary part gives an oscillatory component to the signal which provided a good fit to the data in Ref. 7. Based on this analysis, it is tempting to fit the data in Fig. 4 using Kukhtarev's theory and a complex rate constant with the imaginary part associated with the buildup of an internal field in the sample. Although the mathematical expression can be made to fit the data, it is difficult to understand the formation of a unidirectional electric field in a paraelectric cubic crystal such as BSO.

Figure 5 shows a writing and decay cycle for dark decay in which no erasure beam is present after the writing period. The weak red probe beam is less than 3 mW/cm^2 and does not affect the grating decay kinetics. The writing part of the cycle is the same as that shown in Fig. 4(b) for the same temperature. However, the secondary peak in the dark part
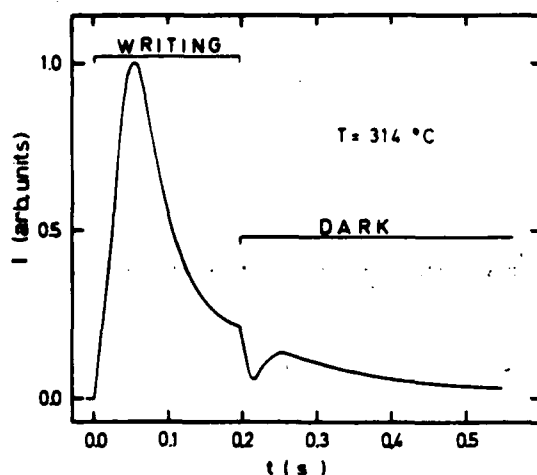
FIG. 5. Time evolution of the signal patterns for writing and dark decay of holographic gratings in BSO at 314 °C.

of the cycle is much less intense and has a slower rise and longer decay when no erase beam is present.

A process of fixing holograms in BSO crystals at room temperature has been described recently.[5] After writing a grating, the sample is kept in the dark for several minutes until the photorefractive efficiency decays to zero. Then the crystal is illuminated homogeneously causing the diffracted beam to appear once again. The signal quickly reaches about one half of its original value and then decays back to zero in a few minutes. This behavior is explained on the basis of the presence of mobile positive charges in BSO at room temperature. The decay during the dark part of the cycle is associated with the movement of the positive charges by drift to compensate the electric field produced by the negative charges during the writing of the grating. Since the signal decreases to zero, there must be enough positive charges to completely compensate the negative charges so the internal field and thus the refractive index change goes to zero. The characteristic time of this process depends on the mobility and density of positive charges. This process leads to inhomogeneous distributions of both positive and negative charges. The next step involves erasing the negative charge grating with light that photoionizes only the trapped negative charges and leaves a positive charge phase grating. The final process is the thermal erasure of the positive charge grating. This is slower than the initial compensation process because there is no field to provide a drift contribution to the mobility.

The signal patterns we observed at high temperature can be explained by a model similar to that described above. The photorefractive grating is produced through the production and trapping of negative charges. As this process reaches saturation, the slower process of positive charge compensation causes the signal to decrease. If one or both of the write beams are turned off while a diffracted signal is still visible, the initial decrease in the signal is associated with the combined effects of erasure (either optical or thermal) of the negative charge grating and positive charge compensation. The secondary maximum in the time evolution patterns is caused by diffraction from the positive charge grating which

continues to form as the negative charge grating decays. The final decay in the pattern is associated with thermal erasure of the positive charge grating.

The results show that the positive charge compensation process is thermally activated. It is not active at room temperature while at temperatures above about 220 °C the speed of the compensation process clearly increases with temperature. The dark decay results in Fig. 5 show a smaller positive charge phase grating peak than the optical erasure results shown in Fig. 4 because the thermal erasure of the negative charge grating is slower thus giving the positive charge distribution time to become more uniform through diffusion.

IV. CONCLUSIONS

The time evolution patterns of writing and erasing photorefractive holographic gratings in BSO show normal responses between room temperature and 220 °C with both the thermal and optical erasure decay time constants decreasing with increasing temperature. At higher temperatures anomalous photorefractive response patterns are observed which can be explained through the compensation effects of mobile positive charges. This compensation process is shown to be thermally activated.

The properties of BSO crystals reported here suggest the possibility of application to photorefractive devices. Holograms can be written at moderately high temperatures where the crystal has a faster photorefractive response. Through rapid cooling to moderately low temperatures, the hologram can be developed with homogeneous light. Since the positive charges are not mobile at low temperatures, the hologram can be stored for long periods of time.

ACKNOWLEDGMENTS

[1] R. A. Mullen and R. W. Hellwarth, J. Appl. Phys. 58, 40 (1985).
[2] S. I. Stepanov, V. V. Kulikov, and M. P. Petrov, Opt. Commun. 44, 19 (1982).
[3] M. G. Miteva, IEEE J. Quantum Electron. QE-22, 1365 (1986).
[4] G. Lesaux, G. Roosen, and A. Brun, Opt. Commun. 56, 374 (1986).
[5] J. P. Herriau and J. P. Huignard, Appl. Phys. Lett. 49, 1140 (1986).
[6] G. C. Valley and M. B. Klein, Opt. Eng. 22, 704 (1983).
[7] J. M. Jonathan, R. W. Hellwarth, and G. Roosen, IEEE J. Quantum Electron. QE-22, 1936 (1986).
[8] M. A. Powell and C. R. Petts, Opt. Lett. 11, 36 (1986).
[9] V. N. Astranov, A. V. Il'inskii, and M. B. Mel'nikov, Fiz. Tverd. Tella 28, 926 (1986) [Sov. Phys. Solid State 28, 519 (1986)].
[10] G. Pouliat, J. M. Cohen-Jonathan, M. Allain, J. C. Launay, and G. Roosen, Opt. Commun. 59, 266 (1986).
[11] J. P. Huignard, H. Rajbenbach, Ph. Refregier, and L. Solymar, Opt. Eng. 24, 586 (1985).
[12] N. V. Kukhtarev, V. Markov, S. Odulov, M. Soskin, and V. Vinetskii, Ferroelectrics 22, 949 (1977); 22, 961 (1977).
[13] N. V. Kukhtarev, Pis'ma Zh. Tekh. Fiz. 2, 1114 (1976) [Sov. Tech. Phys. Lett. 2, 438 (1976)].
[14] A. Marrakchi, R. V. Johnson, and A. R. Tanguay, Jr., J. Opt. Soc. Am. B 3, 321 (1986).
[15] P. Gunter, Phys. Rep. 93, 199 (1982).
[16] N. V. Kukhtarev, E. Kratzig, H. C. Kulich, R. A. Rupp, and J. Albers, Appl. Phys. B 35, 17 (1984).
[17] S. L. Hou, R. B. Lauer, and R. E. Aldrich, J. Appl. Phys. 44, 2652 (1973).

V.   EFFECTS OF DISORDER AND NONLINEAR OPTICAL PROPERTIES OF RARE EARTH DOPED GLASSES

The three manuscripts in this section focus on the properties of rare earth doped glasses. The first involves a study of the interaction of the vibrational modes of the host glass with the electrons on the Eu^{3+} ion. The results are explained by treating the vibrational modes of the glass host as fractons. This provides new insight in understanding lattice vibrations in a disordered solid. This type of information is important since these glasses are used for active optical applications such as laser hosts.

The final two manuscripts describe a new method for producing laser-induced holographic gratings in glasses. This type of laser-induced refractive index change forms the basis of devices for optical technology applications such as demultiplexers, filters, beam deflectors, and optical limiters. Other attempts to make these devices in standard glasses have generally not been successful. This is an important result since glass will be the best choice of material for future optical systems involving signal processing. The method developed in this research involves generating a significant number of local vibrational modes by radiationless relaxation of the resonantly pumped rare earth ion. These local vibrational modes provide enough energy to cause a structural change in the glass host surrounding the rare earth ion and this changes the refractive index. The gratings are stable at room temperature and can be erased both thermally and optically.

COMPARISON OF THE SPECTRAL AND TEMPERATURE DEPENDENCES OF THE HOMOGENEOUS LINEWIDTHS IN Eu^{3+}-DOPED FLUORIDE AND OXIDE GLASSES

Frederic DURVILLE *, George S. DIXON and Richard C. POWELL

Department of Physics, Oklahoma State University, Stillwater, Oklahoma 74078-0444, U.S.A.

Laser-induced fluorescence line narrowing was used to measure the homogeneous linewidth of the $^5D_0-^7F_0$ transition of Eu^{3+} in a lithium silicate oxide glass and ZBLA fluoride glass. The linewidths were determined as a function of temperature and spectral position within the inhomogeneous line profile. In general, the homogeneous linewidth increases as T^2 in the temperature range between 10 and 160 K for both types of glass with the magnitude of the linewidth in the fluoride glass being approximately an order of magnitude smaller than in the oxide glass. The recently developed model of line broadening by Raman scattering of fractons is used to interpret the data. In addition, the variation in homogeneous linewidth with spectral position is observed to have an inflection in the region of structure in the profile of the inhomogeneous band.

1. Introduction

The homogeneous linewidths of fluorescence transitions of ions in glasses have been reported by several authors to have an approximately quadratic temperature dependence over a wide range of temperatures [1], which is quite different from the properties of ions in crystals. In addition, other physical properties involving atomic vibrations such as thermal conductivity, heat capacity, and ultrasonic attenuation behave quite differently at low temperatures in glasses compared to crystals [2]. These differences have been attributed to additional degrees of freedom in glasses, described by a phenomenological model consisting of two possible local structural configurations, usually referred to as two-level systems (TLS) [3]. Recently Orbach and coworkers [4] have developed a new model based on the fractal concept to describe the anomalous vibrational properties of glasses. In a previous paper [5], we reported the results of a study of the temperature dependence of the homogeneous linewidth of the $^5D_0-^7F_0$ transition of several Eu^{3+}-doped oxide glasses. A

* Permanent address: UA 442 CNRS Université Lyon I, Villeurbanne, France.

theoretical model based on line broadening due to the Raman scattering of fractons was developed using the vibrational density of states suggested by Orbach and coworkers [4] and this model was shown to be consistent with experimental results.

In this paper, we report the results of similar studies performed on Eu^{3+}-doped fluoride glass which is known to have much weaker chemical bonds and a different type of structure than the oxide glasses. The results are compared to those obtained on the oxide glasses and are shown to be consistent with the model of broadening by Raman scattering of fractons. In addition, anomalies are observed in the homogeneous linewidth at positions of spectral structure within the inhomogeneous band profile for both the fluoride and oxide glasses. Similar linewidth studies reported previously on Eu-doped silicate glass have focused on low temperature results and utilized a TLS model for interpreting the data [6].

2. Experimental

The experimental technique of laser-induced fluorescence line narrowing (FLN) was used to measure the homogeneous linewidths. The high-

resolution laser source selectively excites only those ions in sites having transition energies in resonance with the laser frequency. This subset of excited ions produces emission spectra with much narrower widths than the total inhomogeneously broadened line profile. The experimental setup used in this study has been described previously [5]. The $^5D_0-^7F_0$ transition was resonantly excited by a nitrogen laser-pumped tunable dye laser with Rh6G dye. The emission was a pulse of 10 ns in duration with a linewidth of 0.1 cm^{-1}. The fluorescence was focused on the entrance slit of a 1 m monochromator set for a resolution of 0.008 nm. An RCA C31034 photomultiplier tube was used for detection and an EGG/PAR boxcar integrator and strip-chart recorder were used to record the signal. An electronic shutter gated to open 0.6 ms after the excitation was placed between the sample and the monochromator to eliminate the scattered laser light. The window of the boxcar integrator was set to look at the spectrum 1.0 ms after the excitation pulse. It was shown previously that energy transfer does not broaden the fluorescence on this time scale [7]. Sample temperature was controlled by a cryogenic refrigerator.

The results obtained on two glasses are reported here. The first is a lithium silicate (LS) glass with the following composition (in mole percent): 57.0 SiO_2, 27.5 Li_2O, 10.0 CaO, 2.5 Al_2O_3, 3.0 Eu_2O_3. The second is a fluoride (ZBLA) glass with the following composition: 57.0 ZrF_4, 34.0 BaF_2, 4.0 AlF_3, 3.0 LaF_3, 2.0 EuF_3.

The linewidth of a fluorescence transition after resonant excitation $\Delta\bar{\nu}$ is given by [8]

$$2\,\Delta\bar{\nu} = \Delta\bar{\nu}_{obs} - \Delta\bar{\nu}_{res}, \tag{1}$$

where $\Delta\bar{\nu}_{obs}$ is the observed linewidth and $\Delta\bar{\nu}_{res}$ is the instrumental resolution determined by the laser pulse width and the monochromator resolution. For this work $\Delta\bar{\nu}_{res} \approx 0.1$ cm^{-1}. In general, the laser linewidth is not narrow enough to excite ions in only one set of sites and thus some residual inhomogeneous broadening is usually present. This can be approximately accounted for through simple subtraction

$$\Delta\bar{\nu} = \Delta\bar{\nu}_h + \Delta\bar{\nu}_{ri}. \tag{2}$$

where $\Delta\bar{\nu}_h$ and $\Delta\bar{\nu}_n$ are the homogeneous and residual inhomogeneous contribution to the line-

width, respectively. The latter can generally be determined from the limiting value of the data at very low temperatures.

Figures 1 and 2 show the variations in the transition linewidths as a function of position within the inhomogeneous band profile at different temperature. Although there is a general increase in $\Delta\bar{\nu}$ with increasing energy, the variation is not monotonic and distinct changes occur in the linewidth at low temperature at positions where structure occurs in the inhomogeneous band profile. Previous studies of Eu^{3+}-doped phosphotungstate glass have reported a discontinuity in the residual inhomogeneous linewidth of the $^5D_0-^7F_1$ fluorescence transition after selective $^7F_0-^5D_0$ excitation [9,10]. This was also related to a shoulder in the excitation band and has been interpreted as evidence for different local site environments. These spectral features have been observed for several different oxide glasses [6,11] suggesting nonuniform variations in the number densities or transition probabilities of ions in the different types of sites. Figure 3 shows the temperature dependences of the homogeneous linewidths for
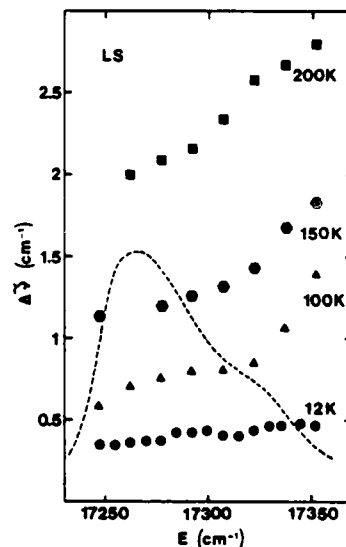

Fig. 1. Inhomogeneous spectral profile of the $^7F_0-^5D_0$ absorption transition and the variation of the FLN linewidth of the transition across the band for Eu^{3+} in LS glass.
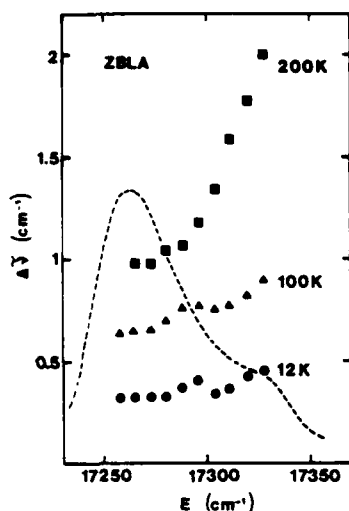
Fig. 2. Inhomogeneous spectral profile of the $^7F_0-^5D_0$ absorption transition and the variation of the FLN linewidth of the transition across the band for Eu^{3+} in ZBLA glass.
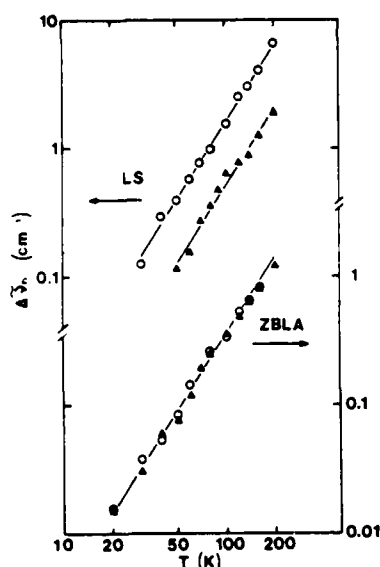

Fig. 3 Temperature dependences of the homogeneous linewidths for the $^5D_0-^7F_0$ transition of Eu^{3+} in LS and ZBLA glass hosts. (○) Low-energy spectral region: 17240 cm^{-1} for LS and 17260 cm^{-1} for ZBLA. (△) High-energy spectral region: 17315 cm^{-1} for LS and ZBLA.

the LS and ZBLA glasses. The magnitude of $\Delta\tilde{\nu}_h$ is significantly less for the fluoride glass than for the oxide glass, but a quadratic temperature dependence is observed for both samples.

3. Theoretical

There is no fundamental reason to believe that the types of electron–lattice vibration interactions that are responsible for the homogeneous linewidth of optical transitions in crystals should not also operate in glasses. One might then expect that the differences between glasses and crystals, in both the magnitude and temperature dependence of their linewidth, originate in the differences in the spectral distributions of the vibrational modes.

In crystals the Debye approximation for the phonon spectrum suffices to account for the observed linewidth. In glasses, however, the vibrational normal modes are not well represented by dispersionless plane waves. Not only is the approximate continuous translational symmetry of the Debye model lost, but also the discrete translational symmetry that makes lattice dynamics tractable in crystals is not valid. The alteration in the vibrational mode spectrum that may result from this loss of symmetry makes it not surprising that line broadening in glasses is quite different from that predicted using the Debye approximation for phonons.

An exact treatment of the vibrational states of glasses poses a formidable problem. However many, if not all, continuous random network glasses possess another approximate structural symmetry than can be exploited to obtain the most important features of the vibrational spectrum. This is dilation or scaling symmetry. Examination of ball and stick models for specific glass structures reveals the presence of loops or rings of varying size within the structure. This is also deduced from the results of Raman scattering on glasses [12]. A two-dimensional example is shown in fig. 4. These glass structural elements, and possibly others as well, possess approximate dilation symmetry over a limited range extending from a few interatomic distances to between 50 to 100 Å.
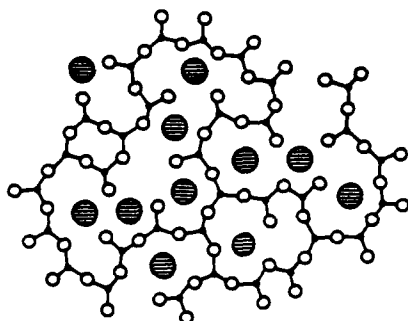
Fig. 4. Two-dimensional model structure for a random network glass such as sodium silicate. The small black dots, open circles, and large shaded circles are Si^{4+}, O^{2-} and Na^+ ions, respectively. Note the variation in the size of covalently bonded loops. (Reprinted from ref. [28] with the permission of the author and publishers.)

Fractals are structures for which dilation is an exact symmetry [13]. The vibrational spectra of fractals have been elegantly treated by Alexander and Orbach [4]. Their work was motivated by the experiments of Stapleton et al. [14] who suggested that the anomalous spin–lattice relaxation times seen for iron-containing proteins might be due to the vibrational density of states of these nearly fractal objects. In this approach the details of the underlying structure is ignored except as it contributes to the dilation symmetry, in much the same way that the details of the crystal structure are ignored in the Debye approximation. The resulting normal modes are localized, rather than propagating, and are called fractons. Their spectral properties are characterized by two parameters $\bar{d}$ and $\tilde{d}$ that characterize how the structures scale. The fractal dimensionality (or Hausdorff dimensionality) $\bar{d}$ characterizes the mass of a sphere of radius r about a representative point in the structure, $M \approx r^{\bar{d}}$. The spectral dimensionality (or mode-counting dimensionality) $\tilde{d}$ describes the number of fractons with frequency less than ω, $N(\omega) \approx \omega^{\tilde{d}}$. The fractal dimensionality is dependent on structure, and one expects $2.5 < \bar{d} < 3$ bounded by the percolation limit and the Euclidean dimension. Alexander and Orbach have conjectured that the spectral dimensionality is independent of structure with $\tilde{d} \approx 4/3$. The fracton frequencies vary with the localization length l as

$\omega \approx l^{-\bar{d}/\tilde{d}}$, the analogue of dispersion for propagating modes. As we shall see, this dispersion plays a central role in producing the linewidth observed in glasses.

A continuous random network glass is not, strictly speaking, a fractal in that it has both translation and dilation as approximate symmetries, but over different scales of length. Even though the range of lengths which exhibits dilation symmetry is restricted, it nevertheless is broad enough to encompass the characteristic length scales of the vast majority of normal modes. The first attempt to apply fractons as an approximation to the normal modes of a glass was due to Alexander et al. [15] who applied it to the specific heat of epoxy. Further refinement [16,17] of these ideas has produced what may be called "the fracton approximation" for the vibrational states of glass. The essence of this is the following. For wavelengths long enough that the disorder in the glass is outside the limit of resolution of the wave, the glass has approximate translation symmetry and the Debye approximation is a good representation of the normal modes. For wavelengths shorter than the scale of disorder, 50–100 Å, there
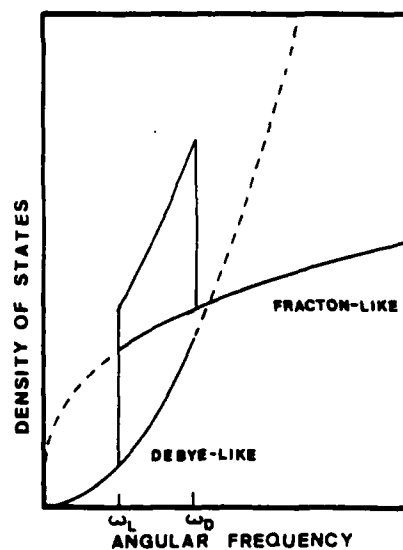

Fig. 5. Model density of states for the vibrational modes of a glass in the fracton approximation.

is approximate dilation symmetry, and fractons are a good representation. At length scales near the disorder horizon there will be a crossover between these two types of vibrational modes.

In fig. 5 a density of states corresponding to these ideas is shown. As Aharony et al. [17] have noted, the fracton density of states, extrapolated to low frequencies, is larger than the density of Debye phonons at low frequencies, while the extrapolation of the Debye phonons to high frequencies yields a density of states larger than that of the fractons. This requires that the vibrational density of states be peaked in the crossover region to obtain the correct mode counting. This feature has also been seen experimentally in neutron scattering from g-SiO$_2$ [18]. The density of states shown in fig. 5 is a simple, but not unique treatment of the crossover region. Here ω_D is the upper limit of the Debye-like modes, and ω_L is the fracton edge, the lower limit of the fracton-like modes. These cut-off frequencies are adjusted to obtain the correct mode counting [17]. The density of states of the Debye-like modes is given in this approximation by

$$g_P(\omega) = d(d/L^d)\omega^{d-1}/\omega_D^d, \qquad \omega \le \omega_D, \qquad (3)$$

where $d = 3$ is the Euclidean dimensionality of the glass. The density of states for the fracton-like modes is

$$g_F(\omega) = \bar{d}(d/L^d)(L/a)^{\bar{d}}\omega^{\bar{d}-1}/\omega_F^{\bar{d}}, \qquad \omega \ge \omega_L, \qquad (4)$$

where a is the interatomic distance and ω_F is the maximum frequency of the fracton-like modes. Note that with sufficient structural information on the glass $\bar{d}$ could be determined more precisely. However, this information is not presently available for the glasses studied here.

It has recently been found that during the time evolution of the fluorescence-line-narrowed spectra of many Eu^{3+}-doped glasses, regularly spaced minima develop in the sidebands due to phonon-assisted energy transfer [7]. These have been interpreted as arising from the transition from Debye-like to fracton-like modes [19] and thus provide a measure of ω_L. For the LS glass ω_L was found to

be 12 cm^{-1}, while the ZBLA glass was found to have an ω_L of 12.5 cm^{-1}.

The mechanisms that are normally responsible for the line broadening in crystals come from modulation of the crystal fields by the phonon strain field. The low-order processes in the strains are direct processes, Raman processes, and resonant Raman (or Orbach) processes. These are treated in the Debye approximation in a variety of places [20] and these have been generalized for vibrational spectra that are not dispersionless plane waves [5].

The contribution to the linewidth due to direct processes is given by

$$\Delta \bar{\nu}_D = (2\pi/\hbar)\sum_j |\langle e_j'|V_1|e\rangle|^2 |\langle v'|\epsilon|v\rangle|^2$$

$$\times g(\Delta_j/\hbar), \qquad (5)$$

where $\langle v'|\epsilon|v\rangle$ is a matrix element of the average local strain, V_1 is the first-order coupling parameter of the interaction Hamiltonian, and Δ_j is the splitting of the jth final electronic state from the initial one.

For Raman processes one has

$$\Delta \bar{\nu}_R = (4\pi^2/\hbar)\int_0^\infty |\langle e'|V_2|e\rangle\langle v|\epsilon^2|v\rangle$$

$$+ \sum_j |\langle e_j'|V_1|e\rangle\langle v'|\epsilon|v\rangle|^2/[\hbar\omega - \Delta_j]|^2$$

$$\times [g(\omega)]^2 \, d\omega, \qquad (6)$$

where there are now contributions from both the first- and second-order coupling parameters V_1 and V_2 in the interaction Hamiltonian. For Kramers states the first-order matrix elements $\langle e'|V_2|e\rangle$ vanish from symmetry considerations. The Orbach processes are also contained in eq. (6) when the phonons are in resonance with an electronic state.

To evaluate eqs. (5) and (6) for the fracton-like modes one needs the matrix elements of the strain. Because of dilation symmetry the wavefunctions of the fractons must be of the form $\phi(r/l)$ where l is the localization length and r is the distance from the center of the fracton. The average local strain will then be proportional to Q/l where Q is the amplitude of the vibration. This gives strain

matrix elements of the form

$$\left|\langle n-1|\epsilon|n\rangle\right|^2 \propto (\hbar/2\rho\omega)l^{-2}n \qquad (7)$$

for fracton absorption and a similar expression for fracton emission with the fracton occupation number n replaced by $n+1$. Similarly,

$$\left|\langle n|\epsilon^2|n\rangle\right|^2 \propto (\hbar/2\rho\omega)^2 l^{-4}n(n+1). \qquad (8)$$

Note that both eqs. (7) and (8) are of the same form as one finds in the Debye model of phonons except that there the wavelength appears in place of the localization length. Using the dispersion relation for fractons, $l^{-1} = L^{-1}(\omega/\omega_L)^{d/\bar{d}}$. This contrasts with the linear dependence of λ^{-1} on ω for Debye phonons.

For fracton-like modes the contribution of the direct processes to the linewidth becomes

$$\Delta\tilde{\nu}_D = A_1 \sum_j \Delta_j q_n(\Delta_j) \qquad (9)$$

for states reached by fracton absorption. If some states are accessible by fracton emission, there will be additional terms with n replaced by $n+1$. The frequency exponent $q = \bar{d}(1 + 2/\bar{d}) - 2$ giving a
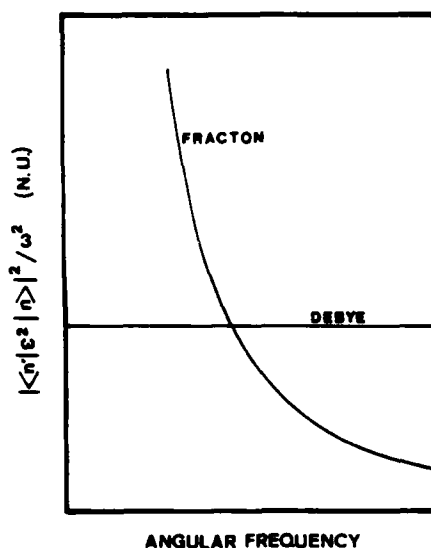
much slower increase with Δ than is found in crystals. In the high-temperature limit where $n = kT/\Delta$, $\Delta\tilde{\nu}_D$ will be a decreasing function of frequency. The temperature dependence of this contribution to the linewidth will be the same as found for crystals, but its magnitude will be smaller if all the $\Delta_j \gg \hbar\omega_L$. This reduction comes from the smaller density of states that the fracton-like modes have at high frequencies, as shown in fig. 5. In particular it accounts for the relative lack of importance of the direct processes in the linewidth of the $^5D_0-^7F_0$ transition in Eu^{3+}-doped glasses [1]. The $^7F_1$ state which in crystals controls the linewidth through either direct or Orbach processes, is approximately 200 cm^{-1} above the $^7F_0$ level, placing it far above the fracton edge which is typically 10 cm^{-1}. For states with $\Delta_j < \hbar\omega_L$ the Debye approximation will hold as in crystals.

The strain matrix elements for the fracton-like modes in the Raman processes have the frequency dependence

$$\left|\langle n|\epsilon^2|n\rangle\right|^2 \propto \left|\langle n|\epsilon|n\pm1\rangle\langle n\pm1|\epsilon|n\rangle\right|^2$$

$$\propto \omega^{-2+4(d/\bar{d})}n(n+1). \qquad (10)$$

For $kT \gg \hbar\omega$ this diverges at low frequencies as shown in fig. 6. Thus the dispersion of the fracton-like modes has the effect of coupling the electronic states much more strongly to vibrational modes near ω_L than those of higher frequency. Since, as fig. 5 shows, the density of states for the fracton-like modes is a slowing varying function of ω, only those modes with frequencies near the fracton edge contribute significantly to the linewidth. This is in contrast to Debye-like phonons, where the major contribution to the linewidth shifts to higher frequency with increasing temperature because of the rapid increase in $g(\omega)$.

When the strain matrix elements and density of states for fracton-like modes are substituted into eq. (6) one obtains with the Raman processes for non-Kramers states

$$\Delta\tilde{\nu}_R = A_2(T/\theta_D)^{p+1}\int_{\theta_L/T}^{\theta_F/T} x^p e^x(e^x-1)^{-2} dx$$

$$+\bar{\alpha}(T/\theta_L)^7\int_0^{\theta_D/T} x^6 e^x(e^x-1)^{-2} dx. \qquad (11)$$

The first integral is over the fracton-like modes and the second over the Debye-like modes. The exponent $p = 2q$, $\theta_i = \hbar\omega_i/k$, and $x = \hbar\omega/kT$. For $kT > \hbar\omega_L$, both these contributions increase as T^2. This agrees closely with the present experiments and earlier work on Eu- and Pr-doped glasses [1,5,21]. Note however, if there are neighboring electronic states accessible to radiationless transitions, there will be additional contributions from Orbach processes. These have an $e^{-\Delta/kT}$ temperature dependence.

In the Kramers case the energy denominators $1/(\hbar\omega - \Delta_j)$ in eq. (6) must be treated carefully. The sum over the other electronic states of the system includes the other Kramers-degenerate pairs and also, with $\Delta = 0$, the time-conjugate of the state being broadened. The former contributes to T_1 while the latter does not [22]. In the first instance, summing over the Kramers pair gives a factor $[\hbar\omega/(\Delta^2 - \hbar^2\omega^2)]$ in each integral in eq. (11). If $\Delta \gg \hbar\omega$ for all vibrational modes, this increases each power of x by 2. In the second instance, the power of x will be reduced by 2 in each integral. Since Δ is typically > 100 cm^{-1} and the most important vibrational modes have energies near $\hbar\omega_L$ in this term, it will dominate and a T^2 dependence again results. This agrees with the results on Nd- and Yb-doped glasses for $T > 50$ K [23,24].

The strength of the interaction can easily be estimated [5] by considering the McCumber and Sturge [25] $\bar{\alpha}$ parameter for an equivalent crystal with the same mean density and sound velocity as the glass. This is given by

$$\bar{\alpha} \approx A_2\theta_D^{10}/(\theta_L^3\theta_x^7),\tag{12}$$

where θ_x is the Debye temperature of the equivalent crystal. For the ZBLA sample the homogeneous linewidth is approximately $0.36 \times 10^{-4}T^2$ cm^{-1}, which is less than the value of about $10^{-4}T^2$ cm^{-1} found for the oxide glass hosts. The latter value gives $\alpha \approx 10^2$ cm^{-1}, about the same coupling strength seen for rare-earth transitions in oxide crystals, with the results for fluorides being proportionally smaller. Thus the same electron-phonon interactions that govern the homogeneous linewidth in crystals can also account for the linewidth in glass when the vibrational modes are treated in the fracton approximation.

This same treatment also allows one to account qualitatively for the variation of $\Delta\tilde{\nu}_H$ across the inhomogeneous profile. $\Delta\tilde{\nu}$ is the sum of the widths of the initial and final states of the optical transition which are determined at low temperature by the interaction strength parameter A_2. This contains the electron-phonon coupling matrix element which involves local crystal field parameters. In addition the position of any transition within the inhomogeneous profile depends on the difference in the energy of the initial and final states of the transition which is determined by the local crystal field parameters. Shorter Eu-ligand distances (either Eu-O or Eu-F) lead to stronger electron-network interactions producing higher $^7F_0 - {}^5D_0$ transition energies and broader homogeneous linewidths. Thus, assuming the local symmetry changes smoothly, the homogeneous linewidth should increase monotonically across the inhomogeneous transition profile. However, an abrupt change in local site symmetry can produce a discontinuity in the direct relationship between the transition energy and homogeneous linewidth. This might occur when the active ions change from being modifiers to substituting for network formers. Rare-earth ions have been identified in both positions in zirconium fluoride glasses [26]. Also, the electron-network interaction may vary differently with transition energy for the excited state and the ground state. The combination of these phenomena can account for the anomalies in the linewidth variation at high temperatures shown in figs. 1 and 2. At low temperatures the FLN linewidth is dominated by residual inhomogeneous broadening. The same arguments also apply here with only slight modification.

This interpretation is supported by the presence of a shoulder in the inhomogeneous band profile in the same spectral region where the linewidth anomaly occurs. This type of spectral structure has been observed in many different types of rare-earth-doped glasses [9-11] and is commonly attributed to changes in local site symmetry. The same considerations can explain the smaller homogeneous linewidth observed in the fluoride glass. The chemical bonds in fluoride materials are well known to be weaker with higher ionicity than

in oxide materials, leading to a smaller electron–lattice interaction strength. In addition, the mean interatomic distances are expected to be greater in the ZBLA glass compared to the LS glass due to the larger ionic radius of the Zr network former ions compared to the Si, thus, further reducing the relative interaction strength in the fluoride glass. These structural considerations have no effect on the temperature dependence of the homogeneous linewidth since this is determined only by the nature of the coupling between the lattice vibrations and the fluorescent ion.

Alexander, Entin-Wohlman, and Orbach [27] have recently calculated T_1 for fractons by considering only the largest relaxation rate at a given impurity site. Their result reduces to ours for the case that their parameter $d_{min} = 1$ and there is rapid cross-relaxation among non-Kramers ions. As we have already noted, the dominant contribution to the homogeneous linewidth for Kramers ions comes from a process that does not contribute to T_1. It seems unlikely that this cross-relaxation occurs in the glasses that we have studied since the Eu^{3+} concentration is small and energy transfer is important only on the scale of several milliseconds [7]. Their calculation is directed toward understanding T_1 in systems such as the iron-containing proteins studied by Stapleton et al. [14]. In that case the probe ions occupy a single type of site in the molecule, and the differences in crystal field over the ensemble arise from the fractal structure. In random network glasses other factors, such as the presence or absence of network modifier ions in the immediate environment of the probe, may dominate the site-to-site differences in crystal field, thus producing the same effect that would result from rapid energy transfer in the case studied by Alexander et al. [27]. It is also possible that over the time scale of our experiments the fracton population has sufficient time to rearrange itself, and thus for the ensemble of excited ions the largest relaxation rate approach would not be appropriate to the present experimental situation. There would be, in effect, a mixing of the spatial distribution of fractons that is rapid on the scale of these experiments, rather than cross-relaxation of the ions. In addition linewidth measurements usually involve signal averaging over many repetitions of the experiment further averaging over phonon populations.

4. Conclusions

The theoretical analysis of the FLN results described in this paper shows that the same types of physical mechanisms responsible for optical linewidths of ions in crystals can be used to explain the properties of optical linewidths of ions in glass hosts. The differences in line broadening properties of doped crystals and glasses is associated with the treatment of the vibrational modes. The translational symmetry of crystals is replaced by an approximate dilational symmetry in glasses leading to the fracton approximation instead of the Debye approximation for treating the vibrational modes. For the specific samples and temperature range investigated here, Raman scattering of vibrational modes are found to be responsible for the temperature variation of the homogeneous linewidths. Treating these processes in the fracton approximation predicts the observed T^2 temperature dependence. The structural differences between glass hosts is mainly reflected in the magnitude of the homogeneous linewidth. Thus the smaller linewidths observed in the fluoride glasses compared to the oxide glasses are due to weaker chemical bonds and larger interatomic distances. Significant structural differences resulting from the presence of different local site configurations are not only reflected as structure in the inhomogeneous band profile, but also as deviations from the simple monotonic variations of both the homogeneous and residual inhomogeneous linewidths as a function of energy within the inhomogeneous band.

The FLN technique used here is a powerful method for probing the effects of local structural changes on the properties of an optically active probe ion. For a complete understanding of these effects it is important to obtain precise structural information on the glass hosts.

Office. The authors are grateful to Drs. M.G. Drexhage and M.J. Weber for providing the samples used in this research.

References

[1] P. Selzer, D.L. Huber, D.S. Hamilton, W.M. Yen and M.J. Weber, Phys. Rev. Lett. 36 (1976) 813.

[2] Amorphous Solids, Low Temperature Properties, ed. W.A. Phillips (Springer, Berlin, 1981).

[3] P.W. Anderson, B.J. Halperin and C.M. Varma, Phyl. Mag. 25 (1972) 1; W.A. Phillips, J. Low Temp. Phys. 7 (1972) 351.

[4] S. Alexander and R. Orbach, J. Phys. (Paris) 43 (1982) L625.

[5] G.S. Dixon, R.C. Powell and X. Gang, Phys. Rev. B 33 (1986) 2713; J. Phys. (Paris) 10 (1985) C7-331.

[6] P.M. Selzer, D.L. Huber, D.S. Hamilton, W.M. Yen and M.J. Weber, in; Structure and Excitations of Amorphous Solids, eds. G. Lucovsky and F.L. Galeener (Am. Inst. Phys., New York, 1976).

[7] X. Gang and R.C. Powell, J. Appl. Phys. 57 (1985) 1299.

[8] T. Kushida and E. Takushi, Phys. Rev. B 12 (1975) 824.

[9] G. Boulon, M. Bouderbala and J. Seriot, J. Less-Common Met. 112 (1985) 41.

[10] F. Durville, G. Boulon, R. Reisfeld, H. Mack and C.K. Jorgensen, Chem. Phys. Lett. 102 (1983) 393.

[11] M. Bouderbala, Doctoral dissertation, University of Lyon I, France (1985).

[12] F.L. Galeener, Solid State Commun. 44 (1982) 1037.

[13] B.B. Mandelbrot, Fractals (Freeman, San Francisco, 1977).

[14] H.J. Stapleton, J.P. Allen, C.P. Flynn, D.G. Stinson and S.R. Kurtz, Phys. Rev. Lett. 45 (1980) 1456.

[15] S. Alexander, C. Laermans, R. Orbach and H.M. Rosenberg, Phys. Rev. B 28 (1983) 4615.

[16] P.F. Tua, S.J. Putterman and R. Orbach, Phys. Lett. A 98, (1983) 357.

[17] A. Aharony, S. Alexander, O. Entin-Wohlman and R. Orbach, Phys. Rev. B 31 (1985) 2565.

[18] U. Buchenau, N. Nuecker and A.J. Dianoux, Phys. Rev. Lett. 53 (1984) 2316.

[19] G.S. Dixon, to be published.

[20] B. DiBartolo, Optical Interactions in Solids (Wiley, New York, 1968) Chapt. 15.

[21] J. Hegarty and W.M. Yen, Phys. Rev. Lett. 43 (1979) 1126.

[22] R. Orbach, Proc. Royal Soc. A 264 (1961) 458.

[23] J.M. Pellegrino, W.M. Yen and M.J. Weber, J. Appl. Phys. 51 (1981) 6332.

[24] R. Bundage and W.M. Yen. Phys. Rev. B 33 (1986) 4436.

[25] D.E. McCumber and M.D. Sturge, J. Appl. Phys. 34 (1963) 1682.

[26] K. Lucas, M. Chanthanasinh, M. Poulain, M. Poulain, P. Brun and M.J. Weber, J. Non-Cryst. Sol. 27 (1978) 273.

[27] S. Alexander, O. Entin-Wohlman and R. Orbach, J. Phys. (Paris) Lett. 46 (1985) L-555.

[28] M.J. Weber, in: Laser Spectroscopy of Solids, eds. W.M. Yen and P.M. Selzer (Springer-Verlag, New York) p. 189.

Laser-induced refractive-index gratings in Eu-doped glasses

Frederic M. Durville, Edward G. Behrens, and Richard C. Powell

Department of Physics, Oklahoma State University, Stillwater, Oklahoma 74078-0444

(Received 25 April 1986)

Four-wave-mixing techniques were used to establish and probe refractive-index gratings in Eu^{3+}-doped silicate and phosphate glasses. When the Eu^{3+} ions are resonantly excited, superimposed transient and permanent gratings are formed. The former are characteristic of population gratings of excited Eu^{3+} ions while the latter are attributed to local structural modifications of the glass hosts. The time dependences of the grating buildup, decay, and erasure are reported as a function of temperature, laser power, and "write"-beam crossing angle for each of the samples. The results suggest the use of laser-induced gratings in these glasses in applications such as amplitude-modulated phase-conjugate reflectors.

I. INTRODUCTION

During the past ten years, a significant amount of work has been done in developing new optical devices designed to provide functions such a switching, modulation, phase conjugation, and bistability which are important in optical data processing applications. Glasses are very attractive materials for these devices because of the low cost and ease of fabrication compared to single crystals, and because they provide the opportunity for developing monolithic devices within systems based on fiber-optic transmission. Laser-induced refractive-index changes have been observed in several types of glasses[1−5] and used to produce holographic storage, narrow-band filters, optical switching, and phase conjugation. In most cases, the physical mechanism producing the photorefractive change has not been explained. We report here the observation of laser-induced, superimposed transient and permanent refractive-index changes in a rare-earth-doped glass. This provides a means for amplitude-modulated phase conjugation and switching. Details are presented of the results of four-wave-mixing (FWM) measurements in three different types of Eu^{3+}-doped glasses. For each sample it is found that resonant excitation of the Eu^{3+} ions with crossed laser beams results in both transient population gratings and permanent holographic gratings. The dynamics of establishing and erasing these gratings were investigated as a function of laser power and temperature, and the results are interpreted in terms of a model based on vibrationally-induced structural modification of the host glass.

The glasses used in this work are europium pentaphosphate (EP), lithium phosphate (LP), and sodium silicate (NS). Their compositions are given in Table I and their spectroscopic properties have been reported previously.[6,7] Similar measurements made on Eu^{3+}-doped borate, germanate, and fluoride glasses produced no strong, permanent FWM signal.

The experimental apparatus used for these experiments is shown in Fig. 1. The output of a Spectra Physics cw argon laser is split into two beams which are crossed inside the sample to form an interference pattern in the shape of a sine wave grating. The optical path lengths of both "write beams" are equal to within the coherence length of the laser. The wavelength is tuned to 465.8 nm in order to resonantly excite the $^5D_2$ level of the Eu^{3+} ions. The total power was varied between 10 and 160 mW by a variable neutral density filter. The interference pattern of the crossed laser beams creates a change in the re-

TABLE I. Summary of results.

Parameter	EP	Sample LP	NS
Network former (mol %)	83.3 P_2O_5	52.3 P_2O_5	72.0 SiO_2
Network modifier (mol %)		30.0 Li_2O	15.0 Na_2O
		10.0 CaO	5.0 BaO
		4.7 Al_2O_3	5.0 ZrO
Eu^{3+} content (mol %)	16.7 Eu_2O_3	3.0 Eu_2O_3	3.0 Eu_2O_3
τ_f (ms)	2.7	2.8	2.7
τ_t (ms)	2.67	2.85	2.86
t_{rise} (min)	15	30	0[a]
ΔE_g (cm^{-1})	3983	2101	2890
ΔE_{e0} (cm^{-1})	4016	3213	614
ΔE_f (cm^{-1})	2219	3824	699

[a]After the "write" beams were turned off, a risetime of about 5 min was observed.
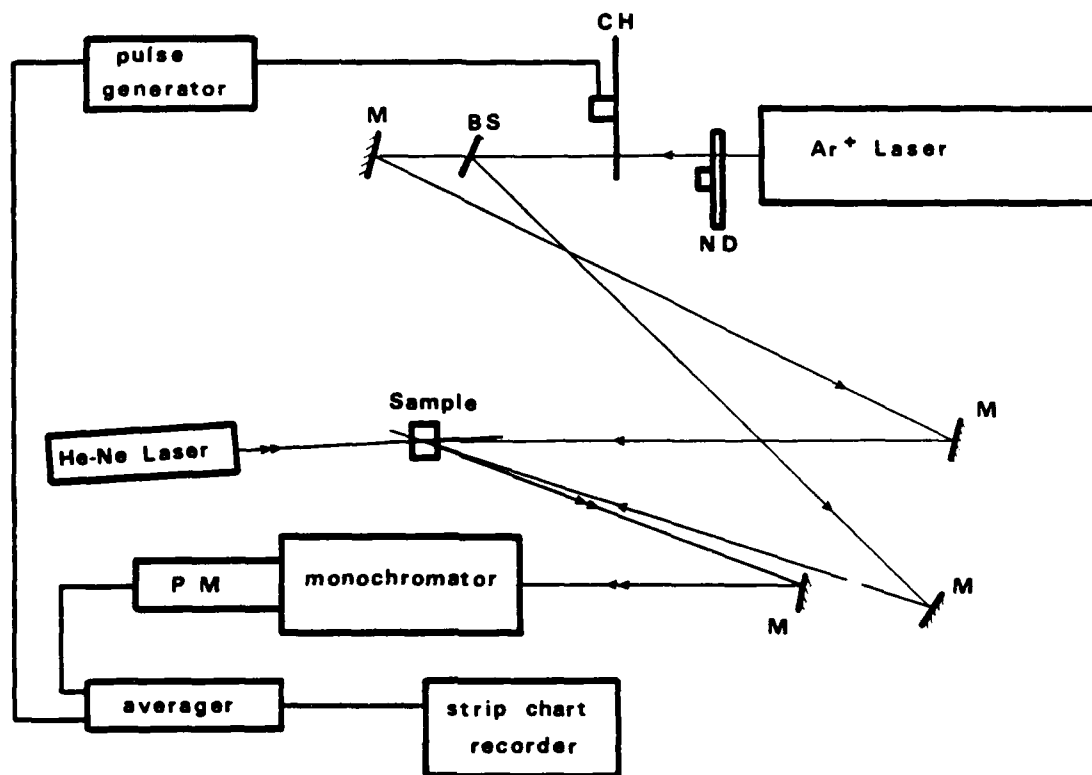
FIG. 1. Schematic diagram of the experimental setup used in the laser-induced grating experiments. ND—variable neutral density-density filter: CH—chopper; BS—beam splitter; M—mirror.

fractive index with the same shape. This acts like a "grating" and scatters the 10 mW "read" beam from a He-Ne laser at 632.8 nm. The maximum scattered signal beam is obtained at the Bragg condition for which the read beam is slightly misaligned from being counter propagating with one of the write beams and the signal beam is slightly off counter propagating with the other write beam. A mirror is used to pick off the signal beam and send it through a 0.25-m monochromator to eliminate sample fluorescence. The signal is detected by a Hamamatsu R1547 photomultiplier tube, processed by an EG&G/PAR signal averager, and read out on a strip chart recorder. For transient decay measurements, a chopper was used to cutoff the write beams while the decay of the signal beam was recorded. A pulse generator established the chopper frequency at about 20 Hz and triggered the signal averager. The erasure of the permanent grating was accomplished by exposure to a single laser beam at 465.8 nm and an EG&G/PAR lock-in amplifier was used to enhance the signal-to-noise ratio while measuring the signal beam scattered from the decaying permanent grating. For low-temperature measurements the sample is mounted in a cryogenic refrigerator with a temperature controller capable of temperature variation between about 10 and 300 K. For high-temperature measurements, the sample is mounted in a resistance heated furnace with a Chromel-Alumel thermocouple that can control the temperature between 300 and 775 K.

II. EXPERIMENTAL RESULTS

For all three samples, strong FWM signals were observed only if the write beams were tuned to resonance with an absorption transition of the Eu^{3+} ions. This shows that the mechanism producing the FWM signal is directly associated with the Eu^{3+} ions and that the impurity-induced nonlinear optical effect is significantly greater than the intrinsic nonlinear optical properties of the host glass.

Typical results for the time evolution of the FWM signals at room temperature are shown in Fig. 2. For both phosphate glasses the signal builds up slowly in time, reaching a maximum after about 15 min for EP and 30 min for LP, whereas for the silicate sample the signal immediately reaches maximum. The rate of signal buildup was found to be independent of write-beam laser intensity and grating spacing. For the same experimental conditions, the maximum signal strength was greatest for the EP sample and least for the NS sample. When the write beams were chopped off, the signal beams initially decayed exponentially with a decay time τ_r of the order of a few milliseconds as listed in Table I. For the EP and LP samples, the signal leveled off at about 70% of its maximum value and remained there indefinitely. For the NS sample the initial decay decreased to almost zero signal intensity, and this was followed by a buildup back to about 40% of the initial level as shown in Fig. 2(b). The
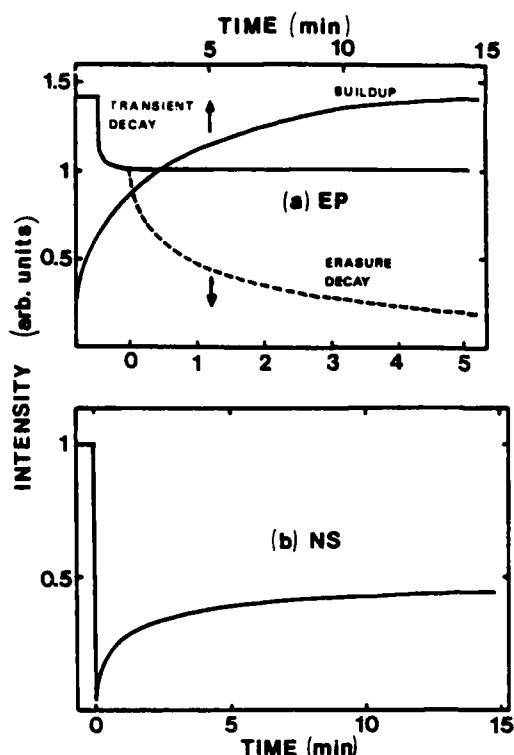
FIG. 2. Time evolution of the buildup, transient decay, and erasure of FWM signals in EP (a) and NS (b) glasses at 300 K. The total power of the laser write beams is 80 mW and the erase beam power is 40 mW.

permanent signal can be erased optically by switching on only one of the write beams in resonance with a Eu^{3+} transition. The rate of erasure varies with the intensity of the laser erase beam, with a typical erasure time shown in Fig. 2(a). The permanent signal can also be erased thermally by heating the samples up to about 390 K for
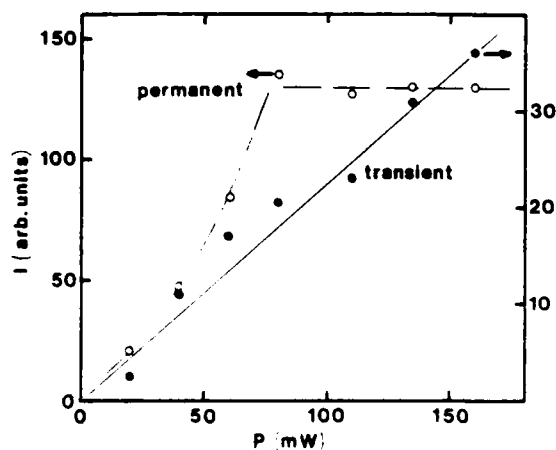

FIG. 3. Transient and permanent FWM signal intensities as a function of total write-beam laser power for EP at 300 K.

EP, 420 K for LP, and 520 K for NS. The total FWM signal can be treated as the superposition of read beams scattered from a transient grating and a permanent grating. Both components of the signal have intensities and decay rates which vary with laser power and crossing angle of the write beams, and with temperature, as described below.

Figure 3 shows an example of the variation of the permanent and transient signal intensities with the total laser power of the write beams. The intensity of the transient component of the signal increases linearly with laser power whereas the intensity of the permanent component of the signal initially increases approximately quadratically with laser power and then becomes independent of laser power above about 80 mW.

Figure 4 shows examples of the variations of the permanent and transient signal intensities with the crossing angle of the write beams. For all three samples, both signal components of the scattering efficiency decreases as the crossing angle increases. This is typical behavior for FWM signals and is associated with the length in which the probe beam interacts with the refractive-index grating
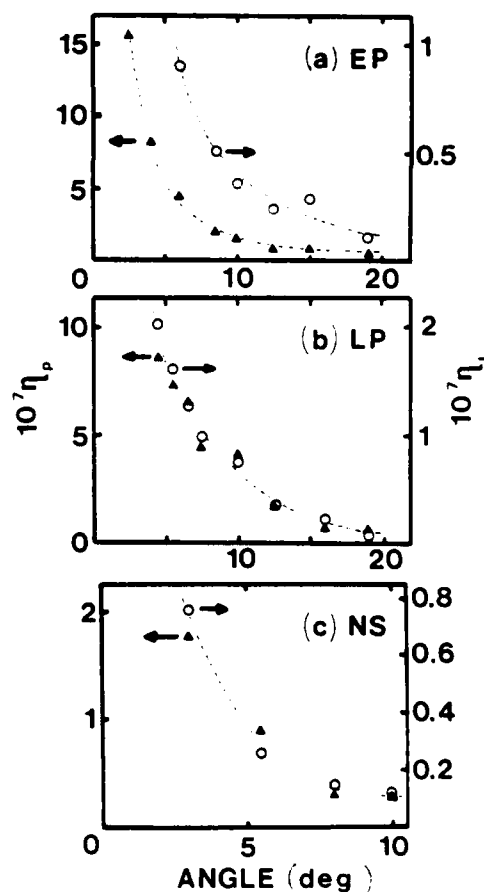

ANGLE (deg)

FIG. 4. Transient (○) and permanent (▲) FWM signal efficiencies as a function of the crossing angle of the write beams in air at 300 K. (a) EP glass; (b) LP glass; (c) NS glass.

as well as the density of fringes and modulation depth of the grating. The exact form of the angular variation depends on the strength and mechanism of the beam coupling.

If a permanent grating is established at room temperature, the signal intensity of scattering from this grating decreases as temperature is increased. Typical results of this type of experiment are shown in Fig. 5. The maximum scattering intensities of both the permanent and transient gratings decrease as the sample temperature at which the grating is established increases. As shown in Fig. 6, the FWM signal components from both types of gratings decrease uniformly in the same way for the EP glass. This is initially true for the LP glass, but above about 350 K the transient signal can no longer be detected while the permanent signal intensity becomes independent of temperature. For the NS glass, both components of the FWM signal intensity initially increase with an increase in temperature, and then decrease uniformly in the same way for temperature increases above about 330 K. This behavior is associated with a change in the buildup of the permanent signal. Above about 330 K the signal in the NS glass has the same time evolution as the signal in the other samples at room temperature.

Both the transient signal decay rate and the permanent signal erasure rate were measured to be independent of the crossing angle of the laser write beams for all three samples. For the transient signal, the value of the grating decay rate is the same as the fluorescence decay rate of the
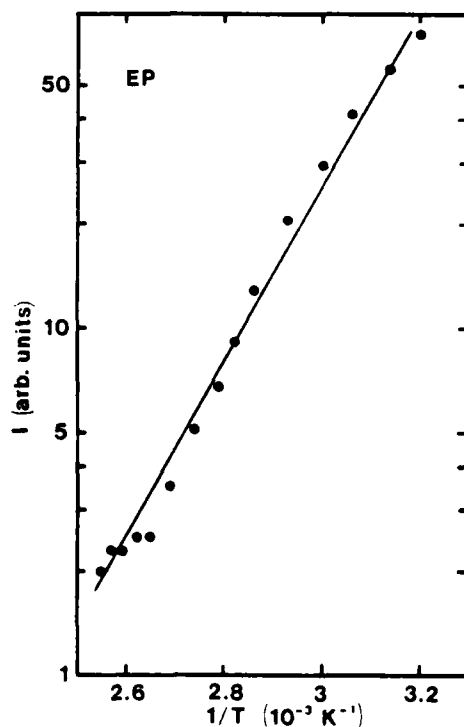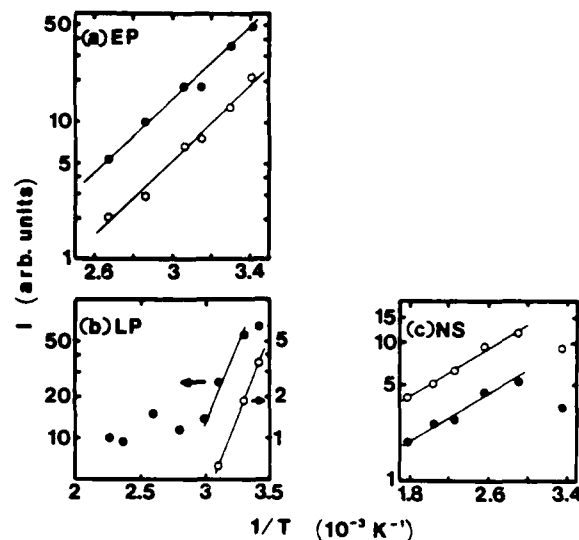

FIG. 6. Variation of the permanent (●) and transient (○) FWM signal intensities as a function of temperature of formation of the laser-induced gratings for (a) EP, (b) LP, and (c) NS samples. The total laser power of the write beams is 80 mW and the crossing angle in air is 7°.

$^5D_0$ level of the Eu^{3+} ions, τ_f, as measured by independent experiments. These are listed in Table I.

The erasure rate for all three samples increases exponentially as the temperature at which the gratings are established and erased is increased. The rate of change of erase rate with temperature is significantly different for each of the samples as shown in Fig. 7.

FIG. 5. Variation of the permanent FWM signal intensity as a function of temperature after laser-induced grating formation at 300 K in EP.
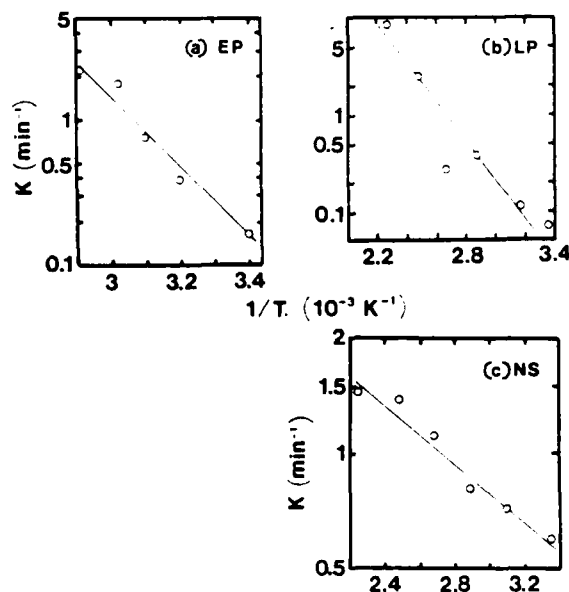

FIG. 7. Erasure decay rate of the permanent FWM signal as a function of temperature for (a) EP, (b) LP, and (c) NS at $\theta = 7°$. The laser power in the erase beam is 40 mW.

III. INTERPRETATION OF RESULTS

The dynamics of the buildup and decay of FWM signals described in the previous section are consistent with scattering from two superimposed, laser-induced gratings. The FWM signal is proportional to the square of the change in the complex refractive-index induced in the material by the interference of the laser write beams,[8] which in this case is the sum of the transient and permanent contributions to the change in the refractive index, $\Delta n \propto \Delta n_t + \Delta n_p$. If the transient component is assumed to decay exponentially with decay time τ_t, while the permanent component is time independent, the signal is described by

$$I_s \propto |\Delta n|^2 = |\Delta n_t|^2 \exp(-2t/\tau_t)$$
$$+ 2\Delta n_t \Delta n_p \exp(-t/\tau_t) + |\Delta n_p|^2 . \quad (1)$$

The data shown in Fig. 2 imply that the first term in Eq. (1) is essentially negligible with respect to the last two terms.

A. Transient grating

Equation (1) predicts that the transient contribution to the FWM signal will decay exponentially with the decay time of the transient grating. This is consistent with the observed exponential transient decay. The fact that the FWM transient signal decay time is the same as the fluorescence decay time of the $^5D_0$ level of the Eu^{3+} ions, coupled with the fact that the FWM signal is observed only when a Eu^{3+} absorption transition is directly excited, shows that the transient grating is associated with a population grating of Eu^{3+} ions in the $^5D_0$ metastable state. Since the crossing angle of the laser write beams determines the grating spacing, the lack of any change of decay time with θ indicates that there is no long-range energy transfer in the excited state.

The linear increase in the transient component of the scattering efficiency with laser power should be described by the middle term in Eq. (1). The variation Δn_p due to the permanent grating is linear with laser power as discussed below. Thus, Δn_t associated with the transient grating appears to be independent of laser power at low powers and to vary linearly with laser power at high powers. It should be noted that the measurements of the signal intensities from the transient gratings took place after the signals from the permanent gratings had reached their maximum value. Thus the measured variation of transient grating scattering efficiency on laser power may be associated with the presence of the strong permanent grating.

The decrease in the intensity of the transient component of the scattering intensity with increasing write-beam crossing angle is the behavior typically observed for FWM signals.[8] The scattering intensity of the transient signal decreases with increasing temperature in the same way as the intensity of the permanent signal. This implies that the refractive-index changes associated with the two gratings vary in the same way with temperature. The solid lines in Fig. 6 describe an exponential temperature variation

$$I = I_0 \exp(\Delta E_f'/kT) , \quad (2)$$

where $\Delta E_f'$ is the activation energy and k is Boltzmann's constant. The values obtained for $\Delta E_f'$ for each sample are listed in Table I and their physical meaning is discussed below.

B. Permanent grating

Scattering of the read beam from the permanent grating contributes to the observed FWM signal through the third term in Eq. (1) as well as the second term describing the interference between the signals from the permanent and transient gratings. The fact that the grating takes times of the order of 15 min to build up and then shows no decay at room temperature over periods of days, indicates that the interference pattern of the laser write beams has produced some permanent change in the glass host. However, this change occurs only if the laser beams directly interact with a resonant transition of the Eu^{3+} ions.

The quadratic dependence of the signal intensity from the permanent grating on the power of the laser write beams as shown in Fig. 3, is consistent with the prediction of Eq. (1). The observed saturation shows that there is a limit to the glass modification that can take place. The decrease in scattering intensity with increasing write beam crossing angle shown in Fig. 4 is typical of FWM signals, as mentioned above.

The fact that the permanent grating can be erased, shows that the laser-induced change in the glass is reversible. The lack of change of the erasure decay rate with the crossing angle of the write beams indicates that the glass modification does not involve long-range migration of charge carriers. Since erasure can occur both thermally and by laser excitation of an absorption transition of the Eu^{3+} ions, the structural modification can be reversed with the Eu^{3+} ions in either the ground or excited state.

The observed temperature dependences of the signal intensities and erasure rates are consistent with exponential processes having activation energies ΔE_g for thermal erasure and ΔE_{e0} for thermally assisted optical erasure. The solid lines in Figs. 5−7 represent the best fits to the experimental data with an exponential expression. The values obtained for the activation energies are listed in Table I. The value of ΔE_g was obtained from the data in Fig. 5 and represents the activation energy of thermal erasure with the Eu^{3+} ions in the ground state. The value of ΔE_{e0} was obtained from the data in Fig. 7 and represents the activation energy of thermally assisted optical erasure with the Eu^{3+} ions in the excited state. The value of ΔE_f was obtained from the data in Fig. 6 and represents the thermal activation energy associated with the grating formation process. This may be affected by concurrent erasure during grating formation, by thermal population of higher energy Eu^{3+} levels, or by thermally activated energy migration.

IV. DISCUSSION AND CONCLUSIONS

The FWM signal from the transient population grating observed here has significantly different properties from laser-induced population gratings studied previously.[9-13]

For example, the decay rate of FWM signals associated with population gratings is usually reported to be twice the fluorescence decay rate, not equal to the fluorescence decay rate as observed here. The reason for these differences is clear from Eq. (1). We are not observing a FWM signal associated with an isolated population grating, but rather the signal associated with the interference between a permanent grating and a transient grating. According to Eq. (1), the intensity variations of the signal associated with this interference term will be affected by changes in the intensity of the permanent grating, while the decay will be described by the fluorescence decay rate. This accurately describes the observations for each of the three samples.

Permanent gratings can be created by crossed laser beams through several physical mechanisms. The most common mechanism is the photorefractive effect associated with the photoionization of defects and subsequent trapping of the free carriers.[14] This type of mechanism can also lead to spectral hole burning, although this effect is seen only at low temperatures.[15] The properties of the permanent gratings reported here are not consistent with this mechanism. The energy-level scheme for Eu^{3+} in these glass hosts is not compatible with an ionization transition at the laser wavelength used in these experiments. Multiphoton transitions are not probable with the low laser powers used and not consistent with the observed power dependence of the signal intensities. Also, no effects of refractive-index changes are observed with a single laser beam as they are for photorefractive materials. In addition, the fact that optical erasure occurs only when Eu^{3+} ions are resonantly excited is not consistent with the photoionization process. No spectral evidence was observed for the presence of Eu ions in valence states other than trivalent. Finally, the intensities of the two write beams were monitored as a function of time and no energy transfer between the two beams was observed. These two-beam mixing results show that the laser-induced grating is in phase with the laser interference pattern. This shows that the mechanism causing the grating is localized, which is not always true for gratings involving the migration of charge carriers.

Thermal processes can also produce refractive-index changes. Laser-induced stress-optic changes including some permanent effects have been seen in rare-earth-doped glasses.[16,17] However, these observations were not dependent on having crossed laser beams and took place at higher powers than those used in our experiments. If local heating effects are the origin of the observed permanent grating, they should be described by the thermal conductivity equation,

$$-\partial Q/\partial t = \kappa A \nabla T ,$$ (3)

where Q is the heat deposited by the laser in an area A, κ is the thermal conductivity of the glass, and ∇T is the local temperature gradient produced by this heat. For the glasses used in this work, the thermal conductivities are of the order of 10^{-2} cm^{-1}K^{-1}. The laser power is less than 0.1 W with a beam cross-section area of less than 0.02 cm^2. Using these conditions, the local rise in temperature predicted by Eq. (3) is only a few degrees. In addition,

these numbers overestimate ∇T because all of the laser power is not absorbed by the Eu^{3+} ions and converted to heat. Thus, standard local heating effects are not large enough to produce any permanent modifications of the glass.

The analysis given in the previous paragraph assumes a thermalized "phonon" bath in the host material. This condition is not satisfied in the local regions where the laser power is absorbed. The radiationless relaxation transitions of rare-earth ions in glasses have been shown to be "multiphonon" emission processes,[18] each of which generates several high-energy "phonons," of the order of 1000 cm^{-1}. Since these are generated by the Eu^{3+} ions and the thermal diffusion in the glass host is slow, the phonons are localized thus creating a high level of nonthermalized vibrational energy around each ion. This can produce a local "effective temperature" which is extremely high compared to the thermal equilibrium temperature reached when these high energy phonons migrate away from their origin and become thermalized with the phonon modes of the host. For the radiationless relaxation processes of the Eu^{3+} ions under the excitation conditions of this experiment, local effective temperatures of the order of several thousand degrees Kelvin can be produced. This is easily enough to allow ionic motion over short ranges and thus produces a local structural modification of the host glass.

Based on the above discussion, we propose a model for the laser-induced permanent grating described by the configuration coordinate diagram shown in Fig. 8. It is assumed that the network forming and modifier ions of the glass host can arrange themselves in two possible configurations in the local environment of the Eu^{3+} ions, leading to double minima potential wells for the Eu^{3+} energy levels. For simplicity, only the three terms of the Eu^{3+} ions of direct relevance to the optical transitions of interest here, are shown in Fig. 8. The material is assumed to have a different index of refraction depending on which configuration is present. Under normal conditions of optical excitation and decay, the configuration coordinates appear as the solid lines in Fig. 8, and the ions will remain in the lower energy configuration, designated as I. The generation of local thermal energy may allow some of the ions to cross the potential barrier into configuration II, but it also will cause transitions in the reverse direction. The relative occupations of the two potential configurations will remain in thermal equilibrium, and as the local temperature returns to normal there will be a predominant occupancy of the lower energy potential well. However, with crossed laser beams, there is a gradient in the number density of high energy phonons resulting in a gradient in the local effective temperature. On a microscopic scale, the atomic motion involved in the configurational rearrangement can be described as an ionic conduction process involving only a few steps. In this picture the tendency of the vibrating atoms is to diffuse away from the peak of the temperature gradient. This gives a directional bias to the hopping of the atoms between sites of the different configurations. The resulting bias can be schematically represented by the change from the solid to the broken line potential curves in Fig. 8. This shifts lower potential minimum from configuration I to configuration II and
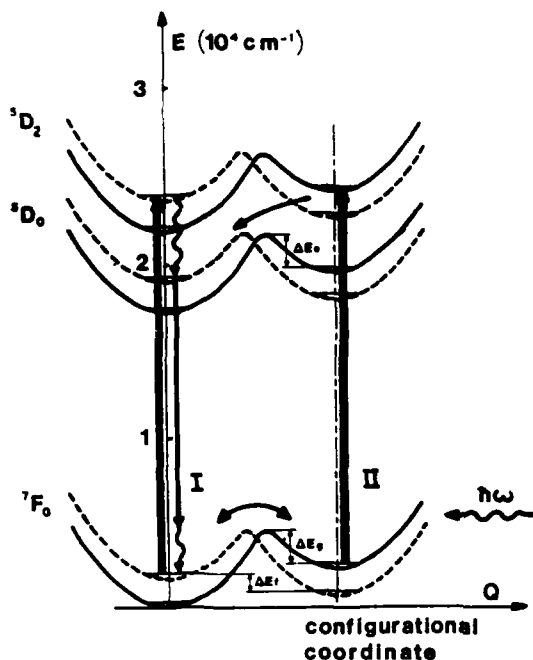
FIG. 8. Configuration coordinate model for laser-induced permanent gratings in Eu^{3+}-doped glass. The diagram shows only the relevant energy levels of the Eu^{3+} ions with two possible local configurations of the glass, I and II. The solid curves are for normal conditions of excitation and decay. The broken curves represent the change in potential coordinates due to the presence of crossed laser beams which creates a directional bias for ion motion. (See the text for explanation of transitions shown in the model).

on the upper multiplets $(J = 1 - 6)$ of the ^7F term and then decay through radiationless transitions to the $^7F_0$ ground-state multiplet. These processes generate several more high-energy phonons. The phonons produced through both excited-state and ground-state radiationless transitions provide the thermal energy needed to increase the occupancy of configuration II.

From this model, the refractive index can be written as the sum of the contributions from both configurations,

$$n = N_I n_I + N_{II} n_{II} , \qquad (4)$$

where N_I and N_{II} are the populations of the two potential wells and n_I and n_{II} are the indices of refraction for the two configurations. For thermal equilibrium with the laser write beams on

$$N_I/N_{II} = \exp(\Delta E_f/kT) , \qquad (5)$$

where ΔE_f is the energy difference between the potential minima for the two configurations in the presence of the crossed laser beams and k is Boltzmann's constant. The FWM signal is proportional to the square of the difference of the index of refraction in the peak and valley region of the grating. If the valley regions of the grating are assumed to be all in configuration I, the FWM signal is given by

$$I \propto |\Delta n_{p-v}|^2 = N_{I_p}^2 |\Delta n_{II-I}|^2 \exp[2\Delta E_f/(kT)] . \qquad (6)$$

The p and v subscripts refer to the peak and valley regions of the grating, respectively. This shows that the measured activation energy for the formation of the permanent grating $\Delta E_f'$ is twice the difference in the energy of the potential minima.

Erasure occurs thermally when the temperature is raised high enough to provide the energy ΔE_g needed to cross the ground-state potential barrier between configuration II and configuration I. With no crossed laser beams present, the solid coordinate curve is the relevant one in Fig. 8. This thermal energy allows the populations of the two potential configurations to redistribute themselves to the normal equilibrium case with predominant occupancy in configuration I. Optical erasure occurs with a single laser beam tuned to resonance with the $^7F_0$-$^5D_2$ transition between the solid coordinate curves in configuration II. Relaxation back to the equilibrium population distribution can take place by several paths. Starting from the $^5D_2$ level in II, the excited Eu^{3+} ions relax back to the ground state and crossover to the I configuration which can take place at any of the levels occupied during the relaxation. Increasing the temperature will enhance optical erasure by making it easier to cross over the potential barriers such as the ΔE_e shown as an example in Fig. 8. Since crossover can occur with several different barriers, it is difficult to assign an exact meaning to the measured values of ΔE_{e0}. However, as for the thermal variation of the scattering, we can use a crude model to explain the thermal variation of the optical erasure rate. Assuming the excited ions relax to the $^5D_0$ state before any cross over to a different configuration occurs, the theory of Jortner and co-workers[19,20] can be used. This was developed for radiationless transitions in large molecules

thus builds up an increased population in configuration II. Even if this effect is quite small, over the several-minute time period of the grating buildup a significant change in configuration occupancy can be produced. When the crossed laser beams are turned off, the directional bias is removed and the configuration coordinates shift back to those shown by solid lines in Fig. 8, but the population built up in II remains. Since this "frozen in" distribution of excess occupation of II has the shape of the laser interference pattern, it appears to the probe beam as a refractive-index grating.

The transitions shown in Fig. 8 represent the processes involved in the formation and erasure of the permanent grating. Initially the ions predominantly occupy configuration I in the solid-line coordinate representation. During the grating formation period, crossed laser beams are tuned to resonance with the $^7F_0$-$^5D_2$ transition of the Eu^{3+} ions. This produces the directional bias to shift the coordinate curves to the broken lines, as discussed above, and excites some of the Eu^{3+} ions to the $^5D_2$ level. The excitation energy is dissipated partially by radiative transitions to the ground terms and partially by radiationless transitions to the $^5D_0$ level through the emission of several high-energy phonons. The $^5D_0$ level also has radiative transitions to the ground terms. Most of the fluorescence transitions from both multiplets of the ^5D term terminate

and has been successfully used to explain the nonradiative recombination of trapped excitons in chalcogenide glasses.[21] At high temperatures and strong displacement of configuration minima, the approximate expression for the radiationless transition rate becomes

$$W_{\mathrm{II-I}} = C^2[4\pi kT/(hE_M)^2]^{1/2}$$

$$\times \exp[-(E_M-\Delta E)^2/(4E_M kT)] , \qquad (7)$$

where C is the matrix element for the transition and $(E_m-\Delta E)^2/(4E_M)$ corresponds to the energy barrier between the two potential wells. This can be simplified in our case to

$$W_{\mathrm{II-I}} = W_0 T^{1/2}\exp(-\Delta E_e/kT) . \qquad (8)$$

For our data the temperature-dependent prefactor is negligible and Eq. (8) is consistent with the observed results. However, the possibility of configuration crossover in the $^5D_2$ state, or between the $^5D_2$ state of II and the $^5D_{1,0}$ states of I, or in levels of the ^7F_J manifold require that we interpret ΔE_{e0} as an "effective energy barrier" for crossover and not specifically associate it with a given level.

The difference in FWM properties between the EP and LP samples can be attributed to the significant difference in the Eu^{3+} concentration between the two samples. The difference between the LP and NS samples is more difficult to determine. Phosphate glasses have lower thermal conductivities, smaller nonlinear refractive indices, and different temperature coefficients of the refractive index compared to silicate glasses. To identify the properties most important in producing the observed FWM characteristics, different combinations of glass hosts and rare-earth ions need to be investigated.

Two-level systems have been proposed previously to explain other physical properties associated with vibrational modes in glasses.[22] However, the effects of having two possible configuration potentials have generally been considered only at very low temperatures. Laser-induced refractive-index changes in glasses have been observed for different types of glasses under different experimental conditions and the results attributed to bond rearrangements associated with trapped exciton effects.[3-5] This mechanism is not consistent with the results observed in our experiments. The model proposed here appears to be consistent with all of the observed characteristics of the laser-induced permanent grating. However, to verify this model more experimental data obtained on different kinds of glasses is needed.

The results reported here represent the first observation of an interference effect in an FWM signal due to the superposition of a transient population grating and a permanent grating due to structural modification of the host. Producing FWM signals in glasses of this type may be useful in optical systems involving fiber-optic transmission since it should be possible to use the techniques described here to establish phase conjugate mirrors and optical switches directly in the glass fibers. Finally, understanding the details of the mechanism for forming the laser-induced permanent gratings may lead to a better understanding of the local structural and vibrational properties of these types of glasses.

ACKNOWLEDGMENT

[1] J. Bures, J. Lapierre, and D. Pascale, Appl. Phys. Lett. 37, 860 (1980).

[2] K. O. Hill, Y. Fujii, D. C. Johnson, and B. S. Kawasaki, Appl. Phys. Lett. 32, 647 (1978); B. S. Kawasaki, K. O. Hill, D. C. Johnson, and Y. Fujii, Opt. Lett. 3, 66 (1978).

[3] R. A. Street, Solid State Commun. 24, 363 (1977).

[4] K. Tanaka and A. Osajima, Appl. Phys. Lett. 38, 481 (1981).

[5] J. H. Kwon, C. H. Kwak, and S. S. Lee, Opt. Lett. 10, 568 (1985).

[6] G. S. Dixon, R. C. Powell, and X. Gang, Phys. Rev. B 33, 2713 (1986).

[7] X. Gang and R. C. Powell, J. Appl. Phys. 57, 1299 (1985).

[8] J. Feinberg, in Optical Phase Conjugation, edited by R. A. Fisher (Academic, New York, 1983), p. 417.

[9] H. J. Eichler, J. Eichler, J. Knof, and Ch. Noack, Phys. Status Solidi A 52, 481 (1979).

[10] P. F. Liao, L. M. Humphrey, D. M. Bloom, and S. Geschwind, Phys. Rev. B 20, 4145 (1979); P. F. Liao and D. M. Bloom, Opt. Lett. 3, 4 (1978).

[11] J. R. Salcedo, A. E. Siegman, D. D. Dlott, and M. D. Fayer, Phys. Rev. Lett. 41, 131 (1978).

[12] J. K. Tyminski, R. C. Powell, and W. K. Zwicker, Phys. Rev. B 29, 6074 (1984).

[13] A. M. Ghazzawi, J. K. Tyminski, R. C. Powell, and J. C. Walling, Phys. Rev. B 30, 7182 (1984).

[14] P. Gunter, Phys. Rep. 93, 199 (1982).

[15] A. Winnacker, R. M. Shelby, and R. M. Macfarlane, Opt. Lett. 10, 350 (1985); R. M. Macfarlane and R. M. Shelby, in Coherence and Energy Transfer in Glasses, edited by P. A. Fleury and B. Golding (Plenum, New York, 1984), p. 189.

[16] L. G. DeShazer (private communication).

[17] C. L. Sauer, Ph.D. thesis, University of Southern California, 1980.

[18] C. B. Layne, W. H. Lowdermilk, and M. J. Weber, Phys. Rev. B 16, 10 (1977).

[19] K. F. Freed and J. Jortner, J. Chem. Phys. 52, 6272 (1970).

[20] R. Englman and J. Jortner, Mol. Phys. 18, 145 (1970); R. Englman, Nonradiative Decay of Ions and Molecules in Solids (North-Holland, Amsterdam, 1979).

[21] N. F. Mott, E. A. Davis, and R. A. Street, Philos. Mag. 32, 961 (1975).

[22] P. W. Anderson, B. I. Halperin, and C. M. Varma, Philos. Mag. 25, 1 (1972).

Relationship between laser-induced gratings and vibrational properties of Eu-doped glasses

Frederic M. Durville,* Edward G. Behrens, and Richard C. Powell

Department of Physics, Oklahoma State University, Stillwater, Oklahoma 74078-0444

(Received 20 October 1986)

Four-wave-mixing techniques have been shown previously to produce permanent refractive index gratings in Eu-doped glasses by resonant excitation of the Eu^{3+} ions. A variety of glass hosts were studied and it was found that permanent holographic gratings could be established in some of these but not in others. We report here an extension of our previous work which includes investigations of new materials, attempts to form gratings with different excitation wavelengths, and a comparison of the Raman and resonant Raman spectra of glasses which do and do not exhibit permanent holographic gratings. It was found that direct excitation into the $^5D_0$ level did not produce permanent gratings. It was also found that glasses which do exhibit permanent gratings have high-frequency vibrational modes which couple strongly to the Eu^{3+} ions. These results help to verify the model proposed previously to explain the origin of the holographic grating in terms of structural changes caused by thermal effects arising from radiationless relaxation through high-frequency local modes.

I. INTRODUCTION

We reported recently the observation of four-wave-mixing (FWM) signals in Eu^{3+}-doped glasses produced through resonant excitation of the Eu^{3+} ions in the $^5D_2$ level.[1] The observed signals had two components: a transient component associated with a Eu^{3+} population grating, and a permanent component associated with a holographic grating. The physical processes responsible for this latter component have not been established. The purpose of this paper is to report the results of further research in this area which provides additional information relevant to our understanding of the mechanism of producing this type of laser-induced grating.

The type of holographic grating of interest here is established with a buildup time of about 15 min with the write beams in resonance with the absorption transition to the $^5D_2$ level of Eu^{3+}. The grating can be erased optically only if the erase beam is in resonance with the $^5D_2$ absorption transition. The grating is stable at room temperature, but thermal erasure occurs with an increasing rate as temperature is raised above room temperature. Seven different types of oxide and fluoride glasses were studied previously, and under the same experimental conditions holographic gratings were observed in only three of these. An empirical model was suggested to explain the origin of these gratings based on having a local glass structure at the site of the Eu^3 ions which allows each electronic state to be described by a double-minimum potential curve. It is assumed in this model that the refractive index of the material is different, depending on which potential minimum is occupied by the Eu^{3+} ions. It is further assumed that the heat generated through radiationless relaxation of the excited Eu^{3+} ions can cause the local structure to change so that the ions move from one potential minimum to the other.

The model described above is consistent with the results reported previously, but further work is required to better understand the physical processes involved. The work reported here extends our previous investigations by looking at different types of glass hosts, different types of rare-earth ions, and different excitation wavelengths. In addition, the Raman and resonant Raman spectra were compared for example glasses that do and do not exhibit holographic gratings.

II. EXPERIMENTAL RESULTS

The initial set of glasses investigated[1] included three that exhibited permanent holographic gratings (europium pentaphosphate, lithium phosphate, and sodium silicate) and four glasses that did not produce holographic gratings (lithium silicate, lithium borate, lithium germanate, and zirconium fluoride). In addition to these, we have now investigated several other heavy-metal fluoride glasses, various other germanate and borate oxide glasses, and $La_xEu_{1-x}(PO_3)_3$ with x between 0.8 and 0.99. Holographic gratings were observed only in the last of these. This sample exhibited similar grating properties to the europium pentaphosphate sample but had a higher diffraction efficiency.

Several additional experiments were performed on the europium pentaphosphate (EuP_5O_{14}) sample which exhibited strong holographic gratings. For example, the effects of changing the polarization direction of the probe beam compared to the polarization directions of the write beams were investigated. No dependence of scattering efficiency on the probe-beam polarization direction was observed. Also, a phosphate glass sample (52.3 P_2O_5, 30.0 Li_2O, 10.0 CaO, 4.7 Al_2O_3, 3.0 Eu_2O_3 in mol %) was investigated which contained approximately the same concentration of europium as the lithium phosphate glass studied earlier but which had a mixture Eu^{3+} and Eu^{2+} valence states. No holographic grating was observed in this sample.

Attempts were made to observe permanent gratings in samples having different rare-earth ions in similar types

of glass hosts, such as NdP_5O_{14} glass. Under excitation conditions which should produce the same amount of heat through radiationless processes as in the EuP_5O_{14} glass, no grating formation was observed. Instead, strong thermal lensing effects were seen. In fact, it was found for several different types of trivalent rare-earth ions that thermal lensing was observed instead of the development of holographic gratings. Apparently the onset of thermal lensing inhibits the formation of holographic gratings. The relationship between these two types of processes is now being studied.

For all of the glasses which exhibit holographic gratings, all of the fluorescence emission occurs from the $^5D_0$ level regardless of the pumping conditions. Although this is also true for many of the glasses in which holographic gratings could not be produced, some of these glasses such as Eu-doped BZLT (27 ZnF_2, 19 BaF_2, 26 LuF_3, 27 ThF_4, 1 EuF_3 in mol %) showed a significant amount of fluorescence emission from the higher-lying ^5D_J levels. In this case there are fewer phonons emitted during relaxation in the excited state. To further establish the importance of radiationless relaxation in the excited state, an attempt was made to produce holographic gratings by exciting directly into the $^5D_0$ level instead of the $^5D_2$ level as was done previously. An argon-laser-pumped ring dye laser with R6G was used for these experiments. The laser power was set to achieve the same density of excited Eu^{3+} ions as obtained in the previous experiment in which grat-

ings were formed. Several samples were investigated, including the europium pentaphosphate sample which exhibits strong holographic gratings for $^5D_2$ excitation. No gratings were observed in any of the samples for $^5D_0$ excitation. This confirms the importance of having radiationless relaxation in the excited state to establish this type of grating. These nonradiative processes for rare-earth ions in glasses are known to take place through multiphonon emission involving several high-energy phonons.[2]

To further understand the vibrational modes involved in the writing of holographic gratings of this type, we compared the Raman spectra and resonant Raman spectra for glasses which exhibited gratings with those of glasses in which no gratings could be produced. Typical results are shown in Figs. 1 and 2. An argon laser was used as the source and an Instruments S. A. Ramanor U-1000 with computer-controlled data acquisition was used to record the spectra. The 514.5-nm argon-laser line gives the normal Raman spectra shown by dashed lines in Figs. 1 and 2, while the 472.7-nm laser line is close to the $^7F_0$-$^5D_2$ Eu^{3+} transition and therefore produces resonant Raman scattering. The solid lines in the figures show the latter type of spectra.

The disordered structure of glasses causes the network vibrations to have a short coherence length compared to the optical wavelength. This causes a breakdown of the wave-vector selection rule which is present for crystalline Raman spectra and results in Raman spectra for glasses
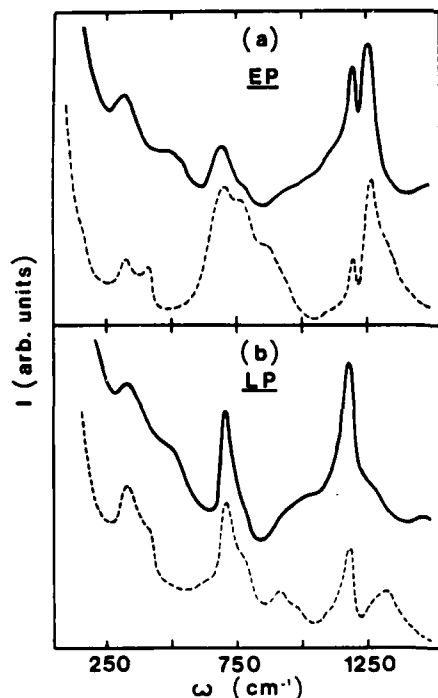

FIG. 1. Raman spectra (dashed lines) and resonant Raman spectra (solid lines) of (a) europium pentaphosphate glass, and (b) Eu^{3+}-doped lithium phosphate glass. (See text for exact glass compositions.)
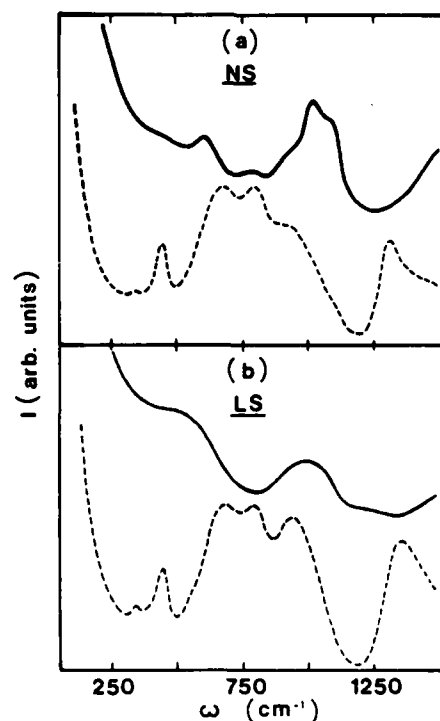
FIG. 2. Raman spectra (dashed lines) and resonant Raman spectra (solid lines) of (a) Eu^{3+}-doped sodium silicate glass, and (b) Eu^{3+}-doped lithium silicate glass. (See text for exact glass compositions.)

which are directly related to the vibrational density of states.[3] In addition, the vibrational modes of a glass are more localized than those of a crystal due to the lack of translational symmetry. The Stokes Raman scattering intensity is given by[4]

$$I(\omega_0,\omega)=(\hbar v E_0^2/2\pi c^3)\{(\omega_0+\omega)^4[n(\omega)+1]/\omega\}$$

$$\times\sum_b C_b(\omega_0,\omega)\rho_b(\omega),$$

where b refers to the different bands, E_0 and ω_0 are the incident electric field and frequency, respectively, ω is the frequency of the Raman shift, $\rho_b(\omega)$ is the vibrational density of states for band b, $n(\omega)=[\exp(\hbar\omega/k_BT)-1]^{-1}$ is the population factor, and $C_b(\omega_0,\omega)=|\sum_l P^l u_l^b(\omega)|^2$ is the coupling constant for the b band. Here P^l is the electronic polarizability and u_l is the normal displacement coordinate where l refers to the $3N$ Cartesian coordinates of the atoms. When ω_0 is close to an electronic transition frequency of Eu^{3+}, the coupling coefficient is dominated by contributions of $P^l u_l^b$ associated with vibrational modes localized around the Eu^{3+} ions.

The Raman spectra for the europium pentaphosphate (EP) and lithium phosphate (LP) (52.3 P_2O_5, 30.0 Li_2O, 10.0 CaO, 4.7 Al_2O_3, 3.0 Eu_2O_3 in mol %) samples shown in Fig. 1 both show a high-frequency band near 1200 cm^{-1} which is enhanced in the resonant Raman spectra. This indicates that the vibrational mode of this frequency is strongly coupled to the Eu^{3+} ions. Figure 2 shows similar spectra obtained on sodium silicate (NS) (15.0 Na_2O, 5.0 BaO, 5.0 ZrO, 72.0 SiO_2, 3.0 Eu_2O_3 in mol %) and lithium silicate (LS) (27.5 Li_2O, 10.0 CaO, 2.5 Al_2O_3, 57.0 SiO_2, 3.0 Eu_2O_3 in mol %) glass. The resonant Raman spectrum of the NS glass shows a strong enhancement of a band near 1050 cm^{-1}. This same band appears in the spectra of the LS sample, but no significant enhancement occurs under resonant excitation conditions. Such high-frequency bands do not appear in the Raman spectra of borate and fluorite glasses.[5-8]

III. DISCUSSION AND CONCLUSIONS

The results described above show that the formation of holographic gratings of the type of interest here requires a glass host having high-frequency local modes of vibration and further requires these modes to be strongly coupled to the Eu^{3+} ions. This enhances the radiationless relaxation processes compared to the radiative processes occurring after excitation of the Eu^{3+} ions, and these produce the local heating necessary for causing the structural modification of the host.

So far the best hosts for establishing these permanent gratings have been found to be phosphate glasses. The fundamental skeletal structure of phosphate glasses can be represented by practically infinite chains of interlinked PO_4 tetrahedra with two of the oxygens shared with neighboring tetrahedra. The vibrational band observed around 1200 cm^{-1} is attributed to stretching vibrations of PO_2 lateral groups[9,10] which involves the two unshared oxygens of the tetrahedra. The resonant enhancement of

this band shows that the Eu^{3+} ions are bonded to the PO_2 lateral groups and not to the chains. Thus the Eu^{3+} enter the glass structure as network modifiers. Because of the motional freedom of the lateral group oxygen ions, it is not unreasonable to expect different possible equilibrium positions for these groups, leading to different local environments for dopant ions such as Eu^{3+}.

On the other hand, silicate glasses have fundamental structures which are generally better described as a continuously randomly packed network with SiO_4 tetrahedra as the basic unit.[11] The introduction of alkali-metal ions partly breaks down this type of structure. These glasses exhibit a vibrational band near 1100 cm^{-1} that is attributed to the bond-stretching vibration of the Si—O nonbridging group.[12,13] In our samples, the resonantly enhanced band between 1000–1100 cm^{-1} can be seen as the superposition of three different bands with frequencies 940, 1020, and 1100 cm^{-1}. This last band corresponds to the stretching vibration of the Si—O nonbridging group. These vibrational bands are weaker in the LS sample due to the weaker activation of this vibrational mode by the Li^+ ion as compared with the Na^+ ions.[12] The Raman spectra suggest that part of the Eu^{3+} ions are bonded with the nonbridging oxygen ions in the NS sample, entering the glass structure as network modifiers along with the Na^+ ions. As in the pentaphosphate glasses, it is not unreasonable to expect different possible equilibrium positions for the nonbridging oxygens, leading to different Eu^{3+} environments.

The types of suggested structural modifications discussed above are not applicable to borate glasses where the structure is more rigid and can be formed by various cyclic units depending on the alkali-metal or alkaline-earth-metal content of the material.[5-7] The major vibrational band of borate glasses is around 805 cm^{-1} and is associated with the breathing mode of the boroxol rings forming the basic structural unit of the glass.[5-7] The other vibrational bands are at lower frequencies. The structure of the ZrF_4-based glasses can be described by chains of ZrF_6 octahedra sharing two oxygens with each of two other octahedra.[8] This is somewhat similar to the phosphate glass structure except that the octahedron are more rigid and exhibit a lower degree of disorder, making it more difficult to consider local structural modifications. The major vibrational bands of these glasses appear around 500–600 cm^{-1} and are associated with stretching vibrations of the Zr—F nonbridging bonds of the ZrF_6 octahedron forming the basic structural unit of the glass.[8]

The results described here are consistent with the model proposed previously for the formation of holographic gratings through resonant excitation of Eu^{3+} ions in glasses. The criteria for forming gratings of this type include having a glass structure which allows different local configurations for the Eu^{3+} ions through different possible equilibrium positions of the surrounding oxygen ions. The mechanism for switching between different types of equilibrium positions requires structures with high-frequency local vibrational modes such as those associated with structural defects (lateral or nonbridging groups) and further requires that the Eu^{3+} ions are strongly coupled to these vibrational modes. It also appears that these modes

should be uncoupled with the rest of the vibrational modes of the structure so that the generation of local heating through radiationless relaxation of the Eu^{3+} ions leads to structural changes instead of becoming thermalized and causing thermal lensing. There are still many questions to be answered concerning the details of grating formation and erasure on the atomic scale.

*Permanent address: UA442CNRS, Université Lyon I, Villeurbanne, France.

[1]F. M. Durville, E. G. Behrens, and R. C. Powell, Phys. Rev. B **34**, 4213 (1986); E. G. Behrens, R. M. Durville, and R. C. Powell, Opt. Lett. **11**, 653 (1986).

[2]C. B. Layne, W. H. Lowdermilk and M. J. Weber, Phys. Rev. B **16**, 10 (1977).

[3]R. Shuker and R. W. Gammon, Phys. Rev. Lett. **25**, 222 (1970).

[4]F. L. Galeener and P. N. Sen, Phys. Rev. B **17**, 1928 (1978).

[5]J. Wong and C. A. Angell, Appl. Spectr. Rev. **4**, 155 (1971).

[6]R. L. Mozzi and B. E. Warren, J. Appl. Cryst. **3**, 251 (1970).

[7]See, for example, M. Irion and M. Couzi, J. Solid State Chem. **31**, 285 (1980).

[8]R. M. Almeida and J. D. Mackenzie, J. Chem. Phys. **74**, 5954 (1981).

[9]Ya. S. Bobovich, Opt. Spectrosc. **13**, 274 (1962).

[10]B. N. Nelson and G. J. Exarhos, J. Chem. Phys. **71**, 2739 (1979).

[11]See, for example, R. J. Bell, N. F. Bird, and P. Dean, J. Phys. C **2**, 299 (1968).

[12]M. Hass, J. Phys. Chem. Solids **31**, 415 (1970).

[13]D. W. Matson, S. K. Sharma, and J. A. Philpotts, J. Non-Cryst. Solids **58**, 323 (1983).

END

DATE
FILMED
DTIC

JULY 88